Chapter 4

APPLICATION OF THE LAMELLAR THEORY TO RELATED STRUCTURES

4.1 INTRODUCTION

The previous two chapters have demonstrated the usefulness of a modal formulation, based on rectangular-waveguide modes, in enabling a detailed analysis of the spectral properties of the basic lamellar grating - both in reflection and transmission. In this chapter, advantage is taken of the simplicity of these modal functions in facilitating analysis of slightly more complicated (although still only singly-periodic) gratings which are a combination of lamellar-type layers.

The subject of Section 4.2 has been recently reported in reference [4.1] and is a device termed the "bottle" grating, consisting of a lamellar wire grating resting on a lamellar reflection grating. The aperture of the former is assumed to be smaller than that of the latter. Unusual interferometric action is obtained from this grating and in Section 4.4 its behaviour is compared with that of a wire grating situated close and parallel to a perfectly-conducting plane. Section 4.5 is concerned with the study of a step grating which is a structure related to the bottle grating. The difference between the two is that provision is now made for a number of transmission gratings to be stacked on the reflection grating and each of these has an aperture *larger* than the one below it. The result is a reflection grating whose grooves can be designed to approximate those of conventional gratings and which is shown to model quite capably their diffraction properties.

4.2 THE BOTTLE GRATING

4.2.1 Introduction

The success encountered in evaluating the resonance behaviour of the simple rectangular-groove profile prompted this investigation into the diffraction properties of a related periodic structure. Due to its unusual cross-sectional appearance, it was thought that this grating might exhibit a particularly striking resonance action and this has indeed proved correct. The device, which is termed a "bottle" grating, consists of a lamellar transmission grating of relatively small aperture width placed on a lamellar reflection grating of the same period, and with a larger aperture width, so that the two axes of periodicity are mutually parallel. The overall structure is a reflection grating in which each groove contains a cavity beneath the surface and it is this feature of the profile which produces interesting resonance phenomena in the efficiency spectra.

A formalism based on the modal expansion technique of Chapter 2 is developed to rigorously solve the scalar-wave diffraction problem for the structure. In Section 4.2.2 the details of this formalism are presented for S polarization, followed by a summary of the P polarization formalism. Section 4.2.3 deals with an outline of the appropriate phase properties which are implied from the work in Section 2.3.

Section 4.2.4 describes the spectacular resonance behaviour of the grating which is manifested in the diffracted order spectra as sharp peaks in efficiency occurring at predictable, but not regular wavelength intervals. Strong similarities are seen between this action and that of a Fabry-Perot interferometer such as the type studied by Casey and Lewis [4.2] and Adams and Botten [4.3]. These authors treat the problem of transmission through a parallel pair of wire gratings and demonstrate the existence of sharp interferometric peaks in the transmitted zero order. Such instruments are

only useful at wavelength-to-period ratios greater than unity and they rely on multiple-scattering between the upper and lower arrays to produce the interference. This mechanism is not appropriate to the bottle grating but good interferometer-like action is still evident.

Efficiency maxima in the diffraction spectra are found to occur at similar normalised wavelengths for both the normal incidence and -1 Littrow mountings, but the latter produces far superior results since the peaks in the diffracted efficiency reach 100% when only two orders are propagating. The minima separating these peaks are also much lower and so efforts are concentrated on this particular mounting.

In order to gain insight into the origin of the resonance behaviour, a single-mode truncation of the theory for *both* polarizations is employed and is detailed in Section 4.2.5. This treatment proves advantageous in explaining why the -1 Littrow mounting provides the best performance and also the influence that each of the grating parameters has on the position and form of the resonance features.

4.2.2 Modal Formulation

The structure under consideration consists of a lamellar transmission grating of period d, symmetrically positioned on a lamellar reflection grating of the same period, with their axes of periodicity being parallel. The geometry for the profile is shown in Figure 4.1, where c and g represent the aperture width and depth respectively of the upper grating, and f and (h-g) are respectively the aperture width and depth of the lower grating. Both gratings are assumed to be perfectly conducting.

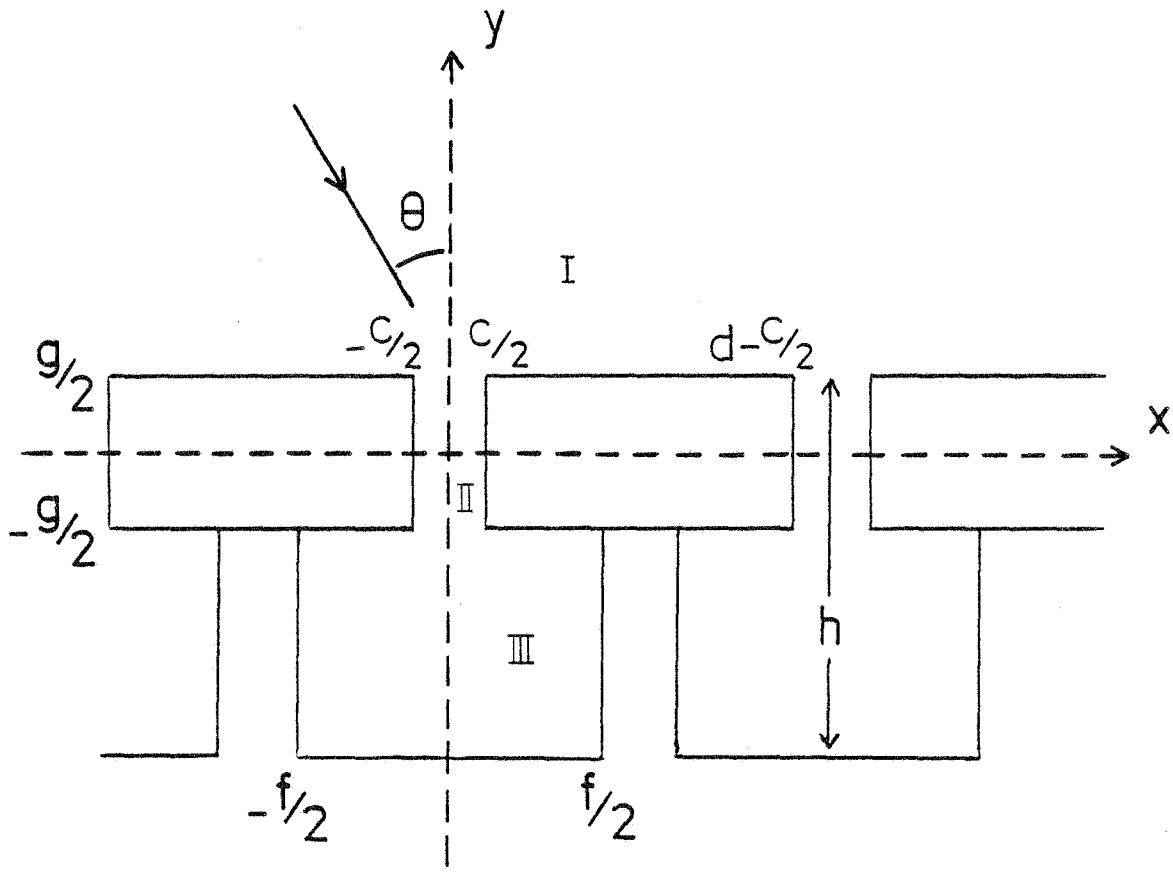

Figure 4.1 The geometry of the diffraction arrangement for the bottle grating.

4.2.2.1 *S Polarization*

Assume that an S-polarized plane wave of wavelength λ, with its wave-vector in the xy plane, is incident upon the grating at an angle θ. Suppressing the time-dependent factor $\exp(-i\omega t)$, the magnetic field above the top surface may be expressed as an incident beam of unit amplitude, plus a series of outgoing plane waves of amplitude B_p. This is the familiar Rayleigh expansion,

$$H^I(x,y) = \exp[i(\alpha_0 x - \chi_0 y)] + \sum_{p=-\infty}^{\infty} B_p \exp\,[i(\alpha_p x + \chi_p y)] \qquad ...(4.1)$$

where $k = 2\pi/\lambda$ is the free-space wave-number, and

$$\left.\begin{aligned} \alpha_0 &= k \sin\theta \\ \alpha_p &= \alpha_0 + \frac{2\pi p}{d} \\ \chi_p &= (k^2 - \alpha_p^2)^{\frac{1}{2}} \qquad \text{if } k \geq |\alpha_p| \\ &= i(\alpha_p^2 - k^2)^{\frac{1}{2}} \qquad \text{if } k < |\alpha_p|, \quad i = \sqrt{-1} \end{aligned}\right\} \qquad ...(4.2)$$

Within the aperture of the upper grating the magnetic field is expressed as a sum of wave-guide modes containing both y-symmetric and y-antisymmetric terms. The relevant boundary conditions for this polarization require that the normal derivative of the field vanishes on all metal walls ,and so using the appropriate x-dependent term, the field in this region is represented by

$$H^{II}(x,y) = \sum_{m=0}^{\infty} \cos\left(\frac{m\pi}{c}\left(x+\frac{c}{2}\right)\right)\,[a_m \sin(\mu_{1,m} y) + b_m \cos(\mu_{1,m} y)] \qquad ...(4.3)$$

where a_m and b_m are unknown modal coefficients and, in order that the Helmholtz equation be satisfied,

$$\left.\begin{aligned} \mu_{1,m} &= \left(k^2 - \frac{m^2\pi^2}{c^2}\right)^{\frac{1}{2}} \qquad \text{if } k \geq \frac{m\pi}{c} \\ &= i\left(\frac{m^2\pi^2}{c^2} - k^2\right)^{\frac{1}{2}} \qquad \text{if } k < \frac{m\pi}{c}\,. \end{aligned}\right\} \qquad ...(4.4)$$

In a similar manner to the above, the field in the groove region of the lower grating is characterised by a superposition of wave-guide modes, but with only y-symmetric terms. It is therefore expressed as

$$H^{III}(x,y) = \sum_{n=0}^{\infty} \hat{b}_n \cos\left(\frac{n\pi}{f}\left(x+\frac{f}{2}\right)\right) \cos\left(\mu_{2,n}\left(y+h-\frac{g}{2}\right)\right) \qquad \ldots(4.5)$$

where the $\hat{b}_n$ are the cavity mode amplitudes and

$$\begin{aligned} \mu_{2,n} &= \left(k^2-\frac{n^2\pi^2}{f^2}\right)^{\frac{1}{2}} \qquad \text{if } k \geqslant \frac{n\pi}{f} \\ &= i\left(\frac{n^2\pi^2}{f^2} - k^2\right)^{\frac{1}{2}} \quad \text{if } k < \frac{n\pi}{f} \quad . \end{aligned} \qquad \ldots(4.6)$$

The solutions for the four unknown sets of amplitudes are now obtained by applying conditions of continuity to H and $\partial H/\partial y$ at the surfaces defined by $y = \pm g/2$. Equating $H^{I}(x,g/2)$ with $H^{II}(x,g/2)$ over the interval $-c/2 \leqslant x \leqslant c/2$, and projecting the result onto the orthogonal set of functions $\{\cos\left(\frac{m\pi}{c}\left(x+\frac{c}{2}\right)\right)\}$ yields

$$c\varepsilon_m\left[a_m \sin\left(\mu_{1,m}\frac{g}{2}\right) + b_m \cos\left(\mu_{1,m}\frac{g}{2}\right)\right] = \exp\left(-i\chi_0\frac{g}{2}\right)\bar{J}_{m0} + \sum_{p=-\infty}^{\infty} B_p \exp\left(i\chi_p\frac{g}{2}\right)\bar{J}_{mp} \qquad \ldots(4.7)$$

where $\varepsilon_m = 1 \qquad \text{if } m = 0$

$\qquad\quad = \frac{1}{2} \qquad \text{if } m \geqslant 1,$

and the inner-product J_{mp} is defined by

$$J_{mp} = \int_{-c/2}^{c/2} \cos\left(\frac{m\pi}{c}\left(x+\frac{c}{2}\right)\right) \exp(-i\alpha_p x)\, dx. \qquad \ldots(4.8)$$

(The closed form for J_{mp} is given in equation 2.18.)

By using the orthogonality properties of the plane-wave terms $\{\exp(i\alpha_p x)\}$ over one period, the continuity of $\partial H/\partial y$ at $y = g/2$ on the interval $-c/2 \leqslant x \leqslant d - c/2$ isolates the plane-wave amplitude B_p, given by

$$B_p = \frac{\sum_{m=0}^{\infty} \mu_{1,m}[a_m \cos(\mu_{1,m}\frac{g}{2}) - b_m \sin(\mu_{1,m}\frac{g}{2})]\, J_{mp}}{i\chi_p d \exp(i\chi_p \frac{g}{2})}$$

$$+ \delta_{0,p} \exp(-i\chi_0 g) \qquad \ldots(4.9)$$

where $\delta_{0,p}$ is the Kronecker delta function.

Similarly, one is able to set $H^{II}(x, \frac{-g}{2})$ equal to $H^{III}(x,\frac{-g}{2})$ on the interval $-c/2 \leqslant x \leqslant c/2$ and equate $\frac{\partial H^{II}}{\partial y}(x,\frac{-g}{2})$ to $\frac{\partial H^{III}}{\partial y}(x,\frac{-g}{2})$ for $-f/2 \leqslant x \leqslant f/2$, thereby deriving the respective equations

$$c\varepsilon_m [b_m \cos(\mu_{1,m}\frac{g}{2}) - a_m \sin(\mu_{1,m}\frac{g}{2})] = \sum_{n=0}^{\infty} \hat{b}_n \cos(\mu_{2,n}(h-g))\, P_{mn} \qquad \ldots(4.10)$$

and

$$\hat{b}_n = \frac{-\sum_{m=0}^{\infty} \mu_{1,m} [a_m \cos(\mu_{1,m}\frac{g}{2}) + b_m \sin(\mu_{1,m}\frac{g}{2})]\, P_{mn}}{\mu_{2,n} \sin(\mu_{2,n}(h-g))\, f\varepsilon_n} \qquad \ldots4.11)$$

Again, advantage has been taken of the orthogonality property of the modal function. The modal inner-product P_{mn} is defined by

$$\left.\begin{aligned} P_{mn} &= \int_{-c/2}^{c/2} \cos\left(\frac{m\pi}{c}(x+\frac{c}{2})\right) \cos\left(\frac{n\pi}{f}(x+\frac{f}{2})\right) dx \\ &= 0, \quad (m+n) \text{ odd} \\ &= \frac{c}{2}\left[(-1)^{\frac{m-n}{2}} \operatorname{sinc}\left(\left(\frac{m}{c}-\frac{n}{f}\right)\frac{\pi c}{2}\right) + (-1)^{\frac{m+n}{2}} \operatorname{sinc}\left(\left(\frac{m}{c}+\frac{n}{f}\right)\frac{\pi c}{2}\right)\right], \\ &\qquad\qquad (m+n) \text{ even and } m/c \neq n/f. \\ &= \frac{c}{2}(-1)^{\frac{m-n}{2}}, \quad m/c = n/f \neq 0 \\ &= c, \quad m = n = 0. \end{aligned}\right\} \qquad \ldots(4.12)$$

Elimination of B_p from equation (4.7), following its substitution from equation (4.9), now furnishes an equation in the mode amplitudes a_m and b_m which is given by

$$\sum_{m=0}^{\infty} a_m^*[\mu_{1,m} \cot(\mu_{1,m} \tfrac{g}{2}) \frac{K_{m\ell}^s}{d} + \delta_{m,\ell}\, \varepsilon_\ell c]$$

$$+ \sum_{m=0}^{\infty} b_m^* [-\mu_{1,m} \tan(\mu_{1,m} \tfrac{g}{2}) \frac{K_{m\ell}^s}{d} + \delta_{m,\ell}\, \varepsilon_\ell c]$$

$$= 2\, \bar{J}_{\ell_0} \exp(-i\chi_0 \tfrac{g}{2}) \qquad \ldots(4.13)$$

$$\text{where } a_m^* = a_m \sin(\mu_{1,m} \tfrac{g}{2}) \qquad \ldots(4.14)$$

$$b_m^* = b_m \cos(\mu_{1,m} \tfrac{g}{2})$$

$$\text{and } K_{m\ell}^s = \sum_{p=-\infty}^{\infty} \frac{iJ_{mp}\, \bar{J}_{\ell p}}{\chi_p} \qquad \ldots(4.15)$$

Inserting $\hat{b}_n$ from equation (4.11) into equation (4.10) provides another equation in these mode amplitudes, namely

$$\sum_{m=0}^{\infty} a_m^* [\mu_{1,m} \cot(\mu_{1,m} \tfrac{g}{2}) \frac{W_{m\ell}^s}{f} - \delta_{m,\ell}\, \varepsilon_\ell c]$$

$$+ \sum_{m=0}^{\infty} b_m^* [\mu_{1,m} \tan(\mu_{1,m} \tfrac{g}{2}) \frac{W_{m\ell}^s}{f} + \delta_{m,\ell}\, \varepsilon_\ell c] = 0 \qquad \ldots(4.16)$$

$$\text{where } W_{m\ell}^s = \sum_{n=0}^{\infty} \frac{\cot(\mu_{2,n}(h-g))\; P_{mn}\, P_{\ell n}}{\varepsilon_n\, \mu_{2,n}} \qquad \ldots(4.17)$$

Equations (4.13) and (4.16) form a coupled pair of infinite matrix equations which must be truncated in order that a numerical solution be computed. Appropriate truncation limits for the series are determined along lines similar to those outlined in Chapter 2, i.e. by carrying out reciprocity and phase checks (it being known that energy conservation is satisfied analytically and offers no indication of convergence). Contained in Table 4.1 is a set of results which demonstrate that the Reciprocity Theorem is satisfied to within a factor of 0.04% in the efficiencies when only 17 order terms and 10 mode terms are employed in the expansions.

TABLE 4.1

Reciprocity Results for the Bottle Grating.

Efficiency and phase values of the order amplitudes are given to confirm agreement with the Reciprocity Theorem. The mounting configurations are defined by:

Problem 1: $\theta = 10°$, $\lambda = 0.6$

Problem 2: $\theta = 25.2363°$, $\lambda = 0.6$ (-1 order returned)

Problem 3: $\theta = -50.6826°$, $\lambda = 0.6$ (+1 order returned)

Groove Parameters: $d = 1.0$, $c = 0.5$, $f = 0.9$, $g = 0.2$, $h = 0.8$

Number of Expansion Terms: 17 plane-wave, 10 modal (in each region).

		P Polarization	S Polarization
Problem 1	$E(0)$, $\arg(R_0)$	.1180, -134.92°	.2551, -172.83°
	$E(-1)$, $\arg(R_{-1})$	.5836, -127.36°	.2812, 103.58°
	$E(1)$, $\arg(R_1)$	.2984, -120.92°	.4637, 99.76°
Problem 2	$E(-1)$, $\arg(R_{-1})$	.5833, -127.35°	.2810, 103.62°
Problem 3	$E(1)$, $\arg(R_1)$	.2982, -120.92°	.4633, 99.76°

Once the a_m and b_m have been evaluated using a standard numerical reduction technique, order amplitudes B_p and the cavity mode amplitudes b_n are calculated from equations (4.9) and (4.11) respectively. Efficiency is calculated from the order amplitudes according to equation (2.2) and should satisfy equation (1.6).

4.2.2.2 *P Polarization*

A summary is now presented of the necessary changes to treat the case for P polarization. For this case the scalar-wave problem is framed in terms of the electric field E, constrained by the boundary conditions to vanish on the metal surfaces. To comply with this, the cosines in the x-dependent terms of the equations (4.3) and (4.5) are changed to sines and hence the m = 0 mode no longer exists. The mode amplitudes for regions II and III are designated a'_m, b'_m and $\hat{a}_n$ respectively. Equation (4.1) remains unchanged except for the Rayleigh coefficients being denoted by A_p. The analysis is then very similar to that described for S polarization.

The appropriate continuity conditions are invoked to yield four equations analogous to equations (4.7), (4.9), (4.10) and (4.11), with inner-products I_{mp} and Q_{mn} defined to be

$$I_{mp} = \int_{-c/2}^{c/2} \sin\left(\frac{m\pi}{c}\left(x + \frac{c}{2}\right)\right) \exp(-i\alpha_p x)\, dx \qquad \ldots(4.18)$$

and

$$Q_{mn} = \int_{-c/2}^{c/2} \sin\left(\frac{m\pi}{c}\left(x + \frac{c}{2}\right)\right) \sin\left(\frac{n\pi}{f}\left(x + \frac{f}{2}\right)\right) dx$$

$$= 0 , \qquad (m + n) \text{ odd}$$

$$= \frac{c}{2}\left[(-1)^{\frac{m-n}{2}} \operatorname{sinc}\left(\left(\frac{m}{c} - \frac{n}{f}\right)\frac{\pi c}{2}\right) - (-1)^{\frac{m+n}{2}} \operatorname{sinc}\left(\left(\frac{m}{c} + \frac{n}{f}\right)\frac{\pi c}{2}\right)\right], \qquad \ldots(4.19)$$

$$(m + n) \text{ even and } m/c \neq n/f$$

$$= \frac{c}{2}(-1)^{\frac{m-n}{2}} , \qquad m/c = n/f.$$

Of these four equations, the one analogous to equation (4.9) for the plane-wave amplitudes is expressed by

$$A_p = \frac{\sum_{m=1}^{\infty} \left[a'_m \sin\left(\mu_{1,m}\frac{g}{2}\right) + b'_m \cos\left(\mu_{1,m}\frac{g}{2}\right)\right] I_{mp}}{d \exp(i\chi_p g/2)} - \delta_{0,p} \exp(-i\chi_0 g) \qquad \ldots(4.20)$$

The modal coefficients a'_m and b'_m are determined exactly as before, with the two final coupled pair of equations being

$$\sum_{m=1}^{\infty} a'^{*}_m \left[\frac{K^P_{m\ell}}{d} - \delta_{m,\ell}\, \mu_{1,\ell} \cot\left(\mu_{1,\ell}\frac{g}{2}\right)\frac{c}{2}\right]$$

$$+ \sum_{m=1}^{\infty} b'^{*}_m \left[\frac{K^P_{m\ell}}{d} + \delta_{m,\ell}\, \mu_{1,\ell} \tan\left(\mu_{1,\ell}\frac{g}{2}\right)\frac{c}{2}\right]$$

$$= 2i\chi_0 \bar{I}_{\ell_0} \exp\left(-i\chi_0\frac{g}{2}\right) \qquad \ldots(4.21)$$

and

$$\sum_{m=1}^{\infty} a'^{*}_{m}\left[\frac{2W^{p}_{m\ell}}{f} + \delta_{m,\ell}\,\mu_{1,\ell}\cot\left(\mu_{1,\ell}\frac{g}{2}\right)\frac{c}{2}\right]$$

$$+ \sum_{m=1}^{\infty} b'^{*}_{m}\left[-\frac{2W^{p}_{m\ell}}{f} + \delta_{m,\ell}\,\mu_{1,\ell}\tan\left(\mu_{1,\ell}\frac{g}{2}\right)\frac{c}{2}\right] = 0. \qquad \ldots(4.22)$$

where $a'^{*}_{m} = a'_{m}\sin\left(\mu_{i,m}\frac{g}{2}\right)$

$b'^{*}_{m} = b'_{m}\cos\left(\mu_{1,m}\frac{g}{2}\right)$ $\qquad \ldots(4.23)$

$$K^{p}_{m\ell} = \sum_{p=-\infty}^{\infty} iX_{p}\, I_{mp}\overline{I}_{\ell p} \qquad \ldots(4.24)$$

$$W^{p}_{m\ell} = \sum_{n=1}^{\infty} \mu_{1,n}\cot\left(\mu_{2,n}(h-g)\right) Q_{mn}\, Q_{\ell n}. \qquad \ldots(4.25)$$

Upon numerical solution of these equations, the diffracted field is reconstructed from equation (4.20).

Results of a reciprocity run, performed with 17 orders and 10 modes in each groove region, are given in Table 4.1.

4.2.3 Phase Properties

With reference to the relations outlined in Section 2.3, it is possible to derive some simple phase properties linking the mode amplitudes a^{*}_{m}, b^{*}_{m} and $\hat{a}^{*}_{n}$ (for both polarizations) where the first two represent the field of the upper transmission grating and the last represents the lower reflection grating. Because the bottle grating is a reflection grating with left-right symmetry, the appropriate relations from Section 2.3 for time reversibility are equation (2.42) for a long-wavelength configuration and equation (2.55) for a -1 Littrow configuration. This implies that for the former mounting, equation (2.44) applies to the diffracted orders while for the latter mounting equations (2.58) and (2.60) to (2.62) are applicable to either a^{*}_{m} or b^{*}_{m}.

For the relevant mode amplitude relations, consider first the cavity region which has L-R symmetry only. The appropriate modal expansion is of the form of equation (2.46) and hence the mode amplitudes will obey the phase relations (2.47) and (2.59), i.e.

$$\left.\begin{aligned} &\text{(i)}\quad \arg(\hat{a}_n^e) = \tfrac{1}{2}\arg(R_0)\quad (+\pi) \\ &\text{(ii)}\quad \arg(\hat{a}_n^o) = \tfrac{1}{2}\arg(R_0) + \tfrac{\pi}{2}\quad (+\pi) \end{aligned}\right\} \quad \text{(long-}\lambda\text{)} \qquad \ldots(4.26)$$

and

$$\left.\begin{aligned} &\text{(i)}\quad \arg(\hat{a}_n^e) = \tfrac{1}{2}\arg(R_0 + R_{-1})\quad (+\pi) \\ &\text{(ii)}\quad \arg(\hat{a}_n^o) = \tfrac{1}{2}\arg(R_{-1} - R_0)\quad (+\pi) \end{aligned}\right\} \quad \text{(-1 Littrow 2 orders)} \qquad \ldots(4.27)$$

(Note that for ease of presentation the asterisks are omitted from the mode amplitudes.)

Now consider the upper groove region which has both left-right and up-down symmetry. The appropriate modal expansion is given by equation (2.48). However, due to the absence of transmitted orders, the corresponding phase properties of equations (2.51) and (2.66) no longer apply. Instead, substitution of (2.48) into equations (2.42) and (2.55) shows that they reduce to

$$\left.\begin{aligned} &\text{(i)}\quad \arg(a_m^e) = \arg(b_m^e) = \tfrac{1}{2}\arg(R_0)\quad (+\pi) \\ &\text{(ii)}\quad \arg(a_m^o) = \arg(b_m^o) = \tfrac{1}{2}\arg(R_0) + \tfrac{\pi}{2}\quad (+\pi) \end{aligned}\right\} \quad \text{(long-}\lambda\text{)} \qquad \ldots(4.28)$$

and

$$\left.\begin{aligned} &\text{(i)}\quad \arg(a_m^e) = \arg(b_m^e) = \tfrac{1}{2}\arg(R_0 + R_{-1})\quad (+\pi) \\ &\text{(ii)}\quad \arg(a_m^o) = \arg(b_m^o) = \tfrac{1}{2}\arg(R_{-1} - R_0)\quad (+\pi) \end{aligned}\right\} \quad \text{(-1 Littrow 2 orders)} \qquad \ldots(4.29)$$

Table 4.2 displays the concordance of some numerical results with the -1 Littrow phase relations for both polarizations.

One now finds that the y-symmetric and the y-antisymmetric modes in the upper region have, for these mountings, the same phase, which in turn is seen from a comparison of equations (4.28) and (4.29) with (4.26) and (4.27), to be equal to its counterpart in the lower groove region. This equivalence

TABLE 4.2

-1 Littrow Symmetry Properties of the Bottle Grating.

Intensity and phase values of the field amplitudes are given for comparison with the requirements of the symmetry relations of Sections 2.3 and 4.2.3.

Groove Parameters: d = 1.0, c = 0.5, f = 0.9, g = 0.2, h = 0.8.
Mounting Parameters: $\lambda = 1.3$, $\theta = 40.5416°$
Number of Expansion Terms: 17 plane-wave, 10 modal.

	P Polarization	S Polarization	Equation Number
$\|R_0\|^2$, $\arg(R_0)$	.8069, 166,7919	.4732, -16.4465	
$\|R_{-1}\|^2$, $\arg(R_{-1})$	.1931, -103.2053	.5268, 73.5570	2.61,2.62
$\arg(R_{-1}) - \arg(R_0)$	90.0028	90.0035	2.60
$\frac{1}{2}\arg(R_0+R_{-1})$	-83.5699	15.0458	4.29(i)
$\frac{1}{2}\arg(R_0-R_{-1})$	160.3624	-121.4904	4.29(ii)
	m = 1 m = 3	m = 0 m = 2	
$\arg(a_m^e)$	-83.5680, -83.5067	15.0463, 15.0192	4.29(i)
$\arg(b_m^e)$	-83.5679, -83.5457	15.0464, 15.0394	4.29(i)
$\arg(\hat{a}_m^e)$	-83.5679, -83.5680	15.0464, 15.0461	4.27(i)
	m = 2	m = 1	
$\arg(a_m^o)$	160.3530	-121.5006	4.29(ii)
$\arg(b_m^o)$	160.3530	-121.5004	4.29(ii)
$\arg(\hat{a}_m^o)$	160.3527	-121.5009	4.27(ii)
$\cos^2[\arg(a_m^e)-\arg(a_m^o)]$	.1933	.5270	2.61
$\arg(a_m^e)+\arg(a_m^o)+\pi$	103.2150	73.5457	2.62

of phase for the upper aperture, when inserted into equations (2.75), implies that no energy can be carried by an individual mode through the aperture. This has been confirmed numerically. Investigations with arbitrary incidence angles and wavelengths have revealed, that although the above phase properties are not applicable, the three mode amplitudes corresponding to any one particular value of m(=n) usually have arguments very close to one another, say within 1^{o}. The fact that $\arg(a_m)$ and $\arg(b_m)$ are not identical means that (see equations (2.75)) a small amount of energy is carried through the hole (upper groove region). Numerical calculations show however, that this amount is always balanced by an equal and opposite flow of energy via another mode, and hence the total nett energy flux through the hole is zero, as required.

4.2.4 Interferometric Action of the Grating

The diffraction properties of the bottle grating have been investigated for constant wavelength, normal incidence and -1 Littrow mounting configurations and with a range of grating parameters c, f, g and h. (Because the grating surface is perfectly conducting, the numerical results have been generalized by setting d equal to unity.) Figures 4.2 and 4.3 exemplify the behaviour for the first two mounting types. However these results have not proved as interesting as those for the -1 Littrow mounting which form the basis of this study. Figures 4.4 to 4.11 typify some efficiency spectra for that mounting in the case where c and g are small compared with the period. In the majority of cases 17 orders and 10 modes (in both groove regions) were more than adequate in representing the respective field expansions.

The distinctive features evident in these spectra strongly resemble the interference maxima obtained in a Fabry-Perot interferometer. Similar phenomena have been obtained by Adams and Botten [4.3] in their evaluation of the behaviour of the double lamellar array, used in transmission at

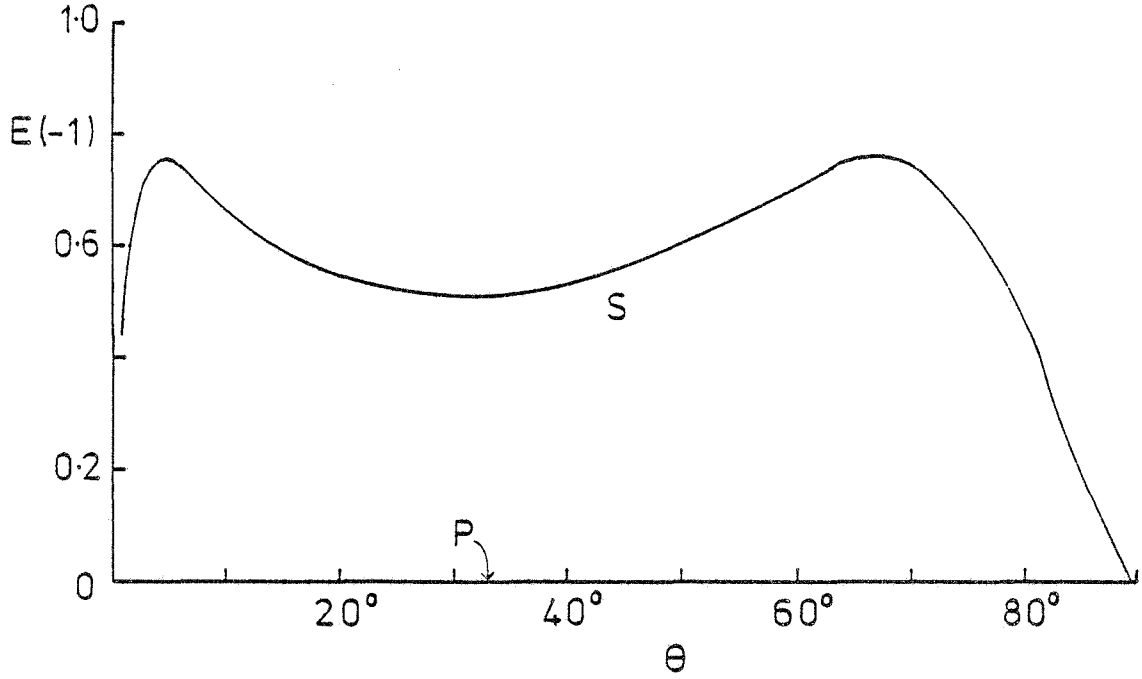

Figure 4.2 -1 order efficiency as a function of angle of incidence for the bottle grating.

Groove parameters: d=1.0,c=0.05,h=2.2,g=0.2,f=0.99

Wavelength: λ=1.0

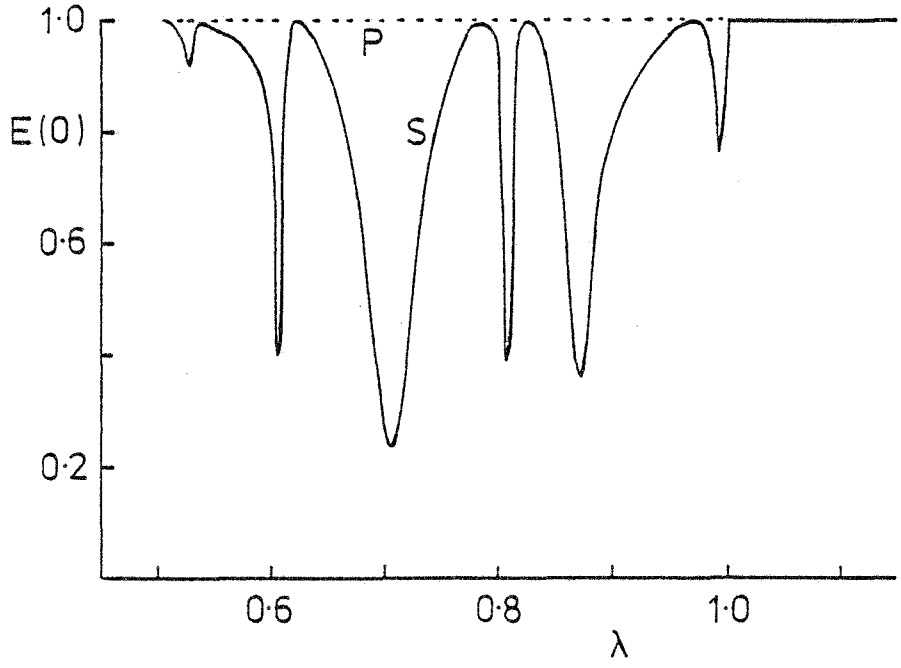

Figure 4.3 Zero order efficiency as a function of wavelength for the bottle grating in a normal incidence mounting.

Groove parameters: d=1.0,c=0.06,h=1.1,g=0.3,f=0.99

Fig. 4.4

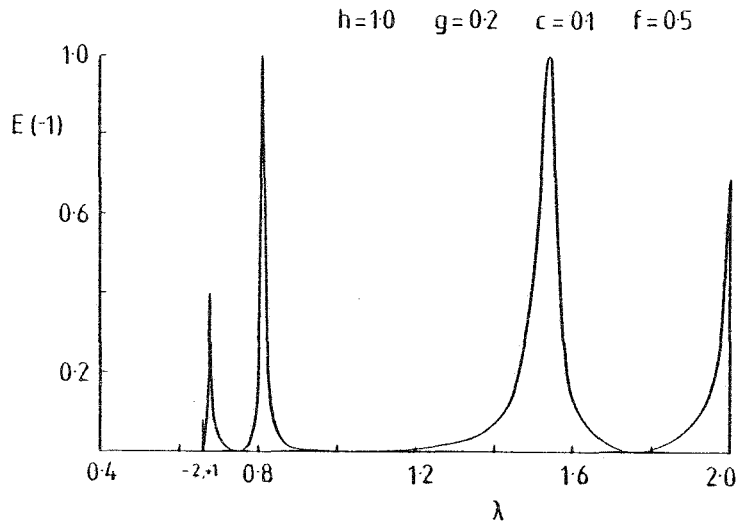

Fig. 4.5

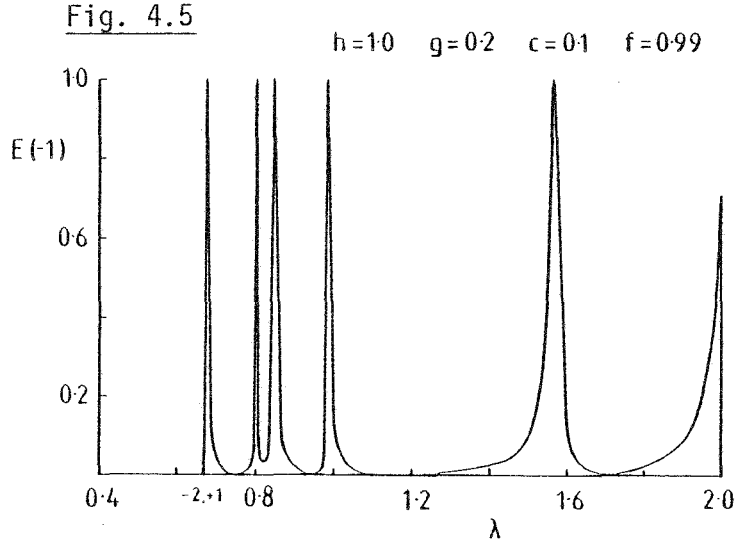

Fig. 4.6

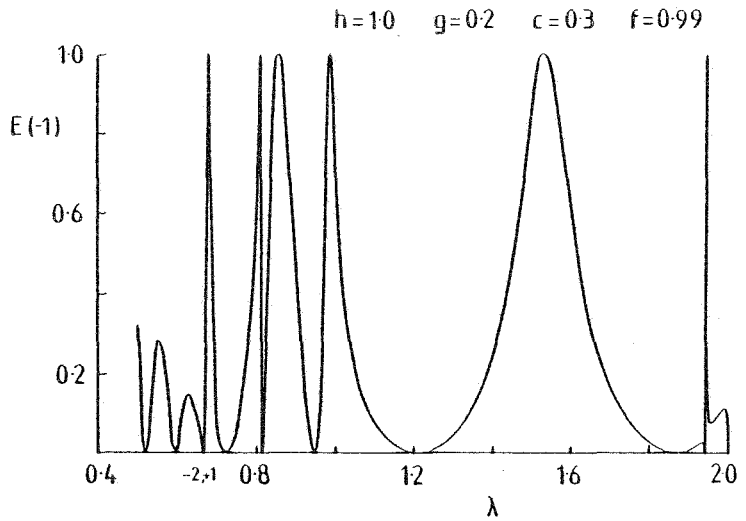

Fig. 4.7

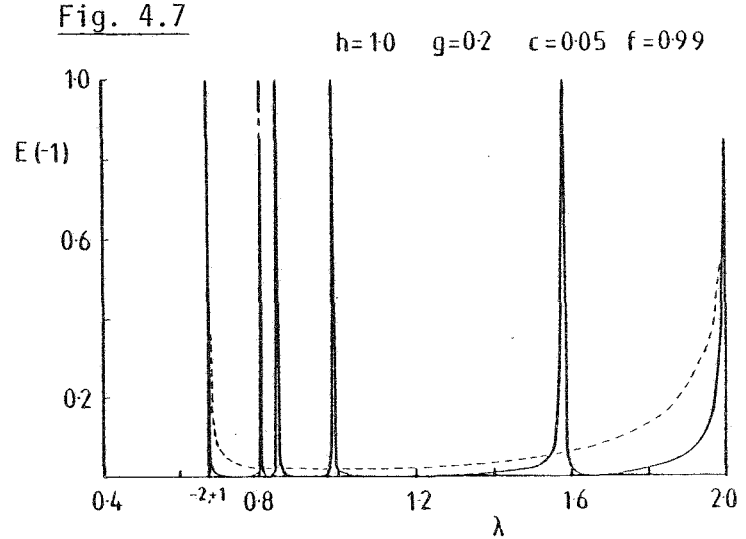

Figures 4.4 - 4.7 S polarization efficiency spectra for a bottle grating of unit period operated in a -1 Littrow mounting.

Figure 4.8 S polarization

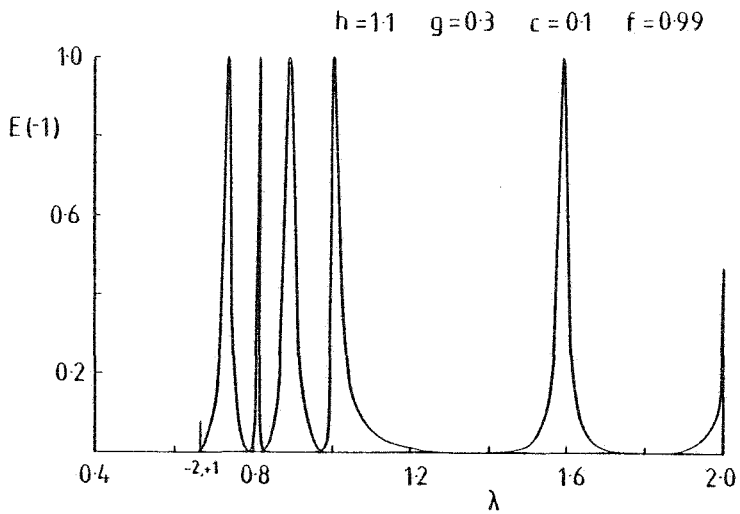

Figure 4.9 S polarization

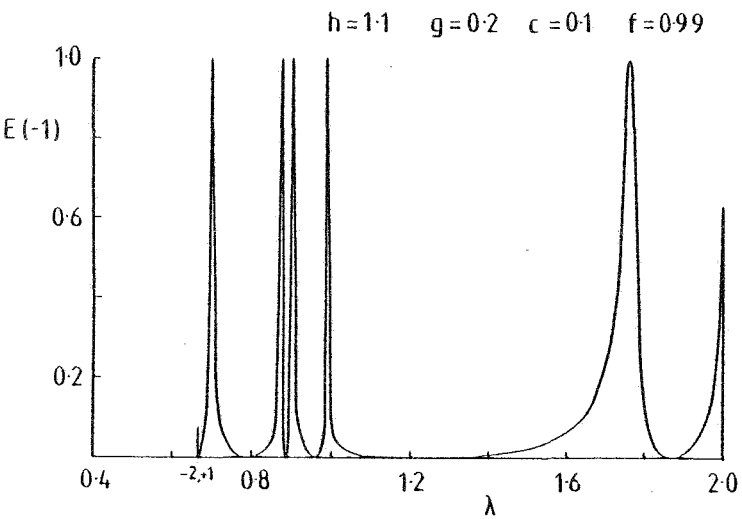

Figure 4.10 P polarization

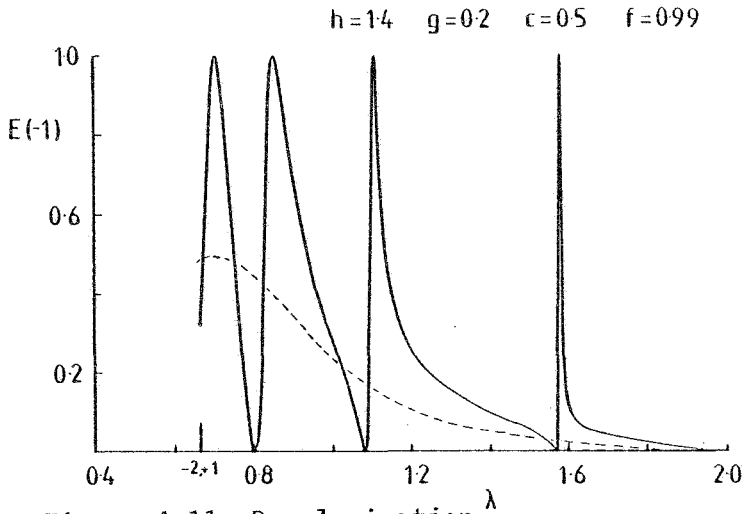

Figure 4.11 P polarization

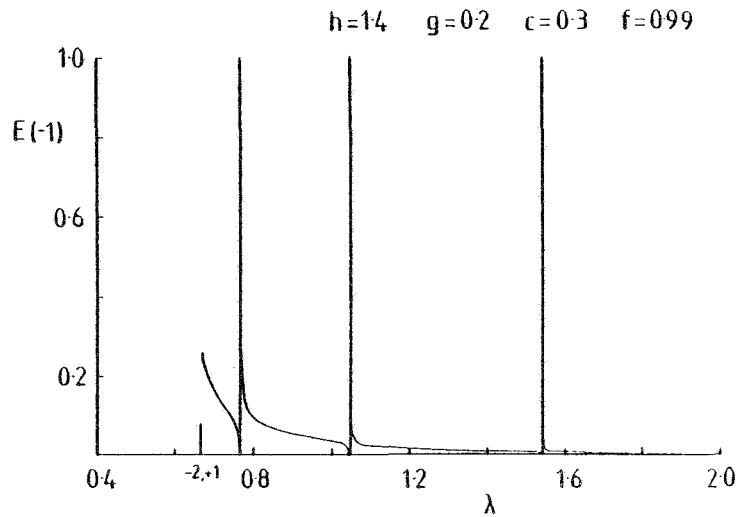

Figures 4.8 - 4.11 -1 Littrow efficiency spectra for the bottle grating.

wavelengths in excess of the grating period. They were able to show that as the reflectance of a single array increased, the finesse of the instrument improved and the maxima moved towards their geometrical limits, given by

$$\lambda_{max} = \frac{2S}{\ell} \qquad \ell = 1,2,... \qquad ...(4.30)$$

where S is the separation of the two arrays.
Because the interference effect they observe is more pronounced if an individual array has high reflectance at long wavelengths, their device functions more efficiently for P polarization. (This variation of reflectance with wavelength is illustrated in the efficiency curve of Figure 2.4(c)).

The interferometric action of the bottle grating appears to be founded on similar principles to the double-lamellar array, but gains its "high-reflectance" by alternative means. Rather than relying on large values of wavelength, this property is achieved through a reduction in the aperture size, which has the effect of decreasing diffracted efficiency for both polarizations (although more strongly for P polarization). Such an explanation is in keeping with Figures 4.4 to 4.11, which illustrate an enhanced performance as c is diminished. This property is given a more definite theoretical basis in the following section.

The dotted lines in Figures 4.7 and 4.10 depict the transmitted energy of an isolated single transmission array, equivalent to the one that forms the upper section of the appropriate bottle structure. These curves confirm that as this array becomes more reflecting (at longer wavelengths for P polarization and shorter wavelengths for S polarization), the resonance features are more finely resolved and the contrast factor increases. They also demonstrate the interesting result that for the Littrow mounting the final diffracted efficiency curve consists approximately of the transmitted

efficiency curve of the top array on which is superimposed resonance peaks, shown later to be produced by the cavity underneath.

4.2.5 Monomodal Treatment

In this section a theoretical understanding of the resonance-type phenomena is sought through the implementation of a single-mode approximation to the theory, as was carried out in Chapter 2 for the basic lamellar grating. The procedure involves truncating the modal expansions for the field in both the upper and lower groove regions to a single term. Such action is justified in the case of the upper region on the basis of the conclusions drawn in Section 2.7: for both polarizations, only the first mode in the expansion plays a dominant role when the aperture width is small. This approximation remains valid for the -1 Littrow mounting for low wavelengths where more orders other than the two fundamental ones are propagating. However, one exception is known to occur for S polarization just below the Rayleigh wavelength, $\lambda_R = 2.0d$, where a bimodal approximation is necessary.

In the lower cavity region of the groove, the mode amplitudes possess poles in the complex wavelength plane. These poles are manifested as resonances in the amplitudes when the physical wavelength approaches the real component of the pole. These resonances are the features of interest and for wavelengths in their vicinity the corresponding cavity mode amplitude is the dominant one. Consequently, one is justified in adopting a monomodal expansion for this region if the single term is chosen to be that one undergoing resonance.

The above assumptions were confirmed numerically by recalculating the spectrum depicted by Figure 4.7, but with only the zeroth mode included in each of the expansions. The result was an efficiency curve identical to the one shown but with resonances due to $\hat{b}_0$ at $\lambda/d = 0.8$ and 1.6 being the only ones present. The resonances shown in Figure 4.7 between these two are due to $\hat{b}_2$ while the two outer features are thought to be either Wood anomalies or "blaze-effects" produced by the narrow upper aperture and related to the discussion of Section 3.3.

The resonant nature of the cavity modes is exemplified in Figure 4.12, which shows a plot of the phase of $\hat{b}_0$ as a function of wavelength. Four resonances are indicated by the four very distinct phase changes of almost exactly 180^o. Although $\hat{b}_0$ is the resonant mode in only two of these cases, its phase indicates all of the even-resonances due to the common phase property expressed by equation (4.27).

Before continuing with the monomodal treatment, it is useful to note that when the first mode in the upper region is the dominant one, only x-symmetric modes are excited in the lower region. This is evident for S polarization from equation (4.11) wherein $P_{0n} = 0$ for n odd, as given by equation (4.12). A similar situation exists for P polarization, but there the non-excited cavity modes correspond to n even. A consequence of the above is that x-antisymmetric modes (n odd - S pol., n even - P pol.) are not usually responsible for any of the resonance behaviour. The word "usually" is used because in certain situations a monomodal model is inadequate in describing the field in the upper groove region. (see above). As a result, x-antisymmetric modes can be

stimulated and this is illustrated in Figure 4.6 where a sharp anomaly near $\lambda/d = 1.95$ appears to be the manifestation of a resonance in the mode $\hat{b}_1$.

Consider now the case when c/d is small and the wavelength domain is such that only a single mode is significant in each of the two groove regions. The situation for S polarization is dealt with initially and hence the relevant mode amplitudes are a_0, b_0 and $\hat{b}_n$ where n is chosen from 0, 2, 4 ... . Under these conditions one is able to derive from equations (4.7), (4.9), (4.10) and (4.11) a closed expression for B_p which is of the form

$$B_p = \frac{2c\mu_{1,0}J_{0p}\exp\left(-i(\chi_0+\chi_p)\frac{g}{2}\right)}{i\chi_p d}\cdot\frac{N}{D} + \delta_{0,p}\exp(-i\chi_0 g) \qquad \ldots(4.31)$$

$$\text{where } N = 1 + \frac{P_{0n}^2\,\mu_{1,0}}{\varepsilon_n\, fc\mu_{2,n}}\tan(\mu_{1,0}\,g)\,\cot(\mu_{2,n}(h-g)), \qquad \ldots(4.32)$$

$$D = c\tan(\mu_{1,0}g) + \frac{\mu_{1,0}\,K_{00}^S}{d}\left[1 + \frac{P_{0n}\,\mu_{1,0}}{\varepsilon_n\, fc\,\mu_{2,n}}\times\right.$$

$$\tan(\mu_{1,0}\,g)\,\cot(\mu_{2,n}(h-g)) - \frac{P_{0n}^2\,\mu_{1,0}}{\varepsilon_n\, f\,\mu_{2,n}}\times$$

$$\left.\cot(\mu_{2,n}(h-g))\right], \qquad \ldots(4.33)$$

$$\text{and } K_{00}^S = \sum_{p=-\infty}^{\infty}\frac{i\,|J_{0p}|^2}{\chi_p} \qquad \ldots(4.34)$$

Since $J_{0p} \to 0$ as c decreases, B_p tends towards $\delta_{0,p}\exp(-i\chi_0 g)$ and consequently very little energy appears in the non-zero orders - unless a singularity occurs. Such a situation exists when either $\chi_p = 0$ or $D = 0$. The former case corresponds to the well known Wood anomalies (which are visible in the spectra near the Rayleigh wavelengths), while the latter case is

associated with resonances and is responsible for the sharp peaks in efficiency removed from the Rayleigh wavelengths. As was the case in Section 3.3, and as proven further below, the apices (or blazes) of these resonances correspond to the condition $Re\ (D) = 0$. When c is small, this condition is satisfied approximately when

$$\frac{\cot(\mu_{2,n}\ (h-g))}{\mu_{2,n}} = \frac{fc\varepsilon_n}{p_{0n}^2}\ \frac{\tan(\mu_{1,0}g)}{\mu_{1,0}} \qquad \ldots(4.35)$$

In the limit of c being equal to zero, the R.H.S. of this equation is infinite but it can still equal the L.H.S. if

$$\mu_{2,n}(h-g) = \ell\pi\ . \qquad \ldots(4.36)$$

As expected, equation (4.36) corresponds to singularities in the cavity mode amplitude $\hat{b}_n$, as seen from equation (4.11). Expanding it shows that the resonance wavelengths are given by

$$\lambda_{max} = \frac{2f(h-g)}{\sqrt{n^2(h-g)^2 + \ell^2 f^2}} \qquad \ell = 0,1,2\ \ldots \qquad \ldots(4.37)$$

Reference to Figures 4.4 to 4.9 provides numerical confirmation of this equation. In all cases the efficiency peaks occur just below wavelengths predicted by this equation for n = 0 or 2 and ℓ = 0, 1 or 2. As c is reduced the maxima approach the values λ_{max}. As an example, see Figures 4.5, 4.6 and 4.7 where h, g and f are held constant while c is reduced from 0.3 to 0.05. The longer-wavelength maximum is observed to move from 1.54 to 1.58, where the value for λ_{max} from equation (4.37) is equal to 1.6.

It is of interest to note that equation (4.36) also corresponds to the vanishing of the normal derivative of the n^{th} mode along the interface between the hole and the cavity. If this mode is the dominant one, then in effect the cavity becomes closed by a "metal surface" along the bottom of the

hole. The outcome is that equation (4.37) is found to be equivalent to the cut-off wavelengths for TE modes in a rectangular wave-guide, while the overall behaviour of the bottle grating compares with that of a conventional lamellar grating whose groove shape is identical with that of the "hole". (Remember that in practice, c > 0 and therefore the values λ_{max} do not correspond exactly, but rather approximately to the efficiency maxima.) The above behaviour was checked for a grating with parameters (h-g) = 0.8, f = 0.99, c = 0.05 and g = 0.2. For the -1 Littrow mount, maxima due to $\hat{b}_2$ resonances occur just below the predictions (4.37) of 0.842 and 0.99. The -1 order efficiencies at these wavelengths λ_{max} were found to be 0.26 and 0.58 respectively. Subsequent calculations for an ordinary lamellar profile of c = 0.05 and h = 0.2 yielded efficiencies of 0.25 and 0.57. The small discrepancies can be attributed to the minor role played by modes other than the n = 2 mode in the bottle grating calculations.

For the fundamental n = 0 mode, equation (4.37) condenses to

$$\lambda_{max} = \frac{2(h-g)}{\ell} \qquad \ldots(4.38)$$

and immediately the similarity is seen between this expression and that determining the positions of maxima for a normal Fabry-Perot interferometer in a normal incidence mounting (equation (4.30)).

Returning to equation (4.31), this is reduced with the insertion of the resonance condition *Re* (D) = 0 to become

$$B_p = \frac{2c\, J_{0p}\, \exp\left(-i(\chi_0+\chi_p)\,\frac{g}{2}\right)}{\chi_p\, Im\,(K^s_{00})} + \delta_{0,p}\, \exp(-i\chi_0 g) \qquad \ldots(4.39)$$

Maximum efficiency in the p^{th} order at resonance is thus seen to depend on the term $Im\,(K^s_{00})$. For the -1 Littrow mounting, when only two orders are real, this is given by

$$Im\ (K^{S}_{0\,0}) \;=\; \frac{2c^2}{\chi_0} \qquad \ldots(4.40)$$

where $\chi_0 = \chi_{-1}$ and $J_{0\,0} = J_{0,-1} = c$. Substitution of this equation into equation (4.39) gives

$$B_{-1} \;=\; -\exp(-i\chi_0 g) \qquad \ldots(4.41)$$

which implies that efficiency in the -1 order (for this mounting) is 100% at the wavelength determined by equation (4.35).

For a normal incidence configuration, when only three orders are propagating, it is straightforward to show using equation (4.39) that the maximum efficiency in the ±1 orders is only about 40% with the maximum in efficiency of the zero order being about 20%. The numerical results shown in Figure 4.2 are in accord with this prediction and further attention is confined to the more interesting -1 Littrow mounting.

The course followed from equation (4.31) through to (4.41) has been duplicated for P polarization and one is able to reach similar conclusions. The condition for efficiency maxima for this polarization is given by

$$\mu_{2,n}\cot(\mu_{2,n}(h-g)) \;=\; \frac{fc}{4Q^2_{1n}}\,\mu_{1\,1}\tan(\mu_{1\,1}\,g) \qquad \ldots(4.42)$$

where it is noted that $Q_{1\,1}$ tends towards $2c/\pi$ as c approaches zero. In the limit of c equalling zero, the above equation leads to the same resonance wavelengths as equation (4.37), but of course resonance only occurs for n odd as opposed to n even for S polarization. Because $\mu_{1\,1}$ depends on c (equal to $i\pi/c$ when c is small) whereas $\mu_{1\,0}$ does not, the spectral peaks for P polarization are shown from an analysis of the relevant equations, to have smaller half-widths and to lie closer to their limiting positions than is the case for the same value of c for S polarization. This conforms with earlier observations concerning reflectance and is illustrated in Figures 4.10 and 4.11.

Because $\mu_{1\,1}$ is imaginary in the region of concern, $\mu_{1\,1}\tan(\mu_{1\,1}\,g) = -|\mu_{1\,1}|\tanh(|\mu_{1\,1}|\,g)$ and this fact used in conjunction with equation (4.42)

shows that the actual positions of the maxima now occur at *longer* wavelengths than their limiting positions, λ_{max}. In Figures 4.10 and 4.11 the longer-wavelength peak moves from 1.56 down to 1.54 as c decreases from 0.5 to 0.3. The limit in this example, given by equation (4.37) with n = 1 and ℓ = 1, is 1.527. Note that for ℓ = 0, there is no associated resonance for P polarization because for the L.H.S. of equation (4.42) to become infinite $\mu_{2,n}$ should be real, i.e. λ must be less than 2f/n, and when this occurs the L.H.S. cannot be negative, as would be required.

We now describe the effect of the grating parameters f, c, g and h on the position and number of possible resonances and also on their half-widths. From equation (4.37) it has already been shown that the cavity depth (h-g) and width f define the limiting positions of the maxima, and that as c tends to zero they move towards these limits from wavelengths given by either equation (4.35) or (4.42). For S polarization, equation (4.37) asserts that only $\hat{b}_0$ and $\hat{b}_2$ resonances are possible between λ_R = 2/3 and λ_R = 2.0. The longest wavelength that a $\hat{b}_2$ maximum can take is equal to f, which is restricted physically to be less than 1.0. Therefore, if f < 2/3, no $\hat{b}_2$ resonances should exist and this is borne out in Figure 4.4 where f = 0.5 and only two resonances due to $\hat{b}_0$ are apparent. In Figure 4.5 f has been increased to 0.99 and two $\hat{b}_2$ maxima appear, these being at λ = 0.85 and 0.99. The cavity depth (h-g) determines, through equation (4.37), how many maxima belonging to one particular mode will occur over the appropriate wavelength interval.

For P polarization, only the mode $\hat{a}_1$ is capable of resonating between λ_R = 2/3 and λ_R = 2.0. For the results displayed in Figures 4.10 and 4.11 a sufficiently large cavity depth was chosen to enable three such resonances to occur.

The depth of the upper groove region affects the positions of the maxima through the terms $\tan(\mu_{1,0}g)$ and $\tan(\mu_{1,1}g)$ in equations (4.35) and (4.42) respectively. For P polarization, $\tan(\mu_{1,1}g)$ becomes $\tanh(|\mu_{1,1}|g)$ and approaches unity as c approaches zero and so a change in g has only a minor effect, if (h-g) is held constant. In the case of S polarization, $\tan(\mu_{1,0}g)$ can vary between $+\infty$ and $-\infty$ and so to avoid complications which this term can introduce it is best to restrict g to be less than 1/3 in order that $0 < \mu_{1,0}g < \pi$. Figures 4.5 and 4.8 demonstrate the minimal changes which are then incurred when g is increased and (h-g) is held fixed.

Figures 4.5, 4.6 and 4.7 along with Figures 4.10 and 4.11 have clearly shown numerically that it is the aperture width c and also the region of the spectrum (i.e. the value of λ) which primarily govern the half-widths or finesse of the peaks. The reason for this may be derived theoretically and is done so in the first instance for S polarization.

By manipulating equation (4.31) for B_{-1}, the efficiency in that order for a -1 Littrow mounting may be expressed as

$$|B_{-1}|^2 = \frac{1}{1 + r^2F^2} \qquad \ldots(4.43)$$

where $r = Re\,(D)$

and $$F = \frac{d\chi_0}{2\mu_{1,0}\, c^2\left[1 + \frac{\mu_{1,0}}{\mu_{2,n}} \frac{P_{0n}^2}{fc} \tan(\mu_{1,0}\, g)\, \cot(\mu_{2,n}(h-g))\right]} \qquad \ldots(4.44)$$

Near a resonance of the mode $\hat{b}_n$, r approaches zero while F is seen to be a measure of the finesse of the device. If c decreases, F increases and hence the finesse improves, i.e. the peaks become narrower. Because χ_0 decreases with increasing wavelength for this particular mounting, equation (4.44)

implies that the finesse should diminish. This is in fact the case as can be seen from the efficiency curves which show the maxima to widen at longer wavelengths.

A similar treatment to the above for P polarization reveals that F is proportional to $1/(X_0 c^2)$. Thus, the half-widths of the maxima are expected to decrease as either the aperture width is reduced or the wavelength is *increased*. Both of these properties are in agreement with the curves displayed in Figures 4.10 and 4.11.

4.2.6 Conclusion

A modal formulation has been presented which illustrates interesting resonance behaviour obtainable from a lamellar transmission grating resting symmetrically upon a lamellar reflection grating and illuminated with either S or P polarized radiation. It has been demonstrated that the efficiency maxima are particularly distinctive in the -1 Littrow configuration, where for a relatively small upper groove aperture, the spectra are seen to consist approximately of a background efficiency curve, corresponding to the transmitted energy of the upper array, on which are superimposed resonance peaks produced by the cavity underneath.

The action of the grating has indicated its possible application as an interferometer in reflection. In fact, it has been pointed out that marked similarities exist between this action and the interference phenomenon obtained with a Fabry-Perot interferometer. It is noteworthy that whereas normal transmission grating interferometers work at wavelengths in excess of the grating period, the bottle grating can be used in reflection with wavelengths over a wide band extending well below the grating period. A description given in the next section on the behaviour of a lamellar transmission grating placed closely in front of a mirror, shows that such a device yields results quite comparable with those presented here and this confirms an interferometric origin for the resonances.

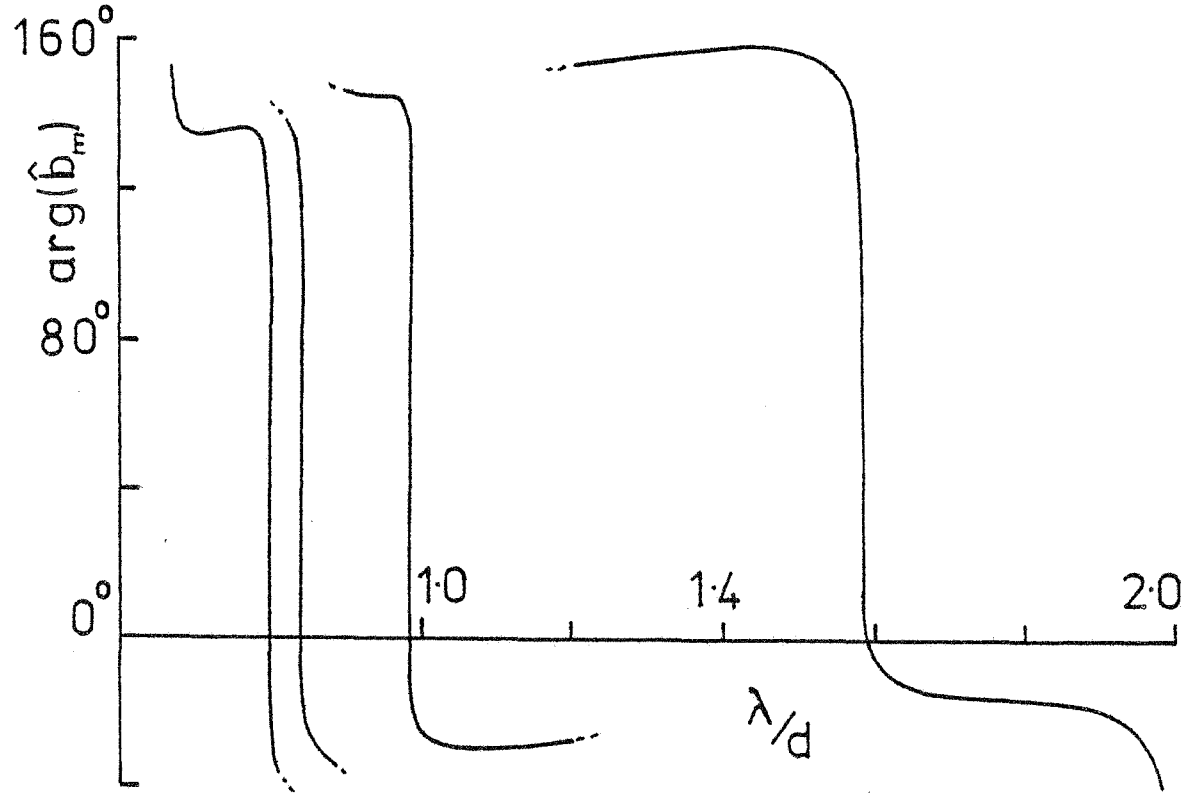

Figure 4.12 Phase plot of the modal amplitudes $\hat{b}_m$,m=0,2,4... for the bottle grating in a -1 Littrow mounting. The π-phase changes show the exact resonance positions. (c.f. Figure 4.7).

Grating parameters: h=1.0,g=0.2,c=0.05,f=0.99

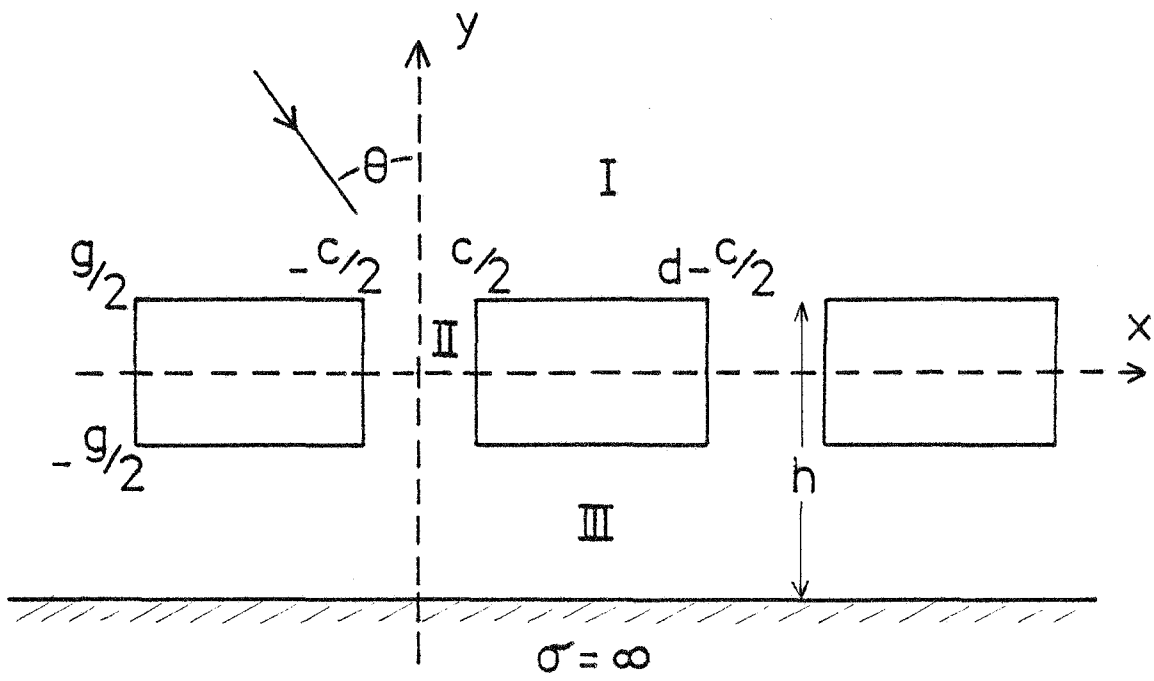

Figure 4.13 The geometry of the diffraction arrangement for the mirror grating.

The use of a single-mode field approximation has been fulfilled by making possible a simple analysis of the diffraction problem and by providing insight into most of the salient features of the bottle grating's behaviour. It has shown that the dimensions of the reflection grating groove dictate the number and limiting wavelength positions of the efficiency maxima, while it is the aperture width of the upper transmission array which primarily governs their half-widths and exact position.

It is hoped that at some stage experimental evidence will confirm the interesting interferometric action of this unusual grating.

4.3 THE RECTANGULAR-WIRE GRATING PARALLEL TO A CONDUCTING PLANE

4.3.1 Introduction

Attention is directed here towards a device which is simply a lamellar transmission grating, as described in Chapter 2, placed in close proximity and parallel to a perfectly-conducting plane. For brevity it is referred to as the "mirror" grating. Such a structure is obviously closely related to not only the bottle grating discussed in the previous section, but also the double-grating interferometer studied by Adams and Botten [4.3]. It was therefore of interest to make the straightforward adaptation of the bottle-grating theory to account for the mirror grating and hence compare its performance with those of the related configurations. The motivation for this comparison is strengthened by the fact that the mechanism for the action of the bottle grating does not include multiple-scattering whereas that for the mirror grating does.

To this date, little work appears to have been performed on the study of transmission gratings backed by a conducting plane. One report given on the subject however, is that of Wait [4.4] who investigated the problem of

scattering of a plane wave from a parallel-wire grid placed near an infinitely-conducting plane. The wires he considered were of circular cross-section and either infinitely-conducting or resistive. The problem was treated for P polarization only and the method was not rigorous. An analogy was drawn with an electrical circuit consisting of a transmission line shunted with an impedance and short-circuited behind that impedance. Very few numerical results were presented in the report and the suggested application for the device was as a simulated anti-reflection coating.

The theory given in Section 4.3.2 for the mirror grating is for both P and S polarizations and is completely rigorous. The only major difference between this formulation and that for the bottle grating is that plane waves now exist in the lower region of the structure.

Section 4.3.3 deals with an analysis of the interference phenomena associated with the mirror grating and comparisons are made with the resonance behaviour of the bottle grating. This is accomplished with the aid of a truncation of the field expansions, and the effects of the various grating parameters on the positions and shapes of the efficiency maxima are examined.

4.3.2 Modal Formulation

To facilitate comparisons, the scalar-wave diffraction problem for this grating is set up exactly as for the bottle grating. The same notation is used throughout and hence c and g are respectively the width and depth of the transmission grating aperture. The conducting plane is situated a distance h below the top surface of the grating. The cross-section for the structure is illustrated in Figure 4.13.

The case for S polarization is discussed first and therefore equations (4.1) and (4.2) appropriately define the magnetic component of the plane-wave diffraction field. Within the grating apertures the field is represented by a modal expansion identical to that of equation (4.3). The first change encountered is in the specification of the field below the transmission grating. For the mirror grating the waveguide mode representation for $H^{III}(x,y)$ is replaced by a series containing both upward-going and downward-going plane-wave terms. In order that $\partial H^{III}/\partial y$ vanishes on the surface of the conducting plane, i.e. at $y = -h + g/2$, $H^{III}(x,y)$ must be of the form

$$H^{III}(x,y) = \sum_{p=-\infty}^{\infty} \hat{B}_p \exp(i\alpha_p x) \left[\exp(i\chi_p y) + \exp\left(i\chi_p(g-2h-y)\right)\right] \qquad ...(4.45)$$

Equations in the unknown mode amplitudes a_m and b_m (from equation (4.3)) are provided by the application of the usual continuity conditions at the interfaces defined by $y = \pm g/2$. At the upper interface, continuity of the field and its y-derivative yields equations identical to (4.7) and (4.9). One set of linear equations in the mode amplitudes is therefore given by equation (4.13). At the lower interface, the field-matching, when projected onto the modal function basis, furnishes the equation

$$c\varepsilon_m \left[b_m \cos(\mu_m \tfrac{g}{2}) - a_m \sin(\mu_m \tfrac{g}{2})\right] =$$

$$\sum_{p=-\infty}^{\infty} \hat{B}_p \left[\exp(-i\chi_p \tfrac{g}{2}) + \exp\left(i\chi_p(\tfrac{3g}{2} - 2h)\right)\right] \overline{J}_{mp} \qquad ...(4.46)$$

In a similar manner, the field derivatives are equated on the interval $-c/2 \leqslant x \leqslant d-c/2$ and the result projected onto the set of plane-wave basis functions giving

$$\hat{B}_p = \frac{\sum_{m=0}^{\infty} \mu_m \left[a_m \cos(\mu_m \frac{g}{2}) + b_m \sin(\mu_m \frac{g}{2})\right] J_{mp}}{i\chi_p d \left[\exp(-i\chi_p \frac{g}{2}) - \exp\left(i\chi_p(\frac{3g}{2} - 2h)\right)\right]} \qquad ...(4.47)$$

The second set of equations in the mode amplitudes is derived by inserting equation (4.47) into (4.46), giving

$$\sum_{m=0}^{\infty} a_m^* \left[\mu_m \cot(\mu_m \frac{g}{2}) \frac{Z_{m\ell}^s}{d} - \delta_{m,\ell}\, \varepsilon_\ell c\right]$$

$$+ \sum_{m=0}^{\infty} b_m^* \left[\mu_m \tan(\mu_m \frac{g}{2}) \frac{Z_{m\ell}^s}{d} + \delta_{m,\ell}\, \varepsilon_\ell c\right] = 0 \qquad ...(4.48)$$

where a_m^* and b_m^* are defined according to equation (4.14) (note that $\mu_{1,m}$ has been replaced by μ_m) and

$$Z_{m\ell}^s = \sum_{p=-\infty}^{\infty} \frac{\cot(\chi_p(h-g))\; J_{mp}\, \overline{J}_{\ell p}}{\chi_p} \qquad ...(4.49)$$

Here one recognizes the resemblance between $Z_{m\ell}^s$ and $W_{m\ell}^s$, the analogous term for the bottle grating defined in equation (4.17).

Equations (4.48) and (4.13) are coupled and solved numerically after truncation, as with the bottle grating. The reflected order amplitudes B_p are recovered from equation (4.9) and the transmitted order amplitudes $\hat{B}_p$ from equation (4.47).

Turning now to the modification to the theory for P polarization, we find they are virtually the same ones necessary in the case of the bottle grating. Mode amplitudes in region II are now denoted by a_m' and b_m' while equation (4.45) which describes the field in region III remains unaltered except for the change of $\hat{B}_p$ to $\hat{A}_p$ and for a minus sign between the exponential terms. The appropriate continuity conditions are applied and in the final analysis the reflected field amplitudes are expressed by equation (4.20) while the internal plane-wave field amplitudes are given by

$$\hat{A}_p = \frac{\sum_{m=1}^{\infty} [b'_m \cos(\mu_m \frac{g}{2}) - a'_m \sin(\mu_m \frac{g}{2})] \; I_{mp}}{d[\exp(-i\chi_p \frac{g}{2}) - \exp(i\chi_p(\frac{3g}{2} - 2h))]} \qquad ..(4.50)$$

The first of the coupled pair of linear equations to be solved for the mode amplitudes a'_m and b'_m is identical to equation (4.21) while the second is

$$\sum_{m=1}^{\infty} a'^*_m \left[\frac{Z^P_{m\ell}}{d} + \delta_{m,\ell} \mu_\ell \cot(\mu_\ell \frac{g}{2}) \frac{c}{2}\right]$$

$$+ \sum_{m=1}^{\infty} b'^*_m \left[-\frac{Z^P_{m\ell}}{d} + \delta_{m,\ell} \mu_\ell \tan(\mu_\ell \frac{g}{2}) \frac{c}{2}\right] = 0 \qquad ...(4.51)$$

where a'^*_m amd b'^*_m are defined in equation (4.23) and $Z^P_{m\ell}$ is given by

$$Z^P_{m\ell} = \sum_{p=-\infty}^{\infty} \chi_p \cot(\chi_p(h-g)) \; I_{mp} \; \bar{I}_{\ell p}. \qquad ...(4.52)$$

Testing of phase symmetry properties and reciprocity has successfully provided a check on the amplitude calculations for both P and S polarizations. Again, 17 diffraction order terms and 10 mode terms are found to be ample in satisfying these conditions.

The appropriate phase properties for this particular structure are now indicated. Because the structure is a symmetrical reflection grating, the time-reversibility equations are as for the bottle grating, i.e. equation (2.42) for the long-wavelength mounting and equation (2.55) for the -1 Littrow mounting. This means that equations (2.44) and (2.58) are the pertinent phase properties for the reflected orders. Equations (2.60), (2.61) and (2.62) also apply to the amplitudes R_0 and R_{-1}, where either a^*_m or b^*_m may be used in the last two equations. For the groove region, the appropriate phase relations for the mode amplitudes are expressed by equations (4.28) and (4.29), i.e. just those for the bottle grating. For the region between

grating and conducting plane, new phase relations must be derived. The general representation for the field in that region is

$$F(x,y) = \sum_p T_p \exp(i\alpha_p x) \left[\exp(i\chi_p y) \pm \exp\left(i\chi_p(g-2h-y)\right)\right] \qquad ...(4.53)$$

When this expression is inserted into equations (2.42) and (2.55), the analagous equations to (4.26) and (4.27) for the bottle grating become

$$\left.\begin{array}{ll} \text{(i)} & \arg(T_0) = \tfrac{1}{2}\arg(R_0) - \dfrac{(g-2h)\chi_0}{2} \quad (+\pi) \\ \text{(ii)} & \arg(T_p) = \tfrac{1}{2}\arg(R_0) \quad (+\pi) \end{array}\right\} \text{ long-}\lambda \qquad ...(4.54)$$

and

$$\left.\begin{array}{ll} \text{(i)} & \arg(T_0 - T_{-1}) = \tfrac{1}{2}\arg(R_0 - R_{-1}) - \dfrac{(g-2h)\chi_0}{2} \quad (+\pi) \\ \text{(ii)} & \arg(T_p - T_{-p-1}) = \tfrac{1}{2}\arg(R_0 - R_{-1}) \quad (+\pi) \end{array}\right\} \text{ -1 Littrow} \qquad ...(4.55)$$

Table 4.3 exhibits the excellent conformity with which the long-wavelength equations (2.44), (4.28) and (4.54) are satisfied.

4.3.3 Spectral Behaviour

Efficiency curves have been computed for the -1 Littrow mounting with the interesting result that this structure does in fact behave very similarly to the bottle grating. For an appropriate choice of groove parameters, distinctive sharp peaks are again observed in the -1 order efficiency at definite wavelength intervals. Examples of some typical efficiency spectra are contained in Figures 4.14 to 4.17. Groove parameters have been selected so that direct comparisons can be made with the curves presented in Section 4.2 for the bottle grating.

An initial observation is that when c, g, h and d are the same for the two gratings, the mirror grating possesses fewer efficiency maxima over the wavelength interval $2/3 < \lambda/d < 2.0$, but the longer wavelength maximum lies

TABLE 4.3

Long-Wavelength Symmetry Properties of the Mirror Grating.

Phases of the field amplitudes are tabulated for checking against the symmetry relations of Sections 2.3, 4.2.3 and 4.3.2.

Grating Parameters: $d = 1.0$, $c = 0.3$, $g = 0.2$, $h = 1.0$
Mounting Parameters: $\lambda = 1.3$, $\theta = 11.0°$
Number of Expansion Terms: 17 plane-wave, 10 modal.

	P Polarization	S Polarization	Equation Number
$\arg(R_0)$	134.9991	-64.1593	
$\arg(T_0)$	-137.8462	-147.4253	4.54(i)
$\frac{1}{2}\arg(R_0)+\pi$	-112.5005	147.9204	
$\frac{1}{2}\arg(R_0)+\pi/2$	157.4996	57.9204	
$\arg(R_p)$	-112.5005	147.9204	2.44
$\arg(T_p)+\pi$	-112.5005	147.9204	4.54(ii)
$\arg(a_m^e)$	-112.5005	147.9204	4.28(i)
$\arg(b_m^e)$	-112.5005	147.9204	4.28(i)
$\arg(a_m^o)$	157.4996	57.9204	4.28(ii)
$\arg(b_m^o)$	157.4996	57.9204	4.28(ii)
R.H.S. of eq. (4.54(i))	-47.8462	-147.4253	4.54(i)

Fig. 4.14

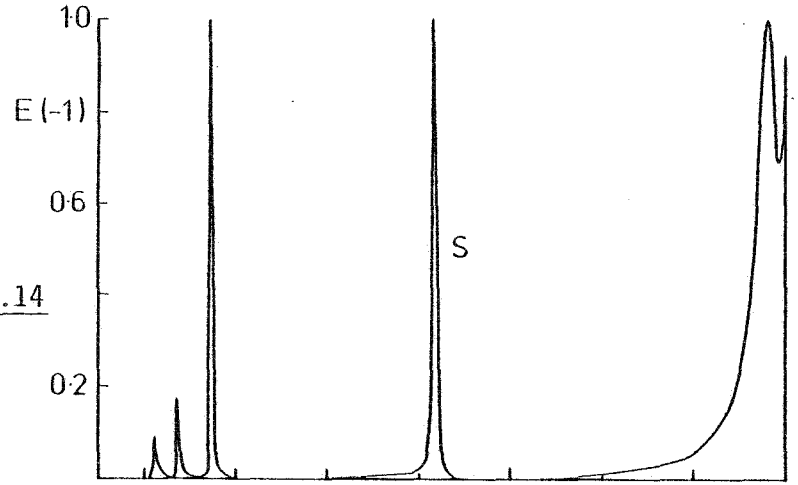

Fig. 4.15

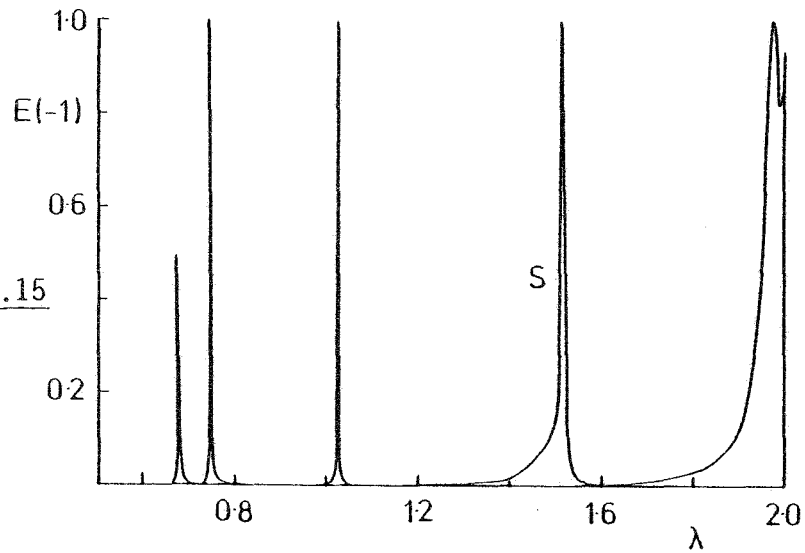

Fig. 4.16

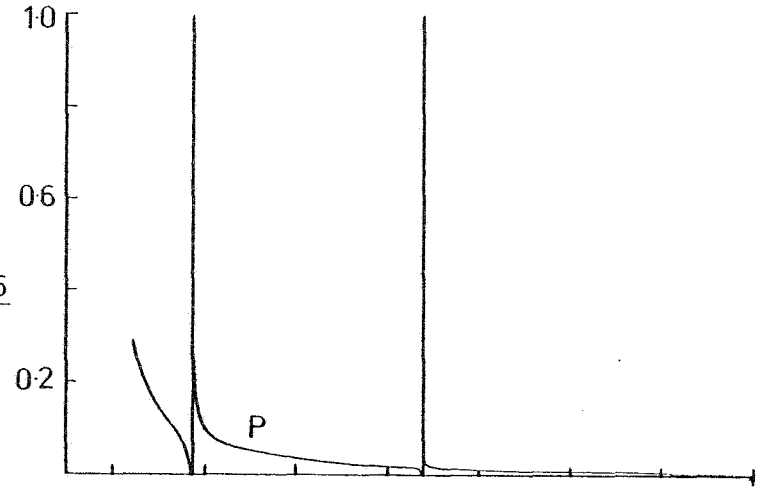

Fig. 4.17

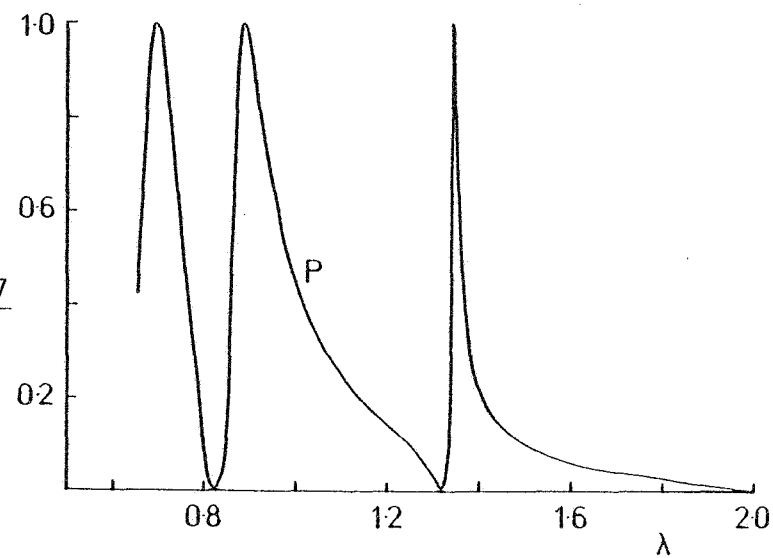

-1 Littrow efficiency spectra for the mirror grating. (d=1.0)

Figure 4.14 c=0.05,g=0.02,h=1.0(S pol.)
Figure 4.15 c=0.05,g=0.02,h=1.4(S pol.)

Figure 4.16 c=0.3,g=0.2,h=1.0(P pol.)
Figure 4.17 c=0.5,g=0.2,h=1.0(P pol.)

further to the right, i.e. closer to 2.0. For an explanation of these observations we again turn to a monomodal approximation to the theory.

In the case of S polarization, consider the relevant equations from which the single-mode model may be derived. For the bottle grating these are equations (4.7), (4.9), (4.10) and (4.11), which when truncated lead to a monomodal expression for B_p framed by equations (4.31) to (4.34). For the mirror grating, the initial equations are (4.7), (4.9), (4.46) and (4.47). The last two of these are of essentially the same form as equations (4.10) and (4.11). Also, by comparing the final coupled pair of linear equations in the mode amplitudes for the two types of grating we can again see their similarity. For the bottle grating these are equations (4.13) and (4.16) while for the mirror grating they are (4.13) and (4.48). The only change in (4.48) from (4.16) is that $W^s_{m\ell}/f$ has become $Z^s_{m\ell}/d$, i.e.

$$\sum_{n=0}^{\infty} \frac{\cot(\mu_{2,n}(h-g))\, P_{mn}\, P_{\ell n}}{f\, \varepsilon_n\, \mu_{2,n}} \rightarrow \sum_{p=-\infty}^{\infty} \frac{\cot(\chi_p(h-g))\;\; J_{mp}\, \overline{J}_{\ell p}}{\chi_p\, d} \qquad \ldots(4.56)$$

It is therefore not necessary to derive the entire monomodal model for this case, but rather it can be deduced from the previous one. However, before continuing, a monomodal approximation, or more strictly speaking, a single-term approximation, must be justified for the field representations in both the aperture region and the region between grating and mirror.

In the case of the former region, nothing has changed from the bottle-grating treatment and just as before the $m = 0$ mode is the dominant one in the narrow apertures. In the case of the other region, the field is now expressed as plane waves instead of waveguide modes.

Whereas for the bottle grating, the maxima were attributed to resonances in the real modes, the appropriate mechanism in this case is an interference amongst the real orders. This phenomenon is expected to manifest itself in the amplitudes $\hat{B}_p$ for which χ_p is real. Numerical evidence confirms this, and for the -1 Littrow mounting, in the vicinity of an efficiency maximum, the intensities of a complementary pair of real orders (i.e. 0,-1 or +1,-2 etc.) are far in excess of those for the other orders. Therefore at those wavelengths, for that particular mounting, the field can legitimately be characterised by the terms containing $\hat{B}_p$ and $\hat{B}_{-1-p}$ only. This does not appear to provide the desired single-term representation until one analyses more closely the transformation (4.56). The term on the R.H.S. reduces in the case of a Littrow mounting, to become

$$\sum_{p=0}^{\infty} \frac{2\cot(\chi_p(h-g))}{\chi_p d} \; Re\,(J_{mp}\,\overline{J}_{\ell p}) \qquad \ldots(4.57)$$

That is, decoupling implies only a summation over positive values of p is necessary. Hence, for p = 0, the p = -1 contribution is taken into account and we effectively have a "single-order" representation.

Continuing then with the approximation, and drawing on the similarities with the bottle-grating expressions, one finds that the singularities in B_p which correspond to equation (4.35) are now given by (for small c)

$$\frac{\cot(\chi_p(h-g))}{\chi_p} = \frac{dc}{2J_{op}^2} \quad \frac{\tan(\mu_0 g)}{\mu_0} \qquad \ldots(4.58)$$

where the appropriate value for p is the positive index of the pair of orders which are "resonating". This equation governs the positions of the efficiency maxima for S polarization.

In the limit of c diminishing to zero, the condition for the above equality to remain true is

$$\chi_p(h-g) = \ell\pi \qquad \ldots(4.59)$$

cf. $\mu_{2,n}(h-g) = \ell\pi$ for the bottle grating. Note that this condition, when inserted into equation (4.47), is seen to produce singularities in $\hat{B}_p$ - as does the condition $\chi_p = 0$ which is related to Rayleigh wavelength anomalies. Expansion of equation (4.59) reveals that the limiting positions of the efficiency maxima are given by

$$\lambda_{max} = \frac{2d(h-g)}{\sqrt{4(p+\frac{1}{2})^2(h-g)^2 + \ell^2 d^2}} \quad \ell = 0,1,2... \qquad \ldots(4.60)$$

We note that through the introduction of χ_p to the resonance conditions, they now depend on the mounting configuration - in contrast with the equivalent situation for the bottle grating where $\mu_{2,n}$ is independent of the mounting. The normal incidence mounting is of lesser interest here, as was the case with the bottle grating, because the maxima do not reach 100% efficiency owing to the increased number of orders propagating. However, if the analysis from expression (4.57) through to equation (4.60) is repeated for this mounting one finds that equation (4.59) still determines the positions of maxima, and hence equation (4.60) becomes

$$\lambda_{max} = \frac{2d(h-g)}{\sqrt{4p^2(h-g)^2 + \ell^2 d^2}} \qquad \ell = 0,1,2... \qquad \ldots(4.61)$$

For $p = 0$ this expression reduces to $\lambda_{max} = 2(h-g)/\ell$ and we again recover the geometric limit positions of the interference maxima for a Fabry-Perot interferometer or the double-grating interferometer of Adams and Botten [4.3]. Note that (h-g) is equivalent to only half of the separation of the two lamellar arrays in the structure studied by the aforementioned authors. The mirror grating is simply a "reflection version" of the symmetrical double-grating interferometer if the mirror in the former coincides with the horizontal plane of symmetry in the latter.

Returning now to the -1 Littrow mounting, equation (4.60) asserts that the longest wavelength for which a p = 0 maximum can occur is $\lambda/d = 2.0$ while for a p = 1 maximum it is $\lambda/d = 2/3$. Thus, in the region where only two orders are propagating and the maxima achieve 100% efficiency, all maxima are due to p = 0. This explains why more maxima are possible in this wavelength region for the bottle grating with the same value of (h-g) if f is chosen sufficiently large. For the bottle grating the index n can take on values 0 or 2 while here p is confined to be 0.

For (h-g) = 0.8 the values predicted by equation (4.60) are 2.0, 1.249 and 0.743 (the period being equal to unity) and in fact reference to Figure 4.14 shows three maxima lying very close to these wavelengths. In Figure 4.15, (h-g) has been increased to 1.2 and an extra peak has appeared with the positions of the resulting four peaks conforming with the predictions of 2.0, 1.536, 1.029 and 0.743. The spikes occurring exactly at $\lambda/d = 2/3$ and $\lambda/d = 2.0$ are presumably the Rayleigh wavelength phenomena also seen in the bottle grating spectra.

For P polarization the same analogies may be drawn between bottle grating and mirror grating with the result that equations (4.59) and (4.60) again determine the positions of the maxima in the limit as $c \to 0$. In contrast to the preceding case, we now find that the P polarization maxima have identical limit positions to those for S polarization. For the bottle grating they differ due to n in equation (4.37) being either odd or even. Figure 4.16 contains the P polarization efficiency curve for (h-g) = 0.8. Two peaks are observed near the predicted wavelengths of 1.249 and 0.743, however the long-wavelength maximum is missing. Just as with the bottle grating, the P polarization maxima lie at longer wavelengths than their limiting positions and so the relevant maximum would have to be in the unphysical region to the right of $\lambda/d = 2.0$.

In Figure 4.17 the aperture width has been increased and the expected occurs. The interference maxima broaden and also move further from their limits. The same behaviour is observed for S polarization, where the peaks move in the opposite direction. The value of c has to be much smaller in the latter case for maxima of equivalent half-width to be formed.

Overall, the arguments which apply to the finesse and position of the peaks for the bottle grating are equally applicable to the mirror grating, as is the influence of the groove width and depth. Reference to the appropriate curves in Figures 4.7 and 4.10, along with the spectra of Figures 4.14 and 4.17, demonstrates that the -1 order efficiency is again given very closely by the transmission of the wire grating with interference maxima superimposed at wavelengths given by equation (4.60).

4.3.4 Conclusion

The results presented here have displayed the allied behaviour which exists between the action of the bottle and mirror gratings. The latter has been found to produce strong efficiency maxima which reach 100% for the -1 Littrow mounting. The separation of the lamellar transmission array can be tuned to determine the number and positioning of the maxima over the entire wavelength interval where two orders are propagating. However, fewer maxima are formed when compared with the bottle grating. The maxima are governed in respect of half-width and fine-positioning by the aperture width of the array.

Although the formalisms of the bottle and mirror gratings are directly comparable, and hence their spectral properties are also comparable, the concept of operation for each is slightly different. In the case of the mirror grating, multiple-scattering of plane waves occurs between the upper

array and the mirror, producing interference, while for the bottle grating, a resonance condition is set up in the waveguide modes in each cavity region.

4.4 THE STEP GRATING

4.4.1 Introduction

The investigation reported here exists at a time when there is considerable interest in the acquisition of a better understanding of grating behaviour, especially with regard to different groove profiles. To this end, the theorists are seeking more simplified theories and models to work with rather than unwieldy integral and differential formalisms. Two papers recently published in this area are those of Breidne and Maystre [4.5] and Loewen *et al.* [4.6], both of which describe attempts to relate the efficiencies of different classes of gratings through the use of empirical or asymptotic methods. One of the most promising solutions to the problem would be the development of a general purpose modal formalism and work along those lines is detailed in Chapter 7. Here a different approach is adopted. It is one which rests on a simple theory but at the same time is completely rigorous.

The subject of this section is a perfectly-conducting reflection grating whose groove profile consists of a number of linear facets aligned parallel with either the x or y directions, where the grating is assumed to lie in xyz coordinate system with the long axis of the grooves coinciding with the z-direction. By choosing an equal number of the resulting "steps" to be on each side of the grating groove, and by prescribing opposite steps to have the same depth, the groove is sub-divided into a number of rectangular tiers. It is also stipulated that each successive tier is narrower than the one above it. The field in each of the rectangular groove regions may then be represented by an expansion of lamellar-type waveguide mode functions.

In the absence of a rigorous modal theory for arbitrary profiles, a motivation for studying the stepped structure was to try and approximate conventional reflection gratings through the appropriate choice of the "steps", and perhaps be able to relate the behaviour of those gratings to the behaviour of the waveguide modes in the step grating. Of course one has to verify first that the step grating is able to reproduce the performance of the conventional grating. For the method to be viable, a profile such as the sinusoidal profile would have to be capably modelled with only a relatively small number of steps.

Because a large proportion of the commonly-used gratings have symmetrical groove profiles, coupled with the fact that an axis of symmetry markedly simplifies the analysis, only the symmetrical step grating has been investigated. Attention has also been confined to S polarization because this is believed to be the more formidable and challenging of the two polarizations. Also, it is more accurate as a "fingerprint" of a particular profile while at the same time being responsible for the more spectacular resonance anomalies.

The theoretical formalism is outlined in the next section while Section 4.4.3 is concerned with numerical aspects of the implementation including the various checks on the results. Finally, in Section 4.4.4, the efficiencies of well-chosen step gratings are compared with those of other profiles.

4.4.2 The Formulation for S Polarization

The geometry for the symmetrical step grating is illustrated in Figure 4.18. A total of t tiers are included, and the i^{th} tier has width c_i and depth $(h_i - h_{i-1})$ where $i = 1, 2 \ldots t$ and $h_0 = 0$. The grating is placed in the xyz coordinate system with the origin situated at the top-centre of the groove. The diffraction problem is set up using the same notation

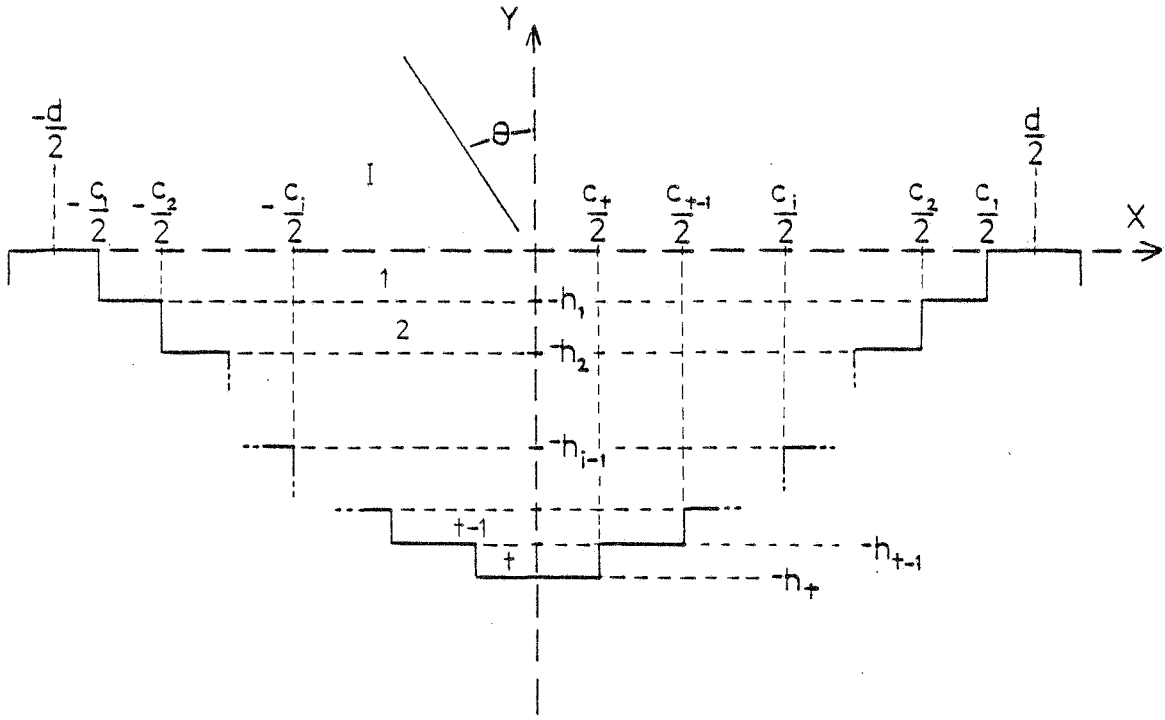

Figure 4.18 The geometry of the diffraction arrangement for the step grating.

defined for the bottle and mirror gratings and so equations (4.1) and (4.2) again represent the plane-wave magnetic field in region I above the top surface.

The field in regions 1 to t-1 can be expanded as a set of mode functions in the same form as those for the lamellar transmission grating. Thus, we define

$$H^i(x,y) = \sum_{m=0}^{\infty} \cos\left(\frac{m\pi}{c_i} \left(x + \frac{c_i}{2}\right)\right) \left[a_{im} \sin(\mu_{im} y) + b_{im} \cos(\mu_{im} y)\right] \qquad ...(4.62)$$

where $-\frac{c_i}{2} \leq x \leq \frac{c_i}{2}$, $-h_i \leq y \leq -h_{i-1}$, $i = 1,2,\ldots\ t-1$

and

$$H^t(x,y) = \sum_{m=0}^{\infty} b_{tm} \cos\left(\frac{m\pi}{c_t} \left(x + \frac{c_t}{2}\right)\right) \cos\left(\mu_{tm}(y + h_t)\right) \qquad ...(4.63)$$

where $\mu_{im} = \left(k^2 - (m^2\pi^2)/c_i^2\right)^{\frac{1}{2}}$ and is chosen to be positive real or positive imaginary.

Applying the method of moments in the usual manner, continuity of the field between regions I and 1 yields

$$\overline{J_m^1} + \sum_{p=0}^{\infty} B_p \overline{J_{mp}^1} = b_{1m} \varepsilon_m c_1 \qquad ...(4.64)$$

where

$$J_{mp}^i = \int_{-c_i/2}^{c_i/2} \cos\left(\frac{m\pi}{c_i}\left(x + \frac{c_i}{2}\right)\right) \exp(-i\alpha_p x)\, dx \ . \qquad ...(4.65)$$

The closed form for the latter integral may be deduced from equation (2.18).

The continuity of the normal derivative between the above two regions results in the expression

$$B_p = \frac{\sum_{m=0}^{\infty} a_{1m} \mu_{1m} J_{mp}^1}{i\chi_p d} + \delta_{0,p} \qquad ...(4.66)$$

Substitution of this equation into equation (4.64) furnishes a set of linear equations in the upper-tier mode amplitudes which may be written in the form

$$\sum_{m=0}^{\infty} a_{1m} \left[\frac{\mu_{1m}}{d} K^1_{m\ell}\right] + \sum_{m=0}^{\infty} b_{1m} \left[\delta_{m,\ell}\, c_1\, \varepsilon_\ell\right] = 2\overline{J^1_{\ell o}} \qquad \ldots(4.67)$$

where $K^i_m = \sum_{p=-\infty}^{\infty} \frac{iJ^i_{mp}\, \overline{J}^i_{\ell p}}{\chi_p}$ $\qquad \ldots(4.68)$

(Note: Where i is not used as a subscript or superscript in an equation it refers to $\sqrt{-1}$.)

Now consider the field-matching between regions i and i+1, where i = 1,2 ... t-2. The field is only continuous along $y = h_i$ over the interval $-(c_i+1)/2 \leq x \leq (c_i+1)/2$. This continuity is therefore projected onto the basis functions for the $(i+1)^{th}$ region, yielding the equation

$$\sum_{m=0}^{\infty} \left[a_{im} \sin(\mu_{im} h_i) - b_{im} \cos(\mu_{im} h_i)\right] Q^i_{m\ell}$$

$$= \left[a_{i+1,\ell} \sin(\mu_{i+1,\ell}\, h_i) - b_{i+1,\ell} \cos(\mu_{i+1,\ell} h_i)\right] \varepsilon_\ell\, c_{i+1} \qquad \ldots(4.69)$$

where

$$Q^i_{mn} = \int_{-c_{i+1}/2}^{c_{i+1}/2} \cos\left(\frac{m\pi}{c_i}\left(x + \frac{c_i}{2}\right)\right) \cos\left(\frac{n\pi}{c_{i+1}}\left(x + \frac{c_{i+1}}{2}\right)\right) \qquad \ldots(4.70)$$

(The closed form for this integral is similar to that of equation (4.12).)

To form part of the final coupled linear system, equation (4.69) is more conveniently written as

$$\sum_{m=0}^{\infty} a_{im}\,[-\sin(\mu_{im}h_i)\;Q^i_{m\ell}] + \sum_{m=0}^{\infty} b_{im}\,[\cos(\mu_{im}h_i)\;Q^i_{m\ell}]$$

$$+ \sum_{m=0}^{\infty} a_{i+1,m}[\delta_{m,\ell}\;\varepsilon_\ell\;c_{i+1}\;\sin(\mu_{i+1,\ell}h_i)]$$

$$+ \sum_{m=0}^{\infty} b_{i+1,m}\,[-\delta_{m,\ell}\;\varepsilon_\ell\;c_{i+1}\;\cos(\mu_{i+1,\ell}h_i)] = 0 \qquad \ldots(4.71)$$

The normal derivative is continuous along $y = h_i$ for $-c_i/2 \leq x \leq c_i/2$ and the projection of this matching onto the basis functions for the i^{th} region can be rearranged into the form

$$\sum_{m=0}^{\infty} a_{im}\,[-\delta_{m,\ell}\;\varepsilon_\ell\;c_i\;\mu_{i\ell}\;\cos(\mu_{i\ell}\;h_i)] + \sum_{m=0}^{\infty} b_{im}[-\delta_{m,\ell}\varepsilon_\ell\;c_i\;\mu_{i\ell}\;\sin(\mu_{i\ell}h_i)]$$

$$+ \sum_{m=0}^{\infty} a_{i+1,m}[\mu_{i+1,m}\;\cos(\mu_{i+1,m}h_i)\;Q^i_{\ell m}]$$

$$+ \sum_{m=0}^{\infty} b_{i+1,m}[\mu_{i+1,m}\;\sin(\mu_{i+1,m}h_i)\;Q^i_{\ell m}] = 0 \qquad \ldots(4.72)$$

The remaining field-matching, which differs slightly from the above, is between regions t-1 and t. The continuity of the field and its y-derivative along the boundary $y = h_{t-1}$ provides the respective equations

$$\sum_{m=0}^{\infty} [-a_{t-1,m}\;\sin(\mu_{t-1,m}h_{t-1}) + b_{t-1,m}\;\cos(\mu_{t-1,m}h_{t-1})]\;Q^{t-1}_{m\ell}$$

$$= b_{t\ell}\;\cos(\mu_{t\ell}(h_t - h_{t-1}))\;\;\varepsilon_\ell\;c_t \qquad \ldots(4.73)$$

and

$$\mu_{t-1,\ell}\;c_{t-1}\;\varepsilon_\ell\;[a_{i-1,\ell}\;\cos\;(\mu_{i-1,\ell}h_{i-1}) + b_{i-1,\ell}\;\sin(\mu_{i-1,\ell}h_{i-1})]$$

$$= -\sum_{m=0}^{\infty} b_{tm}\;\mu_{tm}(\sin\;\mu_{tm}(h_t - h_{t-1}))\;\;Q^{t-1}_{\ell m} \qquad \ldots(4.74)$$

Substitution of equation (4.73) into (4.74) eliminates the lower-region coefficients b_{tm}, leaving the set of linear equations

$$\sum_{m=0}^{\infty} a_{t-1,m} \left[\frac{-\sin(\mu_{t-1,m} h_{t-1})}{c_t} Y_{m\ell} + \delta_{m,\ell} \mu_{t-1,\ell} \varepsilon_\ell c_{t-1} \cos(\mu_{t-1,\ell} h_{t-1})\right]$$

$$+ \sum_{m=0}^{\infty} b_{t-1,m} \left[\frac{\cos(\mu_{t-1,m} h_{t-1})}{c_t} Y_{m\ell}\right.$$

$$\left. + \delta_{m,\ell} \mu_{t-1,\ell} \varepsilon_\ell c_{t-1} \sin(\mu_{t-1,\ell} h_{t-1})\right] = 0 \qquad \ldots(4.75)$$

where $$Y_{m\ell} = \sum_{n=0}^{\infty} (\mu_{tn}/\varepsilon_n) \tan(\mu_{tn}(h_t - h_{t-1})) Q_{\ell n}^{t-1} Q_{mn}^{t-1}.$$

Equations (4.67), (4.71), (4.72) and (4.75) form a coupled set of linear equations in the mode amplitudes $a_{1,m}$, $b_{1,m}$ ... $a_{t-1,m}$, $b_{t-1,m}$. Equations (4.67) and (4.75) are included only once. For equations (4.71) and (4.72), i ranges from 1 to t-2, producing an additional 2t-4 equations. This means there exists a total of 2t-2 equations to be solved simultaneously and if the index m is allowed to vary from 0 to M-1 then the scattering matrix is of length 2M(t-1).

4.4.3 Numerical Considerations

Preliminary implementation of the formalism indicated that numerically it was desirable to keep the dimension of the matrix below a value of about 60. For a size greater than this, the matrix was found to be insufficiently stable to be dealt with satisfactorily by the particular numerical routine used to solve linear systems. (This is the same routine used in Chapter 2 for the lamellar problem.) The first signs of this instability were detected as discrepancies in the satisfying of energy conservation - a condition which should be satisfied analytically.

With the upper-bound of 60, acceptable results were achieved for all but highly modulated profiles, with energy conservation being satisfied to 0.01%. Typical figures used for t and M for a moderately deep grating were 5 and 6 respectively, i.e. five steps and six modes within each region forming a matrix of dimension 48 x 48.

Table 4.4 lists the results of a reciprocity test for five steps and reflects the satisfactory agreement in the efficiencies when as few as six modes are used to characterize each region. Other checks on the calculations included phase tests for both -1 Littrow and long-wavelength mountings. The appropriate symmetry relations are similar to those described for the bottle grating and these were confirmed to be well-satisfied. Boundary conditions along some of the interfaces separating different levels were also tested and although the matching was only fair, it was deemed acceptable in light of the small number of modes used and also when compared with the results obtained from similar tests on the basic lamellar formalism.

One very pertinent test for the step grating is provided by the Maréchal-Stroke Theorem [4.7] . The application of the Theorem to this particular structure requires that for S polarization and a normally-incident plane wave, all energy should be specularly reflected if the vertical walls of the steps are an integral multiple of $\lambda/2$. Under these conditions the field within the groove region should become a standing plane wave.

In implementing the test, a three-step grating was chosen with the depths of each step being 0.2d. The wavelength used was 0.4d giving rise to five diffracted orders. The computed efficiencies along with information regarding the modes in the uppermost and lowest groove regions are presented in Table 4.5. Concordance with the predictions of the Theorem is excellent with virtually 100% efficiency appearing in the 0^{th} order.

It is also noted that the only significant modes are the m = 0 y-symmetric modes which are observed to be real-valued and have moduli equal to 2.0. The reason for this behaviour is as follows. The total field in each tier of the groove region reduces to $b_{i_0} \cos(\mu_{i_0} y) = 2 \cos(ky)$ (for the bottom tier it is $b_{t_0} \cos(\mu_{t_0} h_t) \cos(\mu_{t_0} y)$) which is the sum of an S-polarized normally-incident plane wave and its reflection, i.e. $\exp(i\chi_0 y) + \exp(-i\chi_0 y)$. Looking at the problem another way we note that by

TABLE 4.4

Reciprocity Results for the Step Grating.

Efficiency and phase values of the order amplitudes for S polarization are given to confirm agreement with the Reciprocity Theorem. The mounting configurations are defined by:

Problem 1: $\theta = 11.5°, \lambda = 0.7$
Problem 2: $\theta = 30.0418°, \lambda = 0.7$ (-1 order returned)
Problem 3: $\theta = -64.0751°, \lambda = 0.7$ (+1 order returned).

Groove Parameters: $d = 1.0$, $c_i = 0.9, 0.8, 0.68, 0.52, 0.28.$
$h_i = 0.14, 0.26, 0.34, 0.40, 0.45.$
Number of Expansion Terms: 17 plane-wave, 6 modal (in each region).

		S Polarization
Problem 1	$E(0)$, $\arg(B_0)$	0.1336, -36.74
	$E(-1)$, $\arg(B_{-1})$	0.1586, 113.90
	$E(+1)$, $\arg(B_1)$	0.7078, 5.39
Problem 2	$E(-1)$, $\arg(B_{-1})$	0.1587, 113.89
Problem 3	$E(1)$, $\arg(B_1)$	0.7075, 5.41

TABLE 4.5

The "Marechal-Stroke Test" for the Step Grating.

Results are presented to demonstrate compliance with the Marechal-Stroke Theorem by the step grating in a normal incidence mounting with S polarized radiation.

Groove Parameters: $d = 1.0$, $c_i = 0.86, 0.52, 0.12$
$h_i = 0.2, 0.4, 0.6.$
Number of Expansion Terms: 17 plane-wave, 7 modal (in each region).

p	E(p)	$\arg(B_p)$	m	$\lvert a_{1,m}\rvert^2$	$\lvert b_{1,m}\rvert^2$	$\lvert b_{3,m}\rvert^2$	$\arg(b_{3,m})$
0	1.00	0.0015	0	10^{-9}	4.00	4.00	-179.9988
±1	10^{-10}	73.8494	1	10^{-38}	10^{-37}	10^{-42}	44.9605
±2	10^{-10}	85.9366	2	10^{-10}	10^{-10}	10^{-20}	-57.5626

stipulating $h_i = \ell\lambda/2$, $\ell = 0,1,2...$ the implication is that along the base of each tier, $\mu_0 h_i = \ell\pi$. That is the y-derivative of the field vanishes there and each interface acts as a mirror. This *exact* condition of total reflectance should be compared with equation (2.81) which was demonstrated to yield conditions of *high* reflectance for angles of incidence away from normal if the m = 0 mode remained the dominant one. (Note: The Theorem is equally applicable to the bottle grating under similar conditions.)

4.4.4 General Profile Approximation

The aim of the investigation outlined here was to begin with a small number of steps and gradually increment this number, each time choosing the values for h_i and c_i so that the overall profile resembled as close as possible a particular test profile such as a sinusoidal or semi-circular profile. In this manner it was hoped to gain comparable performances between the step grating and the test grating - ideally with only a few steps being required. The method of selecting the values for h_i and c_i consisted of specifying the overall groove depth h_t to be equal to that of the test grating and then constructing the vertical and horizontal facets so that the test profile passed as close as possible through their midpoints.

The first part of the investigation was to determine how well a step grating with three steps could approximate the efficiencies of a particular known grating. The aim was to also determine whether the method of selection of the values for h_i and c_i would yield efficiencies which could satisfactorily distinguish between *different* test profiles of the *same* depth.

The mounting configuration considered was the -1 Littrow mounting and so an overall groove depth of 0.3 periods was chosen - this being near to the

optimum value for a variety of profile types for S polarization and this mounting. Three profiles were selected for the test, namely a sinusoidal, a symmetrical triangular and a semi-circular profile. Utilising 17 diffraction orders and 6 modes in each groove region, efficiencies were computed over the wavelength interval $2/3 < \lambda/d < 2.0$. They are compared in Figures 4.19(a)-(c) with those generated by an integral equation method [4.8] in the case of the sinusoidal and triangular profiles and with those predicted by the modal theory of Chapter 6 in the case of the semi-circular profile. The results of the test are most encouraging. In each of the three examples the three-step model provides efficiency curves which conform well with the integral theory results for the 'true' gratings. Even though two of the three 'true' curves are fairly similar, individuality is retained amongst the step-grating curves, demonstrating that each curve represents only the intended profile. The regions of resonance behaviour just above the Rayleigh wavelength are quite well accounted for by the models, although some discrepancies are encountered with the triangular profile. An increase in the number of steps has subsequently secured a better matching in that case with five steps moving the first blaze peak back to $\lambda/d = 0.77$ and the efficiency minimum at $\lambda/d = 1.3$ down to 0.73%.

A more demanding test of convergence of efficiency with increasing step number was carried out on a highly modulated sinusoidal profile of $h/d = 0.6$. The parameter t was varied from 3 upwards and the results are summarised in Figure 4.20, where they are compared with the integral theory predictions. For $t = 3$ and 4, six modes were prescribed for each groove region. For $t = 5$ this figure had to be reduced to four for numerical reasons. However this did not appear to be detrimental to the results and excellent convergence was still obtained. The comparison with the true curve for the low number of steps is clearly quite poor in the shorter wavelength region near the resonance anomalies, but for $t = 5$ this has improved markedly and is most acceptable.

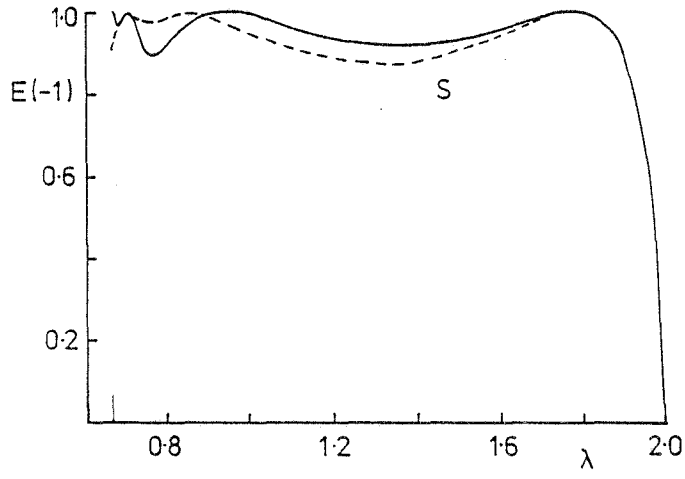

(a) Sinusoidal profile: h/d=0.3

Step-profile parameters: $d=1.0, h_i=0.1,0.2,0.3$
$c_i=0.26,0.50,0.74$

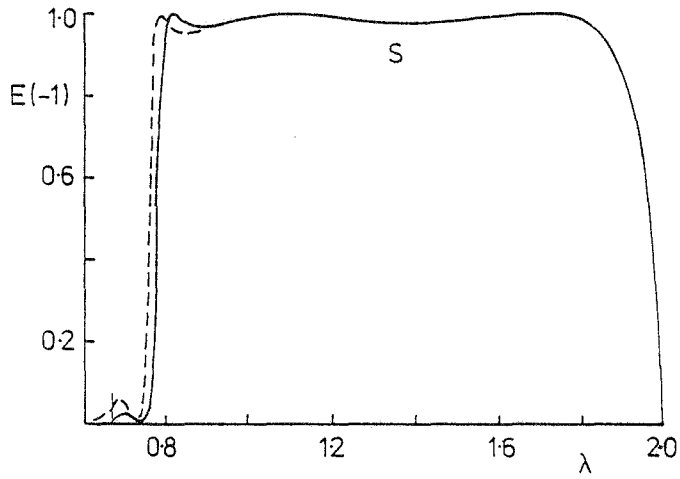

(b) Semi-circular groove profile: h/d=0.3

Step-profile parameters: $d=1.0, h_i=0.14,0.24,0.30$
$c_i=0.28,0.48,0.60$

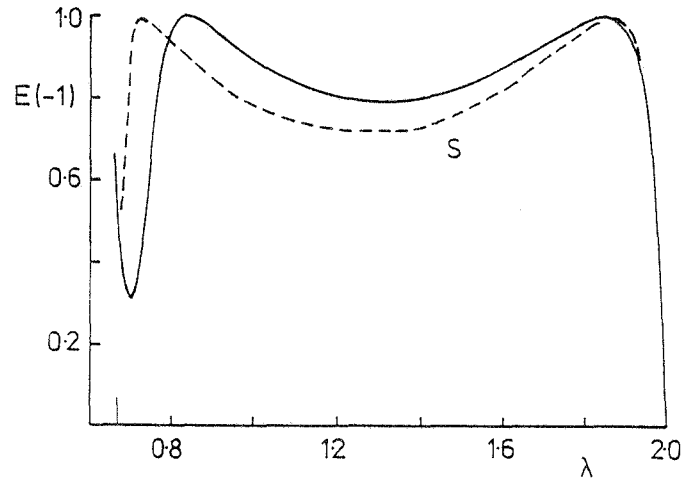

(c) Symmetrical triangular groove profile: h/d=0.3

Step-profile parameters: $d=1.0, h_i=0.1,0.2,0.3$
$c_i=0.18,0.50,0.82$

Figure 4.19 Comparison of -1 Littrow efficiencies for a 3-step grating with the corresponding efficiencies for the 'true' grating.
(———) Step grating (----) True grating

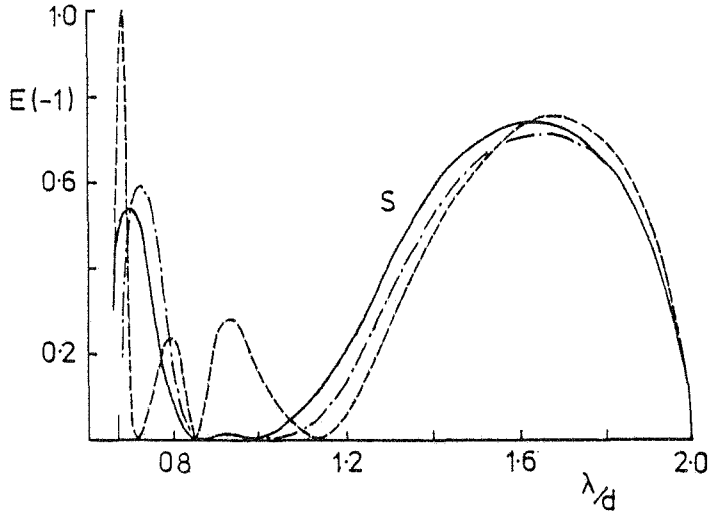

Figure 4.20 -1 Littrow efficiency curves for a 'sinusoidal' profile, h/d=0.6.(----) Step profile, 3 steps, (-·-·-) Step profile, 5 steps,(——) True profile (integral theory).

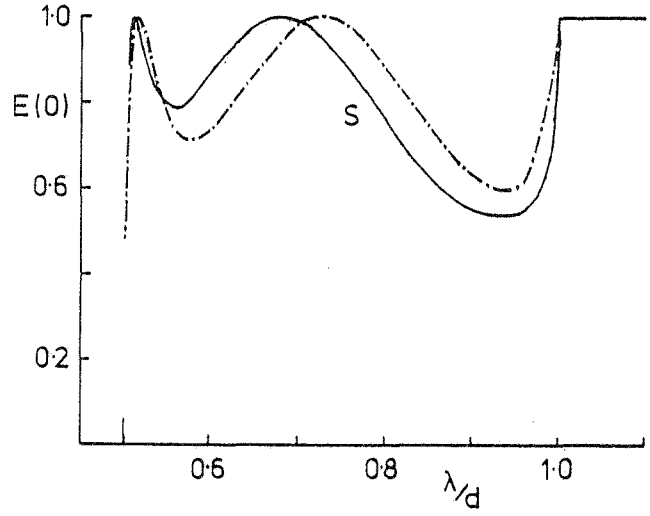

Figure 4.21 Normal incidence efficiency curves for a 'sinusoidal' profile, h/d=0.4.
(-·-·-) Step profile, 5 steps, (——) True profile (integral theory).

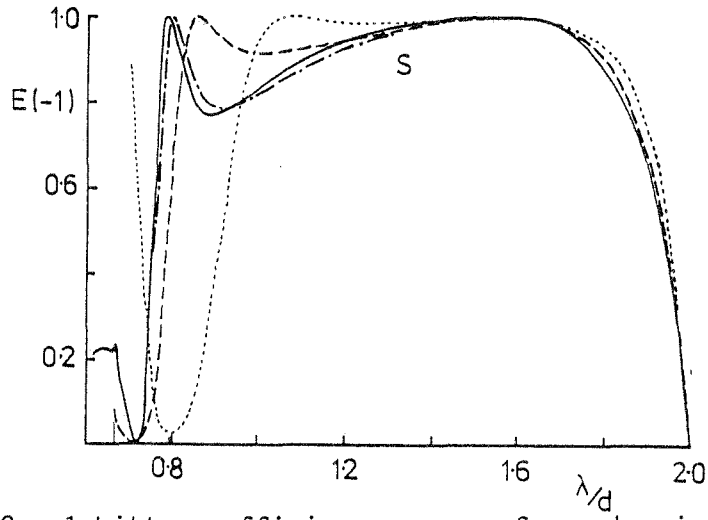

Figure 4.22 -1 Littrow efficiency curves for a 'semi-circular groove' profile, h/d=0.45. (·····) 2 steps, (----) 3 steps, (-·-·-) 5 steps, (——) True profile (modal theory).

Consider now the normal incidence mounting in the case of a "sinusoidal profile" of depth 0.4 periods. Calculations encompass the wavelength band where three orders are real and again six modes and five steps are used to characterize the problem. The comparison with the integral theory results for the true sine profile is displayed in Figure 4.21, and although differences in efficiency of up to 15% are in evidence, the important features are reproduced, but at slightly shorter wavelengths. An increment in the number of steps would probably alleviate this discrepancy and show the model to be quite acceptable for this mounting. It would appear from these results, that the greater the number of propagating orders, the greater the number of steps required to yield an accurate model. This has yet to be verified.

Of the three different gratings approximated by the step profile, the one which has yielded the best results is the semi-circular profile. Contributing factors to this may be its increased symmetry relative to the other profiles or the fact that it more closely resembles the basic lamellar grating. (The step profile for the semi-circular grating is chosen so that on each side of the groove it has a line of symmetry passing through the origin and lying at 45^{o} to the top surface.)
It is also a property of the semi-circular profile, that after the lamellar grating, it exhibits the most spectacular resonance action seen thus far. An example of such an anomaly is illustrated in Figure 4.22, which gives the -1 Littrow efficiency, evaluated for a profile of groove radius h/d = 0.45. Three curves are shown corresponding to two, three and five steps in the profile approximation. These demonstrate the strengthening of the anomaly as the profile approximates more closely the semi-circular shape.

The five-step curve compares extremely well with the true curve, calculated in Chapter 6 where a specific modal method is developed to cater for that particular grating. The formalism there is found not to be suited to

tracing the origin of resonances and so it was of added interest to determine here whether the resonance anomaly of Figure 4.22 could be attributed to any particular behaviour within the set of mode functions used to represent the step grating. A brief investigation has however been unsuccessful. The difficulty is that a number of steps are used and the groove region is split into a multiple of segments. When only two steps are used, a resonance in the lower region mode amplitude $b_{2,1}$ can be detected just above the Rayleigh wavelength, but as t is increased this feature gradually disappears. It therefore seems as though the strong resonance anomaly furnished by the five-step grating is the product of a complicated interaction between several modes in the different groove regions. It is noted however, that the presence of the anomaly is still manifested in the common phase of the modes. In the above example for five steps, this quantity undergoes a rapid change around a central wavelength of $\lambda/d = 0.77$. This correlates with the discovery in Chapter 6 that this particular profile has a complex wavelength pole with a real component of $\lambda_r = 0.76d$.

4.4.5 Conclusion

The work presented here has demonstrated that an arbitrary profile can be modelled to quite a high level of accuracy by a simple step grating which consists of only a relatively small number of steps. The "approximating" structure has been shown capable of reproducing the resonance phenomena of the "true" grating while at the same time no new features are observed in the diffraction spectra. One of the aims of the investigation was to endeavour to gain more information about the anomalies of arbitrary profile gratings, but although only limited time was directed towards this objective, it has appeared that the problem is one which does not lend itself to solution by this method.

Further areas of study with the step grating should include its study for P polarization and also for asymmetric groove profiles. Its numerical stability should also be improved enabling more modes to be used to characterize each region. A superior method of solving the linear system of equations would be useful while a redefinition of the mode amplitudes as "starred" quantities, as was done in Chapter 2, could also prove beneficial. It is unfortunate that limited-mode approximations are not valid as this could simplify the treatment of each region. (The reason that they are not valid, at least in the upper groove regions, is that most profiles have a wide upper aperture and it is known from earlier work that one or two modes are often not sufficient for such cases. Presumably though, gratings with narrow apertures could be accurately modelled with only one or two modes in each region.)

One area of study deserving examination is the performance of the step grating as a new structure in its own right. With just two or three steps it is possible that interesting behaviour could be forthcoming through appropriate selection of the step parameters. High performances comparable with the lamellar and other profiles might be achieved without the severe intrusion of resonance anomalies.

REFERENCES

[4.1] Andrewartha, J.R., 1980, J. Optics (Paris), accepted for publication.

[4.2] Casey, J.P., and Lewis, E.A., 1952, *J. Opt. Soc. Amer., 42,* 971.

[4.3] Adams, J.L., and Botten, L.C., 1979, *J. Optics (Paris), 10,* 109.

[4.4] Wait, J.R., 1954, *Can. J. of Physics, 32,* 571.

[4.5] Breidne, M., and Maystre, D., 1980, *Appl. Optics, 19,* 1812.

[4.6] Loewen, E.G., Nevière, M., and Maystre, D., 1978, *J. Opt. Soc. Amer., 68,* 496.

[4.7] Stroke, G.W., 1967, *Handbuch der Physik, 29,* 570-583 (Springer - Berlin).

[4.8] McPhedran, R.C., 1973, Thesis, University of Tasmania.

Chapter 5

THE DIELECTRIC AND FINITELY-CONDUCTING LAMELLAR GRATING

5.1 INTRODUCTION

As explained in earlier chapters, the perfectly-conducting lamellar grating has received attention from several authors who have exploited the simplicity of the structure to illustrate various diffraction phenomena [5.1-5.5]. However, the application of the simple lamellar theory is limited in practice to long-wavelength situations, where metallic gratings may be approximated by a perfect conductor, i.e. the theory is not generally accurate for wavelengths in the visible, UV or X-ray regions, nor of course is it valid for dielectric gratings.

Both the areas of finite conductivity and dielectrics have attracted interest in the lamellar grating in recent times [5.6-5.9] and this has motivated development of a "non-perfectly conducting" theory. Integral theories, such as that developed by Maystre [5.10], have become available for application to lamellar gratings, but as mentioned previously, they suffer from an inability to provide an explanation of the intrinsic behaviour of gratings.

This chapter is concerned with the diffraction problem for both lossless dielectric and finitely-conducting lamellar gratings through the implementation of a modal expansion technique which is a generalization of the method employed for infinite conductivity. The theory and some of the numerical results presented, are the subject of two recent papers [5.11, 5.12].

The formalism was developed initially for dielectric gratings formed in materials of real refractive index, and was subsequently extended by virtue of the same boundary conditions to deal with gratings of finite

conductivity. The description given in this chapter concentrates on the latter more general case where complex refractive indices are involved. However, relevant simplifications pertaining to the dielectric case are indicated throughout, and where necessary separate sections are established to deal with the two different cases.

Interest in the diffraction of light by holograms prompted Burckhardt [5.13] to develop a rigorous electromagnetic theory for application to dielectric phase gratings. He used an eigenvalue technique to solve the problem for a grating having a sinusoidally varying dielectric constant. Knop [5.14] employed the same theoretical method to solve the diffraction problem for dielectric lamellar gratings. He used them in zero-order diffraction as transmission colour filters in the process of storing pictorial information [5.8, 5.9]. He found that surface-relief phase gratings with rectangular profile are ideally suited to the task owing to their strong wavelength dependence.

The method used by Burckhardt and Knop derives an eigenvalue equation from the solution of the Helmholtz equation. The periodically modulated function equal to the square of the refractive index, is represented by a Fourier series. In Knop's application to the lamellar profile, this series must describe a discontinuous function, a situation which potentially leads to numerical difficulties of the type encountered by Nevière *et al.* [5.15] when working with a differential equation method. Agreement has, however, been obtained between the above two treatments.

The method detailed in this chapter is again an eigenvalue technique, but is tailored specifically to the rectangular profile and thus circumvents any of the above difficulties. At the same time it is able to cater for lossy metallic gratings. The field in the groove region is represented by a modal expansion in which the modes are, to some extent, similar to those used by Marcuse [5.16] in his treatment of an asymmetric

slab waveguide. Although it is more complicated, it retains the neatness of the formalism for the perfectly-conducting lamellar grating.

The method described here differs from the method of Burckhardt and Knop in that in the former method each individual mode consists of a discrete term. In the latter method, each mode is an expansion of terms with each term inherently satisfying the necessary continuity and pseudo-periodicity conditions. By inserting the Fourier series (for the square of the refractive index) into the wave-equation which governs the eigen-modes, the problem becomes an infinite symmetric eigenvalue problem. The matrix involved must then be truncated to permit a numerical solution to be obtained. This task becomes increasingly difficult when the refractive index discontinuity becomes large. This is because the dimension of the matrix is determined by the number of terms in the Fourier series, which is only slowly-converging for a step-function. Once the eigenproblem is solved, the elements of each eigenvector become the expansion coefficients for the corresponding mode.

In contrast to the above, the approach outlined in this chapter relies only on the solution of a single transcendental equation to determine the eigenvalue for each mode. This is arrived at by prescribing each mode to be a solution of the wave-equation, and then constraining them to satisfy the boundary conditions.

The treatment of Burckhardt and Knop does have the advantage that it is capable of handling a wider range of structures, where the change in refractive index is not discontinuous as it is for the lamellar grating. The approach described here is designed solely for step-function refractive index profiles. Because no truncation of infinite series is required in specifying a mode, it provides for a more elegant and a less complex numerical implementation. It is also shown, that for this method the lossless nature of dielectric gratings leads to a self-adjoint problem.

This provides an orthogonal set of modes, thus making it possible to use the Method of Moments [5.17] to match the modal field to the plane-wave fields.

In the case of finite conductivity, the introduction of energy loss to the system renders the problem non-self adjoint. However, the eigenfunctions are shown to possess an bi-orthogonal relationship with their counterparts for the adjoint problem. This enables the Method of Moments to be retained in the solution process.

Section 5.2 gives a detailed account of the theoretical treatment of the problem for S polarization. Although the analysis is basically the same for P polarization, differences exist which result from the different boundary conditions and these are outlined briefly in Section 5.3.

The most involved part of the numerical implementation is the solution of the transcendental equations, especially when the roots are complex in the case of finite conductivity. Section 5.4 is devoted to this problem and discusses the distribution of the roots as well as the techniques used for locating them.

Section 5.5 describes some of the numerical results which have been obtained. First, it examines the validity of the theory through the checking of reciprocity and energy conditions, and also through the comparison of efficiency calculations with those produced by the formalisms of Knop and Maystre. Second, some efficiency spectra are presented to illustrate the behaviour of both dielectric and metallic gratings. In the former case, both low and high refractive indices are considered. In the latter case, an aluminium reflection grating is considered and emphasis is placed on the problem of resonance anomalies. Results are compared with those of Chapter 3.

5.2 THE THEORY FOR S POLARIZATION

5.2.1 The Incident and Diffracted Plane-Wave Fields

The structure considered is composed of a rectangular-wire grating of refractive index r_2, resting on a layer of material of refractive index r_3. Provision is made for a material of refractive index r_1 to fill the apertures (or grooves). The structure is assumed to lie in an xyz co-ordinate system such that the long axis of the grooves coincides with the z-axis, as illustrated in Figure 5.1. The period of the grating is d while c and h represent the groove aperture width and depth respectively. The origin of the co-ordinate system is chosen to lie on the midpoint of the left-hand side-wall of the groove.

Region D_0 denotes the area of free-space above the grating and has refractive index $r_0 = 1$. Regions D_i ($i = 1,2,3$) correspond to regions of the refractive indices r_i, which are given either real values for a dielectric or complex values for the case of finite conductivity.

Consider an S-polarised plane wave of unit amplitude and wavelength λ, to have its wave-vector in the xy plane and to be incident upon the grating at an angle θ. Vector field notation may be suppressed and the diffraction problem is formulated in terms of the scalar magnetic field quantity $H(x,y)$.

Omitting the temporal dependent term $\exp(-i\omega t)$, the total magnetic field in region D_0 may be represented by an incident field term plus a series of outgoing plane wave terms,

$$H^I(x,y) = \exp[i(\alpha_0 x - \chi_0 y)] + \sum_{p=-\infty}^{\infty} B_p \exp[i(\alpha_p x + \chi_p y)], \quad (x,y) \in D_0 \qquad \ldots(5.1)$$

where B_p are the reflected-order amplitudes and

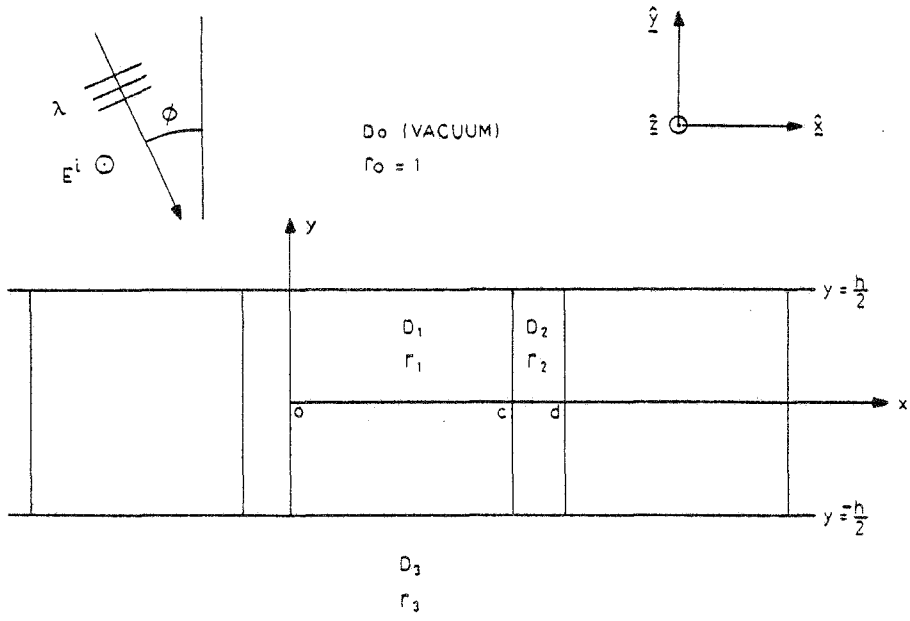

Figure 5.1 The geometry of the diffraction arrangement for the dielectric or finitely-conducting lamellar grating.

$$k_0 = 2\pi/\lambda; \quad k_i = k_0 r_i, \quad i = 0,1,2,3. \qquad ...(5.2)$$

$$\alpha_p = k_0 \sin\theta_p = k_0(\sin\theta + \frac{p\lambda}{d}), \quad p = 0,\pm1,\pm2... \qquad ...(5.3)$$

$$\chi_p = \begin{cases} (k_0^2-\alpha_p^2)^{\frac{1}{2}}, & \sin\theta_p \leq 1 \\ i(\alpha_p^2-k_0^2)^{\frac{1}{2}}, & \sin\theta_p > 1. \end{cases} \qquad ...(5.4)$$

In region D_3, the field is similarly represented by a plane-wave expansion, and is of the form

$$H^{III}(x,y) = \sum_{p=-\infty}^{\infty} \hat{B}_p \exp\ i(\alpha_p x - \xi_p y) \ , \quad (x,y)\in D_3 \qquad ...(5.5)$$

where $\hat{B}_p$ are the transmitted-order amplitudes (or absorption coefficients if r_3 is complex) and

$$\xi_p = (k_3^2 - \alpha_p^2)^{\frac{1}{2}} \qquad ...(5.6)$$

If r_3 is real-valued, ξ_p is chosen to be either positive real or positive imaginary, while if r_3 is complex then both the real and imaginary components, ξ_p^R and ξ_p^I, are positive with the result that downgoing waves are attenuated in the metal.

The above Rayleigh expansions for the magnetic field satisfy the appropriate Helmholtz equations given by

$$(\nabla^2 + k_0^2)\, H^I(x,y) = 0, \quad (x,y)\in D_0$$
$$(\nabla^2 + k_3^2)\, H^{III}(x,y) = 0, \quad (x,y)\in D_3.$$

The remainder of the solution is concerned with expanding the field in the groove region ($D_1 \cup D_2$) in terms of waveguide modes which must confer with the necessary boundary and pseudo-periodicity conditions, as well as satisfying analytically the Helmholtz equation. Once this is achieved, the modal field may be matched to the plane-wave fields in a similar manner to that described in previous chapters. In order that the Method of Moments [5.17] can be implemented, it is essential that the mode

functions be either mutually orthogonal, or orthogonal to a second set of functions. Both of these situations are found to apply - corresponding to lossless and lossy configurations respectively.

5.2.2 The Modal Field in the Groove Region

The boundary conditions for this problem stipulate that the tangential components of the electric and magnetic fields should be continuous. For S polarization they therefore require that H and $\frac{1}{r^2}\frac{\partial H}{\partial \hat{n}}$ be continuous across any interface. Applying these conditions to the vertical interfaces implies that the following relations must be satisfied:

$$H^{II}(c^-,y) = H^{II}(c^+,y); \quad \frac{1}{r_1^2}\frac{\partial H^{II}}{\partial x}(c^-,y) = \frac{1}{r_2^2}\frac{\partial H^{II}}{\partial x}(c^+,y)$$

$$H^{II}(d^-,y) = H^{II}(d^+,y); \quad \frac{1}{r_2^2}\frac{\partial H^{II}}{\partial x}(d^-,y) = \frac{1}{r_1^2}\frac{\partial H^{II}}{\partial x}(d^+,y) \qquad \ldots(5.7)$$

where $H^{II}(x,y)$ denotes the magnetic field in the region $D_1 \cup D_2$.

For the plane-wave incident field, $\alpha_0 d$ represents the phase shift over one period, and so defining $\tau = \exp(i\alpha_0 d)$ the following condition must also be obeyed:

$$\tau\, H^{II}(0^+,y) = H^{II}(d^+,y); \quad \tau\frac{\partial H^{II}}{\partial x}(0^+,y) = \frac{\partial H^{II}}{\partial x}(d^+,y). \qquad \ldots5.8)$$

The third constraint on the groove field is of course the wave equation. Because the refractive index in $D_1 \cup D_2$ is a function of the x-coordinate, this equation takes the form

$$\frac{\partial}{\partial x}\left[\frac{1}{k^2}\frac{\partial H^{II}}{\partial x}\right] + \frac{\partial}{\partial y}\left[\frac{1}{k^2}\frac{\partial H^{II}}{\partial y}\right] + H^{II} = 0, \quad (x,y)\in D_1 \cup D_2 \qquad \ldots(5.9)$$

where $k = k_0 r(x)$

and $$r(x) = \begin{cases} r_1, & 0 < x < c \\ r_2, & c < x < d. \end{cases} \qquad \ldots(5.10)$$

5.2.2.1 *The Eigenvalue Problem*

An alternative expression for the wave-equation is

$$\frac{\partial^2 H^{II}}{\partial x^2} + \frac{\partial^2 H^{II}}{\partial y^2} + k^2 H^{II} = \frac{1}{k^2} \frac{\partial H^{II}}{\partial x} \zeta^2 \delta(x-c) \qquad ...(5.11)$$

where $\zeta^2 = k_2{}^2 - k_1{}^2$ ...(5.12)

and $\delta(x)$ is the Dirac delta function. This equation represents an inhomogenous Helmholtz equation, in which the right-hand side signifies the discontinuity of the x-derivative of H along the interface x = c.

A separable solution to equation (5.11) is now considered, and expressed in the form

$$H^{II}(x,y) = u(x)\, v(y) \qquad ...(5.13)$$

Insertion of this solution back into the wave-equation gives

$$(i) \quad \frac{d^2 v}{dy^2} + \mu^2 v = 0 \qquad ...(5.14)$$

(which has general solution $v(y) = a \sin(\mu y) + b \cos(\mu y)$ ...(5.15))

and

$$(ii) \quad \frac{d^2 u}{dx^2} - \left(\frac{2k'}{k}\right) \frac{du}{dx} + \zeta^2 S(x-c) u = -\beta^2 u \qquad ...(5.16)$$

where ' represents d/dx

and $\beta^2 = k_1{}^2 - \mu^2$ ...(5.17)

$$S(x) = \begin{cases} 0, & x < 0 \\ 1, & x \geqslant 0. \end{cases} \qquad ...(5.18)$$

Equation (5.16) is an eigenvalue equation which must be solved subject to the boundary and pseudo-periodicity conditions, (5.7) and (5.8). A combination of the latter gives

$$\begin{aligned} &(i) \ \tau\, u(o^+) = u(d^-) \\ &(ii) \ \frac{1}{r_1{}^2} \tau\, u'(o^+) = \frac{1}{r_2{}^2} u'(d^-). \end{aligned} \qquad ...(5.19)$$

Equation (5.16) is now assumed to have two linearly independent solutions $\theta(x)$ and $\psi(x)$, which are continuous and continuously differentiable at $x = c$, and which obey the initial conditions

$$\begin{aligned} \theta(0) &= 1; \quad \psi(0) = 0 \\ \theta'(0) &= 0; \quad \psi'(0) = 1. \end{aligned} \qquad \ldots(5.20)$$

The appropriate complete expressions for θ and ψ are

$$\theta(x) = \begin{cases} \cos(\beta x) & , \ 0 < x < c \\ \cos(\beta c)\cos\big(\gamma(x-c)\big) - \left(\frac{r_2}{r_1}\right)^2 \frac{\beta}{\gamma}\sin(\beta c)\sin\big(\gamma(x-c)\big), & c < x < d \end{cases} \qquad \ldots(5.21)$$

$$\psi(x) = \begin{cases} \frac{1}{\beta}\sin(\beta x) & , \ 0 < x < c \\ \frac{1}{\beta}\sin(\beta c)\cos\big(\gamma(x-c)\big) + \left(\frac{r_2}{r_1}\right)^2 \frac{1}{\gamma}\cos(\beta c)\sin\big(\gamma(x-c)\big), & c < x < d \end{cases} \qquad \ldots(5.22)$$

where $\gamma^2 = \beta^2 + \zeta^2$. $\qquad \ldots(5.23)$

Writing $u(x)$ as a weighted combination of $\theta(x)$ and $\psi(x)$,

$$u(x) = \theta(x) + \omega\psi(x) \qquad \ldots(5.24)$$

and substituting this expression into the pseudo-periodicity conditions of equation (5.19) gives

$$\tau \begin{bmatrix} 1 \\ \omega \end{bmatrix} = \begin{bmatrix} \theta(d^-) & \psi(d^-) \\ \frac{r_1^2}{r_2^2}\theta'(d^-) & \frac{r_1^2}{r_2^2}\psi'(d^-) \end{bmatrix} \begin{bmatrix} 1 \\ \omega \end{bmatrix}. \qquad \ldots(5.25)$$

The existence of a non-trivial solution to this homogenous set of equations implies that

$$[\theta(d^-) - \tau]\left[\frac{r_1^2}{r_2^2}\psi'(d^-) - \tau\right] - \frac{r_1^2}{r_2^2}\theta'(d^-)\,\psi(d^-) = 0 \qquad \ldots(5.26)$$

Because both θ and ψ are solutions of equation (5.16), it now follows that

$$[\theta\psi'' - \theta''\psi] - [\theta\psi' - \theta'\psi]\,\frac{2k'}{k} = 0,$$

which implies that

$$\frac{\partial}{\partial x}\left[\frac{\theta\psi' - \psi\theta'}{r^2(x)}\right] = 0,$$

i.e. $\frac{1}{r^2(x)}[\theta\psi' - \theta'\psi]$ is a constant. From the initial conditions this quantity is equal to $1/r_1^2$ and so equation (5.26) reduces to

$$\theta(d^-) + \frac{r_1^2}{r_2^2}\psi'(d^-) = \frac{1+\tau^2}{\tau} = 2\cos(\alpha_0 d). \qquad ...(5.27)$$

Substitution of θ and ψ from equations (5.21) and (5.22), into equation (5.27) furnishes a transcendental equation in the unknown complex eigenvalue β,

$$\cos(\beta c)\cos(\gamma g) - \tfrac{1}{2}\left(\frac{r_2^2}{r_1^2}\frac{\beta}{\gamma} + \frac{r_1^2}{r_2^2}\frac{\beta}{\gamma}\right)\sin(\beta c)\sin(\gamma g) = \cos(\alpha_0 d) \qquad ...(5.28)$$

where $g = d-c$. ...(5.29)

Note that the value of β depends on the wavelength and angle of incidence, as well as the grating aperture width. For the perfectly-conducting lamellar grating, the x-dependent term of the mode depends only on the groove width.

For a given solution to equation (5.28), θ and ψ are determined from equations (5.21) and (5.22). From equation (5.25), ω is then expressed by

$$\omega = \frac{\tau - \theta(d^-)}{\psi(d^-)} \qquad ...(5.30)$$

A combination of equations (5.15) and (5.24) provides the final solution to the groove field,

$$H^{II}(x,y) = [\theta(x)+\omega\psi(x)][a\sin(\mu y) + b\cos(\mu y)] \qquad ...(5.31)$$

Note the simple solution which exists when $r_1 = r_2$, i.e. when the grating is replaced by a homogeneous layer of refractive index r_1. From equation (5.12), $\zeta^2 = 0$, and hence from equation (5.23), $\gamma = \pm\beta$.

Equation (5.28) then reduces to

$$\cos(\beta d) = \cos(\alpha_0 d) \quad , \qquad \ldots(5.32)$$

which has real-valued solutions in the form of the classical grating equation, i.e. $\beta = \alpha_0 + \frac{2\pi p}{d}$, $p = 0,\pm 1,\ldots$. It is then straight-forward to show that $H^{II}(x,y)$, as given by equation (5.31), can be transformed into a plane-wave expansion similar to the right-hand side of equation (5.5).

Consider the possible solutions of equation (5.29) for the dielectric case when both r_1 and r_2 are real. From equations (5.12) and (5.17) both β^2 and ζ^2 must be real and hence from equation (5.23) γ^2 must be real. Therefore, β and γ must be either purely real or purely imaginary. However, inspection of equation (5.28) reveals that it is impossible for β and γ to be imaginary simultaneously, because the left-hand side of the equation would be greater than unity, unless $|\beta| = |\gamma| = 0$. Equation (5.23) shows that β cannot be real when γ is imaginary. Thus the only permissable solutions are those for which γ is real and β is either real or imaginary. The latter is chosen to be positive in either case. A discussion of the distribution of these eigenvalues in the complex plane is presented in Section 5.4.

5.2.2.2 *The Self-Adjoint Case for Lossless Dielectric Gratings*

It is now demonstrated, that if r_1 and r_2 are real, then the eigenfunctions $u_m(x)$, corresponding to different eigenvalues β_m, comprise an orthogonal set of functions on the interval $[0,d]$. This facilitates implementation of the Method of Moments in the final solution to the diffraction problem (Section 5.2.3). That is, it is established that

$$\langle u_m, u_n \rangle = 0 \quad \text{if } m \neq n \ ,$$

where for this case the appropriate inner-product $\langle f,g \rangle$ is defined by

$$\langle f,g \rangle = \int_0^d \frac{1}{k^2(x)} \, \overline{f}(x) \, g(x) \, dx. \qquad \ldots(5.33)$$

The functions f,g must comply with the necessary boundary, pseudo-periodic and Helmholtz equations.

Returning to equation (5.16), this is written in the form

$$Lu = -\beta^2 u \quad , \qquad \ldots(5.34)$$

where L is a differential operator of order 2 and defined over the interval [0,d] by

$$L = \frac{d^2}{dx^2} - \left(\frac{2k'}{k}\right)\frac{d}{dx} + \zeta^2 S(x-c) . \qquad \ldots(5.35)$$

Let $\{-\beta^2{}_m\}$ be the eigenvalues of equation (5.34) and let $\{u_m\}$ be the corresponding eigenfunctions, which are continuously differentiable over the interval [0,d]. It follows that

$$\langle Lu_m, u_n\rangle - \langle u_m, Lu_n\rangle = (\beta_n{}^2 - \bar{\beta}_m{}^2)\langle u_m, u_n\rangle . \qquad \ldots(5.36)$$

Expansion of the left-hand side of this equality, using equation (5.16), gives

$$\text{L.H.S.} = \int_0^d \frac{1}{k^2}\left(\left[\bar{u}_m'' - \frac{2\bar{k}'}{\bar{k}}\bar{u}_m' + \bar{\zeta}^2 S(x-c)\bar{u}_m\right] u_n - \left[u_n'' - \frac{2k'}{k}u_n' + \zeta^2 S(x-c)u_n\right]\bar{u}_m\right) dx$$

$$= \left[\frac{1}{k^2}\bar{u}_m' u_n - \frac{1}{k^2}\bar{u}_m u_n'\right]_0^d \quad \text{since } k \text{ and } \zeta^2 \text{ are real if } r_1 \text{ and } r_2 \text{ are real.}$$

$$= 0 \quad \text{following application of the boundary and pseudo-periodicity conditions (equation (5.19)).}$$

Thus, from equation (5.36), $\langle u_m, u_n\rangle = 0$ for $m \neq n$ and L is found to be a self-adjoint operator with respect to an inner-product incorporating the weight distribution $1/k^2(x)$. Hence, the eigenfunctions u_m corresponding to distinct eigenvalues, are orthogonal. By inserting $m = n$ in equation (5.36), it is seen that the $\beta_m{}^2$ are real-valued, and it can be shown that they always exist for the self-adjoint problem framed by equation (5.34).

5.2.2.3 *The Adjoint Case for Finite Conductivity*

Consider now the situation which exists when r_1 and r_2 may assume complex values. The left-hand side of equation (5.36) is clearly no longer zero due to the complex nature of k and ζ^2. This means that L is not a self-adjoint operator and the eigenfunctions $\{u_m\}$ are not necessarily orthogonal, nor are the eigenvalues necessarily real. However, the Method of Moments can still be used in the field matching if a bi-orthogonality relationship can be established, involving the eigenfunctions u_m with those of the adjoint problem, u_m^+. That is, a set of functions $\{u_m^+\}$ is sought such that

$$\begin{aligned} \langle u_m, u_n^+ \rangle &= 0 \quad , \qquad m \neq n \\ &\neq 0 \quad , \qquad m = n, \end{aligned} \qquad \ldots(5.37)$$

where the inner-product is defined by equation (5.33). To this end, the operator L^+ is defined as

$$L^+ = \frac{d^2}{dx^2} - \left(\frac{2\bar{k}'}{\bar{k}}\right) \frac{d}{dx} + \bar{\zeta}^2 S(x-c) \quad , \qquad \ldots(5.38)$$

and the eigenvalue problem to be investigated is

$$L^+ u^+ = -(\beta^+)^2 \, u^+ . \qquad \ldots(5.39)$$

Note that u^+ does not obey the same boundary and pseudo-periodic conditions as does u, but instead a complementary set which are summarised by

$$\begin{aligned} &\text{(i)} \quad u^+(c^-) = u^+(c^+); \quad \frac{1}{\bar{r}_1^{\,2}} u^{+\prime}(c^-) = \frac{1}{\bar{r}_2^{\,2}} u^{+\prime}(c^+) \\ &\text{(ii)} \quad \tau u^+(0^+) = u^+(d^-); \quad \tau \frac{1}{\bar{r}_1^{\,2}} u^{+\prime}(0^+) = \frac{1}{\bar{r}_2^{\,2}} u^{+\prime}(d^-) \end{aligned} \qquad \ldots(5.40)$$

One expects that if L^+ is the adjoint operator of L, then β^{+2} may be equivalent to $\bar{\beta}^2$ (see reference [5.18]). This is now shown to be the case.

Following the treatment outlined in Section 5.2.2.1, equation (5.39) is solved for the eigenfunctions u^+, subject to the new boundary conditions (5.40). These eigenfunctions are expressed as

$$u^+(x) = \theta^+(x) + \omega^+\psi^+(x) \quad , \qquad \ldots(5.41)$$

where θ^+ and ψ^+ are two linearly independent solutions to equation (5.39), and which satisfy the above boundary conditions as well as the initial conditions,

$$\begin{aligned} \theta^+(0) &= 1 \quad ; \qquad \theta^{+\prime}(0) = 0 \\ \psi^+(0) &= 0 \quad ; \qquad \psi^{+\prime}(0) = 1. \end{aligned} \qquad \ldots(5.42)$$

Consequently, the appropriate expressions for θ^+ and ψ^+ are

$$\theta^+(x) = \begin{cases} \cos(\beta^+ x) & , \ 0 < x < c \\ \cos(\beta^+ c)\cos\left(\gamma^+(x-c)\right) - \left(\frac{\bar{r}_2}{\bar{r}_1}\right)^2 \frac{\beta^+}{\gamma^+}\sin(\beta^+ c)\sin\left(\gamma^+(x-c)\right), & c < x < d \end{cases} \qquad \ldots(5.43)$$

$$\psi^+(x) = \begin{cases} \frac{1}{\beta^+}\sin(\beta^+ x) & , \ 0 < x < c \\ \frac{1}{\beta^+}\sin(\beta^+ c)\cos\left(\gamma^+(x-c)\right) + \left(\frac{\bar{r}_2}{\bar{r}_1}\right)^2 \frac{1}{\gamma^+}\cos(\beta^+ c)\sin\left(\gamma^+(x-c)\right), & c < x < d \end{cases} \qquad \ldots(5.44)$$

where $\gamma^{+2} = \beta^{+2} + \bar{\zeta}^2$. $\qquad \ldots(5.45)$

In a similar manner to the original problem, substitution of equation (5.41) into the pseudo-periodicity equations (5.40(ii)), and extraction of a non-trivial solution for ω^+, leads to a non-linear eigenvalue equation in β^+,

$$\cos(\bar{\beta}^+ c)\cos(\bar{\gamma}^+ g) - \tfrac{1}{2}\left[\frac{r_2^2}{r_1^2}\frac{\bar{\beta}^+}{\bar{\gamma}^+} + \frac{r_1^2}{r_2^2}\frac{\bar{\gamma}^+}{\bar{\beta}^+}\right]\sin(\bar{\beta}^+ c)\sin(\bar{\gamma}^+ g) = \cos(\alpha_0 d) \qquad \ldots(5.46)$$

This equation is identical to equation (5.28) if the transformations $\bar{\beta}^+ \to \beta$ and $\bar{\gamma}^+ \to \gamma$ are made. By comparing equation (5.23) and (5.45), it may be concluded that

$$\beta^+ = \beta \ ; \qquad \gamma^+ = \gamma \qquad \ldots(5.47)$$

and therefore

$$\theta^+(x) = \bar{\theta}(x) \ ; \quad \psi^+(x) = \bar{\psi}(x). \qquad \ldots(5.48)$$

To complete the specifications of the eigenfunctions u^+, corresponding to the eigenvalues $\bar{\beta}^2$ (which are solutions to equation (5.46)), it is straight-forward to derive from the pseudo-periodicity conditions (5.40(ii)), that ω^+ is given by

$$\omega^+ = \frac{\tau - \theta^+(d^-)}{\psi^+(d^-)} \qquad \ldots(5.49)$$

The fact that $\beta^+ = \bar{\beta}$ indicates that the functions $\{u_m\}$ are orthogonal to the functions $\{u_m^+\}$. This is now proven. Let β_n be the eigenvalue of u_n with respect to the operator L and let β_m^+ be the eigenvalue of u_m^+ with respect to the operator L^+. We therefore have

$$\langle L^+u_m^+, u_n\rangle - \langle u_m^+, Lu_n\rangle = (\beta_n^2 - (\bar{\beta}_m^+)^2)\langle u_m^+, u_n\rangle$$

$$= (\beta_n^2 - \beta_m^2)\langle u_m^+, u_n\rangle \quad \text{(by equation (5.47))}. \qquad \ldots(5.50)$$

The left-hand side of this equation may be expanded using equations (5.16) and (5.38, 5.39) to yield

$$\text{L.H.S.} = \int_o^d \frac{1}{k^2}\left([\bar{u}_m^{+\prime\prime} - \frac{2k'}{k}\bar{u}_m^{+\prime} + \zeta^2 S(x-c)\,\bar{u}_m^+]u_n \right.$$

$$\left. - [u_n'' - \frac{2k'}{k}u_n' + \zeta^2 S(x-c)\,u_n]\,\bar{u}_m^+ \right) dx$$

$$= \left[\frac{1}{k^2}(\bar{u}_m^{+\prime}\,u_n - \bar{u}_m^+\,u_n')\right]_o^d$$

$= 0$, if u_n satisfies the boundary conditions (5.19) and u_m^+ satisfies the adjoint boundary conditions (5.40(ii)).

L^+ is thus the adjoint operator of L, while the fact that

$$(\beta_n^2 - \beta_m^2)\langle u_m^+, u_n\rangle = 0$$

implies that

$$\int_o^d \frac{1}{k^2(x)}\bar{u}_m^+(x)\,u_n(x)\,dx \neq 0, \quad m = n$$

$$= 0, \quad m \neq n \qquad \ldots(5.51)$$

which is the required bi-orthogonal relationship linking the $\{u_m\}$ and the $\{u_m^+\}$.

5.2.2.4 *Completeness of the Eigenfunctions*

Using arguments similar to those described in reference [5.18], it may be shown that the countably infinite set of eigenfunctions $u_m(x)$ comprise a complete set in the sense that any continuous and piecewise differentiable function $f(x)$, which satisfies the boundary conditions (5.19), may be represented by a linear combination of the u_m,

$$f(x) = \sum_m^\infty c_m\, u_m(x) \qquad \ldots(5.52)$$

where $c_m = \langle u_m^+, f \rangle$.

Thus, the general solution to the total magnetic field in the groove region may now be expressed by

$$H^{II}(x,y) = \sum_m^\infty [a_m \sin(\mu_m y) + b_m \cos(\mu_m y)]\, u_m(x) \qquad \ldots(5.53)$$

where $u_m(x)$ is given by equation (5.24).

5.2.3 Field Matching by Method of Moments

Having prescribed the expansions for the plane-wave field above and below the grating (equations (5.1) and (5.5)) and also for the field within the grooves (equation (5.53)), it is now possible to match these fields along the top and bottom surfaces to evaluate the unknown expansion coefficients a_m, b_m, B_p and $\hat{B}_p$.

The boundary conditions at these interfaces require that

$$\left.\begin{array}{ll} \text{(i)} & H^I(x, \frac{h}{2}) = H^{II}(x, \frac{h}{2}) \\ \text{(ii)} & H^{III}(x, -\frac{h}{2}) = H^{II}(x, -\frac{h}{2}) \end{array}\right\} \quad 0 < x < d \qquad \ldots(5.54)$$

$$\left.\begin{aligned}
&(i)\quad \frac{1}{k_0^2}\left.\frac{\partial H^{I}(x,y)}{\partial y}\right|_{y=\frac{h}{2}} = \frac{1}{k^2(x)}\left.\frac{\partial H^{II}(x,y)}{\partial y}\right|_{y=\frac{h}{2}} \\
&(ii)\quad \frac{1}{k_0^2}\left.\frac{\partial H^{III}(x,y)}{\partial y}\right|_{y=\frac{h}{2}} = \frac{1}{k^2(x)}\left.\frac{\partial H^{II}(x,y)}{\partial y}\right|_{y=\frac{h}{2}}
\end{aligned}\right\} \quad 0 < x < d \qquad \ldots(5.55)$$

By defining $B_p^* = B_p \exp(i\chi_p \frac{h}{2})$

$\hat{B}_p^* = \hat{B}_p \exp(i\xi_p \frac{h}{2})$

$E_p^* = \delta_{0,p} \exp(-i\chi_0 \frac{h}{2})$

$a_m^* = a_m \sin(\mu_m \frac{h}{2})$

$b_m^* = b_m \cos(\mu_m \frac{h}{2})$

expansion of equation (5.54(i)) gives

$$\sum_{p=-\infty}^{\infty} (B_p^* + E_p^*) \exp(i\alpha_p x) = \sum_{m}^{\infty} (a_m^* + b_m^*)\, u_m(x)$$

Using to advantage the biorthogonality relation (5.51), the above equation is multiplied by $\bar{u}_n^+(x)/k^2(x)$ and integrated over a period to yield

$$\sum_{p=-\infty}^{\infty} (B_p^* + E_p^*)\, \bar{F}_{np} = (a_n^* + b_n^*)\, Q_n \qquad \ldots(5.56)$$

where $F_{mp} = \int_0^d \frac{u_m^+(x)}{k^2(x)} \exp(-i\alpha_p x)\, dx \qquad \ldots(5.57)$

and $Q_m = \int_0^d \frac{u_m(x)\, \bar{u}_m^+(x)}{k^2(x)}\, dx \qquad \ldots(5.58)$

(Note that both of these integrals may be reduced to analytic form for numerical evaluation.)

In the case of the dielectric problem, $u_n^+(x)$ is replaced in the above expressions by $u_n(x)$.

In a similar procedure to that above, expanding equation (5.54(ii)) gives

$$\sum_{p=-\infty}^{\infty} \hat{B}_p^*\, \bar{F}_{np} = (-a_n^* + b_n^*)\, Q_n \qquad \ldots(5.59)$$

Now consider the continuity of the y-derivative of H. Expanding equation (5.55(i)) and projecting the result onto the set of basis functions $\{\exp(-i\alpha_q x)\}$, yields

$$i\chi_q(B_q^*-E_q^*) = \frac{k_0^2}{d}\sum_m^\infty \mu_m[a_m^* \cot(\mu_m \tfrac{h}{2})-b_m^* \tan(\mu_m \tfrac{h}{2})]\ J_{mq} \qquad ...(5.60)$$

where $J_{mp} = \int_0^d \frac{u_m(x)}{k^2(x)}\ \exp(-i\alpha_p x)\ dx.$ ...(5.61)

(For the dielectric case, $J_{mp} = F_{mp}$.)

Applying the same treatment to the field derivative at the lower interface, $y = -\frac{h}{2}$, gives

$$-i\xi_q\hat{B}_q^* = \frac{k_3^2}{d}\sum_m^\infty \mu_m[a_m^* \cot(\mu_m \tfrac{h}{2}) + b_m^* \tan(\mu_m \tfrac{h}{2})]\ J_{mq} \qquad ...(5.62)$$

By substituting equation (5.60) into (5.56) and equation (5.62) into (5.59), one derives a linear system consisting of a coupled pair of equations in the unknown mode amplitudes a_m^* and b_m^*,

$$\sum_m^\infty a_m^* \left(\mu_m \cot(\mu_m \tfrac{h}{2})\ \frac{k_0^2}{d}\ \sum_{p=-\infty}^\infty \left(\frac{i\bar{F}_{np}\ J_{mp}}{\chi_p}\right) + \delta_{m,n}\ Q_m\right)$$

$$+\sum_m^\infty b_m^* \left(-\mu_m \tan(\mu_m \tfrac{h}{2})\ \frac{k_0^2}{d}\ \sum_{p=-\infty}^\infty \left(\frac{i\bar{F}_{np}J_{mp}}{\chi_p}\right) + \delta_{m,n}Q_m\right) = 2E^*\bar{F}_{n0} \qquad ...(5.63)$$

and

$$\sum_m^\infty a_m^* \left(\mu_m \cot(\mu_m \tfrac{h}{2})\ \frac{k_3^2}{d}\ \sum_{p=-\infty}^\infty \left(\frac{i\bar{F}_{np}J_{mp}}{\xi_p}\right) + \delta_{m,n}\ Q_m\right.$$

$$+\sum_m^\infty b_m^* \left(\mu_m \tan(\mu_m \tfrac{h}{2})\ \frac{k_3^2}{d}\ \sum_{p=-\infty}^\infty \left(\frac{i\bar{F}_{np}J_{mp}}{\xi_p}\right) - \delta_{m,n}\ Q_m\right. = 0 \qquad ...(5.64)$$

These equations may be compared directly with those for the perfectly-conducting lamellar grating (equations (2.38) and (2.39)). As in that case, they must be truncated to finite dimension to facilitate numerical evaluation of the a_m^* and b_m^*. This task is carried out using the same standard elimination technique. The reflection and transmission coefficients may then be recovered from equations (5.60) and (5.62) respectively. The propagating order efficiencies for the p^{th} order are then calculated according to the relations,

$$\begin{aligned} &\text{(i)} \quad E_R^S(p) = \frac{\chi_p}{\chi_0} |B_p|^2 \text{ , reflected orders.} \\ &\text{(ii)} \quad E_T^S(p) = \frac{1}{r_3^2} \frac{\xi_p}{\chi_0} |\hat{B}_p|^2 \text{ , transmitted orders.} \end{aligned} \qquad \ldots(5.65)$$

where r_3 is assumed to be real when equation (5.65(ii)) is applicable.

5.2.4 Energy Conservation

As is the case with infinite conductivity, energy conservation fails as a test of the validity of this modal formalism if it is applied to the lossless dielectric grating. This is because the energy balance is satisfied analytically, i.e. irrespective of the number of modal or plane-wave terms included in the expansions. This is not true however, for the case of finite conductivity, where the energy balance is very much dependent on the truncation points of the field expansions. Energy conservation is then able to furnish a useful check on the accuracy of the numerical calculations.

The energy balance within the various regions of the structure is now discussed. Consider the total energy flux across a constant-y plane for $0 < x < d$. It is given by

$$\text{E.F.} = \int_0^d S_y \, dx \qquad \ldots(5.66)$$

where S_y is the y-component of the Poynting vector and is given by

$$S_y = \tfrac{1}{2}\, Re\, [E \times \bar{H}]_y$$

$$= \frac{1}{2\omega}\, Im\, [\frac{1}{\varepsilon}\, \bar{H}\, \frac{\partial H}{\partial y}] \qquad \ldots(5.67)$$

where $\varepsilon = \varepsilon_0 r^2$, r being the complex refractive index of the medium in question. Using this expression, the downgoing flux of the incident wave is derived to be $\chi_0 d/(2\omega\varepsilon_0)$, and so total energy flux, normalised to the incident flux, is expressed as

$$E.F. = \frac{1}{2i\chi_0 d} \int_0^d [\frac{1}{r^2}\, \bar{H}\, \frac{\partial H}{\partial y} - \frac{1}{\bar{r}^2} H\, \frac{\partial \bar{H}}{\partial y}]\, dx \qquad \ldots(5.68)$$

In free-space, above the grating surface, where $H = H^I(x,y)$, E.F. is independent of y and equation (5.68) simplifies to

$$E.F. = \sum_{\substack{\text{real} \\ \text{orders}}} |B_p|^2\, \frac{\chi_p}{\chi_0} - 1\,, \qquad y > \frac{h}{2} \qquad \ldots(5.69)$$

Here, the L.H.S. is either zero (indicating 100% of the incident energy is reflected) or negative if transmission of energy occurs into region D_3, or absorption occurs in either of regions D_2 or D_3.

In D_3, $H = H^{III}(x,y)$ and in the case of a transmission grating, where r_3 is real-valued, E.F. is independent of y and derived from equation (5.68) to be

$$E.F. = \frac{1}{r_3^2} \sum_{\substack{\text{real} \\ \text{orders}}} |\hat{B}_p|^2\, \frac{\xi_p}{\chi_0}\,, \qquad y < -\frac{h}{2}\,,\ r_3 \text{ real.} \qquad \ldots(5.70)$$

If r_3 is a complex, then propagation is attenuated in D_3 and E.F. is dependent upon the value of y. It is given by

$$E.F. = \frac{1}{\chi_0}\, Im\, [\frac{1}{\bar{r}_3^2} \sum_{p=-\infty}^{\infty} |\hat{B}_p|^2\, (\xi_p^I + i\xi_p^R) e^{2y\xi_p^I}]\,, \qquad y < -\frac{h}{2} \qquad \ldots(5.71)$$

r_3 complex.

To consider a conventional lamellar reflection grating for the case of finite conductivity, r_3 is equated to r_2 in equation (5.71), where for $y = -\frac{h}{2}$, E.F. equals the total energy loss below the region of modulation.

The energy flux at $y = h/2^-$ is calculated by inserting $H = H^{II}(x,y)$ into equation (5.68). This gives

$$\text{E.F.} = \frac{1}{\chi_0 d} Im \left[\sum_m \sum_n \bar{\mu}_n (a_m^* + b_m^*)\left(\bar{a}_n^* \cot(\bar{\mu}_n \tfrac{h}{2}) - \bar{b}_n^* \tan(\bar{\mu}_n \tfrac{h}{2})\right) \int_0^{d'} \frac{1}{r^2(x)} u_m(x)\, \bar{u}_n(x)\, dx\right], \quad y = h/2^- \qquad \ldots(5.72)$$

In reference [5.12], is is shown that agreement between the above expression, and the energy flux at $y = h/2^+$ (given by equation (5.69)), is not analytic. Therefore discrepancies in the evaluation of E.F. from both equations provide an estimate of the accuracy of the numerical calculations and indicate if additional terms should be included in the field expansions. The same situation applies at the lower surface, $y = -\frac{h}{2}$.

Now consider the region $D_1 \cup D_2$, where for complex values of r_1 and r_2, E.F. is a function of y, and the relative ohmic loss is given by

$$Q = \frac{1}{2i\chi_0 d} \int\int_{D_1 \cup D_2} \text{div}\left[\frac{1}{r^2} \bar{H}\ \text{grad}\ H - \frac{1}{\bar{r}^2} H\ \text{grad}\ \bar{H}\right] dA, \qquad \ldots(5.73)$$

where the area of integration is defined by $0 < x < d$, $-\frac{h}{2} < y < \frac{h}{2}$. A direct application of Green's Theorem to this region reveals that $\Delta\text{E.F.}\left(= \text{E.F.}[\frac{h}{2}^-] - \text{E.F.}[(-\frac{h}{2})^+]\right)$ and Q are physically identical, while it is demonstrated in reference [5.12] that they are also analytically identical, i.e. they agree irrespective of errors incurred when the infinite field expansions are truncated. As a result, these quantities provide no check of truncation errors.

5.3 THE THEORY FOR P POLARIZATION

This section is concerned with a summary of the treatment for P polarization. The only differences to the previous treatment arise because of the different boundary conditions. The continuity of the tangential components of E and H now requires that $E(x,y)$ and $\frac{\partial E(x,y)}{\partial \hat{n}}$ be continuous across any interface.

The plane-wave fields in regions D_0 and D_3 assume an identical form to those given in Section 5.2.1, allowing only for the notational changes, $H \rightarrow E$ and $B_p \rightarrow A_p$.

5.3.1 The Modal Field

At the interfaces $x = c$ and $x = d$, the electric field obeys boundary and pseudo-periodicity constraints given by,

$$\begin{aligned} &\text{(i)} \quad E^{II}(c^-,y) = E^{II}(c^+,y); \ \frac{\partial E^{II}(c^-,y)}{\partial x} = \frac{\partial E^{II}(c^+,y)}{\partial x} \\ &\text{(ii)} \quad E^{II}(d^-,y) = E^{II}(d^+,y); \ \frac{\partial E^{II}(d^-,y)}{\partial x} = \frac{\partial E^{II}(d^+,y)}{\partial x} \end{aligned} \qquad \ldots(5.74)$$

and

$$\tau\, E^{II}(0^+,y) = E^{II}(d^-,y); \ \tau \frac{\partial E^{II}(0^+,y)}{\partial x} = \frac{\partial E^{II}(d^+,y)}{\partial x} \qquad \ldots(5.75)$$

where $\tau = \exp(i\alpha_0 d)$.

The appropriate form of the wave-equation is now

$$\frac{\partial^2 E^{II}}{\partial x^2} + \frac{\partial^2 E^{II}}{\partial y^2} + k^2(x)E^{II} = 0 \qquad \ldots(5.76)$$

where $k(x) = k_0 r(x)$ and $r(x)$ is defined by equation (5.10).

5.3.1.1 *The Eigenvalue Problem*

To solve equation (5.76), a separable solution is again assumed, namely

$$E(x,y) = u(x)\, v(y), \qquad \ldots(5.77)$$

where $v(y)$ is again given by equation (5.15). On the other hand, $u(x)$ must now satisfy the differential equation

$$Lu = -\beta^2 u \ , \qquad \ldots(5.78)$$

where the differential operator L is defined by

$$L = \frac{d^2}{dx^2} + \zeta^2 S(x-c) \ , \qquad \ldots(5.79)$$

and ζ^2 and β^2 are defined by equations (5.12) and (5.17) respectively.

Subject to the boundary conditions

$$\text{(i)} \quad \tau\, u(0^+) = u(d^-)$$
$$\text{and} \quad \text{(ii)} \quad \tau\, u'(0^+) = u'(d^-) \ , \qquad \ldots(5.80)$$

equation (5.78) is solved by again letting $u(x)$ take the form

$$u(x) = \theta(x) + \omega\psi(x) \ , \qquad \ldots(5.81)$$

where $\theta(x)$ and $\psi(x)$ obey the initial conditions (5.20), and meet the same boundary and pseudo-periodicity constraints described above for u. We therefore have

$$\theta(x) = \begin{cases} \cos(\beta x) & , \ 0 < x < c \\ \cos(\beta c)\cos\big(\gamma(x-c)\big) - \dfrac{\beta}{\gamma}\sin(\beta c)\sin\big(\gamma(x-c)\big), & c < x < d \end{cases} \qquad \ldots(5.82)$$

$$\psi(x) = \begin{cases} \dfrac{1}{\beta}\sin(\beta x) & , \ 0 < x < c \\ \dfrac{1}{\beta}\sin(\beta c)\cos\big(\gamma(x-c)\big) + \dfrac{1}{\gamma}\cos(\beta c)\cos\big(\gamma(x-c)\big), & c < x < d. \end{cases} \qquad \ldots(5.83)$$

Expanding condition (5.80(i)) shows that $\omega(x)$ is unchanged, being expressed by equation (5.30).

To establish the transcendental eigenvalue equation in β, the pseudo-periodicity equations (5.80) are manipulated, using the fact that $\theta\psi' - \psi'\theta$ is a constant. The resulting equation is

$$\theta(d) + \psi'(d) = 2\cos(\alpha_0 d) , \qquad ...(5.84)$$

which when expanded becomes

$$\cos(\beta c)\cos(\gamma g) - \tfrac{1}{2}\left(\frac{\beta}{\gamma} + \frac{\gamma}{\beta}\right)\sin(\beta c)\sin(\gamma g) = \cos(\alpha_0 d) \qquad ...(5.85)$$

where β and γ are related by equation (5.23).

Finally, the solution to the groove-region field takes the form

$$E^{II}(x,y) = [\theta(x) + \omega\psi(x)][a\sin(\mu y) + b\cos(\mu y)] \quad .$$

5.3.1.2 *The Adjoint Nature of L*

By following the reasoning of Section 5.2.2.2, it is a simple matter to establish that the operator L, defined by equation (5.79), is self-adjoint for the dielectric case if the inner-product <f,g> is defined by

$$\langle f,g\rangle = \int_0^d \bar{f}(x)\, g(x)\, dx. \qquad ...(5.86)$$

To deal with the case of finite conductivity, the differential equation,

$$L^+u^+ = -(\beta^+)^2\, u^+ \qquad ...(5.87)$$

is examined, where L^+ is given by

$$L^+ = \frac{d^2}{dx^2} + \bar{\zeta}^2 S(x-c). \qquad ...(5.88)$$

Here we find that because the refractive indices take no part in the boundary conditions, the continuity conditions for u^+ are identical to those imposed on u and are given by equations (5.74) and (5.75).

To solve equation (5.87), u^+ is defined by

$$u^+(x) = \theta^+(x) + \omega\psi^+(x).$$

The procedure of Section 5.2.2.3 is then followed and one finds that θ^+ and ψ^+ are reflected by equations (5.82) and (5.83) if β and γ are replaced by β^+ and γ^+, where $\gamma^{+2} = \beta^{+2} + \bar{\zeta}^2$. From the pseudo-periodicity constraints, ω^+ is again obtained from equation (5.49), while the

transcendental equation derived in β^+ and γ^+ shows that $\beta^+ = \bar{\beta}$ and $\gamma^+ = \bar{\gamma}$, thus implying that $\theta^+ = \bar{\theta}$ and $\psi^+ = \bar{\psi}$.

By expanding the difference, $\langle L^+ u_m^+, u_n \rangle - \langle u_m^+, Lu_n \rangle$, it is straight-forward to show that this expression reduces to zero, thus demonstrating that L^+ is the adjoint operator of L with respect to the inner-product defined by equation (5.86). Consequently the bi-orthogonality relationship of equation (5.37) is established between the sets of functions $\{u_m\}$ and $\{u_m^+\}$.

As discussed previously when considering S polarization, completeness of the functions $\{u_m\}$ is assured for the interval in question. The total electric field in the groove region may therefore be expressed as the series expansion,

$$E^{II}(x,y) = \sum_m^{\infty} [a_m \sin(\mu_m y) + b_m \cos(\mu_m y)] \, u_m(x) \; . \qquad ...(5.89)$$

5.3.2 Field Matching

The final matching problem is again solved, using the Method of Moments. As for S polarization, the continuity of the field quantities at $y = \pm\frac{h}{2}$ is projected onto the biorthogonal set of functions $\{u_m^+\}$, while the y-derivative at these interfaces is projected onto the plane-wave basis functions $\{\exp(-i\alpha_p x)\}$. The analysis proceeds in a similar manner to that for S polarization. Allowing for the appropriate notational changes in the amplitudes, all equations are the same if k_0^2 and k_3^2 are omitted, and if the inner-products F_{mp}, Q_m and J_{mp} are replaced respectively by

$$D_{mp} = \int_0^d u_m^+ \exp(-i\alpha_p x)dx \qquad ...(5.90)$$

$$P_m = \int_0^d u_m(x) \; u_m^+(x)dx \qquad ...(5.91)$$

and $$I_{mp} = \int_0^d u_m(x) \exp(-i\alpha_p x)dx. \qquad ...(5.92)$$

Once the order amplitudes have been evaluated from equations analagous to (5.60) and (5.62), the propagating order efficiencies for this polarization are given by

$$\text{(i)} \quad E_R^P(p) = \frac{\chi_p}{\chi_0} |A_p|^2 \quad , \text{ reflected orders.}$$
$$\text{(ii)} \quad E_T^P(p) = \frac{\xi_p}{\chi_0} |\hat{A}_p|^2 \quad , \text{ transmitted orders.} \qquad \ldots(5.93)$$

5.3.3 Energy Conservation

In this case the y-component of the Poynting vector is expressed by

$$S_y = \frac{1}{2\mu\omega} Im \left[\bar{E} \frac{\partial E}{\partial y}\right]$$

The down-going energy flux of the incident field is therefore $\chi_0 d/(2\omega\mu)$, and the normalised energy flux for a particular value of y becomes

$$\text{E.F.} = \frac{1}{2i\chi_0 d} \int_0^d \left[\bar{E} \frac{\partial E}{\partial y} - E \frac{\partial \bar{E}}{\partial y}\right] dx.$$

Applying this expression to each of the three regions D_0, $D_1 \cup D_2$ and D_3 reveals that in the first case E.F. is unchanged from equation (5.69). In the second case E.F. is furnished by equation (5.72) if the terms r(x) are deleted. In D_3, we have for a dielectric,

$$\text{E.F.} = \sum_{\substack{\text{real} \\ \text{orders}}} |A_p|^2 \frac{\xi_p}{\chi_0} \quad , \quad y < -\frac{h}{2} \, , \; r_3 \text{ real} \qquad \ldots(5.94)$$

while for a metal,

$$\text{E.F.} = \frac{1}{\chi_0} \sum_{p=-\infty}^{\infty} |\hat{A}_p|^2 \xi_p^R \exp(2\xi_p^I y), \quad y < -\frac{h}{2} \qquad ..(5.95)$$
$$r_3 \text{ complex.}$$

where $\xi_p = \xi_p^R + i\xi_p^I$ is given by equation (5.6).

In considering the nature of the energy balance, the ohmic energy loss within the grating structure is now defined by

$$Q = \frac{1}{2i\chi_0 d} \int\int_{D_1 \cup D_2} \text{div } [E \text{ grad } \bar{E} - \bar{E} \text{ grad } E] \, dA \quad , \qquad \ldots(5.96)$$

and is analytically equal to E.F. $[\frac{h}{2}^-]$ - E.F. $[(-\frac{h}{2})^+]$. As before, the fluxes calculated on either side of the interfaces $y = \pm\frac{h}{2}$ are not analytically equal, but depend on the number of terms included in the field expansions.

5.4 NUMERICAL SOLUTION OF THE EIGENVALUE EQUATION

5.4.1 The Dielectric Grating

This section considers the distribution along the real axis of the eigenvalues (β^2) for the lossless dielectric grating. The following section deals with the movement of these eigenvalues out into the complex plane when finite conductivity is introduced.

The transcendental eigenvalue equations to be solved, ((5.27) and (5.84)) may be represented in the form

$$D(\beta^2) = \theta(d) + q\psi'(d) = 2\cos(\alpha_0 d) \qquad \ldots(5.97)$$

where q = 1 for P polarization and r_1^2/r_2^2 for S polarization. It may be shown [5.19] that the function $D(\beta^2)$ behaves in a manner similar to that described in Figure 5.2. That is, the function is continuous and is greater than 2 for $\beta^2 < \Omega$, a number which is $> -\zeta^2$. For $\Omega < \beta^2 < \infty$, $D(\beta^2)$ continually oscillates between maxima which are greater than 2, and minima which are less than 2. Between successive maxima and minima it behaves monotonically. Thus the transcendental eigenvalue equation has an infinite number of discrete solutions β_1^2, β_2^2 ... with $\beta_n^2 \to \infty$ as $n \to \infty$. Provided $\zeta^2 \neq 0$, there exists only one eigenfunction $u_m(x)$

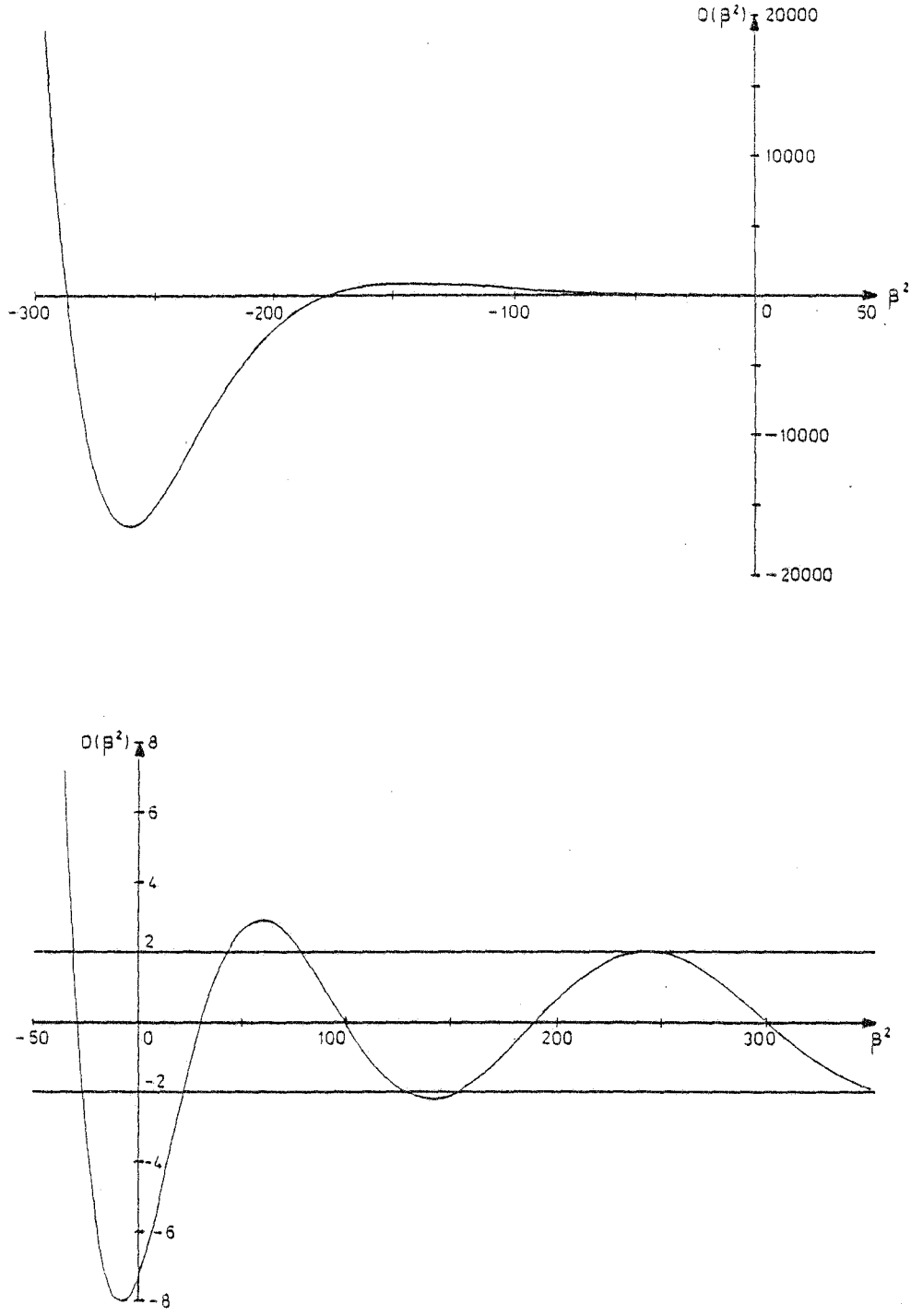

Figure 5.2 Plot of the function $D(\beta^2)$ for the lossless dielectric grating. The eigenvalues correspond to the points where $D(\beta^2)=2\cos(\alpha_0 d)$. In the top figure, at least three eigenvalues occur for $\beta^2<0$. In the bottom figure, only one eigenvalue occurs for $\beta^2<0$ while the first four eigenvalues for $\beta^2>0$ are also shown.

corresponding to any eigenvalue β_m^2 (except possibly at certain isolated points where $\tau = \pm 1$, i.e. where $2\cos(\alpha_0 d) = \pm 2$, producing double roots).

As $\beta_n^2 \to \infty$, inspection of equations (5.85), (5.28) and (5.23) reveals that the values of the real β's will approach those values appropriate to the case of a dielectric slab ($r_1 = r_2$). That is, $\beta_n \to |\alpha_0 + \frac{2\pi n}{d}|$ for large n where $n = 0, \pm 1, \pm 2 \ldots$ This means the β's tend to pair into groups $2\pi/d$ apart.

Table 5.1 presents an example of some eigenvalues calculated for S polarization. The first 12 values of β of lowest modulus are given, along with the corresponding γ values, and the pairing amongst the higher-order values is evident.

5.4.2 The Metal Grating

5.4.2.1 *Location of the Complex Eigenvalues*

The problem of numerically solving the transcendental equations (5.28) and (5.85) becomes substantially more difficult when these equations are complex. This is especially the case considering that upwards of 20 zeros are often required to meet the necessary conditions of energy conservation and reciprocity. (It is usually essential that a complete set of roots with modulus less than a specified tolerance be found.)

The numerical method which was initially employed to solve these complex equations, was based on a generalisation [5.20] to complex functions of the standard "Regula-Falsi" technique [5.21]. Some of the results presented in Section 5.5 were evaluated using this method and it is seen to prove adequate for low conductivity gratings where the modulus of the complex refractive index is not excessive. However, the method was found to be grossly inadequate when applied to situations of medium and high conductivity. In these cases the method was found to require large amounts of computer time without guaranteeing a reliable and complete set of roots. (It is an interesting comparison, that the modal

TABLE 5.1

Eigenvalues for the Dielectric Lamellar Grating Problem.

Solutions of the transcendental equation (5.28) (S polarization) are tabulated for a dielectric transmission grating of refractive index 2.0. The first four imaginary values and the first eight real values of β are given.

Groove Parameters: $d = 1.0$, $c = 0.5$, $g = 0.5$, $h = 1.2$
Refractive Indices: $r_1 = 1.0$, $r_2 = 2.0$, $r_3 = 1.0$
Mounting Parameters: $\lambda = 0.55$, $\theta = 10°$.

β	γ
(0, 0.7129)	19.7741
(0, 9.7795)	17.2012
(0, 15.8619)	11.8289
(0, 18.8656)	5.9675
(7.7516, 0)	21.2511
(11.2565, 0)	22.7647
(16.0356, 0)	25.4688
(18.9032, 0)	27.3651
(23.6725, 0)	30.8530
(25.9066, 0)	32.5987
(30.6785, 0)	36.5061
(32.7808, 0)	38.2898

method presented in this chapter, is more suited from a numerical point of view to low conductivities, whereas Maystre's integral method [5.10] is more suited to high conductivities.)

Botten *et al.* [5.22] have devised a markedly improved method of numerically solving the eigenvalue equation, based on the Argument Principle of complex variable theory. They make use of the relation

$$\frac{1}{2\pi i} \int_C \beta^p \frac{f'(\beta)}{f(\beta)} d\beta = \sum_{i=1}^{n} \beta_i^p \quad , \qquad \ldots(5.98)$$

where $f(\beta)$ is the function of interest and has n unknown roots β_i within a closed contour C in the complex plane. By letting $p = 0$, the left-hand side of equation (5.98) indicates the total number of roots within C. For successively higher values of p, up to n, a polynomial is established, which on solution yields estimates for the roots. The accuracy of these estimates is then improved by applying Muller's method to the original function $f(\beta)$. Because this latter method is also used to solve for the estimates, it is desirable that the degree of the polynomial does not exceed a value of about 5. That is, the contour C should not contain more than five roots. To meet this requirement, Botten *et al.* made provision for the complex plane to be sub-divided into non-overlapping annular regions, and if necessary, a further sub-division of these into sectors. Figure 5.3 illustrates the manner in which the complex plane has been divided to determine the roots for a copper grating irradiated at a wavelength of 0.55μ in P polarization. Note that only half of the plane (say that for which $Re\ (\beta) > 0$) need be searched.

Much of the numerical work presented in Section 5.5 was carried out with the aid of the technique just described. This includes all the cases of high conductivity where the method has worked quite successfully, although some care still had to be exercised when the aperture width c was small.

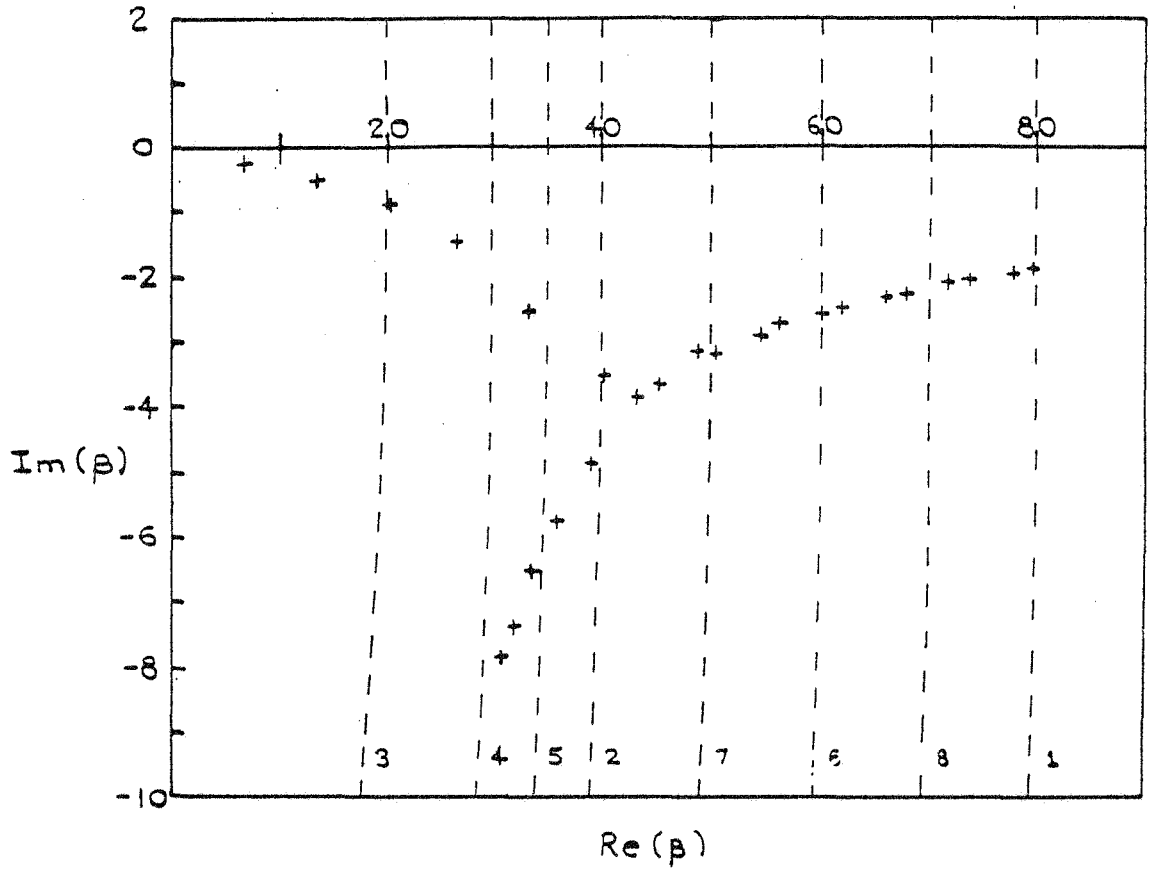

Figure 5.3 A plot of the eigenvalues β_m (within the semi-circle $|\beta|<80, \mathrm{Re}(\beta)\geq 0$) for P polarization and a copper grating with parameters: $d=1.0, c=0.4, r_1=1.0$, $r_2=r_3=0.756+2.462i, \lambda=0.55, \theta=5^0$. The sequence of the subdivision of the annular rings is shown adjacent to the appropriate circular arc. (After Botten et al [5.22]).

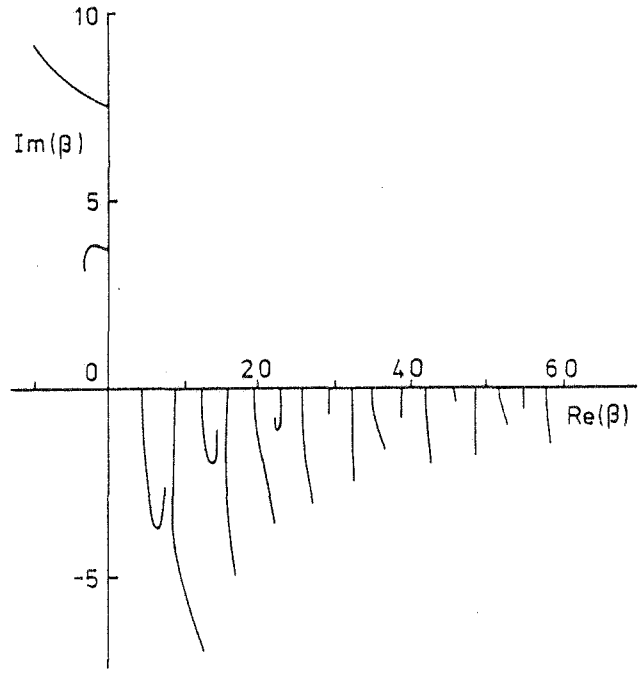

Figure 5.4 Evolution of the first 19 complex eigenvalues β_m with increasing imaginary part of r_2 from 0.0 to 1.0, for the S polarization diffraction problem of Table 5.8.

5.4.2.2 *Distribution of the Eigenvalues*

As mentioned earlier, the eigenvalues β_m^2 are spaced along the real axis for a lossless grating. As energy loss is introduced to the system, by allowing the imaginary components of r_1 and r_2 to gradually increase from zero, the eigenvalues β_m are found to move continuously away from their real (or imaginary) positions and out into the complex plane (see Figure 5.4). *All* complex eigenvalues are located by starting at the real or imaginary eigenvalues and following the paths illustrated. As *Re* (β_n^2) becomes infinite, the complex eigenvalues approach the real eigenvalues of the simpler problem, defined by the differential equation (5.16) with $\varsigma^2 = 0$, and the boundary conditions given by equations (5.7) and (5.8). Furthermore, the eigenfunctions $\{u_m\}$ approach the eigenfunctions of the simpler problem.

5.5 NUMERICAL TESTING AND APPLICATION OF THE THEORY

5.5.1 Verification of the Formalism

Due to the differences which exist within the implementation of the formalism for dielectric gratings as opposed to metal gratings, results are now given which validate the formalism in *both* instances. A comprehensive set of tests is first presented for the lossless dielectric grating, where several phase properties apply. This is followed by some checks appropriate to the finitely-conducting grating.

5.5.1.1 *Numerical Checks for the Lossless Dielectric Grating*

The convergence of the calculations has been tested as the number of modes is increased. The results of one such test are shown in Table 5.2. In that particular example only three imaginary-β modes are evident, the remainder being real. By ordering each of the modes in ascending β-modulus and placing the imaginary-β modes first, the

TABLE 5.2

Efficiency Convergence for the Dielectric Lamellar Grating.

Efficiency and phase of order 0 are given as a function of the number of real and imaginary modes included in the field expansion.

Groove Parameters: $d = 1.0$, $c = 0.5$, $g = 0.5$, $h = 1.2$
Refractive Indices: $r_1 = r_3 = 1.0$, $r_2 = 1.5$ (P polarization)
$r_2 = 2.0$ (S polarization)
Mounting Parameters: $\lambda = 1.55$, $\theta = 0°$.

Modes supporting a significant energy flux are:-
P polarization: 1st and 3rd imaginary, 1st real.
S polarization: 1st and 3rd imaginary, 2nd real.

P Polarization

No. of Modes		$E^T(0)$	$\text{Arg}(\hat{A}_0)$
Real β	Imag β		
1	2	.5568	-35.78
2	2	.5568	-35.78
1	3	.8742	-0.71
3	3	.8742	-0.71
5	3	.8759	-0.81
9	3	.8760	-0.82
13	3	.8761	-0.83

S Polarization

No. of Modes		$E^T(0)$	$\text{Arg}(\hat{B}_0)$
Real β	Imag β		
2	2	.6903	-104.30
2	3	.2828	-76.37
3	3	.4592	-54.06
5	3	.4592	-54.06
6	3	.4616	-52.76
9	3	.4636	-52.44
13	3	.4641	-52.16

energy-carrying modes for P polarization are found to be the first, third and fourth modes while for S polarization they are the first, third and fifth modes. These modes are all termed "propagating" modes since they each possess real values of μ. (Note that for this example $\theta = 0$. For the same problem, but $\theta \neq 0$, all of the first four modes for P polarization and the first five modes for S polarization carry a significant energy flux.) Obviously all of the above modes should be included in the modal expansions, and the results in Table 5.2 indicate that the amplitudes converge quickly once this point has been reached. In fact any further change is less than 2%. It is thus apparent that only a relatively small number of modes is needed to adequately characterize the groove region for the dielectric grating, as is the case with the formalisms for infinite conductivity.

The Reciprocity Theorem has been tested for a grating of refractive index $r_2 = 1.5$, resting on a dielectric slab of refractive index 2.0. These results are displayed in Table 5.3. With ten modes for P polarization and twelve for S polarization, the calculations satisfy the Theorem's requirements to a factor of less than 0.01% in their efficiencies.

Phase properties for both the long-wavelength and -1 Littrow mounting configurations have been successfully checked and results for the latter mounting are contained in Tables 5.4 to 5.6. A structure for which $r_1 = r_3$ possesses both left-right and up-down symmetry and so symmetry properties (2.64), (2.65), (2.66) and (2.71) are applicable. Table 5.4 demonstrates the accuracy with which the first two sets of properties are satisfied by the order amplitudes, while Table 5.5 deals with the last two sets of properties, which connect the mode amplitudes.

When $r_1 \neq r_3$ the structure has left-right symmetry but not up-down symmetry and so only those phase properties pertaining to the former condition apply. Table 5.6 exhibits results which conform well with a

TABLE 5.3

Reciprocity Results for the Dielectric Lamellar Grating.

Efficiency, phase and transmitted energy (E.T.) values are given to confirm agreement with the Reciprocity Theorem. The reciprocal configurations are defined by:

Problem 1: $\theta = 0°$, $\lambda = 0.8$, $r_1 = 1.0$, $r_2 = 1.5$, $r_3 = 2.0$
Problem 2: $\theta = 53.1301°$, $\lambda = 0.8$, $r_1 = 1.0$, $r_2 = 1.5$, $r_3 = 2.0$
Problem 3: $\theta = 23.5782°$, $\lambda = 0.4$, $r_1 = 0.5$, $r_2 = 0.75$, $r_3 = 0.5$.

In problem 2 the -1 reflected order is returned and the refractive indices are unchanged. In problem 3 the refractive indices, and also the wavelength, must be altered to simulate the returning of the -1 transmitted order.

Groove Parameters: $d = 1.0$, $c = 0.5$, $g = 0.5$, $h = 0.2$.
Number of Expansion Terms: 17 plane-wave, 10 modal (P polarization)
17 plane-wave, 12 modal (S polarization)

		P polarization	S polarization
Problem 1	$\lvert R_{-1}\rvert^2$, $\arg(R_{-1})$	.04249, -105.04	.02325, 86.85
	$\lvert T_{-1}\rvert^2$, $\arg(T_{-1})$	.08213, -115.48	.04580, -123.18
	E.T.	.9106	.9384
Problem 2	$\lvert R_{-1}\rvert^2$, $\arg(R_{-1})$	.04249, -105.04	.02325, 86.86
	E.T.	.9501	.9531
Problem 3	$\lvert T_{-1}\rvert^2$, $\arg(T_{-1})$	.08213, -115.48	.04581, -123.18
	E.T.	.9266	.9140

TABLE 5.4

-1 Littrow Symmetry Properties of the Plane-Wave Amplitudes for the Dielectric Grating.

Intensity and phase values of the plane-wave amplitudes are given to confirm agreement with the symmetry relations described in Chapter 2. The equation number of the appropriate relation is given in the final column.

Groove Parameters: $d = 1.0$, $c = 0.8$, $g = 0.2$, $h = 0.2$
Refractive Indices: $r_1 = 1.0$, $r_2 = 1.5$, $r_3 = 1.0$
Mounting Parameters: $\lambda = 1.2$, $\theta = 36.87°$
Number of Expansion Terms: 17 plane-wave, 10 modal (P polarization)
15 plane-wave, 8 modal (S polarization)

	P polarization	S polarization	Equation Number
$\|R_0\|^2$, $\arg(R_0)$	$.2001\times10^{-1}$, 107.48	$.4844\times10^{-3}$, -76.11	
$\|T_0\|^2$, $\arg(T_0)$	.9401 , 9.20	.9914 , 6.27	
$\|R_{-1}\|^2$, $\arg(R_{-1})$	$.1737\times10^{-1}$, -71.25	$.6912\times10^{-2}$, 96.80	
$\|T_{-1}\|^2$, $\arg(T_{-1})$	$.2247\times10^{-1}$, -73.43	$.1223\times10^{-2}$, -80.74	
$\|R_1\|^2$, $\arg(R_1)$	$.7083\times10^{-2}$, -171.41	$.8670\times10^{-2}$, 131.09	
$\|T_1\|^2$, $\arg(T_1)$	$.7942\times10^{-2}$, -158.39	$.7998\times10^{-2}$, -120.19	
$\|R_{-2}\|^2$, $\arg(R_{-2})$	$.4455\times10^{-2}$, 12.29	$.5216\times10^{-2}$, -126.54	
$\|T_{-2}\|^2$, $\arg(T_{-2})$	$.5155\times10^{-2}$, 25.40	$.6078\times10^{-2}$, 139.16	
$\|R_0\|^2+\|R_{-1}\|^2+\|T_0\|^2+\|T_{-1}\|^2$	1.0000	1.0000	2.64(i)
$Re(R_0\bar{R}_{-1}+T_0\bar{T}_{-1})$	5.05×10^{-6}	4.37×10^{-7}	2.64(ii)
$Re(R_0\bar{T}_{-1}+R_{-1}\bar{T}_0)$	-7.50×10^{-7}	1.32×10^{-6}	2.64(iii)
$Re(R_0\bar{T}_0+R_{-1}\bar{T}_{-1})$	1.02×10^{-5}	1.07×10^{-6}	2.64(iv)
$\frac{1}{2}\arg(P_0+P_{-1})$	0.62	3.89	2.65(i), 2.66(iii)
$\frac{1}{2}\arg(P_0-P_{-1})$	16.97	1.13	2.65(iii), 2.66(iv)
$\frac{1}{2}\arg(M_0+M_{-1})$	90.03	90.73	2.65(ii), 2.66(i)
$\frac{1}{2}\arg(M_0-M_{-1})$	91.12	97.16	2.65(iv), 2.66(ii)
$\arg(P_1+P_{-2})$	0.62	3.89	2.65(i)
$\arg(P_1-P_{-2})$	16.97	1.11	2.65(iii)
$\arg(M_1+M_{-2})$	90.07	90.36	2.65(ii)
$\arg(M_1-M_{-2})$	91.12	97.16	2.65(iv)

TABLE 5.5

-1 Littrow Symmetry Properties of the Modal Amplitudes for the Dielectric Grating.

Modal amplitude phases are given for the same configuration described in Table 5.4. Where appropriate they should be compared with the data in that table. The superscript "e" denotes modes of even x-symmetry and "o" denotes odd x-symmetry.

	P polarization	S polarization	Equation Number
$\arg(a_m^e)$, $\arg(a_m^o)$ m=1	90.04, 1.12	90.37, 7.16	2.66(i),(ii)
m=2	90.04, 1.12	90.38, 7.16	
m=3	90.03, 1.12	90.36, 7.14	
m=4	90.03, 1.12	89.16, 7.16	
$\arg(b_m^e)$, $\arg(b_m^o)$ m=1	0.61, 106.97	3.89, 91.13	2.66(iii),(iv)
m=2	0.61, 106.97	3.89, 91.13	
m=3	0.61, 106.97	3.89, 91.13	
m=4	0.61, 106.97	3.89, 91.13	
L.H.S. of equation (2.71)	.0373	.0074	2.71
$\|R_0\|^2+\|R_{-1}\|^2$	.0374	.0074	2.71

TABLE 5.6

-1 Littrow Symmetry Properties for the Dielectric Grating.

The results given below concern a lossless dielectric grating whose profile has left-right symmetry but not up-down symmetry. They confirm agreement with the relations:-

$$A = Re\ (R_0\bar{R}_{-1} + \frac{\sqrt{\xi_0\,\xi_{-1}}}{\chi_0^{\,2}}\ T_0\bar{T}_{-1}) \;=\; 0 \qquad \text{(P polarization)}$$

$$A = Re\ (R_0\bar{R}_{-1} + \frac{\sqrt{\xi_0\,\xi_{-1}}}{r_3^{\,2}\chi_0^{\,2}}\ T_0\bar{T}_{-1}) \;=\; 0 \qquad \text{(S polarization)}$$

Groove Parameters: $d = 1.0$, $c = 0.8$, $g = 0.2$, $h = 0.2$
Refractive Indices: $r_1 = 1.0$, $r_2 = 1.5$, $r_3 = 2.0$
Mounting Parameters: $\lambda = 1.5$, $\theta = 48.5904°$ (P polarization)
$\lambda = 1.6$, $\theta = 53.1301°$ (S polarization)
Number of Expansion Terms: 21 plane-wave, 12 modal (P polarization)
15 plane-wave, 8 modal (S polarization)

	P polarization	S polarization
$\lvert R_0\rvert^2$, $\arg(R_0)$	.1695 , -150.95	$.2021\times10^{-1}$, 47.54
$\lvert T_0\rvert^2$, $\arg(T_0)$	.2915 , -22.41	$.1269\times10^{1}$, -21.67
$\lvert R_{-1}\rvert^2$, $\arg(R_{-1})$	$.3809\times10^{-2}$,-130.38	$.9678\times10^{-2}$, 99.41
$\lvert T_{-1}\rvert^2$, $\arg(T_{-1})$	$.3120\times10^{-2}$,-128.74	$.1315\times10^{-2}$, 84.41
A	-7.04×10^{-6}	-4.42×10^{-6}

-1 Littrow symmetry relation which contains the necessary modifications to (2.64(ii)).

To check the actual magnitude of the computed efficiency values, calculations were performed for comparison with those published by Knop [5.14]. To this end, grating parameters were chosen to coincide with those used by that author and efficiency curves were generated for P polarization and a normal incidence mounting. These spectra are illustrated in Figure 5.5 and are seen to be in complete agreement with Knop's results.

5.5.1.2 *Numerical Checks for Finite Conductivity*

As for the previous case, a convergence test was carried out by studying the change in efficiency as the number of modes was increased. These results are listed in Table 5.7 for an aluminium reflection grating of period 1μm and used in a -1 Littrow mounting with a wavelength of 0.925μm. The β values were located using the improved method [5.22] and were generally found to contain real components lying between 0 and 70, with very small imaginary components. It is interesting that isolated values near 60-7i and 63-11i, were obtained for P polarization and S polarization respectively. These appeared however, to be no more significant than the others. It is clear from the results in Table 5.7, that when compared with the dielectric case, a substantially larger number of modes are needed to represent the groove field for finite conductivity. In fact general observations have shown that the higher is the conductivity, the larger is the number of modes required.

As discussed in Section 5.2.4, energy conservation now constitutes a valid test of the calculations. To this end the energy mismatch is defined by

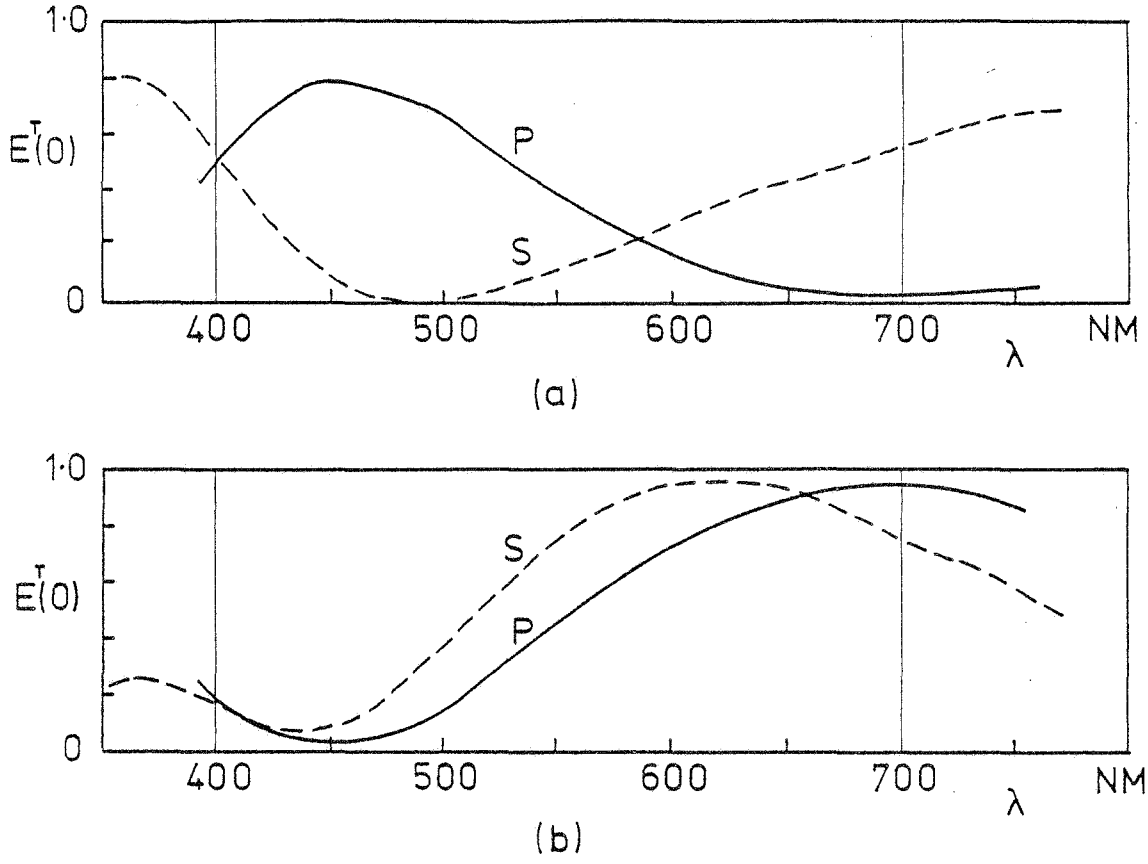

Figure 5.5 Efficiency of the transmitted zero order as a function of wavelength for comparison with the results of Knop [5.14 (Figure 3)].

Groove parameters: d=1.4μm, h=1.56μm (a) c=1.26μm
(b) c=0.98μm

Refractive indices: r_1=1.0, r_2=r_3=1.5.

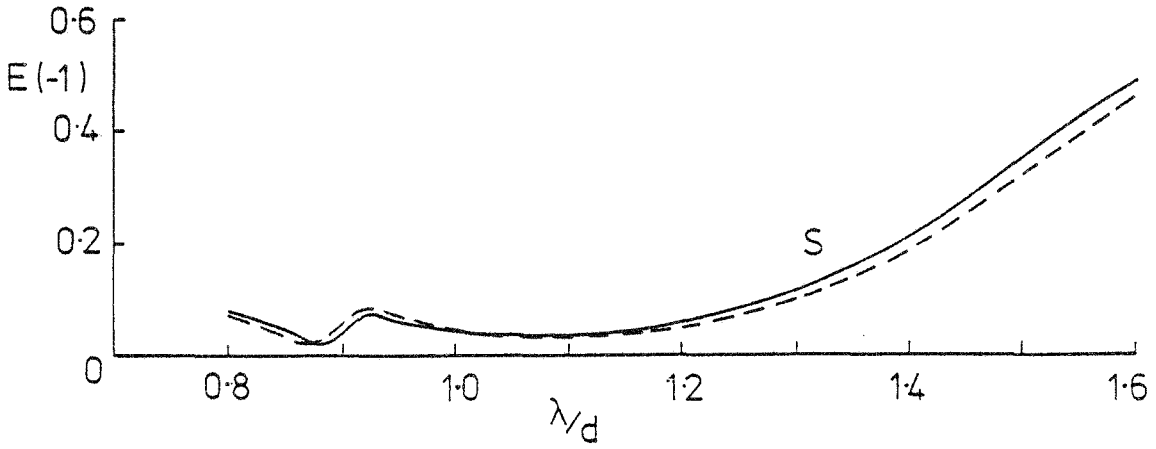

Figure 5.6 S polarization efficiency curves for an aluminium lamellar reflection in a -1 Littrow mounting.

Groove parameters: d=1.0μm, c=0.9μm, h=0.45μm

(———) Modal theory
(----) Integral theory

TABLE 5.7

Efficiency Convergence for an Aluminium Lamellar Reflection Grating.

Efficiency and phase, plus energy mismatch (E.M.), are given as a function of the number of modes included in the expansions.

Groove Parameters: $d = 1.0\mu m, c = 0.9\mu m, h = 0.45\mu m$
Refractive Indices: $r_1 = 1.0$, $r_2 = r_3 = 1.8588 + 8.0813i$
Mounting Parameters: $\lambda = 0.925\mu m, \theta = 27.548°$
Number of Plane-Wave Terms: 29

Number of modes	P polarization			S polarization		
	E(-1)	Arg(A_{-1})	E.M.	E(-1)	Arg(B_{-1})	E.M.
4	.9254	145.79	-.029	.0828	100.88	.007
8	.9345	137.32	.061	.0805	101.44	.008
12	.9413	132.26	-.104	.0801	101.62	.005
15	.9562	130.00	-.142	.0800	101.75	.005
18	.7276	121.38	.011	.0799	101.81	.003
22	.7440	121.81	.000	.0712	103.18	.002
Integral Theory	.7544			.0726		

$$\text{En.Mismatch} = \text{E.D.} - Q \qquad \ldots(5.99)$$

where $\text{E.D.} = 1 - \text{E.R.} - \text{E.T.}$, $\ldots(5.100)$

E.R. = total reflected energy,

E.T. = total transmitted energy.

and Q is the energy absorbed within the groove region. The energy mismatch is also equal to the sum of the energy discrepancies across the top and bottom interfaces - the latter not being analytically zero as explained in Section 5.2.4. Table 5.7 reveals that for that particular example, with approximately 20 modes being used, the mismatch for P polarization is less than that for S polarization. (It is often found with grating formalisms in general, that P polarization results conform better with conservation theorems.)

The Reciprocity Theorem has again been used to confirm the validity of the calculations. In Table 5.8, results are presented which provide excellent agreement for a low refractive index transmission grating, where $r_2 = 1.5 + 1.0i$. For 20 modes the energy mismatches obtained are about 0.001%. (Note that the first-mentioned root-finding method was used to locate the β values here.)

To check a more practical case, where the metal is more conducting, r_2 was increased to $1.55 + 7.0i$ and the β values were calculated with the improved method. The results are given in Table 5.9 and are quite satisfactory, but mismatches have worsened to 0.1%. It is noted however, that the number of modes was not increased, as was possibly desired for the higher conductivity.

A property of the formalism given here, is that the convergence of the modal expansions improves as the normalised groove depth increases. This property has been observed previously for inductive grids [5.23] and to a lesser extent, for the infinitely-conducting lamellar grating (see Chapter 2). In Table 5.10 results are given for an extreme example of $h/d = 200$. A high degree of accuracy has been attained with only three

TABLE 5.8

Reciprocity Results for a Finitely-Conducting Lamellar Grating.

Agreement with the Reciprocity Theorem is demonstrated for the mounting configurations defined by:

Problem 1: $\theta = 11.5°$
Problem 2: $\theta = 36.91518°$ (-1 order returned)
Problem 3: $\theta = -87.96276°$ (+1 order returned)

Groove Parameters: $d = 1.0$, $c = 0.4001$, $h = 0.1000$
Refractive Indices: $r_1 = 1.0$, $r_2 = 1.5 + 1.0i$, $r_3 + 1.0$
Wavelength: $\lambda = 0.8$
Number of Expansion Terms: 51 plane-wave, 20 modal.

	P polarization		S polarization	
Problem 1				
$\|R_{-1}\|^2$, $\arg(R_{-1})$	$.28529\times10^{-1}$,	92.7502	$.16772\times10^{-1}$	-78.6682
$\|T_{-1}\|^2$, $\arg(T_{-1})$	$.38574\times10^{-1}$,	96.3899	$.21372\times10^{-1}$,	117.5688
$\|R_0\|^2$, $\arg(R_0)$	$.62128\times10^{-1}$,	-139.1595	$.95755\times10^{-1}$,	32.6897
$\|T_0\|^2$, $\arg(T_0)$	.46913,	44.8301	.39939,	50.8365
$\|R_1\|^2$, $\arg(R_1)$	$.46011\times10^{-2}$,	-61.1899	$.12779\times10^{-2}$,	120.5751
$\|T_1\|^2$, $\arg(T_1)$	$.5489\times10^{-2}$,	-59.6281	$.36226\times10^{-2}$,	-46.2306
E.R., E.T.	.09526,	.51319	.11381,	.42438
E.D.	.39155		.46181	
Q	.39156		.46047	
Problem 2				
$\|R_{-1}\|^2$, $\arg(R_{-1})$	$.28529\times10^{-1}$,	92.7501	$.16772\times10^{-1}$,	-78.6671
$\|T_{-1}\|^2$, $\arg(T_{-1})$	$.38574\times10^{-1}$,	96.3899	$.21372\times10^{-1}$,	117.5694
E.R., E.T.	.16745,	.37027	.06755,	.43902
E.D.	.46229		.49343	
Q	.46229		.49184	
Problem 3				
$\|R_1\|^2$, $\arg(R_1)$	$.46012\times10^{-2}$,	-61.1899	$.12800\times10^{-2}$,	120.5788
$\|T_1\|^2$, $\arg(T_1)$	$.54894\times10^{-2}$,	-59.6281	$.36223\times10^{-2}$,	-46.2321
E.R., E.T.	.89431,	.00993	.82541,	.02269
E.D.	.09575		.15190	
Q	.09575		.15151	

TABLE 5.9

Reciprocity Results for an Aluminium Lamellar Reflection Grating.

Agreement with the Reciprocity Theorem is demonstrated for S polarization and the configuration defined by:

Problem 1: $\theta = 10.0°$
Problem 2: $\theta = 31.75929°$ (-1 order returned)
Problem 3: $\theta = -60.88539°$ (+1 order returned)

Groove Parameters: $d = 1.0$, $c = 0.8$, $h = 0.1$
Refractive Indices: $r_1 = 1.0$, $r_2 = 1.55+7.0$, $r_3 = 1.0$
Wavelength: $\lambda = 0.7$
Number of Expansion Terms: 29 plane-wave, 19 modal.

	Problem 1	Problem 2	Problem 3
$\|B_0\|^2$, $\arg(B_0)$	.08291, -54.94		
$\|\hat{B}_0\|^2$, $\arg(\hat{B}_0)$	.68180, 11.71		
$\|B_1\|^2$, $\arg(B_1)$	.04849, -24.21		.04847, -24.22
$\|\hat{B}_1\|^2$, $\arg(\hat{B}_1)$	.02694, -178.08		.02694, -178.11
$\|B_{-1}\|^2$, $\arg(B_{-1})$	.08126, -95.50	.08125, -95.50	
$\|\hat{B}_{-1}\|^2$, $\arg(\hat{B}_{-1})$	.04492, 110.85	.04492, 110.85	
E.R.	.2127	.2080	.1226
E.T.	.7537	.7565	.8366
E.D.	.0336	.0354	.0408
Q	.0342	.0362	.0422
E.M.	-.0005	-.0008	-.0014

(Note: For problem 3, $\theta = +60.88539°$ was used and the appropriate correction factor was added to the phases to allow for the origin being offset from the line of symmetry.)

TABLE 5.10

Results for a Finitely-Conducting Lamellar Grating with Large h/d.

Groove Parameters: d = 0.0040, c = 0.0024, h = 0.8000, h/d = 200
Refractive Indices: $r_1 = 1.0$, $r_2 = r_3 = 2.7 + 0.5i$
Mounting Parameters: $\lambda = 0.80$, $\theta = 0°$
Number of Expansion Terms: 31 plane-wave, 3 modal.

	P polarization	S polarization
$\|a_1^*\|$	3.1734×10^{-1}	6.5833×10^{-1}
$\|b_1^*\|$	3.7891×10^{-1}	6.4689×10^{-1}
$\|a_2^*\|$	1.1223×10^{-5}	3.5221×10^{-9}
$\|b_2^*\|$	1.3451×10^{-5}	4.2734×10^{-9}
$\|a_3^*\|$	5.0528×10^{-9}	1.0174×10^{-3}
$\|b_3^*\|$	6.0571×10^{-9}	1.0678×10^{-3}
E.R.	0.10043	0.04284
E.T.	0.02295	0.71290
E.D.	0.87663	0.24426
Q	0.87663	0.24416
E.M.	0.00000	0.00010

modes in the expansions. In fact good accuracy was maintained when monomodal expansions were employed. For comparison, the integral theory of Maystre [5.10] has been found to achieve the same accuracy for similar calculations, but only when h/d is less than about five.

For final confirmation of the formalism, efficiencies were calculated for an aluminium reflection grating of period 1μm and h/d = 0.45. These are compared in Figure 5.6 with those predicted by the formalism of Maystre. With 15 modes included in the calculations, discrepancies between the two theories are observed to never exceed 2% over the wavelength interval used. This agreement is considered excellent.

5.5.2 Efficiency Spectra for Dielectric Gratings

The behaviour of dielectric refraction and transmission gratings has been investigated in the normal incidence mounting for glass gratings (r_2 = 1.5) and for gratings made of a more strongly reflecting material (r_2 = 5.0). Examples of some efficiency curves are contained within Figures 5.7 to 5.12. These spectra encompass regions of marked anomalous behaviour and hence have also served as a test of the convergence of the formalism. Sufficient modes were used in each case to ensure that the efficiency at any point had converged to within 1% of its final value.

Figures 5.7 and 5.8 contain the curves for a glass refraction grating ($r_2 = r_3$ = 1.5) for S and P polarizations. These spectra exhibit both the zero order transmitted energy and the total transmitted energy and they illustrate, that of the two polarizations, it is P polarization which diffracts more energy out of the zero order and which uncharacteristically displays the most pronounced anomalous behaviour. These P-type anomalies are manifested as dark bands which are similar to those observed for reflection gratings by Palmer [5.24]. As $\lambda \to \infty$, the total transmitted energy for each polarization approaches the geometrical optics limit (for r = 1.5) of 96%.

Fig. 5.7

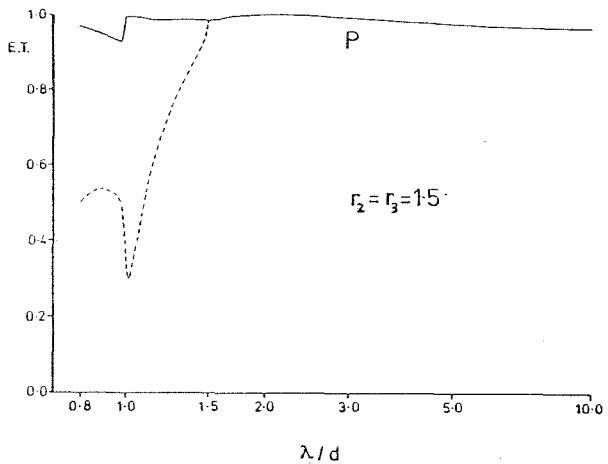

Fig. 5.8

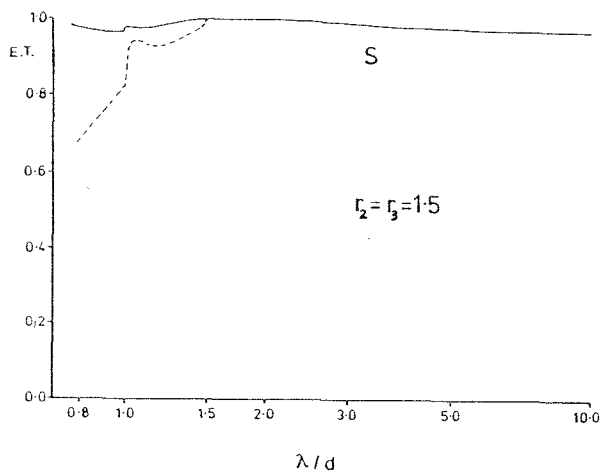

Fig. 5.9

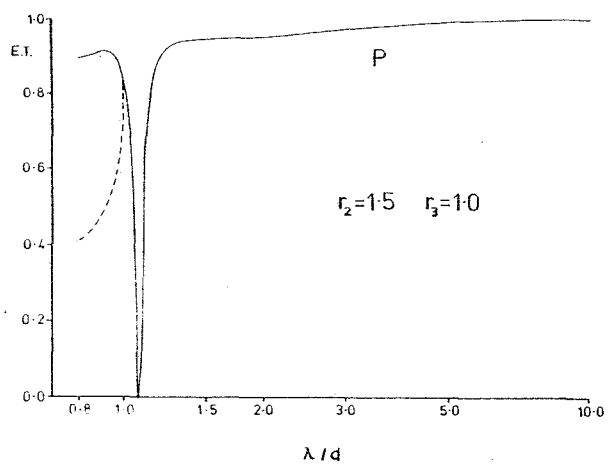

Fig. 5.10

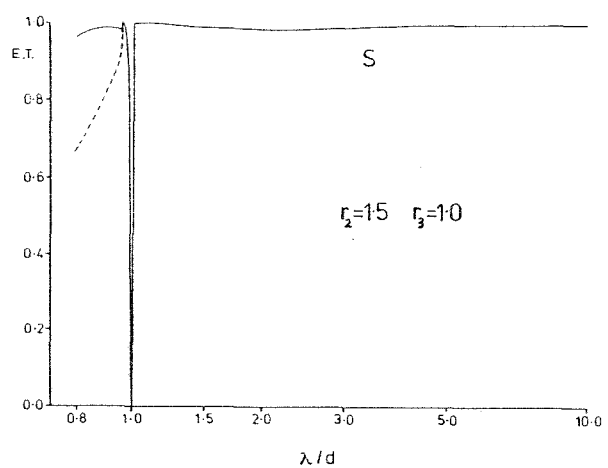

Fig. 5.11

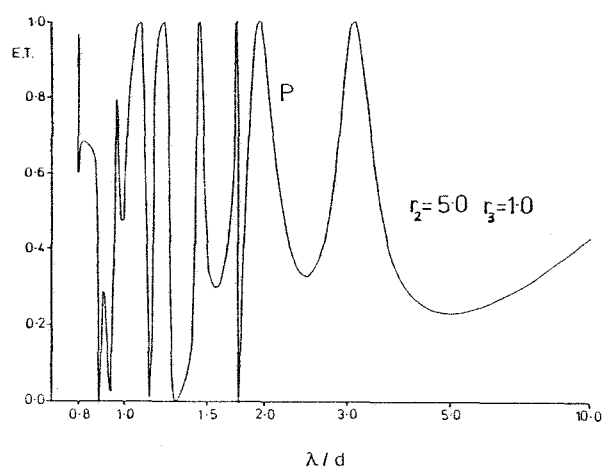

Fig. 5.12

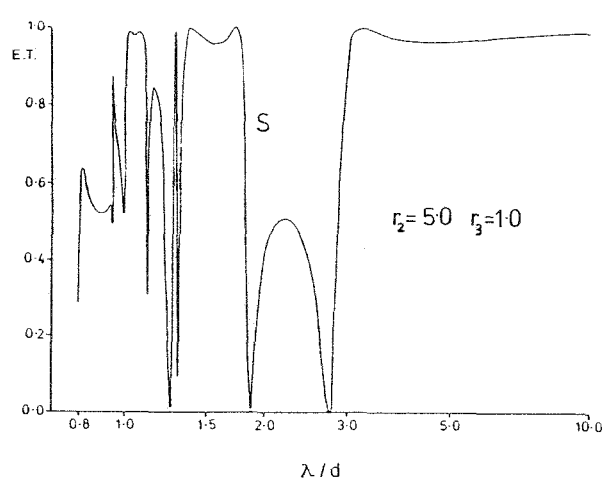

It should be noted in respect of the above spectra, that the Rayleigh wavelengths near which Wood anomalies occur, are at different wavelengths for the reflected and transmitted orders if $r_1 \neq r_3$. For the p^{th} diffracted order these wavelengths are given by

$$\lambda_R = \begin{cases} d(r_i - \sin\theta)/p \ , & p = 1,2 \ldots \\ d(-r_i - \sin\theta)/p \ , & p = -1,-2,\ldots \end{cases} \qquad \ldots(5.101)$$

where i = 1 or 3 depending on the mediun concerned. Thus in Figures 5.7 and 5.8 abrupt changes in efficiency are observed near both $\lambda/d = 1.0$ and $\lambda/d = 1.5$.

Figures 5.9 and 5.10 also correspond to glass gratings, but in this case the transmission type ($r_3 = 1.0$). For both polarizations strong anomalous behaviour is manifested as narrow troughs in the transmitted efficiency just above the Rayleigh wavelength $\lambda_R = 1.0d$. In this case, as $\lambda \to \infty$, the grating again loses its dispersive properties and energy transmitted in the zero order approaches 100%.

Efficiency curves for the high refractive index transmission grating ($r_2 = 5.0$, $r_3 = 1.0$) are contained in Figures 5.11 and 5.12. Only the total transmitted energy has been plotted due to the proliferation of very sharp anomalies for both polarizations. Although not studied in any detail, these phenomena are attributed to resonance-type behaviour in the modes, as discussed in Chapter 3. It is suggested that the increase in refractive index, and consequent increase in the reflectance of the side walls, has enabled complex poles in the mode functions to move closer to the real wavelength axis and hence have a more pronounced influence on efficiency at physical wavelengths. This is evidenced by the increased Q-factor of the spectral peaks. It is also noted, that as r_2 is increased the real β-values decrease. This has the effect of increasing the mode thresholds with the result that more modes are able to undergo resonance.

5.5.3 Resonance Behaviour of Metallic Gratings

This section complements the work of Section 3.2.2.8. It describes an application of the modal formalism given in this chapter, to the study of a particular resonance anomaly observed for the lamellar reflection grating. The behaviour of this anomaly is studied as conductivity is reduced from infinity to low finite values. The existence of such a transition was confirmed in Section 3.2.2.8, where the integral theory method [5.10] was used to perform the finite-conductivity calculations.

The subject of the investigation was chosen to be an extremely sharp -1 Littrow S-type resonance, which is shown by the formalism of Chapter 2 to occur at a wavelength of $\lambda/d = 0.839$ for a perfectly-conducting reflection grating of groove depth $h/d = 0.45$ and aperture width $c/d = 0.9$. With reference to the work of Chapter 3, this particular resonance is due to a pole in the b_2 mode amplitude and it lies just below the $m = 2$ mode threshold of $\lambda/d = 0.9$.

To ascertain the effect of conduction losses on the above anomaly, the modal formalism was used to compute two spectra for an aluminium grating with periods of $d = 2\mu m$ and $d = 1\mu m$ - the latter period corresponding to the lower conductivity. The refractive index data were obtained from reference [5.25] and all grating parameters were adjusted so that the ratios c/d, h/d and λ/d remained unchanged. These spectra are compared with the infinite-conductivity results in Figure 5.13(a). The effects of the resonance remain clearly visible in the finite-conductivity curves, despite the fact that they become weaker and broader and move to longer wavelengths as conductivity decreases. This behaviour is in keeping with the observations of Section 3.2.2.8.

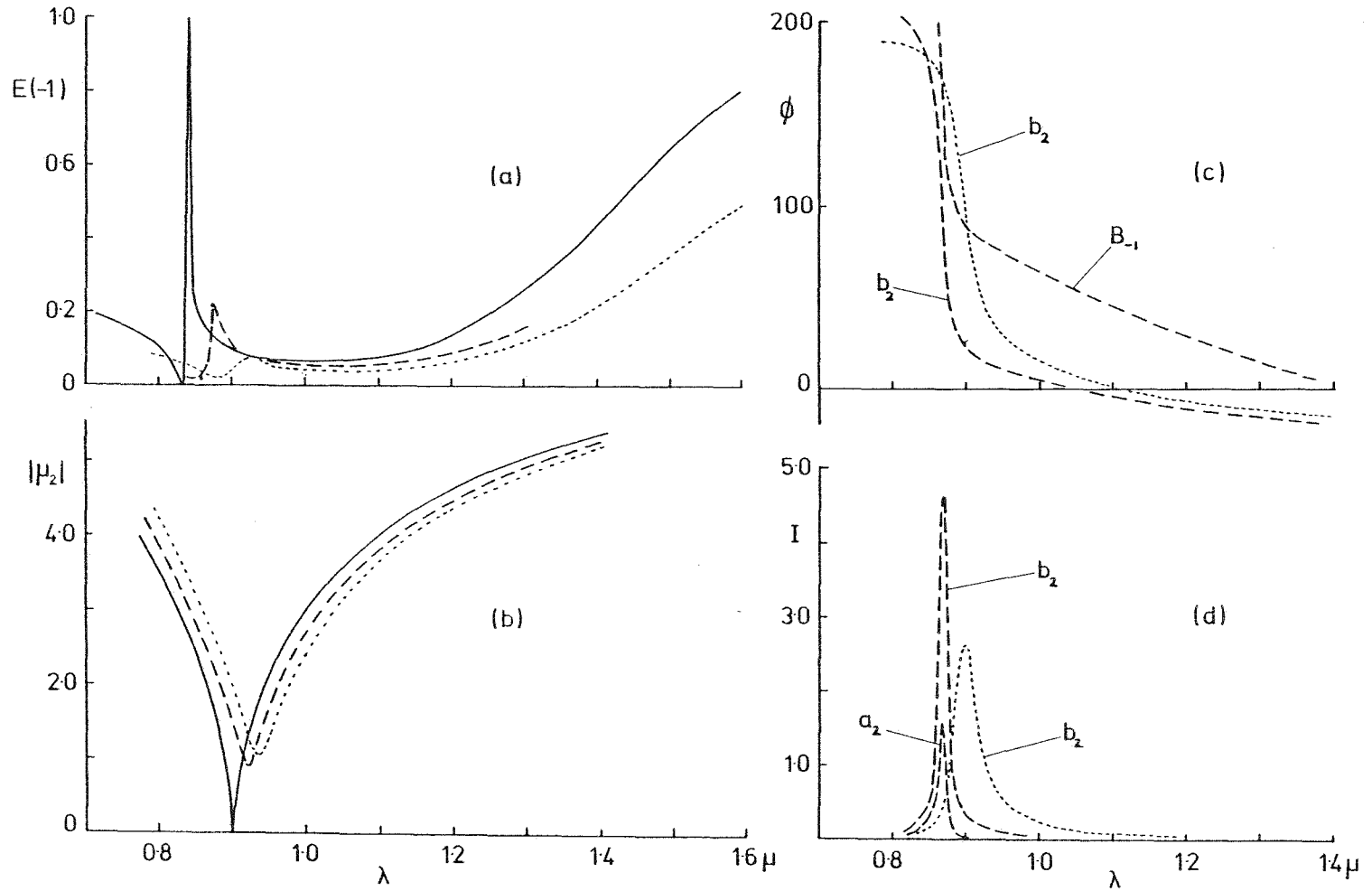

Figure 5.13 An aluminium lamellar reflection grating is considered in a -1 Littrow mounting for S polarization. Grating parameters are c/d=0.9, h/d=0.45. Plotted against wavelength are (a) efficiency (b) modulus of μ_2 (c) phases of B_{-1} and b_2, and (d) intensity of a_2 and b_2.
(——) ∞ conductivity (----) d=2μm (·····) d=1.0μm

Analysis of the finite-conductivity mode amplitudes a_m and b_m, reveals that the anomaly originates from a resonance in the third b_m mode amplitude, if the modes are ordered in terms of increasing real β-values. Labelling the modes m = 0, 1, 2 ... so that they can be compared directly with the infinite-conductivity amplitudes, one ascertains that it is *still* the b_2 mode amplitude which is responsible for the resonance. This is a very encouraging result.

Note that a mode is considered here to be a "propagating" mode if the complex number μ has a real component much larger than the imaginary component, say by a factor of ten. In the above example, the first three modes meet such a requirement for wavelengths less than about 0.9d, but only two modes comply above 0.95d. The value of μ_2 has changed over this interval from being predominantly real to being predominantly imaginary. Therefore this interval contains the m = 2 "mode threshold".

In Figure 5.13(b) the modulus of μ_2 has been plotted as a function of wavelength for the three conductivities. For infinite conductivity $|\mu|$ is a function of wavelength only, and reaches a value of precisely zero at the real wavelength threshold of $\lambda = \frac{2c}{m} = 0.9$. For finite conductivity μ is a function of λ and $\beta(\lambda,\theta,r_2)$, and $|\mu|$ no longer reaches zero but only a minimum at the threshold. With the decreasing conductivity this threshold is seen to move to longer wavelengths and this therefore permits the resonance position to move in a similar manner. It is noted that for a particular value of λ, *Re* (β) decreases and *Im* (β) increases as the conductivity is reduced. Equation (5.17) shows that this increases the possibility of having more propagating modes.

Figures 5.13(c) and (d) illustrate the change in the phase and intensity of the mode amplitude b_2 in the vicinity of the anomaly for the two cases of finite conductivity. These results provide further evidence

to suggest that the mechanism for resonance is just the same as that described in Chapter 3 for the perfectly-conducting lamellar grating.

5.6 CONCLUSION

The classical diffraction problem for metallic and lossless dielectric lamellar gratings has been solved using a modal expansion technique, which is a straight-forward extension of the modal method pertaining to perfectly-conducting lamellar gratings. The modes have been expressed in terms of an eigenvalue which is the solution of a single transcendental equation.

For the case of the dielectric grating, the eigenvalue problem has been expressed in terms of a self-adjoint operator, thus ensuring that the mode eigenfunctions form an orthogonal set with respect to an appropriate inner-product. For the lossy metallic grating, the problem is not self-adjoint and two sets of boundary conditions had to be considered - one belonging to the physical problem and the other belonging to the adjoint problem.

Both the validity of the formalism and the accuracy of numerical calculations have been successfully checked for both types of grating and some examples of efficiency curves have been given. Anomalous behaviour for an aluminium grating has been attributed to a resonance phenomenon originating in a mode amplitude, as found for the perfectly-conducting lamellar grating. Clearly, further work should be done in this area to gain a better understanding of the overall behaviour of metallic gratings.

Further application of the theory must also include the development of a modal formalism for finitely-conducting grids, since this is a structure which has attracted attention in the field of solar selective surfaces.

REFERENCES

[5.1] Wirgin, A., and Deleuil, R., 1969, *J. Opt. Soc. Am., 59,* 1348.

[5.2] Roumiguieres, J.L., Maystre, D., and Petit, R., 1973, *Opt. Commun., 7,* 402.

[5.3] Roumiguieres, J.L., 1976, *Opt. Commun., 19,* 76.

[5.4] Roumiguieres, J.L., 1976, *J. Opt. Soc. Am., 66,* 772.

[5.5] Andrewartha, J.R., Fox, J.R., and Wilson, I.J., 1979, *Optica Acta, 26,* 69.

[5.6] Loewen, E.G., Nevière, M., and Maystre, D., 1979, *Appl. Optics, 18,* 2262.

[5.7] Andrewartha, J.R., Fox, J.R., and Wilson, I.J., 1979, *Optica Acta, 26,* 197.

[5.8] Knop, K., 1976, *Opt. Commun., 18,* 298.

[5.9] Knop, K., 1978, *Appl. Optics, 17,* 3598.

[5.10] Maystre, D., 1978, *J. Opt. Soc. Am., 68,* 490.

[5.11] Botten, L.C., Craig, M.S., McPhedran, R.C., Adams, J.L., and Andrewartha, J.R., *Optica Acta,* accepted for publication.

[5.12] Botten, L.C., Craig, M.S., McPhedran, R.C., Adams, J.L., and Andrewartha, J.R., *Optica Acta,* accepted for publication.

[5.13] Burckhardt, C.B., 1966, *J. Opt. Soc. Am., 56,* 1502.

[5.14] Knop, K., 1978, *J. Opt. Soc. Am., 68,* 1206.

[5.15] Nevière, M., Vincent, P., and Petit, R., 1974, *Nouv. Rev. Opt., 5,* 65.

[5.16] Marcuse, D., 1974, *Theory of Dielectric Optical Waveguides.* (London: Academic Press.)

[5.17] Harrington, R.F., 1968, *Field Computation by Moment Methods.* (London: Collier-Macmillan.)

[5.18] Coddington, E.A., and Levinson, N., 1955, *Theory of Ordinary Differential Equations.* (London: McGraw-Hill.)

[5.19] Eastham, M.S.P., 1973, *The Spectral Theory of Periodic Differential Equations.* (Edinburgh: Scottish Academic Press.)

[5.20] Clayton, E., and Derrick, G.H., 1977, *Aust. J. Phys., 30,* 15.

[5.21] Hamming, R.W., 1973, *Numerical Methods for Scientists and Engineers.* (New York: McGraw-Hill.)

[5.22] Botten, L.C., Craig, M.S., and McPhedran, R.C., 1981, *Optica Acta,* accepted for publication.

[5.23] McPhedran, R.C., and Maystre, D., 1977, *Appl. Phys., 14,* 1.

[5.24] Palmer, C.H., 1952, *J. Opt. Soc. Am., 42,* 269.

[5.25] Gray, D.E. (editor), 1963, *American Institute of Physics Handbook,* second edition (McGraw-Hill).

Chapter 6

THE SEMI-CIRCULAR GROOVE GRATING

6.1 INTRODUCTION

This chapter describes a modal expansion technique for solving the diffraction problem for a perfectly-conducting reflection grating whose grooves are semi-circular in cross-section. A report based on the investigation has been recently accepted for publication [6.1].

This work represents only the third known application of a modal method to a specific reflection grating profile. The previous applications were of course to the lamellar and triangular groove gratings. As with those two cases, the method given here takes advantage of the separability of the Helmholtz equation as a result of the groove profile coinciding with a "coordinate surface". However, in contrast to those two cases, here we find that the Helmholtz equation and the boundary conditions are not sufficient to completely specify the field in the groove region. It is therefore necessary to impose an extra constraint in order that the modes be fully determined. This constraint takes the form of an eigenvalue condition which has been chosen to relate each groove mode function to its normal derivative on the interface along the groove-top. As with other semi-analytic techniques, it is then a straight-forward process to complete the solution by matching the modal field to a Rayleigh expansion along the interface separating the grating from the free-space region.

The formalisms for both P and S polarizations are presented in Section 6.2, while Section 6.3 deals with the numerical applications. The latter section includes a discussion of the computer implementation as well as tests carried out to check the validity and accuracy of the theory. Section 6.4 presents some efficiency spectra for different groove

radii when the grating is operated in the first-order Littrow mounting. These spectra are compared with analagous results for other groove profiles. The groove radius which yields optimum blazing action is also determined. The section is concluded with a discussion of resonance phenomena, the effects of which may be clearly seen in the efficiency curves, especially for S polarized radiation.

6.2 THEORETICAL FORMULATION

6.2.1 The Diffraction Arrangement

The grating under consideration is assumed to be perfectly conducting and to have grooves which are semi-circular in cross-section. The geometrical configuration is shown in Figure 6.1, where the structure is assumed to extend infinitely in both the x and z directions. The grating period is d and the radius of cross-section of the grooves is a, the latter being restricted to lie between 0 and d/2.

For convenience the origin has been chosen to lie at the top centre of a groove, thus enabling a cylindrical coordinate system (r, θ, z) to be used in conjunction with conventional (x, y, z) coordinates. In the former system, the groove region is defined as the area bounded by $0 < r < a$ and $\pi < \theta < 2\pi$.

A plane wave of unit amplitude and wavelength λ is assumed to strike the grating at an angle of incidence ϕ, and with its wave-vector in the xy plane.

The detailed solution for a P-polarized incident wave is given first, and this is followed by the necessary changes to the formulation for S polarization.

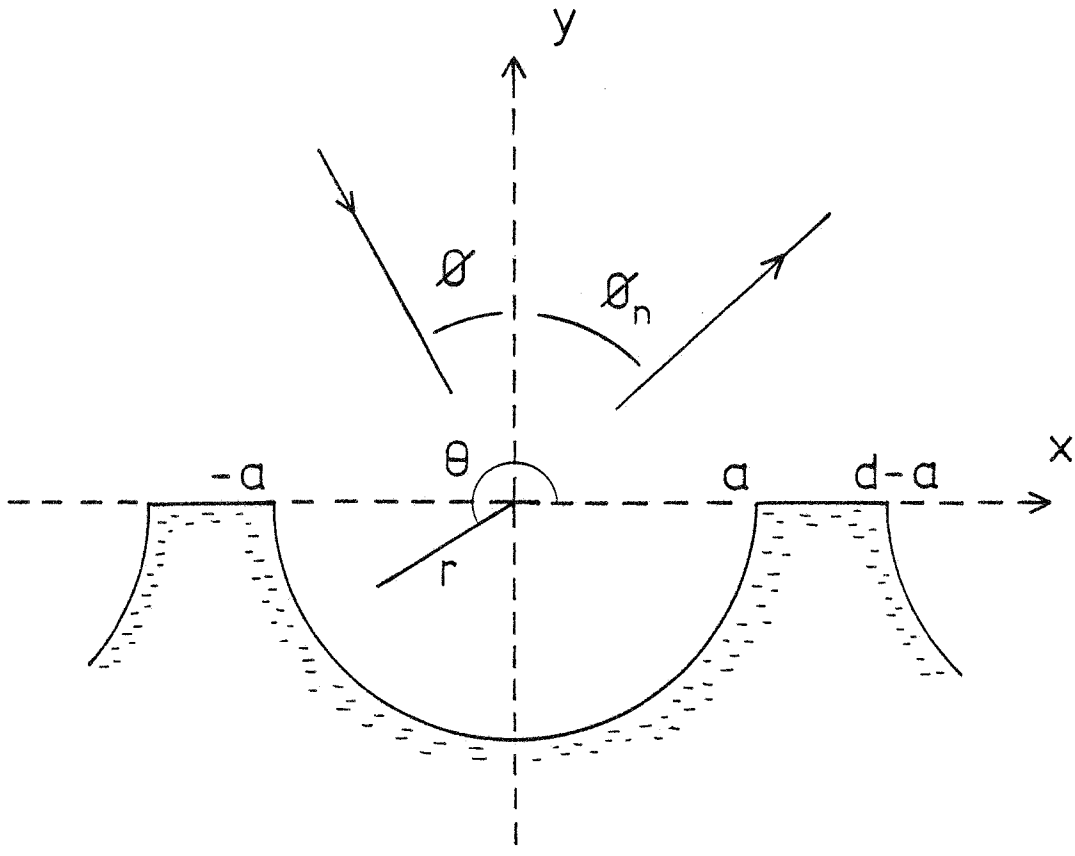

Figure 6.1 The geometry of the diffraction arrangement for the semi-circular groove grating.

6.2.2 Solution of the Diffraction Problem for P Polarization

6.2.2.1 *Specification of the Plane-Wave Field*

The total electric field $\underline{E}$ is assumed to be aligned with the z-axis or generating axis of the grooves. The problem is therefore a scalar one and completely determined in terms of the z-component of the field, $E(x,y)$.

Above the grating surface, the total electric field is expressed as the familiar Rayleigh expansion,

$$E^R(x,y) = \exp[i(\alpha_0 x - \chi_0 y)] + \sum_{p=-\infty}^{\infty} A_p \exp[i(\alpha_p x + \chi_p y)], \quad y > 0. \qquad ...(6.1)$$

$$\left.\begin{aligned} \text{where } \alpha_p &= k(\sin\phi + \frac{p\lambda}{d}), \quad k = \frac{2\pi}{\lambda} \\ \chi_p &= (k^2 - \alpha_p{}^2)^{\frac{1}{2}}, \quad |\alpha_p| \leqslant k \\ &= i(\alpha_p{}^2 - k^2)^{\frac{1}{2}}, \quad |\alpha_p| > k. \end{aligned}\right\} \qquad ...(6.2)$$

6.2.2.2 *Specification of the Modal Field in the Groove Region*

The field within the groove region is described by an infinite modal expansion,

$$E^M(r,\theta) = \sum_{m=1}^{\infty} a_m u_m(r,\theta) \qquad ...(6.3)$$

where each function $u_m(r,\theta)$ must satisfy the wave equation and the appropriate boundary conditions. It is found that these two constraints are insufficient to completely characterize the problem. A further stipulation is therefore made, requiring that each mode obeys an impedance condition which relates the field along the top of the groove aperture to its y-derivative. The above three constraints on the modal field are expressed as follows:

For $0 < r < a$,

$$\text{(i)} \quad [\frac{\partial^2}{\partial r^2} + \frac{1}{r}\frac{\partial}{\partial r} + \frac{1}{r^2}\frac{\partial^2}{\partial \theta^2} + k^2]\, u_m(r,\theta) = 0, \quad \pi < \theta < 2\pi \qquad ...(6.4)$$

(ii) $u_m(a,\theta) = 0, \qquad \pi < \theta < 2\pi$ ...(6.5)

(iii) $$\frac{1}{r}\frac{\partial u_m(r,\theta)}{\partial \theta} = \begin{cases} \beta_m\, u_m(r,\theta), & \theta = 0 \\ -\beta_m\, u_m(r,\theta), & \theta = \pi \end{cases}$$ ...(6.6)

where β_m is an eigenvalue. In rectangular coordinates, equation (6.6) becomes

$$\frac{\partial u_m(x,y)}{\partial y} = \beta_m\, u_m(x,y) \quad , \qquad y = 0, \quad -a < x < a. \qquad ...(6.7)$$

The eigenvalue β_m is closely related to the quantity D_{mm} used by Fox [6.2] in his general analysis of the diffraction problem using modal methods. Based on the conclusions of that study, the modal field should possess the following properties:

(i) the eigenvalues β_m should be real-valued,

(ii) the eigenfunctions u_m may be chosen to be real-valued,

(iii) the u_m are orthogonal over the aperture in the sense that

$$\int_{-a}^{a} u_m(x,0)\, u_n(x,0)\, dx = 0, \quad \beta_m \neq \beta_n.$$

(Appendix 3 elucidates the latter property.)

Expanding $u_m(r,\theta)$ over the complete set of functions $\{\exp(i\ell\theta)\}$ to give its angular dependence, and knowing that u_m must be finite at the origin, the appropriate solution of the wave equation is an expansion in terms of Bessel functions of the form

$$u_m(r,\theta) = \sum_{\ell=-\infty}^{\infty} g_{m\ell}\, J_\ell(kr)\, \exp(i\ell\theta) \qquad ...(6.8)$$

where the $g_{m\ell}$ are expansion coefficients. These must be identified before the modal field can be matched to the plane-wave field - hence the need for the third constraint on the mode functions. This should be compared with the treatment of the triangular profile where each mode is a *discrete* term involving a Bessel function.

The $u_m(r,\theta)$ are real-valued functions, and so equation (6.8) implies that

$$\bar{g}_{m\ell} = (-1)^{\ell} g_{m,-\ell} \qquad \ldots(6.9)$$

where it is noted that g_{m0} is real. Inserting the boundary condition given by equation (6.5) into the expression for $u_m(a,\theta)$ from equation (6.8), yields

$$g_{m\ell} = \frac{1}{2\pi J_{\ell}(ka)} \int_0^{\pi} u_m(a,\theta) \exp(-i\ell\theta)\, d\theta. \qquad \ldots(6.10)$$

To simplify this expression, $u_m(a,\theta)$ is expanded as a Fourier series of period π,

$$u_m(a,\theta) = \sum_{j=-\infty}^{\infty} c_{mj} \exp(2ij\theta) \qquad \ldots(6.11)$$

where the real nature of $u_m(a,\theta)$ demands that

$$\bar{c}_{mj} = c_{m,-j}. \qquad \ldots(6.12)$$

Substitution of equation (6.11) into equation (6.10) then gives

$$g_{m\ell} = \frac{1}{2\pi J_{\ell}(ka)} \sum_{j=-\infty}^{\infty} c_{mj} \int_0^{\pi} \exp\left[i\theta(2j-\ell)\right]\, d\theta$$

which reduces to

$$\text{(i)} \quad g_{m\ell} = \frac{c_{m\ell}}{2J_{\ell}(ka)}, \qquad \ell \text{ even} \qquad \ldots(6.13)$$

$$\text{(ii)} \quad g_{m\ell} = \frac{i}{\pi J_{\ell}(ka)} \sum_{j=-\infty}^{\infty} \frac{c_{mj}}{(2j-\ell)}, \qquad \ell \text{ odd}.$$

The Fourier coefficients c_{mj} can now be evaluated by invoking the impedance condition of equation (6.6). Substitution of expansion (6.8) into that condition gives

$$\frac{i}{r} \sum_{\ell=-\infty}^{\infty} \ell g_{m\ell} J_\ell(kr) = \beta_m \sum_{\ell=-\infty}^{\infty} g_{m\ell} J_\ell (kr), \quad \theta = 0 ,$$

which on manipulation with the aid of the Bessel function recurrence relation,

$$J_\nu(z) + J_{\nu+1}(z) = \frac{2\nu}{z} J_\nu(z)$$

finally yields

$$\sum_{\ell=-\infty}^{\infty} J_\ell(kr) \left[g_{m,\ell+1} + g_{m,\ell-1} + \frac{2i\beta_m}{k} g_{m\ell}\right] = 0.$$

By expanding this expression and collecting terms, it is straight-forward to derive the equations

$$\text{(i)} \quad Im\ (g_{m1}) = \frac{-\beta_m}{k} g_{m0} , \quad \ell = 0$$

$$\text{(ii)} \quad Im\ (g_{m,\ell+1}) + Im\ (g_{m,\ell-1}) = \frac{-2\beta_m}{k} Re\ (g_{m\ell}), \ \ell \geqslant 1. \qquad \ldots(6.14)$$

The left-right symmetry of the profile is now exploited and the problem divided into two parts - one for "even" modes and the other for "odd" modes, where these terms are defined by the relations

$$\text{(i)} \quad u_m(r,\theta) = u_m(r,\pi-\theta) , \quad \text{even modes}$$

$$\text{(ii)} \quad u_m(r,\theta) = -u_m(r,\pi-\theta) , \quad \text{odd modes.} \qquad \ldots(6.15)$$

Even Modes:

For this case it is easily shown that the Fourier coefficients satisfy the relation

$$c_{mj} = c_{m,-j} . \qquad \ldots(6.16)$$

In light of equation (6.12) this implies that the c_{mj} are real-valued for even modes.

On expanding equation (6.15(i)) it follows that

$$g^e_{m\ell} = g^e_{m,-\ell} \quad , \qquad \ldots(6.17)$$

where the superscript "e" designates even modes. This relation, together with equation (6.9), infers that the $g^e_{m\ell}$ are real for ℓ even and imaginary for ℓ odd. By inserting this information into equation (6.14), the latter becomes

$$\begin{aligned} &(i) \quad g^e_{m1} = \frac{-\beta_m g^e_{m0}}{k} \quad , \qquad \ell = 0 \\ &(ii) \quad g^e_{m,2\ell+1} + g^e_{m,2\ell-1} = \frac{-2i\beta_m}{k} g^e_{m,2\ell} \quad , \quad \ell \geqslant 1. \end{aligned} \qquad \ldots(6.18)$$

If the expressions for $g^e_{m\ell}$ from equation (6.13) are substituted into equations (6.18), and the result simplified, the final equations are

$$\sum_{j=1}^{\infty} c_{mj} \left(\frac{J_0(ka)}{J_1(ka)} \frac{4}{4j^2-1} \right) - 2c_{m0} \frac{J_0(ka)}{J_1(ka)} = \frac{-\pi\beta_m}{k} c_{m0} \quad , \quad \ell = 0$$

and

$$\begin{aligned} &\sum_{j=1}^{\infty} c_{mj} \left(\frac{1}{J_{2\ell+1}(ka)} \frac{2(2\ell+1)}{4j^2-(2\ell+1)^2} + \frac{1}{J_{2\ell-1}(ka)} \frac{2(2\ell-1)}{4j^2-(2\ell-1)^2} \right) J_{2p}(ka) \\ &\quad - c_{m0} \left(\frac{1}{J_{2\ell+1}(ka)} \frac{1}{(2\ell+1)} + \frac{1}{J_{2\ell-1}(ka)} \frac{1}{(2\ell-1)} \right) J_{2p}(ka) \\ &\quad = \frac{-\pi\beta_m}{k} c_{m\ell} \quad , \quad \ell \geqslant 1. \end{aligned} \qquad \ldots(6.19)$$

Odd Modes:

The Fourier coefficients are now linked by the relation

$$c_{mj} = -c_{m,-j} \qquad \ldots(6.20)$$

which implies that the c_{mj} are imaginary except for c_{m0} which is zero.

Combining equations (6.15(ii)) and (6.9) gives

$$g^{o}_{m\ell} = g^{o}_{m,-\ell} \qquad \ldots(6.21)$$

which implies the $g^{o}_{m\ell}$ are imaginary for ℓ even and real for ℓ odd.

Manipulation of equations (6.14) and (6.13) results in an equation for odd modes, which corresponds to equations (6.19) for even modes, namely

$$c_{m\ell}\ \frac{J_{2\ell+1}(ka)}{J_{2\ell}(ka)} + c_{m,\ell+1}\ \frac{J_{2\ell+1}(ka)}{J_{2\ell+2}(ka)}$$

$$= \frac{4\beta_m}{k\pi} \sum_{j=1}^{\infty} \frac{4j}{4j^2-(2\ell+1)^2}\ c_{mj} \quad , \qquad \ell \geqslant 1. \qquad \ldots(6.22)$$

Equations (6.19) and (6.22) now represent two infinite eigenvalue equations, which may be solved numerically for the eigenvalues β_m and Fourier coefficients (eigenvectors) c_{mj}. (It is noted, that depending on the method employed, the eigenvalues themselves are not necessarily required for the remainder of the solution.)

The expansion coefficients $g_{m\ell}$ may now be evaluated by substituting the values for the c_{mj} into equation (6.13). The modal functions $u_m(r,\theta)$, as expressed by equation (6.8), are then fully determined and substitution of this equation into equation (6.3) specifies the field for the groove region as

$$E^{M}(r,\theta) = \sum_{m=1}^{\infty} a_m \sum_{\ell=-\infty}^{\infty} g_{m\ell}\ J_{\ell}(kr)\ \exp(i\ell\theta) \quad . \qquad \ldots(6.23)$$

6.2.2.3 *Field Matching*

The field amplitudes a_m and A_p are resolved by matching the expansions (6.1) and (6.23) along the interface represented by $y = 0$. The conditions of continuity of the electric and magnetic fields across this interface are expressed by

$$\text{(i)} \quad E^R(x,0) = \begin{cases} E^M(x,0) , & -a < x < a \\ 0 , & a < x < d-a \end{cases}$$

and ...(6.24)

$$\text{(ii)} \quad \left.\frac{\partial E^R(x,y)}{\partial y}\right|_{y=0} = \left.\frac{\partial E^M(x,y)}{\partial y}\right|_{y=0} , \quad -a < x < a$$

Consider initially the continuity of the field. The modal field on $y = 0$ is split into its symmetric and anti-symmetric parts, giving

$$E^M(x,0) = \sum_{m=1}^{\infty} a_m^e \sum_{\ell=-\infty}^{\infty} g_{m\ell} J_\ell(k|x|) + \varepsilon(x) \sum_{m=1}^{\infty} a_m^o \sum_{\ell=-\infty}^{\infty} g_{m\ell}^o J_\ell(k|x|) \quad ...(6.25)$$

$$\text{where} \quad \varepsilon(x) = \begin{cases} 1 , & x \geqslant 0 \\ -1 , & x < 0. \end{cases} \quad ...(6.26)$$

By using the orthogonality properties of the functions $\{\exp(i\alpha_p x)\}$, expansion of equation (6.24(i)) gives

$$\delta_{o,p} + A_p = \sum_{m=1}^{\infty} a_m^e \sum_{\ell=-\infty}^{\infty} g_{m\ell}^e I_{\ell p}^e + \sum_{m=1}^{\infty} a_m^o \sum_{\ell=-\infty}^{\infty} g_{m\ell}^o I_{\ell p}^o \quad ...(6.27)$$

where $I_{\ell p}^e$ and $I_{\ell p}^o$ are inner-products defined by

$$\text{(i)} \quad I_{\ell p}^e = \frac{2}{d} \int_0^a J_\ell(kx) \cos(\alpha_p x)\, dx$$

$$\text{(ii)} \quad I_{\ell p}^o = -\frac{2i}{d} \int_0^a J_\ell(kx) \sin(\alpha_p x)\, dx. \quad ...(6.28)$$

Now consider the continuity of the field derivative. Because the Bessel function has no useful orthogonality properties over [0,a], equation (6.24(ii)) is first expanded and multiplied by $J_q(k|x|)$. The result is then integrated over the groove aperture, giving

$$-\chi_0 \overline{I^e_{q0}} + \sum_{p=-\infty}^{\infty} \chi_p A_p \overline{I^e_{qp}} = \sum_{m=1}^{\infty} a^e_m \sum_{\ell=-\infty}^{\infty} \ell\, g^e_{m\ell} Q_{\ell q} \qquad ...(6.29)$$

where the mode coupling coefficient $Q_{\ell q}$ is defined by

$$Q_{\ell q} = \frac{2}{d} \int_0^a \frac{J_\ell(kx)\, J_q(kx)}{x}\, dx. \qquad ...(6.30)$$

(Note: The integral $Q_{\ell q}$ can be easily evaluated analytically in the case $\ell \neq q$ [6.3]. This provided the motive for dealing with equation (6.24(ii)) in the above manner. An alternative method involves the use of equation (6.6) and the orthogonality properties of the u_m. Both methods have been implemented numerically and found to yield identical results, but with the former method requiring less computer time.)

Through the choice of an even sampling function, equation (6.29) contains no information concerning the odd modes and so the above procedure is repeated with the odd sampling function, $\varepsilon(x)\, J_q(k|x|)$, to give

$$-\chi_0 \overline{I^o_{q0}} + \sum_{p=-\infty}^{\infty} \chi_p A_p \overline{I^o_{qp}} = \sum_{m=1}^{\infty} a^o_m \sum_{\ell=-\infty}^{\infty} \ell\, g^o_{m\ell} Q_{\ell q}\,. \qquad ...(6.31)$$

Eliminating A_p by substituting equation (6.27) into equations (6.29) and (6.31), produces the coupled pair of linear equations,

$$\sum_{m=1}^{\infty} a_m^e \left[\sum_{p=-\infty}^{\infty} \left\{ \chi_p \overline{I_{qp}^e} \left(\sum_{\ell=-\infty}^{\infty} g_{m\ell}^e I_{\ell p}^e \right) \right\} - \sum_{\ell=-\infty}^{\infty} \ell \, g_{m\ell}^e Q_{\ell q} \right]$$

$$+ \sum_{m=1}^{\infty} a_m^o \left[\sum_{p=-\infty}^{\infty} \left\{ \chi_p \overline{I_{qp}^e} \left(\sum_{\ell=-\infty}^{\infty} g_{m\ell}^o I_{\ell p}^o \right) \right\} \right] = 2\chi_0 \overline{I_{q0}^e}$$

and ...(6.32)

$$\sum_{m=1}^{\infty} a_m^e \left[\sum_{p=-\infty}^{\infty} \left\{ \chi_p \overline{I_{qp}^o} \left(\sum_{\ell=-\infty}^{\infty} g_{m\ell}^e I_{\ell p}^e \right) \right\} \right]$$

$$+ \sum_{m=1}^{\infty} a_m^o \left[\sum_{p=-\infty}^{\infty} \left\{ \chi_p \overline{I_{qp}^o} \left(\sum_{\ell=-\infty}^{\infty} g_{m\ell}^o I_{\ell p}^o \right) \right\} \right.$$

$$\left. - \sum_{\ell=-\infty}^{\infty} \ell \, g_{m\ell}^o Q_{\ell q} \right] = 2\chi_0 \overline{I_{q0}^o} \, .$$

Upon truncation to finite limits, this system may be solved numerically for the mode amplitudes a_m^e and a_m^o, thus facilitating recovery of the order amplitudes A_p from equation (6.27).

6.2.3 Solution of the Diffraction Problem for S Polarization

The description of the analysis for S polarization is confined to an outline of the changes to the treatment for P polarization. Allowing for a re-definition of the order and mode amplitudes as B_p and b_m respectively, equations (6.1) to (6.9) are unchanged, except for the boundary condition of equation (6.5) which must be re-written as

$$u_m'(a,\theta) \equiv \frac{\partial u_m(a,\theta)}{\partial r} = 0 \, , \qquad \pi < \theta < 2\pi. \qquad ...(6.33)$$

Insertion of this condition into the expression for $u_m'(r,\theta)$, derived from equation (6.8), yields

$$g_{m\ell} = \frac{1}{2\pi k J_\ell'(ka)} \int_0^{\pi} u_m'(a,\theta) \exp(-i\ell\theta) \, d\theta. \qquad ...(6.34)$$

By now expanding $u_m'(a,\theta)$ as a Fourier series of the form

$$u_m'(a,\theta) = \sum_{j=-\infty}^{\infty} c_{mj} \exp(2ij\Theta) \qquad ...(6.35)$$

the determination of the $g_{m\ell}$ parallels the treatment described for P polarization from equation (6.12) to equation (6.22), but with $J_\ell(ka)$ replaced by $kJ_\ell'(ka)$.

The final expression for the magnetic field in the groove region is

$$H^M(r,\theta) = \sum_{m=1}^{\infty} b_m \sum_{\ell=-\infty}^{\infty} g_{m\ell} J_\ell(kr) \exp(i\ell\theta). \qquad ...(6.36)$$

Consider now the field matching along y = 0. Because of the different boundary condition for this polarization, it is the continuity of the field derivative on the interval $-a < x < d-a$ which is projected onto the orthogonal set $\{\exp(i\alpha_p x)\}$. The resulting equation is

$$-\chi_0\delta_{0,p} + \chi_p B_p = \sum_{m=1}^{\infty} b_m^e \sum_{\ell=-\infty}^{\infty} \ell\, g_{m\ell}^e J_{\ell p}^e + \sum_{m=1}^{\infty} b_m^o \sum_{\ell=-\infty}^{\infty} \ell\, g_{m\ell}^o J_{\ell p}^o \qquad ...(6.37)$$

where the inner-products $J_{\ell p}$ are given by

$$\text{(i)} \quad J_{\ell p}^e = \frac{2}{d} \int_0^a \frac{J_\ell(kx)}{x} \cos(\alpha_p x)\, dx$$

$$\text{(ii)} \quad J_{\ell p}^o = \frac{-2i}{d} \int_0^a \frac{J_\ell(kx)}{x} \sin(\alpha_p x)\, dx. \qquad ...(6.38)$$

Continuity of the magnetic field on the interval $-a < x < a$ leads to two more equations linking the order and mode amplitudes. These two equations are analagous to equations (6.29) and (6.31) and arise from the use of the two sampling functions $J_\ell(k|x|)/|x|$ and $\varepsilon(x)J_\ell(k|x|)/|x|$ respectively. Substitition of equation (6.37) into those two equations yields

$$\sum_{m=1}^{\infty} b_m^e \left[\sum_{p=-\infty}^{\infty} \left(\frac{\overline{J_{qp}^e}}{\chi_p} \left(\sum_{\ell=-\infty}^{\infty} g_{m\ell}^e J_{\ell p}^e \right) \right) - \sum_{\ell=-\infty}^{\infty} g_{m\ell}^e Q_{\ell q} \right]$$

$$+ \sum_{m=1}^{\infty} b_m^o \left[\sum_{p=-\infty}^{\infty} \left(\frac{\overline{J_{qp}^e}}{\chi_p} \left(\sum_{\ell=-\infty}^{\infty} g_{m\ell}^o J_{\ell p}^o \right) \right) \right] = -\overline{2J_{q0}^e}$$

and ...(6.39)

$$\sum_{m=1}^{\infty} b_m^e \left[\sum_{p=-\infty}^{\infty} \left(\frac{\overline{J_{qp}^o}}{\chi_p} \left(\sum_{\ell=-\infty}^{\infty} g_{m\ell}^e J_{\ell p}^e \right) \right) \right]$$

$$+ \sum_{m=1}^{\infty} \left[b_m^o \left(\sum_{p=-\infty}^{\infty} \frac{\overline{J_{qp}^o}}{\chi_p} \left(\sum_{\ell=-\infty}^{\infty} g_{m\ell}^o J_{\ell p}^o \right) \right) - \sum_{\ell=-\infty}^{\infty} g_{m\ell}^o Q_{\ell q} \right] = \overline{2J_{q0}^o}.$$

From this coupled pair of linear equations, the mode amplitudes b_m^e and b_m^o may be numerically determined as before, after which the diffracted wave amplitude B_p may be reconstructed from equation (6.37).

6.3 APPLICATION OF THE THEORY

6.3.1 The Numerical Implementation

Because the same arguments concerning the implementation of the theory apply for both fundamental polarizations, only those equations pertaining to the solution for P polarization are discussed here.

Two different integrations must be dealt with in the implementation. The first involves the evaluation of the inner-products expressed by equation (6.28). Since no simple analytic form is available for these, they had to be integrated numerically. The second involves the evaluation of $Q_{\ell q}$, as given by equation (6.30). As mentioned earlier, a simplification of this integral exists when $\ell \neq q$ [6.3], i.e.

$$Q_{\ell q} = \frac{2ak}{d(\ell^2 - q^2)} \left[J_\ell(ka)\, J_q'(ka) - J_q(ka)\, J_\ell'(ka) \right] \qquad ...(6.40)$$

where ' is derivative with respect to argument. For $\ell = q$ the integration was performed numerically.

Equations (6.19), (6.22) and (6.32) contain infinite summations over the indices p, m, j, ℓ and q and these must be truncated to finite limits to secure a numerical solution. Only those limits involving p and j are totally independent - the remainder being dependent upon that for j.

The index p is allowed to vary from -P to P making provision for 2P+1 diffraction orders.

The index j is allowed to vary from 0 to L-1 and so ideally equations (6.19) and (6.22) would provide L real eigensolutions. However, since the matrices involved are not symmetric, their truncation does not guarantee real solutions and both real and complex solutions are possible. In practice it is found that approximately 30% of the solutions are real, and if this number is designated by M ($M \leqslant L$) then there exists a total of 2M modes to be included. The modal index m is thus permitted to run from 1 to M. Reference to equations (6.13) reveals that the index ℓ is restricted to the range from 0 to 2L+1, while from equation (6.32) it is seen that q must vary from 0 to M-1.

Investigation with increasing values of P and L has shown that for satisfactory convergence, as indicated by the tests described in the next section, values for P and L of about 8 and 14 respectively are desirable. However, these values were not always obtainable on the available computer for some combinations of wavelength and groove radius. This is because the Bessel function calculations for $J_{\ell}(ka)$ were found to underflow to zero for large values of ℓ. Thus, for the majority of the results presented here, L = 12 is the appropriate limit with M = 4 being a typical figure for the resulting number of real eigensolutions. Consequently, computations have generally included 8 modes and 17 orders to characterise the field. These values are found to give quite satisfactory results for wavelengths down to 0.4 periods.

6.3.2 Verification of the Formalism

Numerical convergence of the method has been tested using relations of energy conservation, reciprocity and phase symmetry and also by the comparison of efficiencies with those generated by an alternative theory.

Unlike the situation for the lamellar grating, energy conservation is not analytic. For the numbers of order and mode terms mentioned in the previous section, energy conservation is found to be satisfied to within 0.5% over the spectral ranges considered, where up to three orders are propagating.

The Reciprocity Theorem has been tested for an incident beam of wavelength 0.6d and an angle of incidence of 30^{o}. For these parameters three orders are propagating. The two reciprocity comparisons have revealed efficiency differences of 0.2% in the -1 order and 0.1% in the -2 order. These figures are approximately equal to the energy defects (the discrepancy between total energy sum and unity) encountered, and so along with other similar checks, these calculations have shown the Reciprocity Theorem to be satisfied within the bounds of accuracy established by the numerical solution.

A third check on the results has been provided by the phase relations discussed in Chapter 2. For 17 orders and 8 modes the long-wavelength relations were found to be satisfied to four figures of accuracy. Results of -1 Littrow phase tests are shown in Table 6.1. These are slightly inferior to the long-wavelength results but are nevertheless quite satisfactory, with the P polarization results conforming the better. General observations to be made regarding the common phase properties (2.58) to (2.59) are (i) phase agreement is usually better than 0.5^{o}, except near regions of rapid efficiency fluctuation where this figure

TABLE 6.1

-1 Littrow Symmetry Properties of the Semi-Circular Groove Grating.

Intensity and phase values of the field amplitudes are tabulated for verifying agreement with the symmetry relations of Chapter 2. The equation number of the appropriate relation is given in the final column.

Groove Parameters: $d = 1.0$, $a = 0.4$
Mounting Parameters: $\lambda = 1.4$, $\phi = 44.427°$
Number of Expansion Terms: $P = 8$, $L = 12$, $M = 4$.

	P polarization	S polarization	Equation Number
$\|R_0\|^2$, $\arg(R_0)$	.5789, -122.92	$.3034\times10^{-3}$, -94.44	2.60
$\|R_{-1}\|^2$, $\arg(R_{-1})$	.4208, -32.87	.9996, 175.71	2.60, 2.61 2.62
$\|R_1\|^2$, $\arg(R_1)$	$.4551\times10^{-1}$, -63.11	$.6318\times10^{-3}$, -66.90	
$\|R_{-2}\|^2$, $\arg(R_{-2})$	$.6359\times10^{-2}$, 40.35	$.6126\times10^{-3}$, -117.11	
$\frac{1}{2}\arg(R_0+R_{-1})$	41.22	88.35	2.58,2.59
$\frac{1}{2}\arg(R_0-R_{-1})$	-81.67	-2.64	2.58,2.59
$\arg(R_1+R_{-2})$	-41.39	88.20	2.58
$\arg(R_1-R_{-2})$	-81.61	-2.94	2.58
$\arg(a_m^e)$, m = 1,2,3	-41.21,-41.05,-40.98	88.36,88.25,89.38	2.59
$\arg(a_m^o)$, m = 1,2,3	-171.65,-171.56,-171.67	84.33,84.73,81.76	2.59
$\cos^2[\arg(a_1^e)-\arg(a_1^o)]$	.4207	.9951	2.61
$\arg(a_1^e)+\arg(a_1^o)$	-32.86	172.69	2.62

can worsen to 3^{o}, and (ii) the phases of the lower order modes are found to more accurately meet the constraints than are those of the higher order modes. However, the latter are found to improve in cases where it is numerically possible to increase M.

Although the above tests have indicated reasonable accuracy for the results, it has been observed that in certain circumstances, when these tests were well-satisfied, the efficiency could still alter by an amount exceeding the energy defect when more modal terms were included. This shows that the energy defect is not sufficient indication of the true error in the efficiencies and it was therefore valuable to compare the efficiencies predicted by this formalism with those provided by an alternative method. This was done by computing spectra using a programme based on a well-proven integral formalism [6.4, 6.5]. Although the latter method is not well suited to gratings with grooves having vertical walls, it was found to be adequate for the semi-circular profile, and has provided efficiencies which satisfy energy conservation to within 3%.

Comparisons between the two methods were made for both normal incidence and -1 Littrow mounting configurations. In the first case, agreement is excellent for both P and S polarizations over the entire wavelength range $0.3 < \lambda/d < 1.0$, even in the vicinity of a Wood anomaly near $\lambda/d = 0.5$. Slight differences in efficiency, which occur between the two methods, are too small to be shown graphically. In the case of the -1 Littrow mounting, discrepancies are still small, but are slightly larger than for the previous mounting. Figure 6.2 displays the -1 Littrow comparison for groove radii of $a/d = 0.10$ and 0.25. As expected, the maximum discrepancies occur in regions of Wood and resonance anomalies. For S polarization they also occur near passing-off, where again efficiency changes rapidly. Excluding these areas (where agreement is nevertheless satisfactory), the maximum discrepancy for P polarization

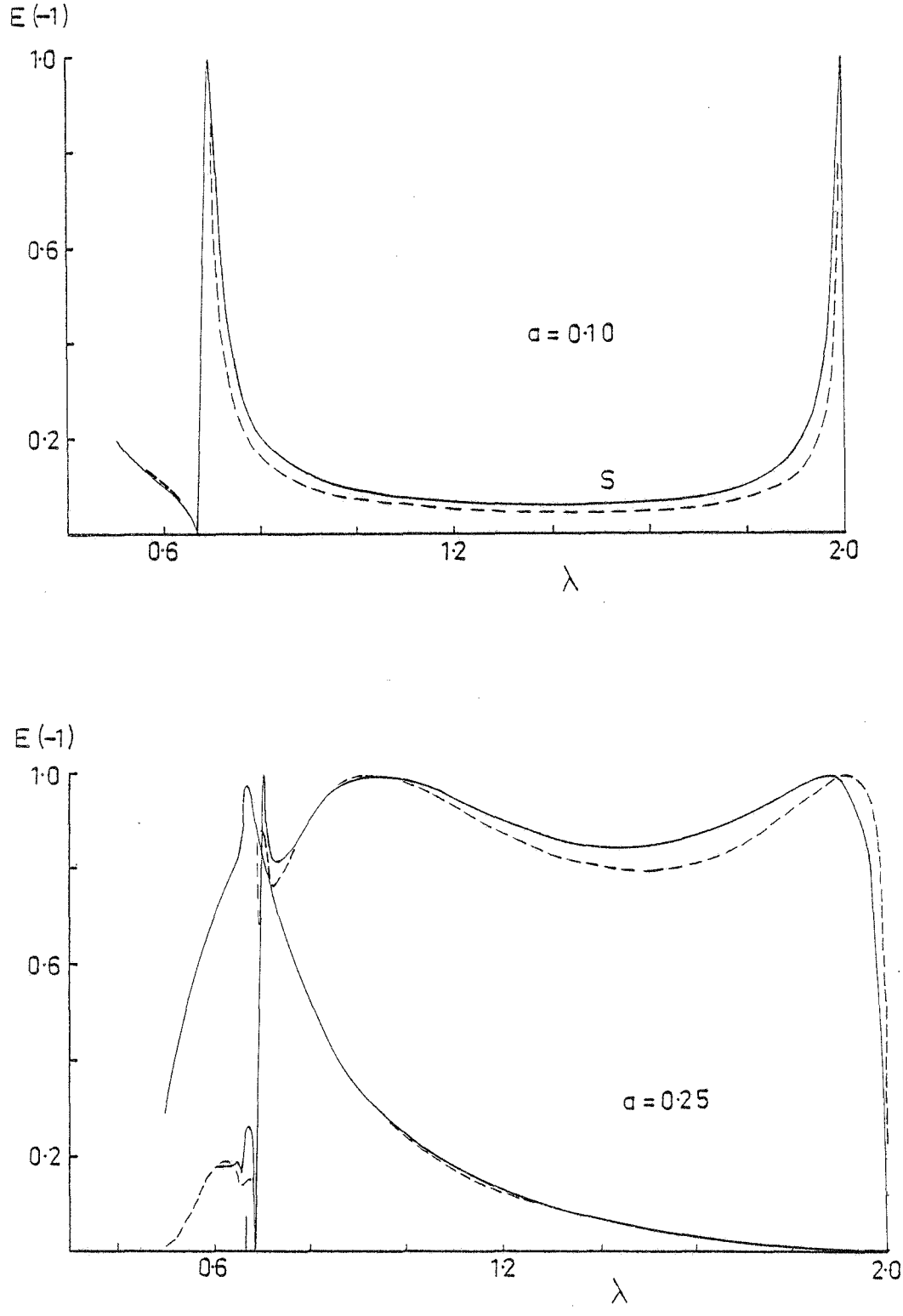

Figure 6.2 First-order Littrow efficiency curves for the semi-circular groove grating (d=1.0).
(———) Modal theory P=8, L=12, M=4
(- - - -) Integral theory.

is about 2% and for S polarization it is about 6%. It should be noted in respect of these results, that energy defects for the integral formalism were often found to be slightly inferior to those of the modal formalism.

Overall then, it is encouraging that both the modal and integral theories similarly describe the behaviour of the grating, even in the regions of sharp anomalies. This, along with the other test results presented, justifies complete confidence in the formalism.

6.4 DIFFRACTION PROPERTIES

6.4.1 Efficiency Spectra

The aim of the investigation described here, was to assess the overall performance of the semi-circular groove grating, particularly in relation to the performance of reflection gratings with alternative profiles. To this end, a comprehensive study was made of diffracted order efficiency for both the normal incident and -1 Littrow mountings for a range of groove radii from 0.1d to the maximum of 0.5d. These spectra, which are contained in Appendix 4, were computed using typical values for P and L of 8 and 14 respectively. The lower limit on the wavelength range considered was usually governed by the accuracy with which energy conservation was satisfied. The energy defect was not permitted to exceed 1%.

Because the -1 Littrow mount is considered the more interesting from a practical viewpoint, this has received the most attention and Figure 6.3 illustrates three efficiency curves for both polarizations over the bandwidth $0.5 < \lambda/d < 2.0$. This encompasses the useful region between the Rayleigh wavelengths $\lambda_R = \frac{2}{3} d$ and $\lambda_R = 2.0d$ where only the -1 and 0 orders are propagating.

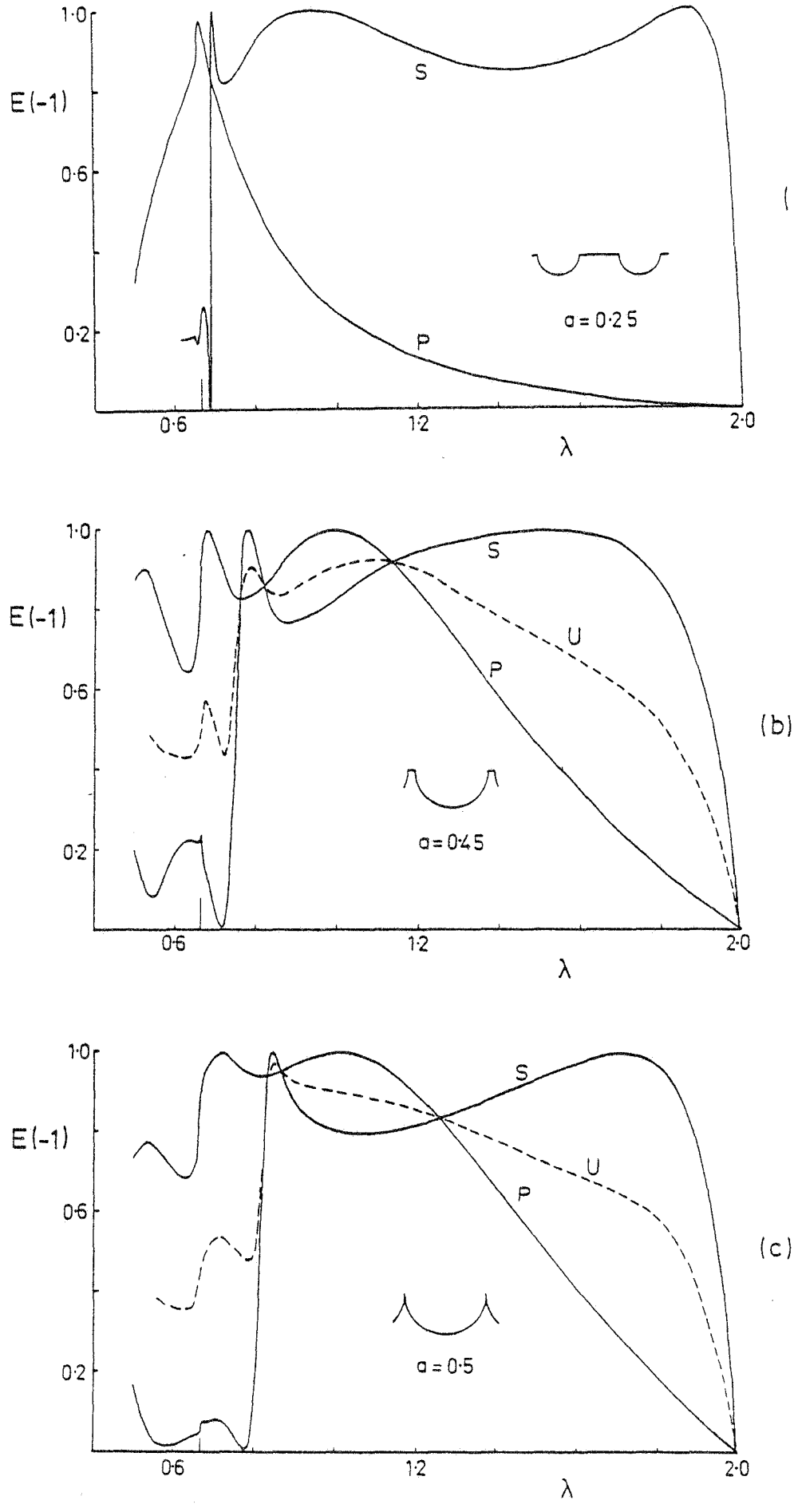

Figure 6.3 First-order Littrow efficiency curves for S, P and U polarizations for the semi-circular groove grating (d=1.0).

Figure 6.3(a) contains the spectra for a/d = 0.25. This represents the lowest value of normalised groove radius for which P polarization has an efficiency blaze of 100% between the two Rayleigh wavelengths. As a/d is increased beyond 0.25, the spectra for this polarization react similarly to those for other profiles such as the sinusoidal, triangular and lamellar profiles [6.5, Appendix 1]. That is, the blaze peak moves out from $\lambda_R = \frac{2}{3}$ d and towards longer wavelengths as the groove depth increases. Under the influence of a second peak, which emerges from the Rayleigh wavelength at a groove depth of 0.4d, the first peak gradually broadens and eventually combines with that peak for large groove depths. Consequently, P polarization exhibits its best performance for the largest possible groove radius of a = d/2. This is illustrated in Figure 6.3(c).

As expected, the above blaze properties are inferior to those for S polarization, which has a good blaze action for a normalised groove radius ranging from 0.22 to 0.5. In fact over this range, the efficiency in the -1 order surpasses 70% over a continuous normalised wavelength band of not less than 1.1.

As is the case with the sinusoidal profile grating, the -1 Littrow efficiency spectra for the semi-circular profile grating depend only on the wavelength and the groove depth (equal to the groove radius in this instance). Hence, a procedure paralleling that of McPhedran *et al.* [6.6] was found appropriate to ascertain the groove radius which yields optimum efficiency blazewidth for S and U polarizations. (The latter denotes "unpolarized" radiation whose efficiency is simply the average of P and S efficiencies.) Thus by calculating the blazewidths for various minimum efficiency levels, it was found that for the 90% level, the optimum groove radii for S and U polarizations are 0.27d and 0.43d

respectively. For the 80% level these figures change only slightly to become 0.25d and 0.45d. The latter figures correspond to the excellent normalised blazewidths of 1.25 and 0.64 respectively. While the tolerance on the groove radius to give these figures is fairly critical for S polarization, it is not for U polarization where a fair degree of latitude is permissable. Figure 6.3(b) displays the efficiency curves for P, S and U polarizations for a groove radius of a/d = 0.45, which is the optimum for U polarization.

Apart from the good blaze action, a dominant feature of the curves in Figure 6.3 is the occurrence of strong S-type resonances visible just above the Rayleigh wavelength, $\lambda_R = \frac{2}{3} d$. It is these phenomena which markedly influence the blaze action for S polarization and which are discussed more fully in the next section.

Another notable characteristic of the curves shown in Appendix 4 and Figure 6.3, is their similarity with those which may be obtained for a perfectly-conducting lamellar grating of similar period and having a groove depth h equal to a, and a groove width c equal to 2a. This similarity is not unexpected since the top portions of the groove profiles are similar and they only differ in the lower groove region. For groove depths up to approximately 0.35d, the spectra for the two profiles very closely resemble one another for both polarizations (see Figure 6.4(a)). It is only for greater depths that major differences occur for S polarization. This is because the resonance anomaly moves to longer wavelengths more rapidly in the case of the lamellar grating and has a more pronounced effect in reducing the blazewidth (see Figure 6.4(b) where a/d = 0.45). For all depths, especially larger ones, the semi-circular profile does exhibit a superior blaze action to the lamellar profile. This is especially so for U polarization. It can be concluded therefore, that a 'rounding' of the groove bottom of lamellar gratings would markedly improve their performance.

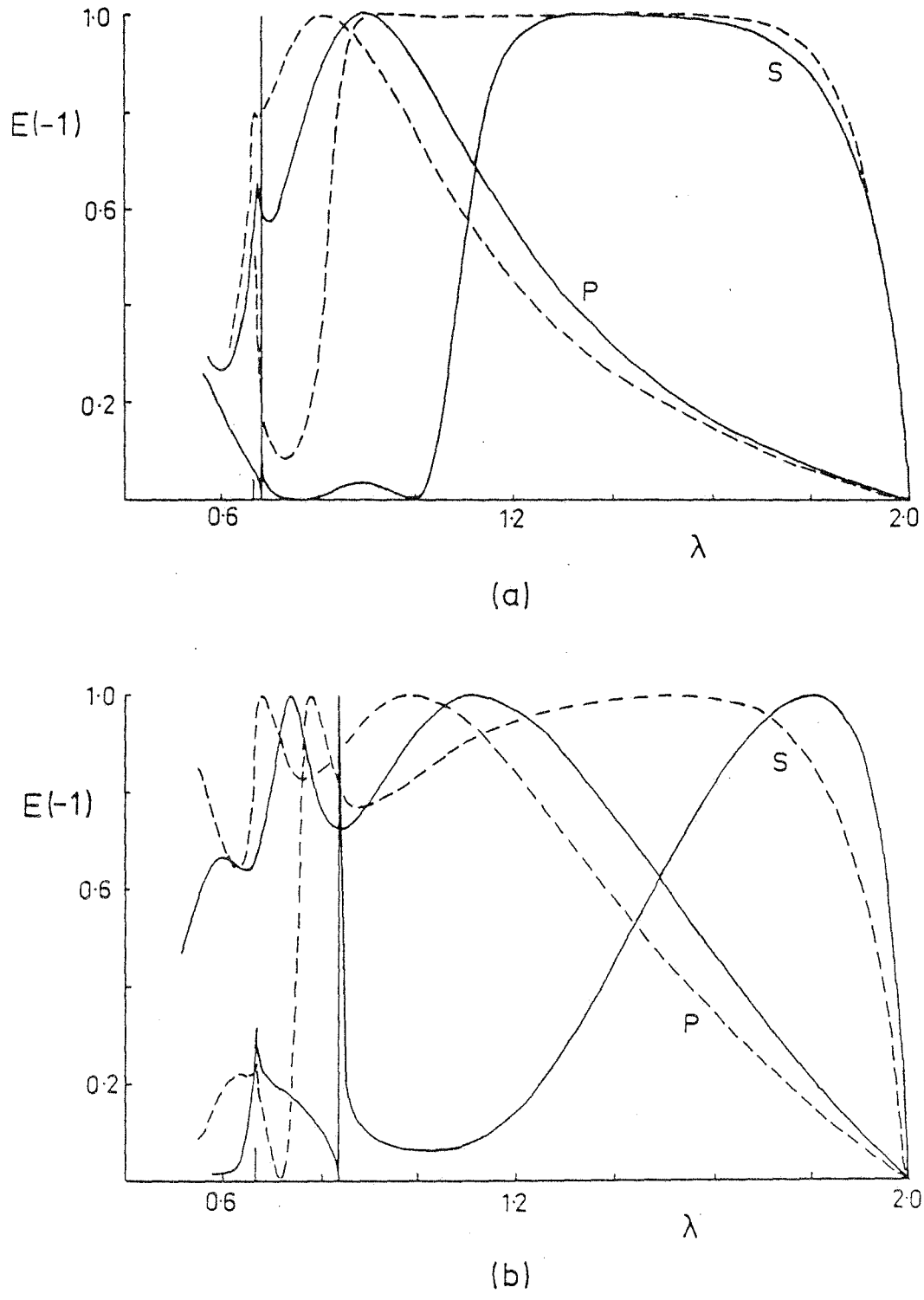

Figure 6.4 Comparison of -1 Littrow mount efficiencies for a semi-circular groove grating (broken line) and a lamellar grating (solid line) of the same aperture width and groove depth (d=1.0).

(a) ⌒ a=0.35, ⌐¬ c=0.7, h=0.35

(b) ⌒ a=0.45, ⌐¬ c=0.9, h=0.45

Thus, as a result of the above investigations, it is evident that the blazing action of this new grating is quite comparable, if not sometimes superior to that of the lamellar, sinusoidal and triangular profile gratings. In fact,overall behaviour (including the location of resonance anomalies as discussed below) is very similar and suggests that studies made by Breidne and Maystre [6.7] on an equivalence rule for different profiles would be equally applicable to the one described here.

6.4.2 Resonance Behaviour

Because the subject of resonance,as it applies to diffraction gratings, has been extensively discussed within Chapter 3, it is the purpose of this section to simply describe the evidence for this phenomenon in the results obtained for the semi-circular groove grating.

The first-order Littrow efficiency curves of Figure 6.3 and Appendix 4 illustrate the presence of resonance anomalies just above the Rayleigh wavelength of $\lambda_R = \frac{2}{3} d$. They are clearly more evident for S polarization, but in keeping with the lamellar grating results it seems probable that the broad blaze peaks for P polarization are the result of the same phenomenon. Also in agreement with past observations, Figures 6.3(a,b,c) show that the resonance peaks emerge from the Rayleigh wavelength and move to longer wavelengths as the groove depth (radius) increases.

Because the eigenvalue formalism presented in this chapter is more complex than that given earlier for the lamellar grating, it is not a straight-forward task to determine the actual resonance conditions. However, because the mechanism for resonance, which involves complex poles in mode amplitudes, appears to be applicable to all gratings, including this one (see Section 3.2.3), a search was made for resonance poles in the field amplitudes. It was expected that they should generally lie farther from the real wavelength axis than those for lamellar grating.

This is because they are manifested in the efficiency spectra as broader features.

The description given below is restricted to the "natural" resonances for S polarization. That is, although the work on the lamellar grating has shown poles exist in the entire (λ, sin ϕ) plane, only those resonances for the normal incidence and -1 Littrow mountings are discussed here.

6.4.2.1 *Normal Incidence Resonances*

For the long-wavelength region, where only the reflected order propagates, Figure 6.5 shows the variation with wavelength of the phase of the even mode amplitudes for a/d = 0.1. The phase drop of nearly 180^{o} indicates the presence of a pole near the real wavelength of $\lambda/d = 1.018$. Similar curves have been obtained for a range of groove radii, and by fitting $B_0(\lambda)$ to the parameterization given by equation (3.24), the complex poles position were located using the procedure described in Section 3.2.2.2. The trajectory of these poles is plotted in Figure 6.6, and reference to Figure 3.6 reveals that this trajectory lies very close to the corresponding lamellar grating trajectory for a constant groove width of c/d = 0.13.

It is interesting to note that the poles occur in an even mode amplitude, as in fact they do for the lamellar grating in a similar configuration. Presumably then, as with that case, it is the lowest order mode which is responsible for these resonances. Unfortunately, a study of mode intensities was unable to confirm this since all intensities are observed to remain approximately equal, even near resonance.

6.4.2.2 *First-Order Littrow Resonances*

For this mounting configuration the pole positions were located using the graphical method described in Section 3.2.2.4. As an example, Figure 6.7 illustrates an Argand plot of the amplitude B_{-1} in the vicinity of a resonance anomaly. Note that in this case, the

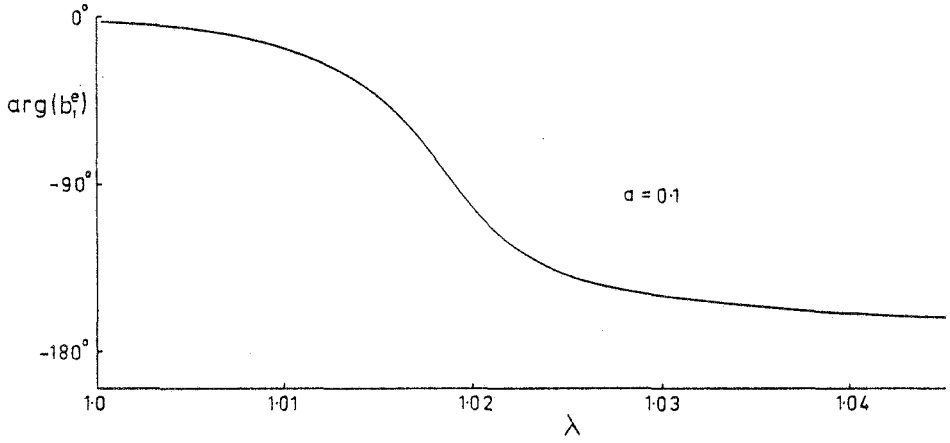

Figure 6.5 Phase variation of the first even-mode amplitude in the vicinity of a resonance anomaly for S polarization and a normal incidence mounting.

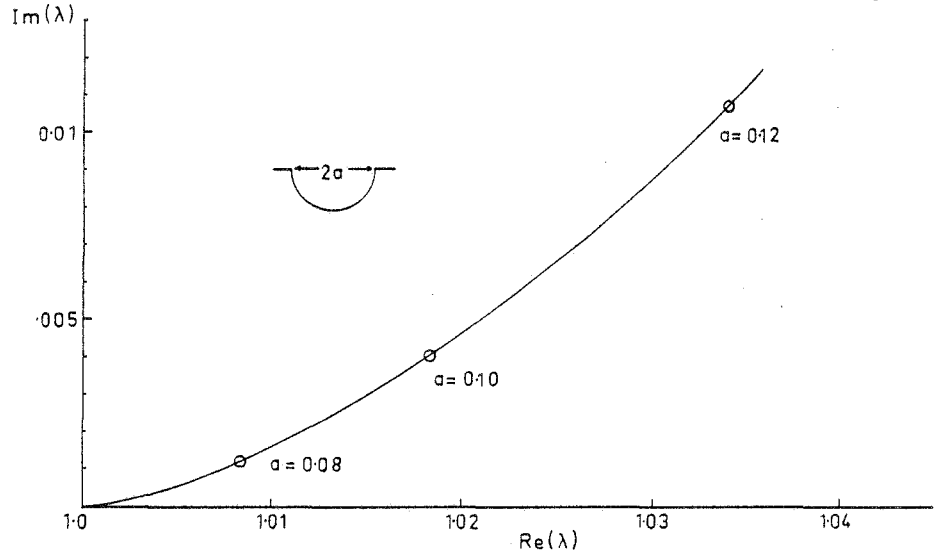

Figure 6.6 Resonance pole trajectory in the complex wavelength plane for the normal incidence mounting and S polarization.

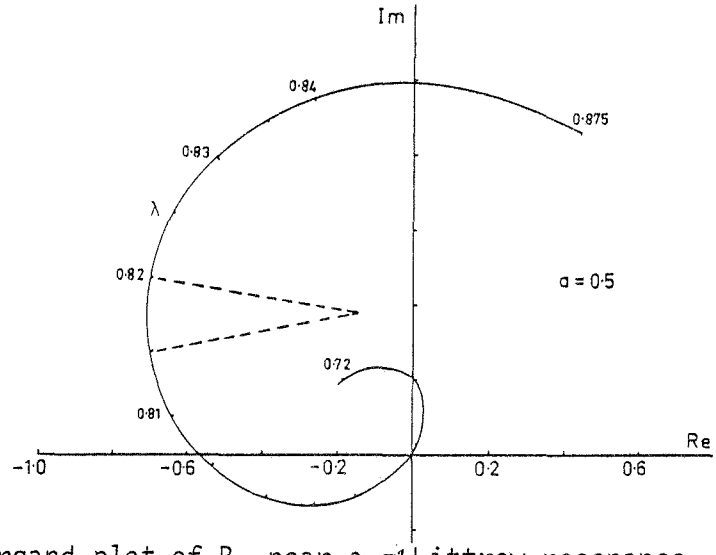

Figure 6.7 Argand plot of B_{-1} near a -1 Littrow resonance anomaly.

resonance is due to an *odd* mode amplitude.

The positions of some poles obtained using the above method are listed in Table 6.2. As foreshadowed earlier, the imaginary components of these positions are in fact generally greater than those encountered for the lamellar grating (see Figure 3.5). For a/d = 0.35 (see Appendix 4) the pole is so far into the complex wavelength plane in fact, that little evidence is seen of it in the efficiency spectrum.

Reference to the values in Table 6.2, and to the efficiency spectra of Figure 6.3, shows that there is excellent correlation between the real part of the pole position and the location of the resonance anomaly. Because of the non-uniform change in the tabulated values with increasing groove depth, it seems probable that the values for a/d > 0.35 correspond to a second pole having emerged from the Rayleigh wavelength. This has not been verified due to insufficient data having been collected. The task would prove difficult however, since the first pole would probably have moved too far into the complex plane to be easily detected.

TABLE 6.2

Resonance Pole Positions for the Semi-Circular Groove Grating.

Resonance pole positions in the complex wavelength plane are given as a function of groove radius for S polarization and the -1 Littrow mounting.

Groove Radius	Resonance Pole Position
0.3	0.76 + 0.008i
0.35	0.83 + 0.032i
0.4	0.69 + 0.009i
0.45	0.76 + 0.014i
0.5	0.82 + 0.013i

6.5 CONCLUSION

A formulation based on a modal expansion has been derived to solve the diffraction problem for a reflection grating whose grooves have a semi-circular profile. The theory includes the introduction of an eigenvalue condition which is of the impedance type, relating the modal field to its normal derivative along the groove-top interface. Validity of the method has been confirmed by the application of numerical tests, as well as by comparing predicted efficiency spectra with those generated by an integral theory.

As expected, the spectra were found not to differ markedly from those produced by more conventional profiles such as those of the sinusoidal and triangular gratings and also the lamellar grating. With regard to spectral behaviour, emphasis was given to the first-order Littrow mounting wherein the performance was found to depend heavily on the polarization of the incident radiation. As is usual, S polarization performs the better of the two polarizations with its optimum blaze being achieved for a groove radius of approximately 0.27 periods, depending on the efficiency threshold required. For unpolarized radiation the optimum radius is 0.45 periods for the 80% efficiency level and this corresponds to a normalised blazewidth superior to that of the sinusoidal grating for the same efficiency level.

The presence of resonance anomalies has been noted in the efficiency spectra. These phenomena are found to have a narrower bandwidth and lie at longer wavelengths than those of the sinusoidal grating. However, in general they are broader and closer to the Rayleigh wavelength than those of the lamellar grating of similar depth. The reason for the above behaviour, recalling the results of Section 3.2.3, is that the singularities in the mode amplitudes for the semi-circular groove grating

lie in the complex plane somewhere between those of the other two types of grating. Because the overall behaviour of the new grating is observed to also lie somewhere between that of the other two, this lends support to the argument that it is the resonance poles in the mode amplitudes which govern the dynamical behaviour of gratings.

By showing itself to possess some of the high blaze characteristics of the lamellar grating, but with the reduced intrusion of resonance anomalies as befits the sinusoidal grating, the semi-circular grating could prove a useful spectroscopic tool. This invites the question as to whether gratings having semi-circular grooves could be made in practice. The task should not be difficult since investigations by Maystre and Petit into certain holographic gratings [6.8] have shown that through the use of a negative photoresist with a sensitivity threshold, these gratings have profiles close to a mirror image of that in Figure 6.1. By making a replica of such a grating, the profile of Figure 6.1 could be recovered.

It is unfortunate that the eigenvalue theory developed here does not allow such a detailed analysis of modal resonances as has the lamellar grating theory. It has however, fulfilled the useful purpose of satisfactorily accounting for the properties of the semi-circular groove grating while also introducing an eigenvalue constraint as a potential tool for further application. (It is in fact employed in the problem discussed in Chapter 7.)

REFERENCES

[6.1] Andrewartha, J.R., Derrick, G.H., McPhedran, R.C., 1981, *Optica Acta,* accepted for publication.

[6.2] Fox, J.R., 1980, *Optica Acta, 27,* 289.

[6.3] Wheeldon, D., 1968, *Tables of Summable Series and Integrals Involving Bessel Functions.* (Holden Day: San Francisco), 83.

[6.4] Pavageau, J., and Bousquet, J., 1970, *Optica Acta, 17,* 469.

[6.5] McPhedran, R.C., 1973, Thesis, University of Tasmania (unpubl.).

[6.6] McPhedran, R.C., Wilson, I.J., and Waterworth, M.D., 1973, *Opt. Commun., 7,* 331.

[6.7] Breidne, M., and Maystre, D., 1980, *Appl. Opt., 19,* 1812.

[6.8] Maystre, D., and Petit, R., 1971, *Opt. Commun., 4,* 25.

Chapter 7

A GENERAL MODAL THEORY FOR REFLECTION GRATINGS

7.1 INTRODUCTION

The only currently available theories which can successfully account for the diffraction from singly-periodic plane gratings with grooves of arbitrary profile are those which are based predominantly on integral [7.1 - 7.4] or differential methods [7.5, 7.6]. As stated earlier in reference to these methods, the mechanism of the diffraction process for gratings with differing groove shapes is obscured in complex mathematics.

Analytic methods, in which the appropriate field quantity is everywhere describable by known expansions, have been shown throughout this thesis to be less complex than the aforementioned methods, while also providing an enhanced explanation of the action of particular gratings. So far, analytic methods have only been rigorously applied to specific grating profiles. These are the rectangular (lamellar) profile which has been discussed extensively in Chapters 2 to 5, the semi-circular groove profile which was the subject of Chapter 6, and the triangular profile studied by Jovicevic and Sesnic [7.7]. A modal expansion method was also employed by Beunen [7.8] in his investigation of the circular-wire grating.

A recent paper by Fox [7.9], concerning the general application of the modal method, verifies the validity of such a treatment wherein the field in the groove region is expanded over a complete set of eigenfunctions and then matched to the diffracted field represented by a plane-wave Rayleigh expansion.

Clearly then, a method based on these principles and applicable to gratings with grooves of general cross-section would be valuable.

Towards such a goal, this chapter reports on an investigation into a new modal expansion technique to solve the classical diffraction problem for perfectly-conducting reflection gratings. Following successful application to the semi-circular profile grating, this formulation incorporates an impedance eigenvalue condition on the mode functions along the groove aperture. As in that case, the eigenvalue is analagous to the quantity D_{mm} used by Fox in reference [7.9].

The theoretical formulation of the scalar-wave problem is given in detail for P polarization in Section 7.2. The subsequent section contains a brief description for S polarization. Section 7.4 is concerned with the numerical implementation of the theory and describes some of the difficulties which were encountered, particularly in the case of gratings with deep grooves. In areas where convergence has been found satisfactory, efficiencies in the diffracted orders have been calculated and compared with those provided by alternative formalisms. This comparison is illustrated for the sinusoidal and the semi-circular profiles in the first-order Littrow mounting, and also for a symmetrical triangular profile in a normal incidence mounting.

In the final section, possible reasons are suggested for the occurrence of instabilities in the numerical application of the formalism. These arise whenever the groove depth-to-period ratio becomes too large, or when an excessive number of modal terms is included in the calculations.

The work presented in this chapter has been reported in a recent paper [7.15].

7.2 THE THEORETICAL FORMALISM FOR P POLARIZATION

7.2.1 Notation and Theoretical Outline

The geometrical configuration for the structure considered is depicted in Figure 7.1. The periodic function, $y = f(x) = f(x+d)$, for all x, has been chosen to represent the surface separating free-space ($y > f(x)$) from the perfectly-conducting grating material ($y \leqslant f(x)$). This function is taken to lie in the lower-half xy plane and is assumed to be continuous and equal to zero on the intervals given by $\ell d + c < x < (\ell + 1)d$ where $\ell = 0, \pm 1, \pm 2 \ldots$ These intervals are referred to as the "land" between the grooves. The minimum value of $f(x)$ represents the overall groove depth h, while the aperture width is c and has a maximum value equal to the period d.

Consider then an incident plane wave, which has its electric vector in the z-direction and its wave-vector $\underline{k}$ lying in the xy plane, to strike the grating at an angle θ to the y-axis. Because the outgoing scattered plane waves also have their electric fields aligned parallel with the grooves, the problem is characterized entirely by the z-component of the electric field. This is a function of x and y only and denoted $E_z(x,y)$. The z-subscript may be omitted and so using the familiar Rayleigh expansion with the temporal dependent term $\exp(-i\omega t)$ suppressed, the total electric field in the free-space region is represented by

$$E^R(x,y) = \exp[i(\alpha_0 x - \chi_0 y)] + \sum_{p=-\infty}^{\infty} A_p \exp[i(\alpha_p x + \chi_p y)] \quad , y \geqslant 0 \qquad \ldots(7.1)$$

where λ is the wavelength,

$k = |\underline{k}| = 2\pi/\lambda$ is the wave-number,

$\alpha_p = k \sin \theta_p = k(\sin \theta + p\lambda/d)$, $\qquad \ldots(7.2)$

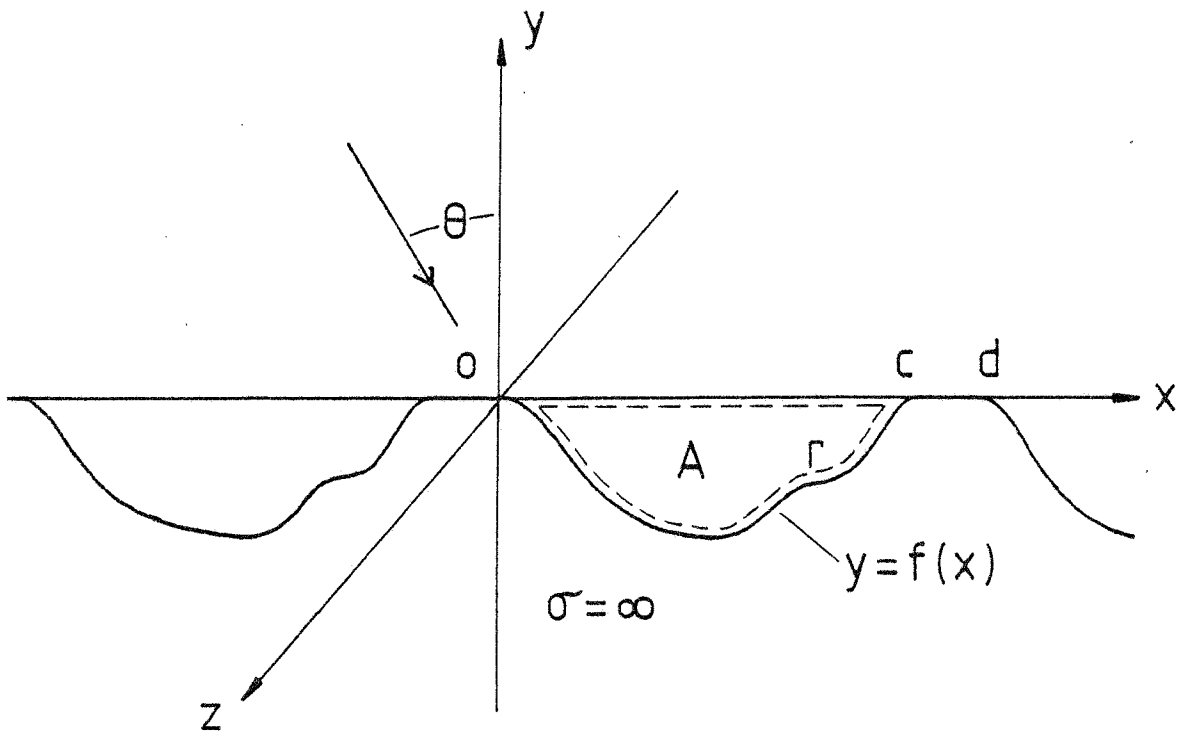

Figure 7.1 The geometry of the diffraction arrangement for the reflection grating with arbitrary groove profile.

$$\text{and} \quad \chi_p = (k^2 - \alpha_p^2)^{\frac{1}{2}}, \quad \sin\theta_p \leq 1 \quad \text{(real orders)}$$
$$= i(\alpha_p^2 - k^2)^{\frac{1}{2}}, \quad \sin\theta_p > 1 \quad \text{(evanescent orders)} \qquad \ldots(7.2)$$

The first term on the right-hand side of equation (7.1) corresponds to the incident wave of unit amplitude while the coefficients A_p are the amplitudes of the diffracted wave-field. In terms of these coefficients, energy propagating in the y-direction is conserved according to the relation

$$\sum_{\substack{\text{real} \\ \text{orders}}} \left(|A_p|^2 \frac{\chi_p}{\chi_0}\right) = 1 \qquad \ldots(7.3)$$

where each term in the expansion on the left is the efficiency in the p^{th} order.

Within the groove region A, the field is expanded in terms of a series of discrete eigenfunctions (modes) $u_m(x,y)$:

$$E^M(x,y) = \sum_{m=1}^{\infty} a_m u_m(x,y) \quad , \quad 0 \leq x \leq c$$
$$f(x) \leq y \leq 0 \qquad \ldots(7.4)$$

where the coefficients a_m are the complex mode amplitudes. Each mode function u_m is chosen to be real-valued [7.9] and must also be a solution of the wave-equation given by

$$\left[\frac{\partial^2}{\partial x^2} + \frac{\partial^2}{\partial y^2} + k^2\right]u(x,y) = 0 \, . \qquad \ldots(7.5)$$

The boundary conditions appropriate to a perfectly-conducting surface must also be satisfied by the mode functions. For P polarization these are represented by the equation

$$u(x,f(x)) = 0, \qquad 0 \leq x \leq c. \qquad \ldots(7.6)$$

The above two constraints are not sufficient to uniquely determine the mode functions and so a third constraint must be imposed. The constraint proposed here has been successfully used in the previous chapter to specify the modal field in the groove region for the semi-circular profile grating. This constraint takes the form of an impedance condition, by demanding that the field along the top of the groove aperture conforms to the relation

$$\frac{\partial u(x,y)}{\partial y} = \beta u(x,y) \ , \quad y = 0 \qquad 0 \leqslant x \leqslant c, \qquad \ldots(7.7)$$

where β is an unknown real eigenvalue.

7.2.2 The Eigenvalue Problem

7.2.2.1 *Specification of the Modal Field*

Based on the wave-guide mode functions used for the perfectly-conducting lamellar grating, a set of real-valued functions $\{\psi_\ell(x,y)\}$ is defined by

$$\psi_\ell(x,y) = \sin\left(\frac{\ell\pi x}{c}\right) \frac{\sin(\mu_\ell y)}{\mu_\ell} \qquad \ell = 1,2,3... \qquad \ldots(7.8)$$

where

$$\mu_\ell = \begin{cases} \left(k^2 - \dfrac{\ell^2\pi^2}{c^2}\right)^{\frac{1}{2}} & , \quad \lambda \leqslant \dfrac{2c}{\ell} \\ \\ i\left(\dfrac{\ell^2\pi^2}{c^2} - k^2\right)^{\frac{1}{2}} & , \quad \lambda > \dfrac{2c}{\ell} \ . \end{cases} \qquad \ldots(7.9)$$

The ψ_ℓ are solutions to the wave-equation (7.5) and are seen to vanish along $y = 0$. Along the same boundary, the functions $\partial\psi_\ell/\partial y$ form an orthogonal set over the interval $0 \leqslant x \leqslant c$.

A set of functions $\{\phi_\ell(x,y)\}$ is now defined by

$$\phi_\ell(x,y) = \frac{\partial\psi_\ell(x,y)}{\partial y} + \beta\psi_\ell(x,y) \ . \qquad \ldots(7.10)$$

By linearity, the ϕ_ℓ are also solutions to the wave-equation while at the same time they satisfy the eigenvalue condition (7.7). Since $\psi_\ell(x,0) = 0$, the functions $\phi_\ell(x,0)$ also form an orthogonal set for $x\in[0,c]$. The mode functions are now expanded in terms of the ϕ_ℓ,

$$u(x,y) = \sum_{\ell=1}^{\infty} g_\ell \, \phi_\ell(x,y) \; . \qquad \ldots(7.11)$$

On insertion of equations (7.10) and (7.8) this expansion becomes

$$u(x,y) = \sum_{\ell=1}^{\infty} g_\ell \, \sin(\frac{\ell\pi x}{c}) [\cos(\mu_\ell y) + \beta \, \frac{\sin(\mu_\ell y)}{\mu_\ell}] \; . \qquad \ldots(7.12)$$

Application of the boundary condition (7.6) now leads to an infinite eigenvalue equation of the form

$$u(x,f(x)) = \sum_{\ell=1}^{\infty} g_\ell \, [G_\ell + \beta H_\ell] = 0 \qquad \ldots(7.13)$$

where β is the eigenvalue, $\underline{g}$ is the corresponding eigenvector and G_ℓ and H_ℓ are real functions of x given by

$$\left.\begin{aligned} G_\ell(x) &= \sin(\frac{\ell\pi x}{c}) \cos(\mu_\ell \, f(x)) \\ H_\ell(x) &= \sin(\frac{\ell\pi x}{c}) \, \frac{\sin(\mu_\ell \, f(x))}{\mu_\ell} \end{aligned}\right\} \quad , \; 0 < x < c \; . \qquad \ldots(7.14)$$

Once the mode boundary problem expressed by equation (7.13) has been solved for β and $\underline{g}$, the modal field is specified in terms of equation (7.12).

7.2.2.2 *The Mode Boundary Problem*

The solution of equation (7.13) has been attempted by two different methods - a point-matching method (P.M.M.) and a Fourier series method (F.S.M.). Both of these methods have been used in the past by such authors as Petit [7.10] and Jiracek [7.11] who were at that time attempting to solve the diffraction problem for triangular and sinusoidal profile

gratings using the now discredited Rayleigh approximation.

A third means for satisfying boundary conditions is to do so in a least-squares sense, whereby the average mismatch across the boundary is minimised. The method has been extensively discussed by Millar [7.12] and an example of its application can be found in the work of Beunen [7.8]. Unfortunately, this proven method cannot be applied to the case in question since there is no known means for formulating a least-squares eigenvalue problem.

Point-Matching Method: This technique simply involves sampling the profile at a discrete number of points $((x_q, f(x_q)), q = 1,2,3,\ldots)$ over a single period. As a result, the boundary conditions are precisely satisfied, but only at the chosen points on the profile. By applying this method, equation (7.13) reduces to the eigenvalue matrix equation

$$(\underline{G} + \beta\underline{H})\underline{g} = 0 \qquad \ldots(7.15)$$

where $\underline{G}$ and $\underline{H}$ are matrices whose elements are given by

$$\left.\begin{aligned} G_{q\ell} &= \sin\left(\frac{\ell\pi x_q}{c}\right) \cos\left(\mu_\ell f(x_q)\right) \\ H_{q\ell} &= \sin\left(\frac{\ell\pi x_q}{c}\right) \frac{\sin\left(\mu_\ell f(x_q)\right)}{\mu_\ell} \end{aligned}\right\} \qquad \ldots(7.16)$$

Following the choice of a suitable points distribution and an appropriate truncation point, the linear system described by equation (7.15) can be solved by numerical means for the eigenvalues β and eigenvectors $\underline{g}$.

Fourier Series Method: This method consists of replacing the function given in the left-hand side of equation (7.13) by a Fourier series, and then satisfying that equation by equating each Fourier coefficient to zero. Because the series must be truncated for numerical implementation, the boundary conditions are nowhere precisely satisfied but are approximately satisfied at all points. Because $u(x, f(x))$ vanishes at $x = 0,c$ it may be expanded in terms of the complete set of functions $\{\sin(\frac{q\pi x}{c})\}$:

$$u(x,\ f(x)) = \sum_{q=1}^{\infty} c_q \sin\left(\frac{q\pi x}{c}\right) . \qquad \ldots(7.17)$$

Equating the Fourier coefficients c_q to zero for q = 1,2,... leads again to an eigenvalue equation in the form of equation (7.15), where the matrix elements $G_{q\ell}$ and $H_{q\ell}$ are now given by

$$\left.\begin{aligned} G_{q\ell} &= \frac{1}{c}\int_0^c \cos\left(\mu_\ell\ f(x)\right) \sin\left(\frac{\ell\pi x}{c}\right) \sin\left(\frac{q\pi x}{c}\right) dx \\ H_{q\ell} &= \frac{1}{c}\int_0^c \frac{\sin\left(\mu_\ell\ f(x)\right)}{\mu_\ell} \sin\left(\frac{\ell\pi x}{c}\right) \sin\left(\frac{q\pi x}{c}\right) dx \end{aligned}\right\} \qquad \ldots(7.18)$$

(Note that in the case where f(x) is an even function of x about c/2, only those matrix elements with $(\ell + q)$ even are non-zero.) Limiting the Fourier series to a finite number of terms allows the eigenvalues and eigenvectors to be evaluated numerically as with the P.M.M.

Labelling the m^{th} solutions of equation (7.15) for the eigenvectors and eigenvalues as g_m and β_m respectively, combination of equations (7.12) and (7.4) shows that the total field in the groove region is expressed by the expansion

$$E^M(x,y) = \sum_{m=1}^{\infty} a_m \sum_{\ell=1}^{\infty} g_{m\ell} \sin\left(\frac{\ell\pi x}{c}\right)\left[\cos(\mu_\ell y) + \beta_m \frac{\sin(\mu_\ell y)}{\mu_\ell}\right] \qquad \ldots(7.19)$$

7.2.2.3 *Orthogonality Properties of the Modes*

Consider the groove region A, enclosed by the contour Γ, as illustrated in Figure 7.1. It is shown in Appendix 3 that application of Green's theorem to this region establishes that the eigenvalues β_m are real, and that modes corresponding to distinct eigenvalues are orthogonal on the interval $0 \leqslant x \leqslant c$ in the sense that

$$\int_0^c u_m(x,0)\, u_n(x,0)\, dx = 0 \quad , \quad m \neq n . \qquad ...(7.20)$$

There is no loss of generality in taking the eigenfunctions u_m corresponding to the real eigenvalues β_m, to also be real.

Substitution of equation (7.12) into equation (7.20) now gives the relation

$$\frac{c}{2} \sum_{\ell} g_{m\ell}\, g_{n\ell} = 0 \quad , \quad m \neq n \qquad ...(7.21)$$

which serves as a check on the orthogonality of the eigenvectors obtained from the numerical computation.

7.2.3 Field Matching

Having specified the electric field in the free-space region by (7.1), and in the groove region by (7.19), it is now possible to solve the diffraction problem, i.e. determine the field amplitudes a_m and A_p. This is accomplished by matching the field and its y-derivative across the interface separating the two regions.

Continuity of E along y = 0, for one period, is expressed by

$$E^R(x,0) = \begin{cases} E^M(x,0) & , 0 \leq x \leq c \\ 0 & , c \leq x \leq d. \end{cases}$$

By expanding this equality, multiplying both sides by $\exp(-i\alpha_p x)$, and finally integrating over the period, one obtains

$$\delta_{0,p} + A_p = \frac{1}{d} \sum_{m=1}^{\infty} a_m \sum_{\ell=1}^{\infty} g_{m\ell}\, I_{\ell p} \qquad ...(7.22)$$

where $I_{\ell p}$ is the inner-product defined by

$$I_{\ell p} = \int_0^c \sin\left(\frac{\ell \pi x}{c}\right) \exp(-i\alpha_p x)\, dx \qquad ...(7.23)$$

and which may be reduced to a closed form similar to equation (2.8).

The y-derivative of E is continuous only on the groove aperture, thus demanding that

$$\left.\frac{\partial E^R(x,y)}{\partial y}\right|_{y=0} = \left.\frac{\partial E^M(x,y)}{\partial y}\right|_{y=0} , \quad 0 \leqslant x \leqslant c.$$

Projection of this equality onto the set of functions $\{\sin(q\pi x/c)\}$ yields

$$-i\chi_0 \bar{I}_{q0} + \sum_{p=-\infty}^{\infty} i\chi_p A_p \bar{I}_{qp} = \frac{c}{2} \sum_{m=1}^{\infty} a_m \beta_m g_{mq} . \qquad ...(7.24)$$

By eliminating A_p between equations (7.22) and (7.24), the following infinite system of linear equations in the a_m is derived:

$$\sum_{m=1}^{\infty} a_m W_{mq} = 2i\chi_0 \bar{I}_{q0} \qquad ...(7.25)$$

where

$$W_{mq} = \sum_{p=-\infty}^{\infty} \left[\frac{i\chi_p \bar{I}_{qp}}{d} \left(\sum_{\ell=1}^{\infty} g_{m\ell} I_{\ell p} \right)\right] - \frac{c\beta_m g_{mq}}{2} . \qquad ...(7.26)$$

Using standard numerical methods, equation (7.25) may be solved for the a_m, after which the plane-wave amplitudes may be reconstructed from equation (7.22). The efficiencies in the propagating orders may then be computed from equation (7.3).

7.3 THE THEORETICAL FORMALISM FOR S POLARIZATION

In this case the only non-zero component of the magnetic field, $H_z(x,y)$, is aligned parallel with the generating axis of the grating. This is then the single unknown function. The treatment is very similar to that for P polarization and so the description is confined to a summary of the essential differences.

The wave-equation is unaltered and so with the exception of equation (7.6) (the boundary condition), equations (7.1) to (7.7) remain unchanged if $E(x,y)$, A_p and a_m are replaced by $H(x,y)$, B_p and b_m respectively.

The appropriate boundary condition stipulates that the normal derivative of H be continuous. The equation analagous to equation (7.6) is therefore

$$n_x \frac{\partial u(x,f(x))}{\partial x} + n_y \frac{\partial u(x,f(x))}{\partial y} = 0, \qquad 0 \leqslant x \leqslant c \qquad \ldots(7.27)$$

where $\underline{n} = (n_x, n_y, 0)$ is a unit vector normal to the grating profile. Its elements are given by

$$n_x = \frac{-f'(x)}{\sqrt{1 + (f'(x))^2}}$$

$$n_y = \frac{1}{\sqrt{1 + (f'(x))^2}} \qquad \ldots(7.28)$$

where ' denotes d/dx.

The function from which the modes are to be generated is now defined as

$$\psi_\ell(x,y) = \cos\left(\frac{\ell\pi x}{c}\right) \frac{\sin(\mu_\ell y)}{\mu_\ell} \qquad \ell = 0,1,2,\ldots \qquad \ldots(7.29)$$

and hence using the previous definition of ϕ_ℓ, the expression equivalent to equation (7.12) for the eigenfunctions is

$$u(x,y) = \sum_{\ell=0}^{\infty} g_\ell \cos\left(\frac{\ell\pi x}{c}\right) \left[\cos(\mu_\ell y) + \beta \frac{\sin(\mu_\ell y)}{\mu_\ell}\right] \qquad \ldots(7.30)$$

Note that the $\ell = 0$ term is now included in the expansion.

In satisfying the mode boundary problem produced by substituting equation (7.30) into equation (7.27), an eigenvalue equation in the same form as equation (7.15) is secured, wherein the matrix elements for the P.M.M. corresponding to equation (7.16) are given by

$$G_{q\ell} = -\mu_\ell n_{y,q} \cos\left(\frac{\ell\pi x_q}{c}\right) \sin\left(\mu_\ell f(x_q)\right) - \frac{\ell\pi}{c} n_{x,q} \sin\left(\frac{\ell\pi x_q}{c}\right) \cos\left(\mu_\ell f(x_q)\right)$$

and $\qquad \ldots(7.31)$

$$H_{q\ell} = n_{y,q} \cos\left(\frac{\ell\pi x_q}{c}\right) \cos\left(\mu_\ell f(x_q)\right) - \frac{\ell\pi}{c} n_{x,q} \sin\left(\frac{\ell\pi x_q}{c}\right) \frac{\sin\left(\mu_\ell f(x_q)\right)}{\mu_\ell}$$

Here $n_{x,q}$, $n_{y,q}$ are obtained if x is replaced by x_q in equation (7.28).

For the F.S.M., a similar treatment to that for P polarization is valid, but with a Fourier cosine series being the appropriate representation. The matrix elements analagous to those of equation (7.18) are derived to be

$$G_{q\ell} = \frac{1}{c} \int_0^c \left[\frac{-\ell\pi}{c} n_x \sin\left(\frac{\ell\pi x}{c}\right) \cos\left(\mu_\ell f(x)\right) - \mu_\ell n_y \cos\left(\frac{\ell\pi x}{c}\right) \sin\left(\mu_\ell f(x)\right)\right] \cos\left(\frac{q\pi x}{c}\right) dx$$

$$H_{q\ell} = \frac{1}{c} \int_0^c \left[\frac{-\ell\pi}{c} n_x \sin\left(\frac{\ell\pi x}{c}\right) \frac{\sin\left(\mu_\ell f(x)\right)}{\mu_\ell} + n_y \cos\left(\frac{\ell\pi x}{c}\right) \cos\left(\mu_\ell f(x)\right)\right] \cos\left(\frac{q\pi x}{c}\right) dx \; . \qquad \ldots(7.32)$$

Again, if $f(x)$ is an even function of x about $c/2$, only those matrix elements with $(p+q)$ even are non-zero.

The total field in the groove region is finally given by the expansion

$$H^M(x,y) = \sum_{m=1}^{\infty} b_m \sum_{\ell=0}^{\infty} g_{m\ell} \cos(\frac{\ell\pi x}{c})[\cos(\mu_\ell y) + \beta_m \frac{\sin(\mu_\ell y)}{\mu_\ell}] \qquad ...(7.33)$$

The field matching along $y = 0$ proceeds as before but with H being continuous only for $0 \leq x \leq c$ while $\partial H/\partial y$ is continuous from $x = 0$ to $x = d$. By projecting the first of these conditions onto the set of functions $\{\cos(q\pi x/c)\}$, and the second onto $\{\exp(-i\alpha_p x)\}$, one obtains the two equations

$$\overline{J}_{q0} + \sum_{p=-\infty}^{\infty} B_p \overline{J}_{qp} = c\varepsilon_q \sum_{m=1}^{\infty} b_m g_{mq} \qquad ...(7.34)$$

and

$$-\delta_{0,p} + B_p = \frac{1}{i\chi_p d} \sum_{m=1}^{\infty} b_m \beta_m (\sum_{\ell=0}^{\infty} g_{m\ell} J_{\ell p}) \qquad ...(7.35)$$

where

$$J_{\ell p} = \int_0^c \cos(\frac{\ell\pi x}{c}) \exp(-i\alpha_p x)\, dx \qquad ...(7.36)$$

and

$$\varepsilon_\ell = \begin{cases} \frac{1}{2}, & \ell \geq 1 \\ 1, & \ell = 0. \end{cases}$$

By inserting equation (7.35) into equation (7.34), the final linear system in the unknown mode amplitudes b_m is derived to be

$$\sum_{m=1}^{\infty} b_m Z_{mq} = 2\overline{J}_{q0} \qquad ...(7.37)$$

where

$$Z_{mq} = \beta_m \sum_{p=-\infty}^{\infty} [\frac{i\overline{J}_{qp}}{d\chi_p} (\sum_{\ell=0}^{\infty} g_{m\ell} J_{\ell p})] + c\varepsilon_q g_{mq} . \qquad ...(7.38)$$

This system is solved numerically as before, with the order amplitudes B_p being recovered from equation (7.35) and efficiency values from (7.3).

7.4 APPLICATION OF THE THEORY

Extensive work on the numerical application of the theory has produced many fruitful results. But at the same time it has unfortunately unearthed limitations which detract from its potential usefulness. This section is concerned with various aspects of the numerical implementation. It includes a description of tests performed on the calculations as well as a discussion of the problems encountered and the attempts made to overcome them. Eigenvalue trajectories are also presented.

7.4.1 Numerical Considerations

Two different forms of integrals need to be evaluated within the implementation. The first one concerns the inner-products given by equations (7.23) and (7.36). These may be dealt with straightforwardly since they are easily converted to simple analytic form. The second type pertains to the use of the F.S.M. and is contained in equations (7.18) and (7.32). These integrals are more difficult to evaluate since unless the profile is composed of linear facets (i.e. $f(x)$ is a piece-wise linear function of x), they do not reduce to analytic form and must be computed numerically. The routine employed for this purpose [7.13] uses adaptive Romberg extrapolation and it was found that great care had to be exercised, especially in the case of deep grooves where instabilities were encountered.

Two truncations of infinite series are also necessary before numerical calculations can be performed. One directly determines the number

of plane-wave terms to be considered while the other indirectly determines the number of modal terms to be considered - the latter being subject to the number of real solutions secured from the solution of the eigenvalue problem. If the formalism is to prove valid, then the calculated solutions for the amplitudes (a_m, b_m) and (A_p, B_p) should converge towards their true values as the truncation limits are extended. Ideally, the accepted limit occurs when successive calculations lie within a desired tolerance and comply with the usual numerical checks of energy conservation, reciprocity and phase properties. For many of the tests implemented, compliance with these criteria was unfortunately not always satisfactory due to the occurrence of numerical problems.

The infinite series contained in equation (7.1) was truncated at $p = \pm P$. No numerical difficulties were encountered in determining a suitable value for P and a value of 8 was usually sufficient when only two or three orders are propagating. This limit allows for a total of $2P + 1 = 17$ orders to be taken into account.

Consider now the truncation of the modal series in equations (7.12) and (7.30). If the P.P.M. is used then the limit on the number of modal terms in these series is equal to the number of profile sample points chosen. If the F.S.M. is selected then the limit equals the number of terms chosen in the Fourier series. In both cases these choices ensure that the matrices G and H are square. Denoting either limit as L, then these matrices have dimension L, making this equal to the maximum possible number of real eigensolutions.

It is noted that the matrix $H^{-1}G$, whose eigenvalues ($-\beta$) are sought via equation (7.15), is asymmetric. For the untruncated matrix all the eigenvalues must be real, but no such guarantee exists when the matrix has finite dimension. Furthermore, there is no assurance that the

eigenvectors form a complete set. As was the case with the semi-circular profile theory, and for reasons of orthogonality discussed in Section 7.2.2.3, only the real eigensolutions were chosen from the total of possible real and complex solutions. This procedure was found to result in the rejection of only a small fraction of the eigensolutions, especially if the F.S.M. was used.

Occasionally with the P.M.M., and for large values of L, say greater than 16, a complex-conjugate pair of eigenvalues was produced. These were discarded in an attempt to form a solution with the remainder of the real eigenvalues. Such a procedure was usually successful but sometimes led to intolerable instability, especially if the result was an imbalance in the number of even and odd modes.

Let the number of real solutions obtained from the eigenvalue problem be denoted M where $M \leqslant L$. This parameter equals the number of useful modes and consequently equals the limit of the index m in the expansions of equations(7.19) and (7.33).

Unlike the determination of a satisfactory value for P, numerical difficulties were often met in optimizing the parameter L(M). Again these difficulties became more apparent for large groove depths where high values of L could cause the formation of complex eigenvalues, or could make the matrices G and H badly-conditioned. For L = M = 12 to 16 however, quite reasonable results have been achieved for some profiles up to a normalised groove depth of h/d = 0.5 when only a few orders are propagating. For shallower grooves, as few as eight modes were usually found to be sufficient.

Consider now the case of profiles possessing left-right symmetry about x = c/2. This accounts for a large portion of the profiles in common usage. With regard to the F.S.M., it can be seen for P polarization from equation (7.18) that the matrix elements $G_{q\ell}$ and $H_{q\ell}$ are non-zero

for $(\ell+q)$ odd and are zero for $(\ell+q)$ even, where $\ell,q = 1,2,3,\ldots$. Hence the eigenvectors may be divided into two sets - one for "even" modes with $g_{m\ell}$ equal to zero for ℓ even, and the other for "odd" modes with $g_{m\ell}$ equal to zero for ℓ odd. It is easily shown that these definitions correspond to the symmetry relations:

$$\begin{aligned} u_m(\tfrac{c}{2} + x,y) &= u_m(\tfrac{c}{2}-x,y) \quad , \text{ even modes} \\ u_m(\tfrac{c}{2} + x,y) &= -u_m(\tfrac{c}{2}-x,y) \quad , \text{ odd modes.} \end{aligned} \qquad \ldots(7.39)$$

For S polarization, the eigenvectors with elements $g_{m\ell}$ equal to zero for $\ell = 1,3,5\ldots$ correspond to even modes, while those with zero elements for $\ell = 0,2,4\ldots$ correspond to odd modes. This internal structure of G and H for symmetric profiles permits decoupling of the eigenvalue problem (7.15) into two separate eigenvalue problems - one for even modes and one for odd modes. (This was also the case in the solution of the problem for the semi-circular groove grating as described in Chapter 6.) The decoupling means that on reconstruction of the eigenvectors, alternate elements (depending on whether ℓ is odd or even) may be given values of precisely zero. It also means that computing time is shortened due to the halving of the matrix dimensions, while the determinants of the matrices involved are also improved.

With regard to the P.M.M., if the sample points distribution is chosen to be symmetrical about $x = c/2$, then this symmetry is manifested in G and H to the extent that the eigenvectors, after computation, should have alternate elements again identically equal to zero. However, in practice it has been found that following the numerical manipulation, some of these elements do not always exactly equal zero. Computational errors are incurred. Therefore, in this respect the F.S.M. is superior.

For asymmetric profiles, the properties of evenness and oddness do not apply.

The F.S.M. was also generally the better of the two methods in satisfying the boundary conditions. Although the P.P.M. satisfies these conditions analytically at a finite number of points, the boundary values at the intervening points were found to not necessarily improve as this number was increased, but would often simply oscillate more rapidly between poor values.

One exception to the superiority of the F.S.M. occurs with the semi-circular groove profile, for which more acceptable results were obtained with the P.M.M. It appears that this method is well-suited to the semi-circular groove profile because alterations in the points distributions had only a marginal effect on the results. This is in contrast to other profiles tested where significant changes were detected following the same procedure.

Of the different numerical problems encountered, many could often be overcome by choosing the better method of the F.S.M. and the P.M.M., by altering the points distribution of the latter, or by redefining ψ_ℓ as $\psi_\ell/\cos(\mu_\ell h)$. This latter step was an attempt to stabilize the large range which exists in the size of the elements of the matrices G and H when L is large. It was only successful in some instances. Overall, the F.S.M. was found to be the more successful of the two methods. It enables computations to be carried out for deeper grooves and accepts higher values for L before numerical instabilities appear. It does however, carry the added complexity of the numerical integration.

7.4.2 Testing of the Formalism

An obvious first test was to apply the formalism to the lamellar grating, since for this profile the eigenvalues β_m satisfying equation (7.7) are known analytically. They are $\mu_m \cot(\mu_m h)$ for P polarization and $-\mu_m \tan(\mu_m h)$ for S polarization, where h is the groove depth and μ_m is given by equation (7.9). Using the P.M.M., the profile was sampled at points $(x_q,-h)$, $q = 1,2,...L$ where $0 < x_q < c$. The subsequent computations of eigenvalues, eigenvectors, field amplitudes and efficiencies were found to be in perfect agreement with those furnished by the formalism described in Chapter 2. As expected from an examination of expansions (7.19) and (7.33), the eigenvectors reduce to $g_{m\ell} = \delta_{m,\ell}$, while a factor of $\sin(\mu_m h)$ or $\cos(\mu_m h)$ (depending on polarization) exists between the moduli of the mode amplitudes given by this formalism and those provided by the lamellar grating formalism.

Of the various groove profiles investigated, the sinisoidal profile has been found to provide very rewarding results. For $c/d = 1.0$ and depths up to $h/d = 0.4$, calculations have adequately satisfied numerical checks, while also conforming well with predictions of an integral theory [7.2, 7.14] in configurations where only a few orders propagate. Table 7.1 displays the results of a convergence test for this profile by showing variation in efficiency with increasing L(M) for a particular wavelength and a normal incidence mounting. The results are compared with efficiencies furnished by the integral theory. Note that because mode orthogonality is not guaranteed, energy conservation is not analytic and so in these and later results, total diffracted energy (T.D.E.) represents the sum of the diffracted order efficiencies, while the term "energy defect" gives the discrepancy between T.D.E. and unity. It is unusual that the S polarization efficiencies are observed to converge faster

TABLE 7.1

Efficiency Convergence

Efficiency and phase of the zeroth order amplitude, plus energy defect (E.D.) are given as a function of the number of modes characterizing the groove field for a sinusoidal profile.

Groove Parameters: $d = 1.0$, $c = 1.0$, $h = 0.4$
Mounting Parameters: $\lambda = 0.9$, $\theta = 0°$
Number of Plane-Wave Terms: $P = 8$

	P polarizarion			S polarization		
M	E(0)	Arg(A_0)	E.D.	E(0)	Arg(B_0)	E.D.
8	.3180	-7.70	2.505%	.5405	-20.45	.121%
10	.3157	-6.72	.896%	.5434	-20.46	-.198%
12	.3146	-6.26	.487%	.5416	-20.45	.003%
14	.3150	-5.96	.248%	.5415	-20.44	.005%
16	.3154	-5.77	.127%	.5415	-20.44	.000%
18	.3159	-5.66	.039%	.5416	-20.44	.001%
Integral Theory	.3172	-4.65	.000%	.5415	-20.58	.010%

TABLE 7.2

Reciprocity

Efficiency, phase and total diffracted energy (T.D.E.) are given for the reciprocal configurations defined by: Problem 1: $\theta = 0°$
Problem 2: $\theta = 53.1301°$ (-1 order returned)

Groove Parameters: $d = 1.0$, $c = 1.0$, $h = 0.4$
Wavelength : $\lambda = 0.8$
Number of Expansion Terms: $P = 8$, $L = M = 14$.

Order p	P polarization			S polarization		
	E(p)	Arg(A_p)	T.D.E.	E(p)	Arg(B_p)	T.D.E.
Problem 1						
0	0.1628	52.17	0.9985	0.7451	5.95	1.0001
±1	0.4179	-148.72	-	0.1275	-121.49	-
Problem 2						
-1	0.4194	-148.72	1.0008	0.1274	-121.49	1.0000

and appear more accurate than those for P polarization when compared to the integral theory results.

Tables 7.2 and 7.3 demonstrate the accuracy with which a reciprocity test and the appropriate phase properties of Chapter 2 are satisfied for the same sinusoidal profile. The S polarization results are excellent and again superior to those for P polarization. These results also conform with the observation that energy conservation is more accurately satisfied for the situation of two real orders in a Littrow mounting than it is for other configurations.

Figure 7.2 illustrates efficiency behaviour for the above grating when operated in a -1 Littrow configuration. Calculations were performed for L = M = 10 modes and predictions of both the F.S.M. and P.M.M. methods are compared with those of the integral theory. Excellent agreement is reached between the F.S.M. and the integral theory, with the maximum discrepancy being only 10% in the wavelength interval where only two orders propagate. Note that this occurs near a resonance anomaly. Elsewhere discrepancies are less than 3%.

Acceptable results have been achieved for the symmetrical triangular profile, but only using the F.S.M. Figure 7.3 demonstrates the closeness of efficiencies calculated using this method (with L = M = 12 modes) to those of the integral theory for a normal incidence mounting. The small discrepancy seen in these spectra for S polarization at wavelengths below $\lambda/d = 0.6$, coincides with poor energy balance for the modal formalism at shorter wavelengths. For normalised groove depths greater than the value of 0.2 used for these curves, energy defects have been found to worsen to the extent that calculations for this profile become grossly inaccurate.

As previously mentioned, and in contrast to the above, it is the P.M.M. which has provided the better agreement with alternative theories when consideration is given to the semi-circular groove profile.

TABLE 7.3

Symmetry Properties.

Intensity and phase values of the field amplitudes for a sinusoidal grating are tabulated and confirm agreement with symmetry relations of Chapter 2. The equation number of the appropriate relation is given in the final column.

Groove Parameters: d = 1.0, c = 1.0, h = 0.4
Mounting Parameters: (a) $\lambda = 1.4$, $\theta = 44.427°$, (b) $\lambda = 1.3$, $\theta = 10.0°$
Number of Expansion Terms: P = 8, L = M = 16
Boundary Solution: F.S.M.

	P polarization	S polarization	Equation Number
(a) -1 Littrow Relations			
$\|R_0\|^2$, $\arg(R_0)$	.7630, -131.50	.9998, 163.90	2.60
$\|R_{-1}\|^2$, $\arg(R_{-1})$	.2370, -41.50	$.1735\times10^{-3}$, 73.90	2.60-1-2
$\|R_1\|^2$, $\arg(R_1)$	$.3198\times10^{-1}$, -65.87	$.2652\times10^{-3}$, 143.99	
$\|R_{-2}\|^2$, $\arg(R_{-2})$	$.2161\times10^{-2}$, 26.00	$.2711\times10^{-3}$, 20.34	
$\frac{1}{2}\arg(R_0+R_{-1})$	-51.18	81.57	2.58-9
$\frac{1}{2}\arg(R_0-R_{-1})$	-80.32	-7.67	2.58-9
$\arg(R_1+R_{-2})$	-51.17	81.58	2.58
$\arg(R_1-R_{-2})$	-80.30	-7.66	2.58
$\arg(a_m^e)$	-51.19	81.57	2.59
$\arg(a_m^o)$	9.68	-7.67	2.59
$\cos^2[\arg(a_m^e)-\arg(a_m^o)]$	.2370	$.1759\times10^{-3}$	2.61
$\arg(a_m^e)+\arg(a_m^o)$	-41.50	73.90	2.62
(b) Long-Wavelength Relations			
$\|R_0\|^2$, $\arg(R_0)$	1.0000, -105.34	1.0000, -142.55	
$\frac{1}{2}\arg(R_0)$	-52.67	-71.28	2.44
$\frac{1}{2}\arg(R_0)+\pi/2$	37.33	18.73	2.47
$\arg(R_{\pm1})$	-52.67	-71.28	2.44
$\arg(a_m^e)$	-52.67	-71.28	2.47
$\arg(a_m^o)$	37.33	18.72	2.47

(Note: The above amplitudes have been multiplied by the appropriate phase correction factor so that in keeping with the symmetry requirements, they relate to an origin at x = c/2.)

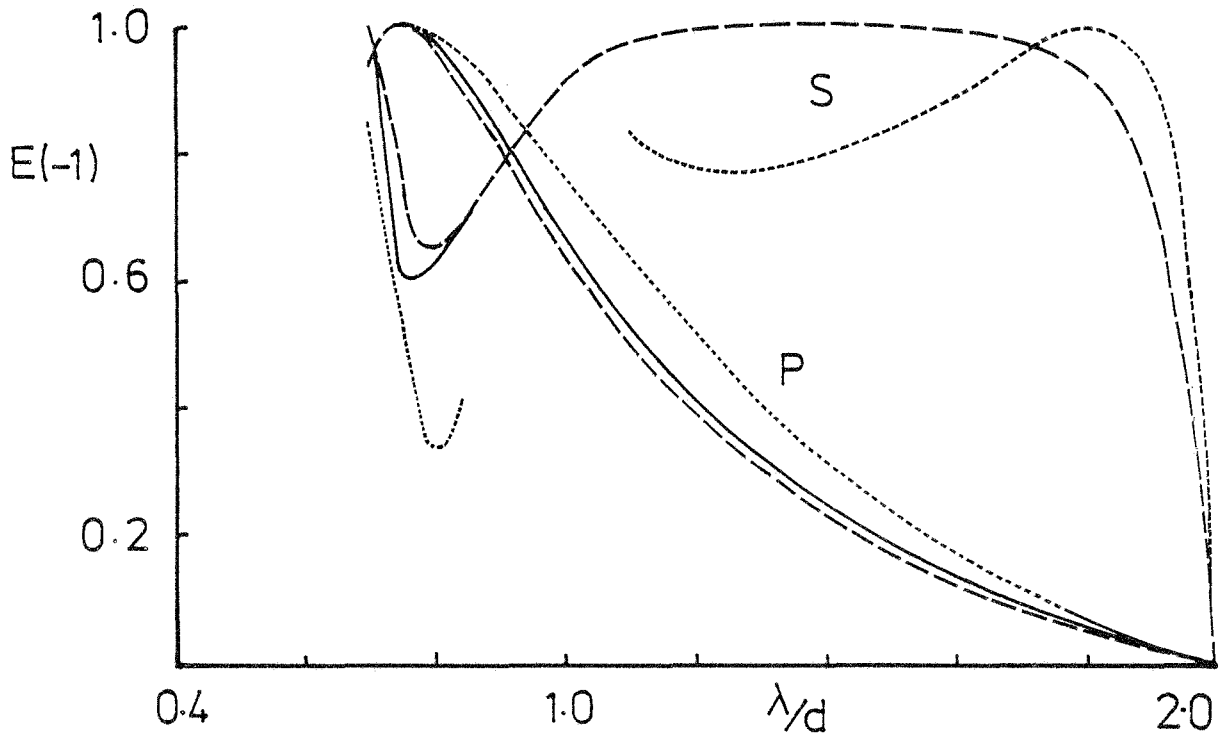

Figure 7.2 First-order Littrow efficiency curves for a sinusoidal profile of normalised groove depth 0.4.
(——) Integral theory
(- - - -) Modal theory F.S.M. (M=10)
(·····) Modal theory P.M.M. (M=10)

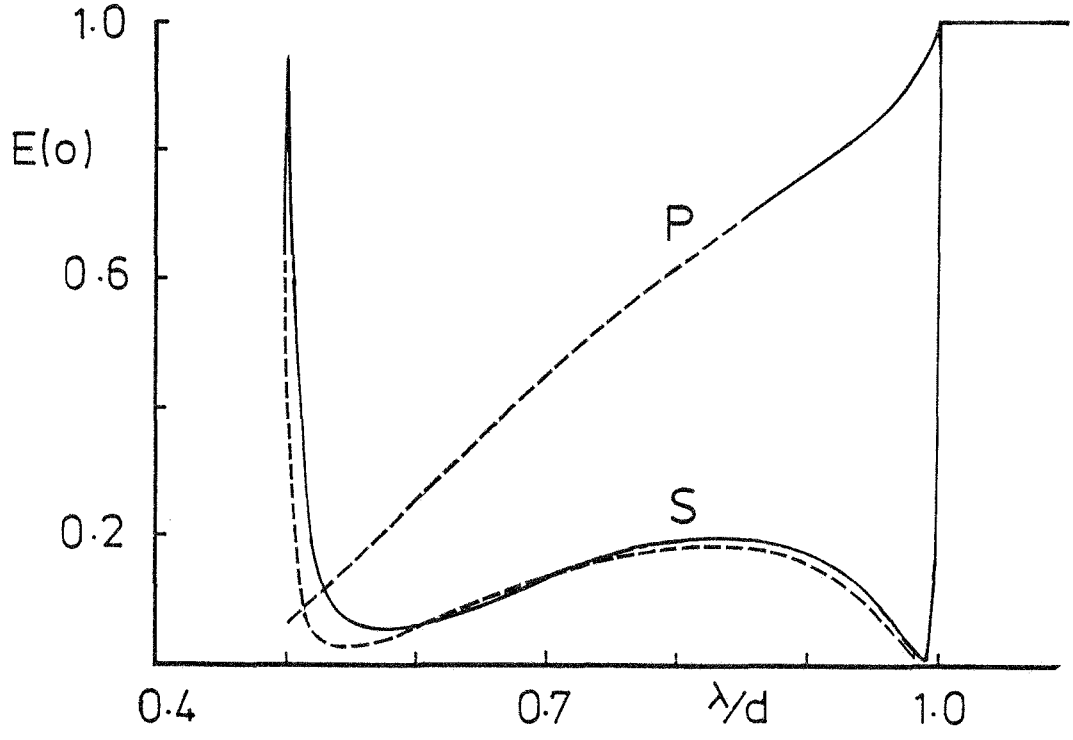

Figure 7.3 Normal incidence efficiency curves for a symmetrical triangular profile of normalised groove depth 0.2.
(——) Integral theory
(- - - -) Modal theory F.S.M. (M=12)

In Figure 7.4, these comparisons are exhibited for the -1 Littrow mount and a normalised groove radius of 0.4. The excellent conformity seen here for 10 profile points is maintained for this grating for groove radii up to the maximum permissible of 0.5 periods.

It is interesting to note, that when applied to the semi-circular groove profile, the formalism given in this chapter secures a far greater proportion of real eigensolutions than does the formalism presented in Chapter 5.

7.4.3 Distribution of the Eigenvalues

It was mentioned in the previous section that the eigenvalues for the lamellar grating are known analytically and that these values have been verified by the new formalism. It is of interest to determine the distribution of these eigenvalues as predicted by the new formalism as the groove shape is altered. To this end eigenvalue trajectories have been plotted for the semi-circular and sinusoidal groove gratings and compared with those for the lamellar grating. (Note that reference was made in the previous chapter to the fact that the behaviour of the semi-circular groove grating appears to lie somewhere between that of the other two.)

As a preliminary step, the eigenvalues generated by this formalism for the semi-circular groove grating were checked against those provided by the modal formalism of Chapter 6. Table 7.4 displays this comparison for a grating with a normalised groove radius of $h/d = 0.4$ when operated in a -1 Littrow mounting with a wavelength of $\lambda/d = 1.4$. The results are in good agreement. At this point it is interesting to observe that for the higher order modes, the S and P polarization eigenvalues become equal at values very close to $m\pi/c$, which is the common value reached by the eigenvalues of the lamellar profile for large m.

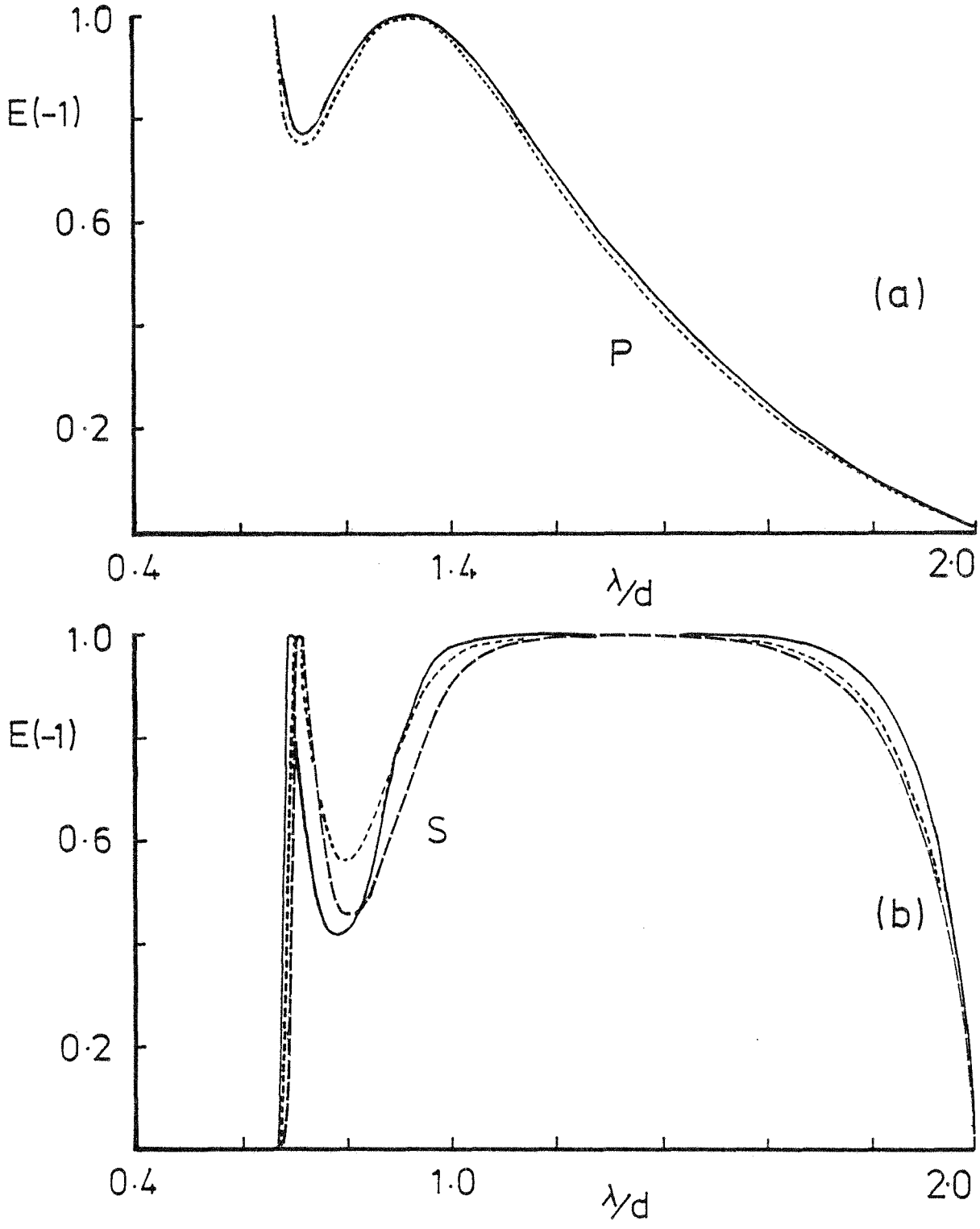

Figure 7.4 First-order Littrow efficiency curves for a semi-circular groove grating of normalised groove depth 0.4.
(a) P polarization (b) S polarization
(———) Integral theory (- - - -) Modal theory F.S.M.
(·····) Modal theory P.M.M.
(The formalism of Chapter 6 predicts results coinciding closely with the dotted line.)

TABLE 7.4

Eigenvalue Comparison.

Eigenvalues provided by the formalism of this chapter and the formalism of Chapter 6 are presented for the semi-circular groove grating.

Groove Parameters: $d = 1.0, c = 0.8, h = 0.4$
Mounting Parameters: $\lambda = 1.4, \theta = 44.427°$
Number of Expansion Terms: $P = 8, L = M = 12$
Boundary Solution: P.M.M.

P polarization		S polarization	
General Modal Theory	Semi-Circular Profile Theory	General Modal Theory	Semi-Circular Profile Theory
2.38†	2.39	-104.90†	-100.39
6.85*	6.89	0.23*	0.23
11.02†	11.09	6.28†	6.07
15.10*	15.18	10.89*	10.73
19.13†	19.25	15.06†	14.91
23.13*	23.29	19.12*	19.03
27.12†	22.90	23.13†	21.46
31.09*	26.46	27.12*	25.18

† even modes

* odd modes

Figure 7.5 contains some sketch graphs which illustrate the trajectories of the lamellar grating eigenvalues as a function of groove depth. They show that for modes less than their threshold values of 2c/m, the trajectories differ from those above their threshold. In the example given, the wavelength has been chosen so that the m = 0 and m = 1 modes are below their thresholds while the remainder are above. For the latter modes, the eigenvalues for both polarizations approach $|\mu_m|$ as h becomes large.

For comparison with the above graphs, Figure 7.6 contains some trajectories for the semi-circular groove profile and a wavelength of $\lambda = 1.9d$. Due to the proximity of the even mode trajectories for P polarization to the odd mode trajectories for S polarization, they are split up into two sets of curves. (It should be noted, that with the eigenvalue formalism the modes emerge from the calculations unordered. To order them with respect to the index m, they are simply arranged in order of increasing eigenvalue. For the Littrow mounting, the even and odd modes are easily identified by their common amplitude phases given by equation (2.59).) It is interesting to observe that a near constant β-separation exists between the trajectories at a given value of h. That is, there is a near linear relationship between β and m. (Such a relationship *does* exist for large m for a lamellar grating of groove width equal to twice its groove depth.)

Although definite similarities are seen to exist between the curves of Figure 7.6 and those of Figure 7.5, a direct comparison cannot be made, because as h is increased for the semi-circular grating, the groove width c increases also. To remove this difference, trajectories have been plotted in Figure 7.7(a) for a groove profile whose aperture width remains constant at c/d = 1.0, but whose cross-section always consists of the arc of a circle. The result is a set of trajectories which clearly

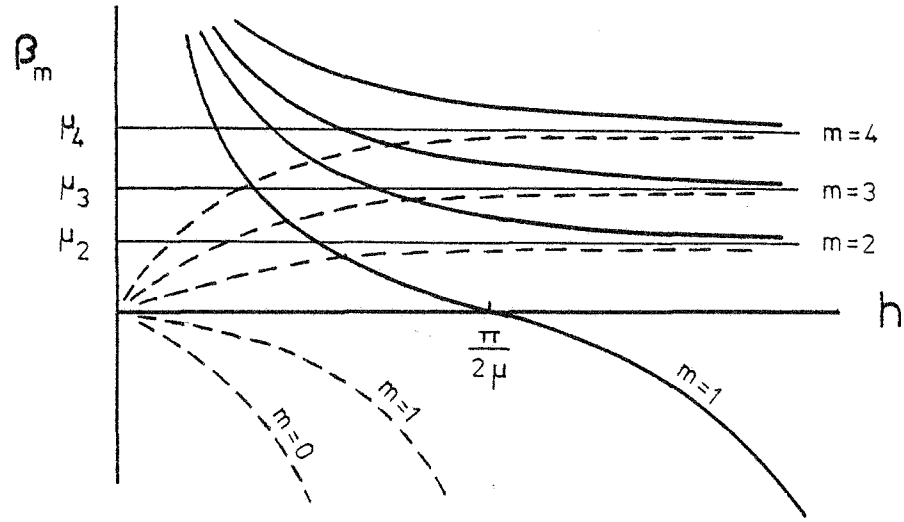

Figure 7.5 Eigenvalues β_m are plotted as a function of groove depth h/d for the lamellar grating and a wavelength λ, where $c<\lambda<2c$.
(——) P polarization, $\beta_m=\mu_m\cot(\mu_m h)$
(----) S polarization, $\beta_m=-\mu_m\tan(\mu_m h)$

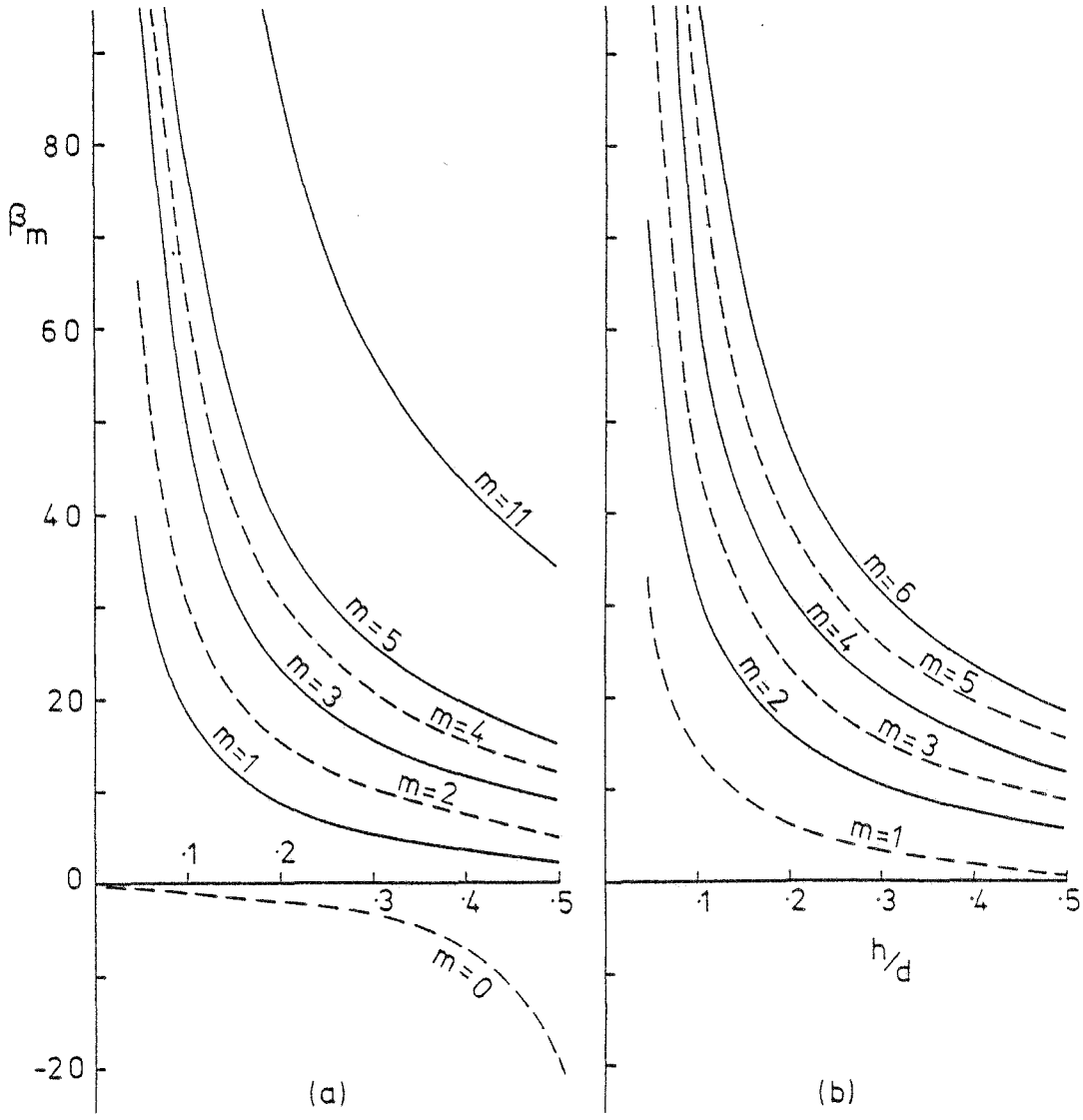

Figure 7.6 Eigenvalues are plotted as a function of groove depth for the semi-circular groove grating and a wavelength $\lambda/d=1.9$ (a) even modes (b) odd modes.
(——) P polarization (----) S polarization

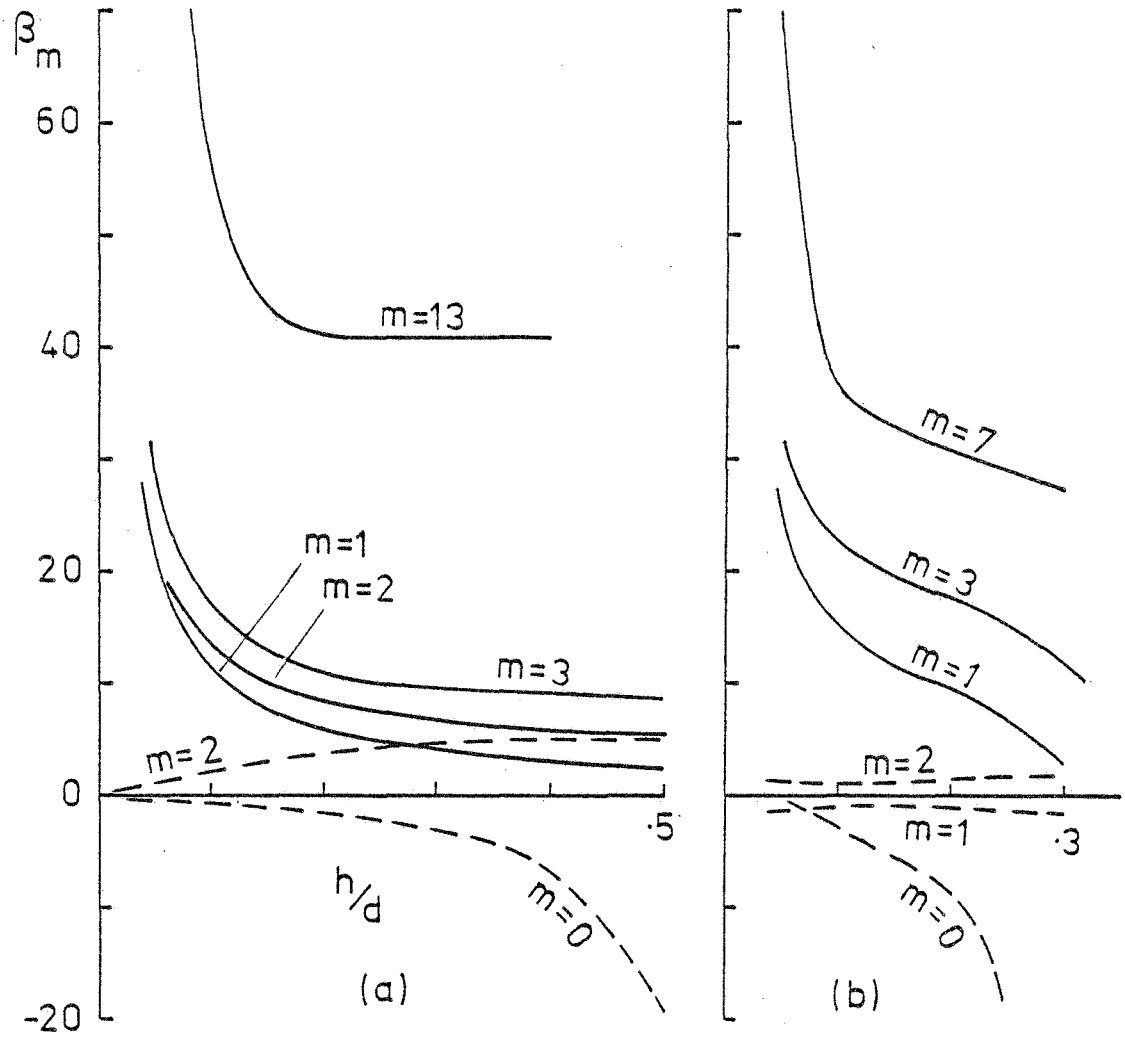

Figure 7.7 Eigenvalues β_m are plotted as a function of groove depth h/d.

(a) Constant-aperture circular-arc profile c/d=1.0, λ/d=1.0, M=14.

(b) Sinusoidal profile c/d=1.0, λ/d=1.0, M=10.

(——) P polarization (----) S polarization

resemble those for the lamellar grating. In particular, the two S polarization trajectories appear to belong one to a real mode and one to an evanescent mode.

For final comparison, Figure 7.7(b) contains a set of trajectories for the sinusoidal profile with depths ranging up to h/d = 0.3. Again, the same sort of behaviour is evident, but as expected it is further removed from that of the lamellar profile.

7.5 DISCUSSION OF THE METHOD

It is apparent from findings discussed in Section 7.4, that instabilities prevent extensive application of this method in its present form to general profile gratings with arbitrarily deep grooves. A brief discussion given here outlines reasons which could lie behind this failing.

Although the majority of problems encountered are numerical ones, the underlying faults with the formalism are most probably due to the mode eigenfunctions not forming a complete set over the groove region as a consequence of the eigenvalue problem not being framed in terms of symmetric matrices.

Consider the eigenvalue equation (7.15). It has been shown in Section 7.2.2.3, with reference to Appendix 3, that if the matrices G and H are not truncated, then all eigenvalues β are real, and all eigenvectors $\underline{g}$ corresponding to different eigenvalues are orthogonal on the interval $0 < x < c$, $y = 0$. However, when G and H are truncated, the boundary conditions on $y = f(x)$ are only approximately satisfied. Some complex eigenvalues can then occur, and (especially for deeper grooves) eigenvectors fail to be (even approximately) orthogonal. (This has been borne out by the poor conformity of some calculations with equation (7.21).) The somewhat arbitrary procedure of discarding

complex eigenvalues and corresponding eigenvectors has been adopted and this has resulted in a numerical procedure with (in some cases) inadequate convergence.

To overcome this defect, it would be sufficient to reformulate the eigenvalue problem in such a way as to lead to an expression of the form of equation (7.15), but with $(H^{-1}G)$ a real, symmetric matrix.

7.6 CONCLUSION

Investigations have been described, which concern the application of a modal expansion technique to the scalar-wave diffraction problem for perfectly-conducting reflection gratings of arbitrary groove profile. The formalism described is based on an impedance constraint which is applied at the interface separating the groove region from the free-space region above the grating. This constraint specifies that on that boundary, the value of each eigenfunction representing the field in the groove region is proportional to its normal derivative. The constant of proportionality is an eigenvalue. The modes are subsequently formulated from waveguide functions of the type appropriate to the lamellar grating.

The theory for the two fundamental polarizations has been subjected to numerical tests and efficiencies have been computed for three known profiles and compared with those predicted by an integral formalism. The profiles considered were those of the sinusoidal, semi-circular and symmetrical triangular groove gratings. Satisfactory agreement in efficiency has been achieved, but only for moderate groove depths, i.e. those ranging up to half a period for the first two profiles mentioned and up to a fifth of a period for the third.

Eigenvalues produced by the method for a semi-circular groove grating were found to conform well with those provided by an alternative modal treatment dependent on the same impedance constraint. Trajectories of these eigenvalues, for an increasing groove depth, were demonstrated to follow similar paths to the known analytic values for the lamellar grating.

Numerical problems were encountered in the implementation whenever groove depths exceeded those listed above, or whenever a large number of modes was included in the groove field expansion. These problems have been attributed to the fact that the prescribed eigenvalue constraint does not lead to an eigenvalue problem for symmetric matrices.

Future work in this area should be directed towards the development of a formulation, which, if based on an eigenvalue technique, must necessarily generate real and orthogonal solutions for the mode functions. A further aim would be of course, to extend the method to account for finitely-conducting gratings.

REFERENCES

[7.1] Petit, R., and Cadilhac, M., 1967, *C. R. Acad. Sci. Paris, 264,* 1441.

[7.2] Pavageau, J., and Bousquet, J., 1970, *Optica Acta, 17,* 469.

[7.3] Van den Berg, P.M., 1971, Thesis, Delft.

[7.4] Kalhor, H., and Neureuther, A., 1971, *J. Opt. Soc. Am., 61,* 43.

[7.5] Nevière, M., Cerutti-Maori, G., and Cadilhac, M., 1971, *Opt. Commun., 3,* 48.

[7.6] Nevière, M., Cadilhac, M., and Petit, R., 1973, *I.E.E.E. Trans., AP-21,* 37.

[7.7] Jovicevic, S., and Sesnic, S., 1972, *J. Opt. Soc. Am., 62,* 865.

[7.8] Beunen, J.A., 1976, University of Sydney, Thesis (unpublished).

[7.9] Fox, J.R., 1980, *Optica Acta, 27,* 289.

[7.10] Petit, R., 1963, *Rev. Opt., 42,* 263.

[7.11] Jiracek, G.R., 1973, *I.E.E.E. Trans., AP-21,* 393.

[7.12] Millar, R.F., 1973, *Radio Sci., 8,* 785.

[7.13] De Boor, C., 1971, *Mathematical Software.* (New York: Academic Press).

[7.14] McPhedran, R.C., 1973, University of Tasmania, Thesis (unpublished).

[7.15] Andrewartha, J.R., McPhedran, R.C., and Derrick, G.H., 1981, *Optica Acta,* accepted for publication.

Appendix 1

EFFICIENCY SPECTRA FOR THE INFINITELY-CONDUCTING LAMELLAR GRATING

S and P polarization efficiency curves are presented for the infinitely-conducting lamellar grating. First-order Littrow spectra are given for the reflection grating and normal incidence spectra are given for the transmission grating. (Efficiency for unpolarized radiation is also plotted for the reflection grating for some groove parameters considered near optimum for this polarization.) These spectra complement several already presented throughout the text. Calculations were performed using the modal formalisms of Chapter 2. Typically 15 plane-wave terms and 8 modal terms were used in the field expansions.

Efficiency in the -1 order for the reflection grating, and in the zeroth transmitted order for the transmission grating, is shown as a function of wavelength for the following groove parameters. (All parameters are normalised to the period.)

Reflection Grating: -1 Littrow Mounting

h = 0.2 c = 0.4 ; h = 0.3 c = 0.8
h = 0.3 c = 0.6 ; h = 0.365 c = 0.75

h = 0.45 c = 0.15, 0.45, 0.6, 0.8

h = 1.2 c = 0.2, 0.5, 0.9

c = 0.999 h = 0.3, 0.45, 0.9.

Transmission Grating: Normal Incidence

c = 0.5 h = 0.2 ; c = 0.4 h = 0.5, 1.0

c = 0.8 h = 0.02;0.5, 1.0.

(———) P polarization (-----) S polarization

(-·-·-) U polarization.

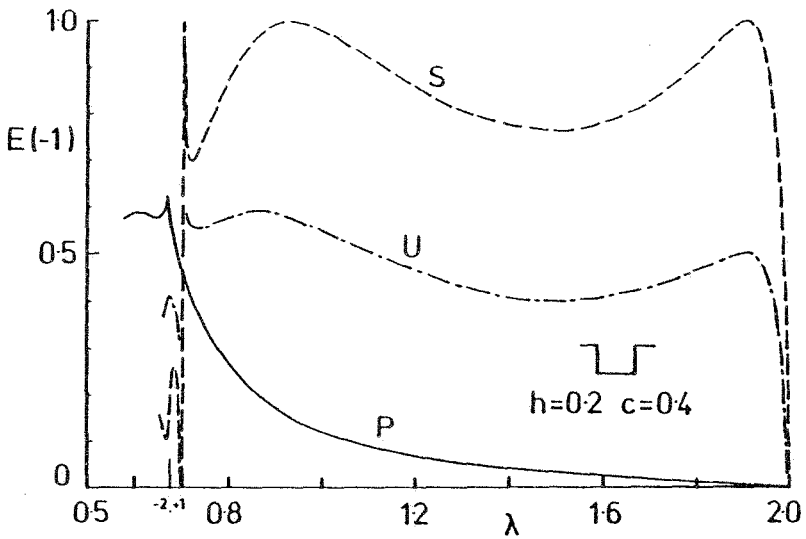
1·0
E(-1)
0·5
0
S
U
P
h=0·2 c=0·4
0·5
-2,-1
0·8
1·2
λ
1·6
2·0

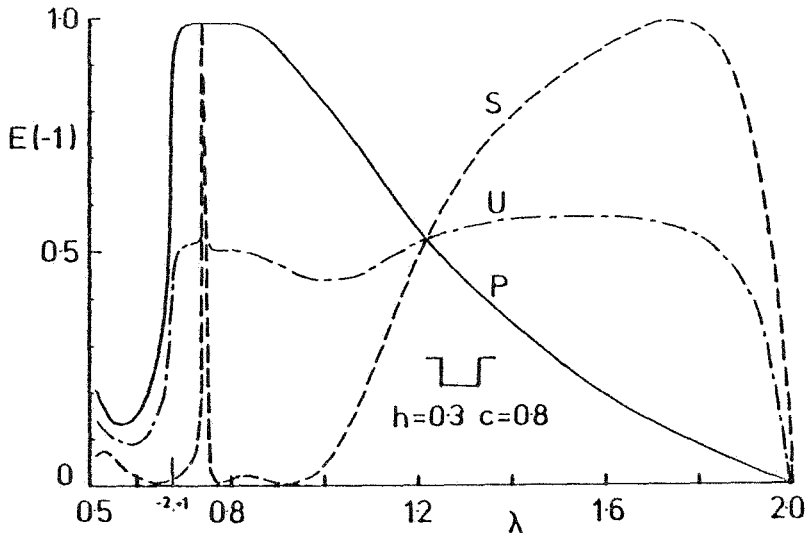
1·0
E(-1)
0·5
0
S
U
P
h=0·3 c=0·8
0·5
-2,-1
0·8
1·2
λ
1·6
2·0

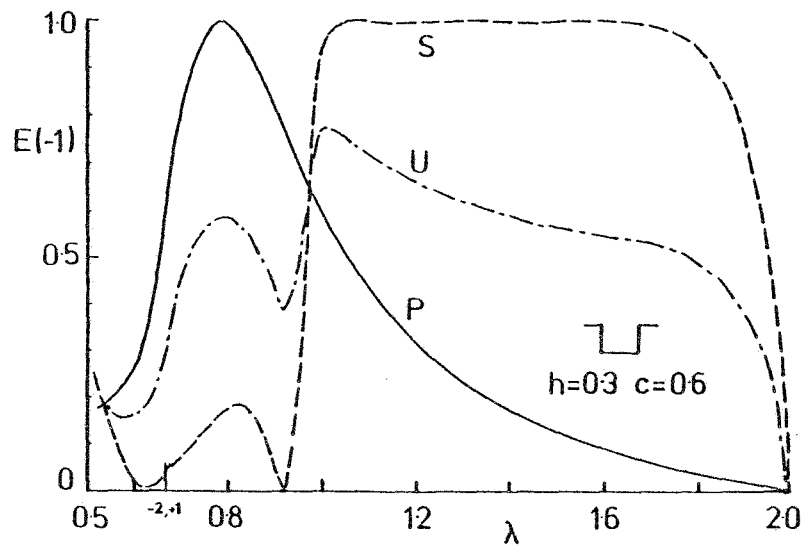
1·0
E(-1)
0·5
0
S
U
P
h=0·3 c=0·6
0·5
-2,-1
0·8
1·2
λ
1·6
2·0

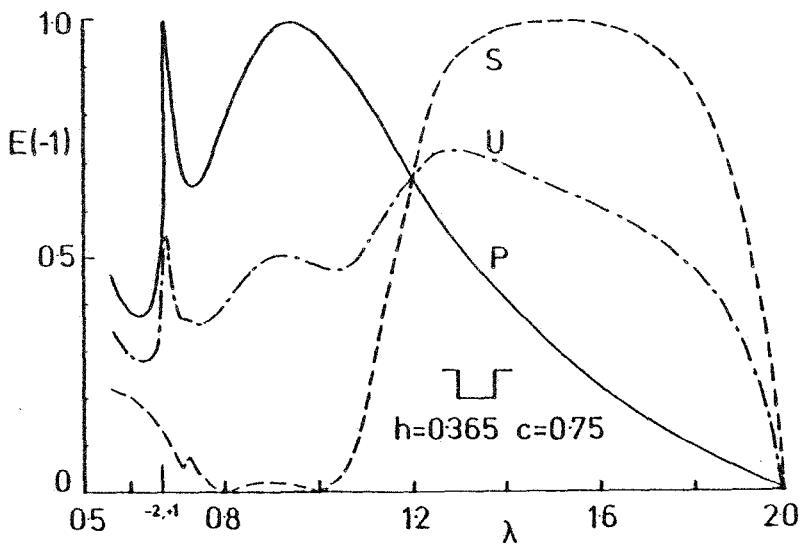
1·0
E(-1)
0·5
0
S
U
P
h=0·365 c=0·75
0·5
-2,-1
0·8
1·2
λ
1·6
2·0

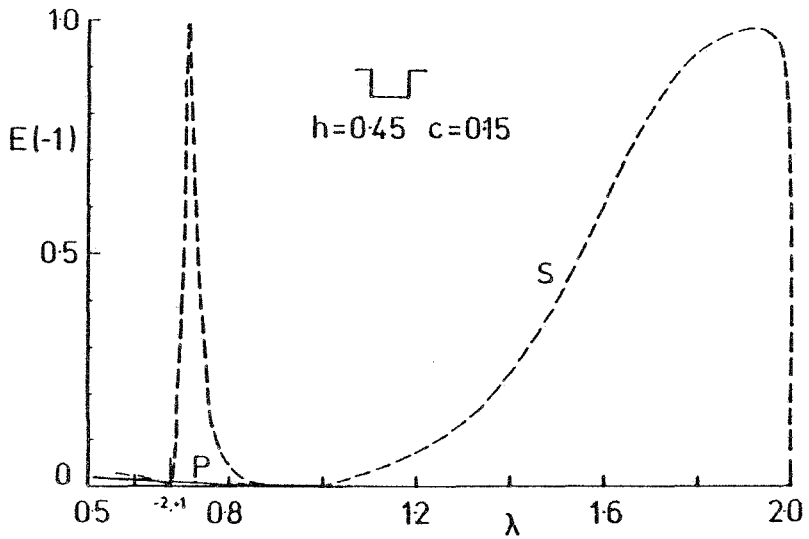

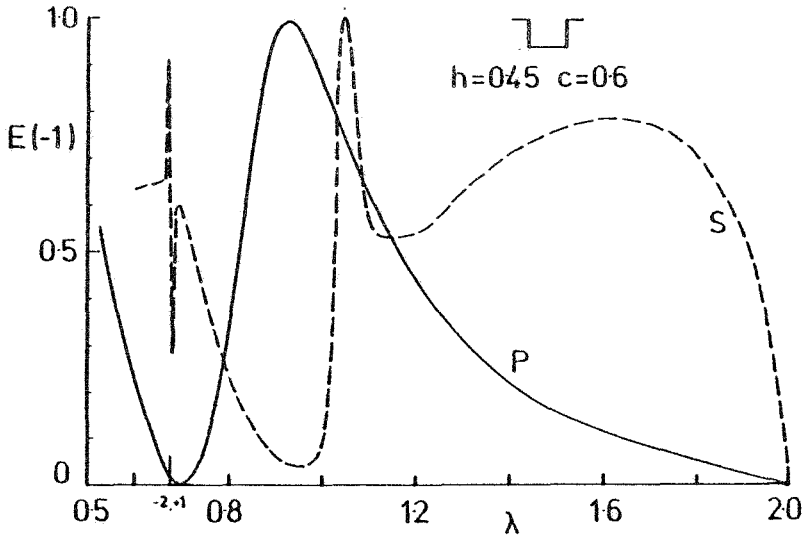

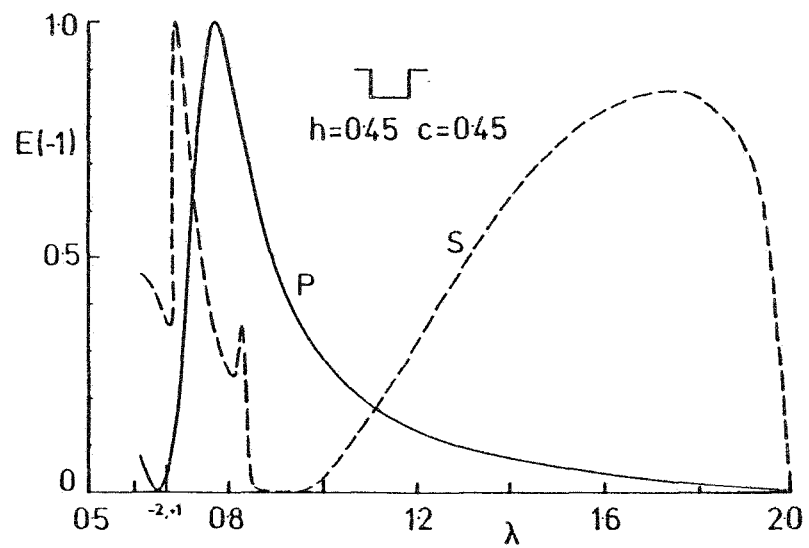

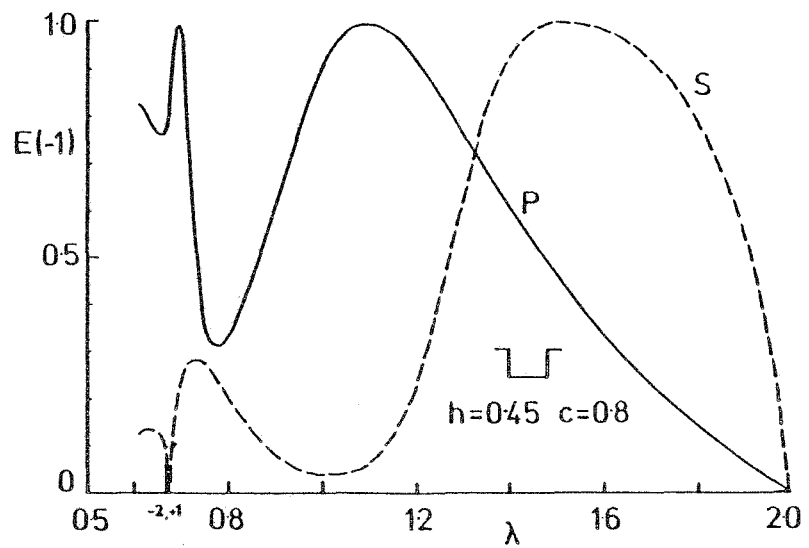

Reflection Grating : -1 Littrow Mounting

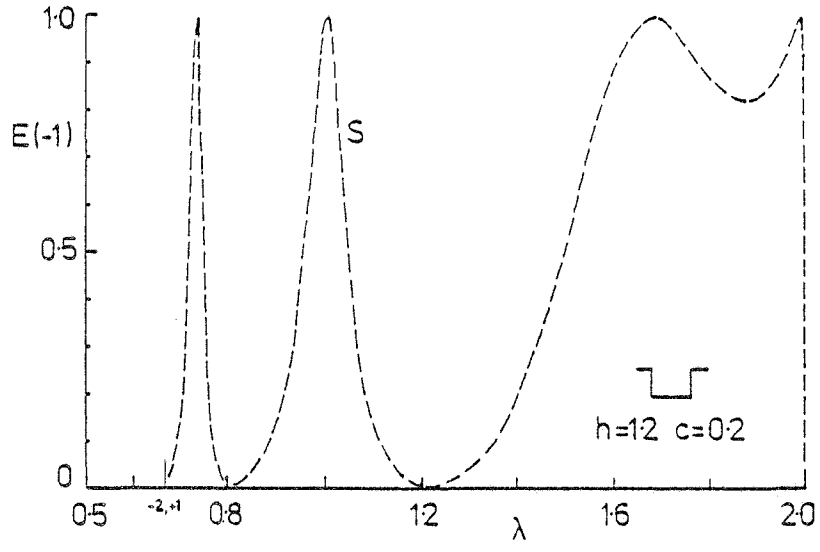

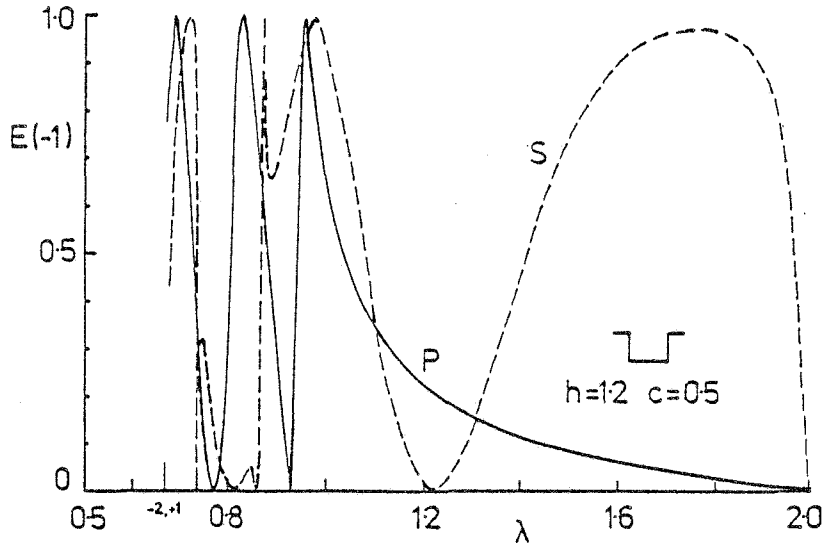

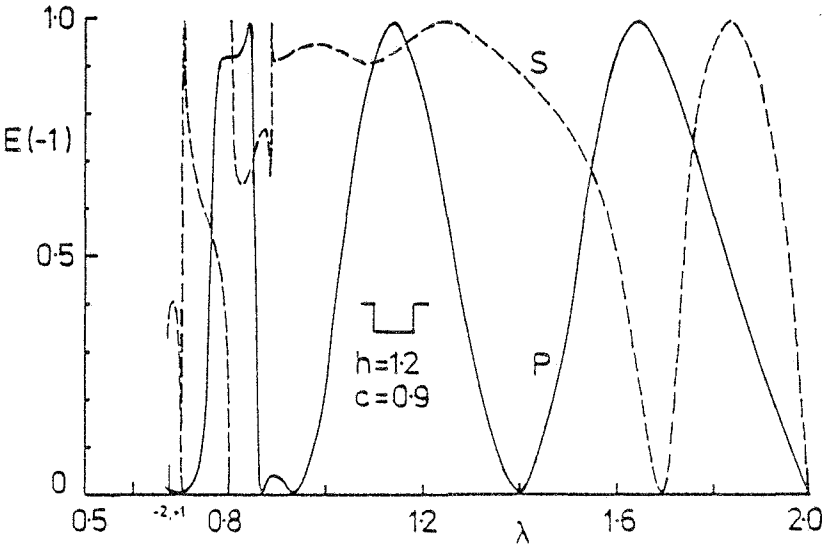

Reflection Grating : -1 Littrow Mounting

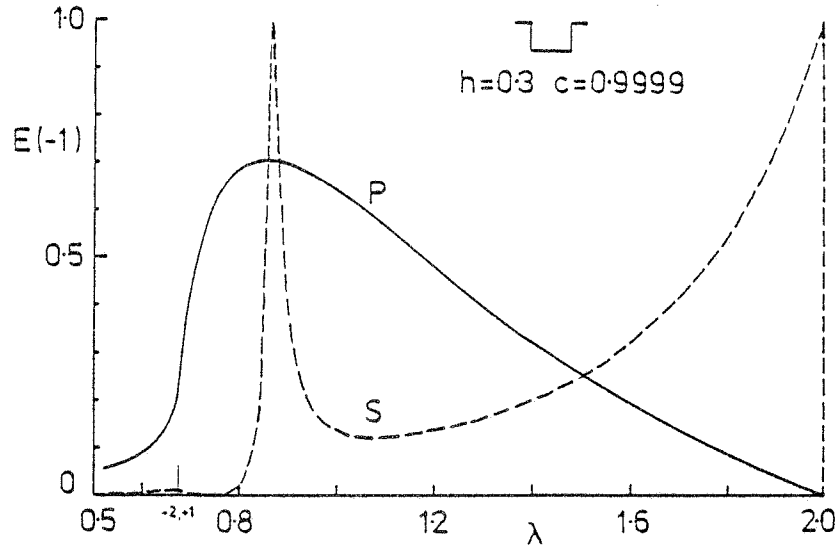

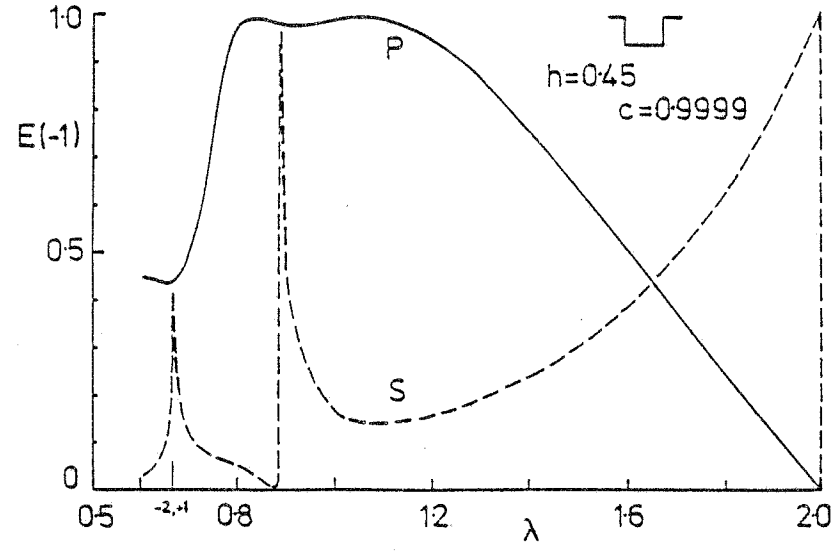

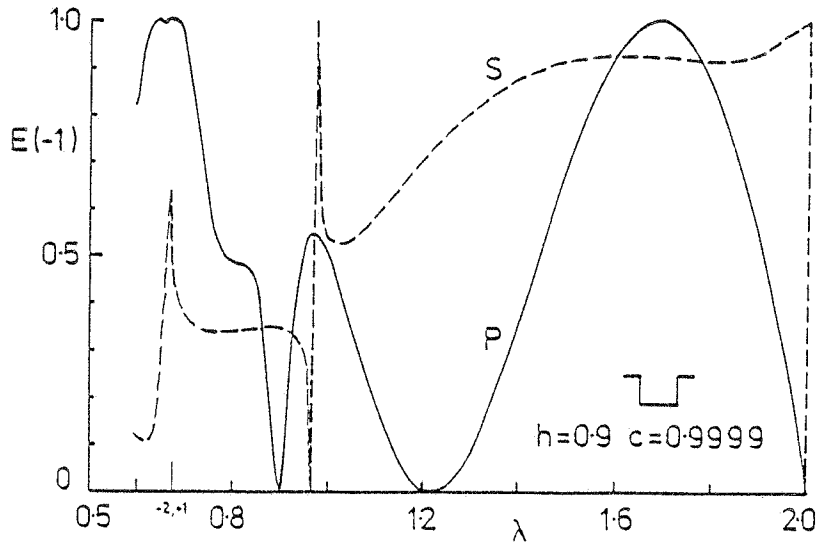

Reflection Grating : -1 Littrow Mounting

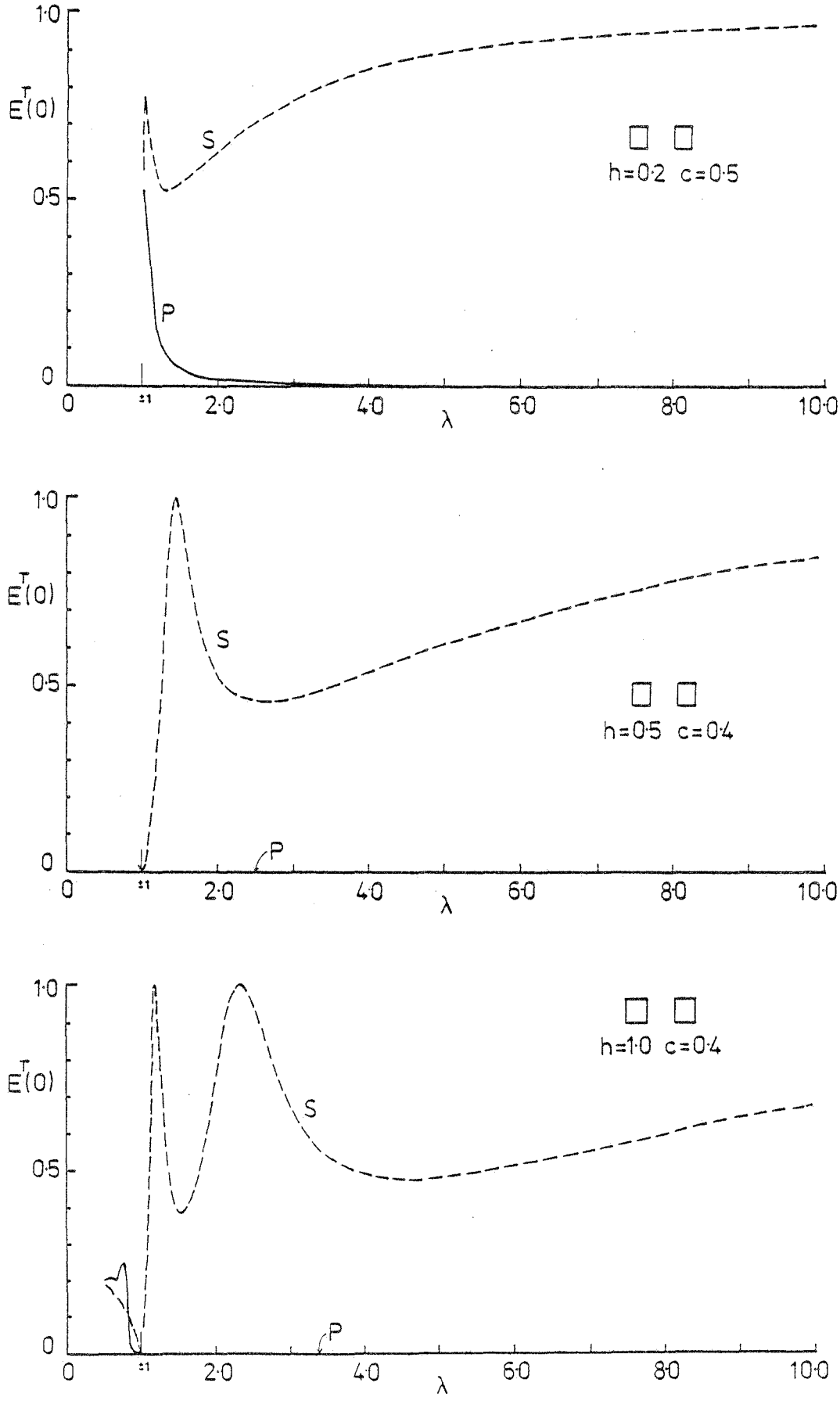

Transmission Grating : Normal Incidence Mounting

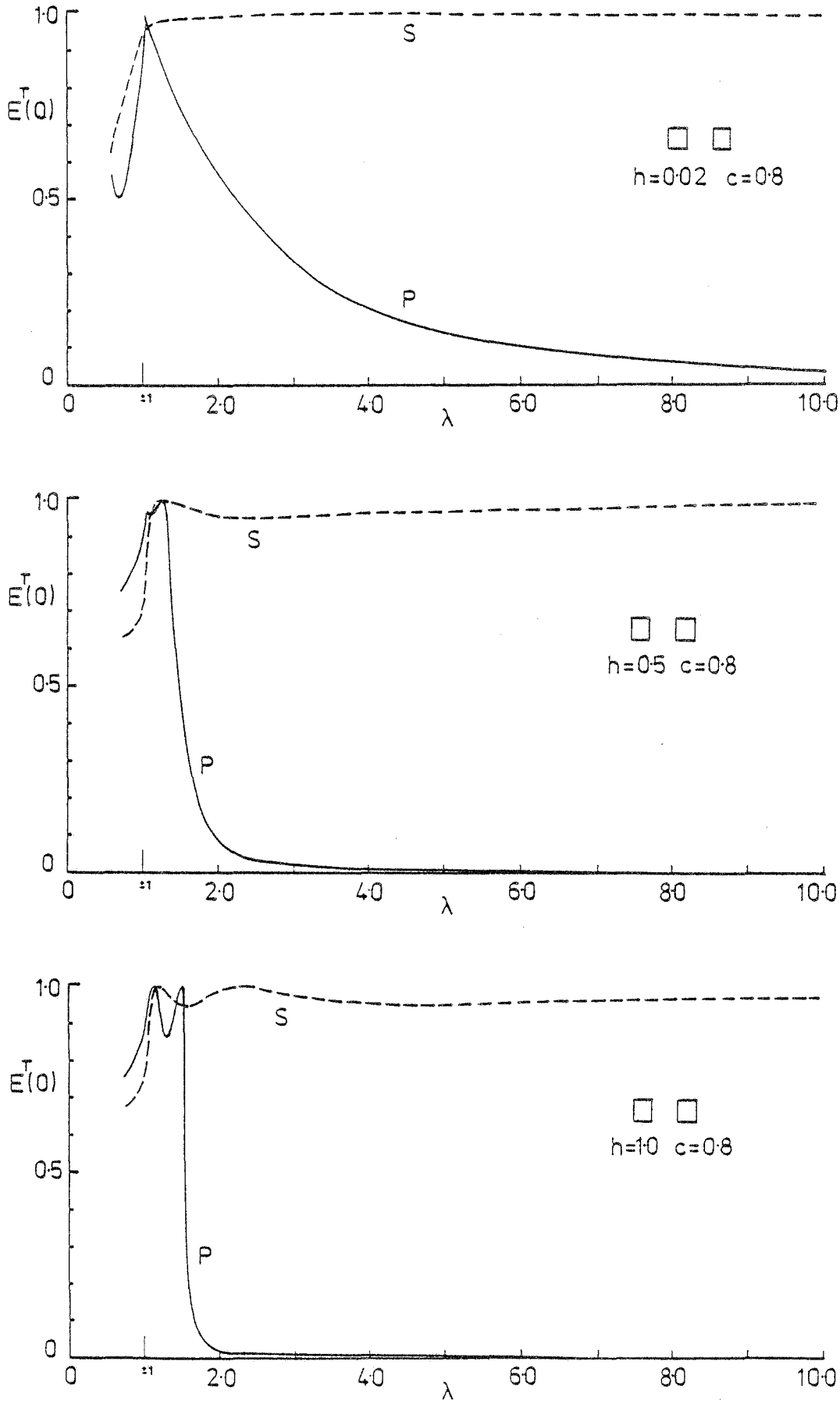

Transmission Grating : Normal Incidence Mounting

Appendix 2

ANALYTIC STRUCTURE OF THE FIELD AMPLITUDES

The plane-wave and modal field amplitudes possess branch points at the Rayleigh wavelengths where one or two of the direction cosines χ_p have square-root branch points. Defining frequency as $\nu \equiv 1/\lambda$, the branch points occur at frequencies ν_p, $p = 0,\pm1,\pm2 \ldots$ and depend on the order p and the angle of incidence.

A multi-sheeted Riemann surface exists on which the amplitudes are meromorphic. This surface is constructed from a complex-ν plane, termed the physical sheet, which is cut along the real axis from the lowest branch point $\nu_{\gamma 0}$ to infinity. The amplitudes are holomorphic on this cut plane, except perhaps for poles on the real axis below $\nu_{\gamma 0}$ where no orders propagate. (For convenience, negative frequencies are neglected.) The physical frequencies are defined as those along the top edge of the cut, i.e. ν_r+i0. For $\nu_r > \nu_{\gamma 0}$, $\chi_{\gamma 0}$ is defined to be positive real for the physical frequencies and negative real for frequencies on the lower side of the cut (ν_r-i0). The other χ_{0i} are positive imaginary on both sides of the cut. For $\nu < \nu_{\gamma 0}$, $\chi_{\gamma 0}$ is positive imaginary as are all other values of χ. These definitions are consistent with the choices for χ_p made in the diffraction formalisms.

A second sheet, cut similarly to the first, has the lower edge of this cut joined to the upper edge of the physical sheet from $\nu_{\gamma 0}$ to the next Rayleigh frequency $\nu_{\gamma 1}$. From $\nu_{\gamma 1}$ to infinity they are unjoined. The upper edge of the second sheet is joined to the lower edge of the physical sheet on the same interval. In this double-sheeted surface, $\chi_{\gamma 0}$ is holomorphic and is negative imaginary for $\nu < \nu_{\gamma 0}$ on the second sheet where the other $\chi_{\gamma i}$ remain positive imaginary.

By joining higher-order sheets to the first two between the appropriate Rayleigh frequencies, a multi-sheeted surface is formed. Only those sheets adjacent to the physical sheet are of interest, since it is only on these sheets that resonance pole trajectories are located.

Figure A2.1 depicts the Riemann surface for the -1 Littrow mounting and shows the location of the S polarization pole trajectory illustrated in Figure 3.5(a).

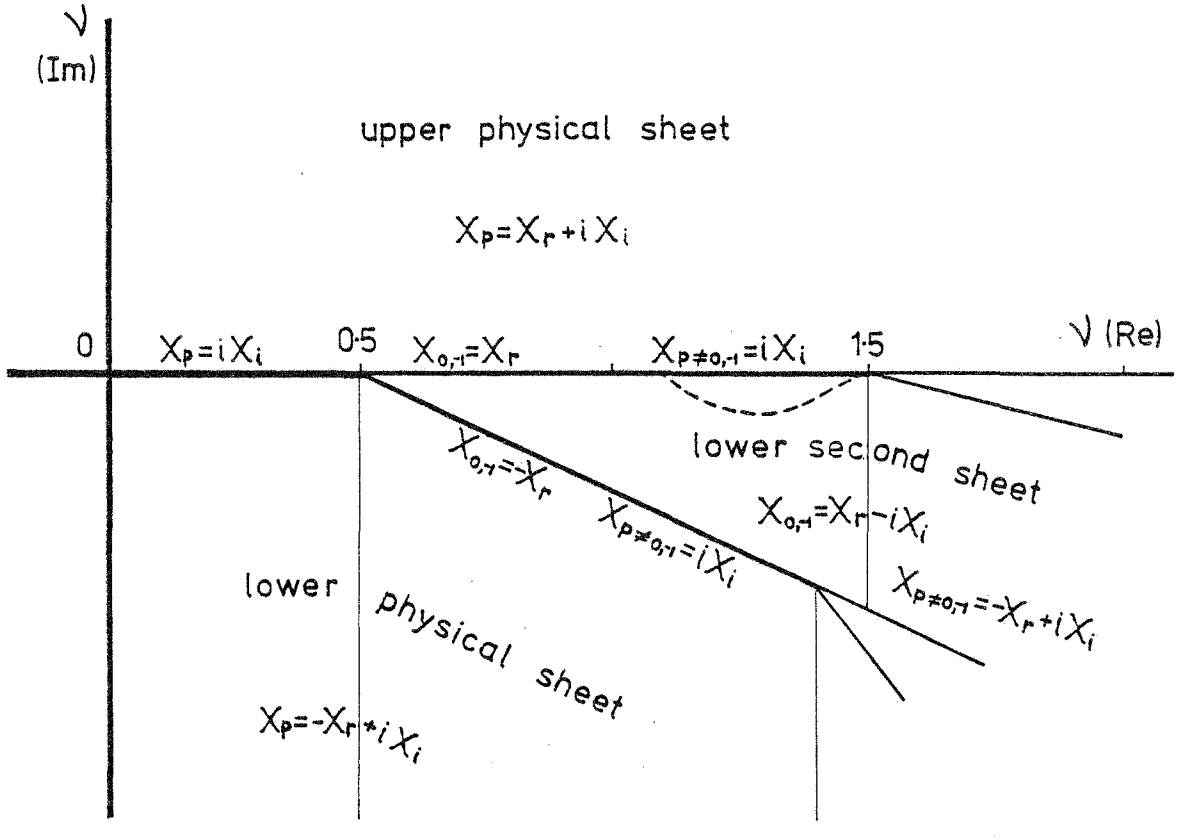

Figure A2.1: A representation of the multi-sheeted Riemann surface is given for the -1 Littrow mounting. The lower half of the second sheet is joined to the upper physical sheet between the branch points at $\nu = 0.5, 1.5$. The upper half of the second sheet is located "behind" the lower half of the physical sheet and joined to it along the lower side of the cut between $\nu = 0.5$ and $\nu = 1.5$. From the branch points $\nu = 1.5$, two further cuts extend, introducing two more sheets. The lower halves of these sheets are just visible, with only the topmost being attached to physical values. The broken line corresponds to the pole trajectory in the mode amplitude b_1 for the perfectly-conducting lamellar reflection grating of groove width $c/d = 0.43$.

(χ_r and χ_i are positive real and positive imaginary components respectively of the functions χ_p, $p=0,\pm1,\ldots$)

Appendix 3

ORTHOGONALITY OF THE MODE FUNCTIONS WHICH OBEY AN IMPEDANCE CONDITION ON THE GROOVE APERTURE

Consider a reflection grating whose grooves have arbitrary cross-section defined by the function $y = f(x)$, as shown in Figure A3.1. The top surface of the grating is chosen to coincide with the x-axis. The groove region A, bounded by the contour Γ, lies between $y = 0$ and $y = f(x)$.

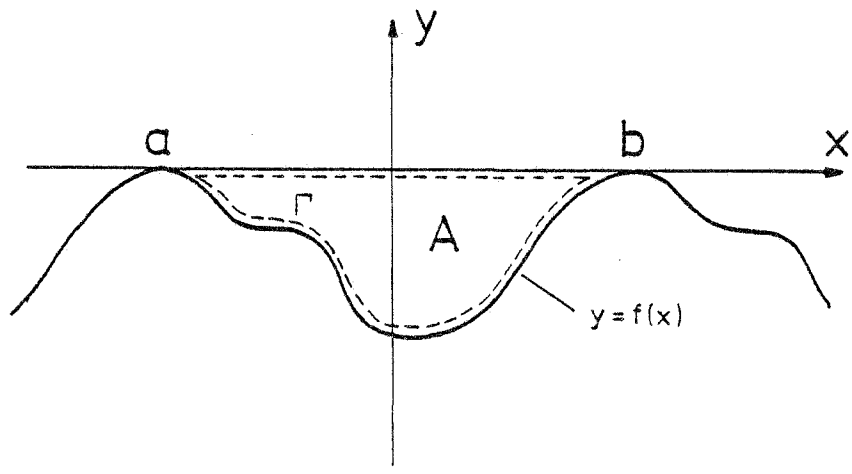

Figure A3.1

Assume a set of functions $u_m(x,y)$ to be defined on the region A and assume that all of the u_m satisfy the wave-equation plus one of the following boundary conditions:

$$\left.\begin{aligned} &\text{(i)} \qquad u_m(x,f(x)) \;=\; 0 \\ &\text{(ii)} \qquad n_x \frac{\partial u_m(x,f(x))}{\partial x} + n_y \frac{\partial u_m\,x,f(x)}{\partial y} \;=\; 0 \end{aligned}\right\} \qquad \ldots(A3.1)$$

where $\underline{n} = (n_x, n_y, 0)$ is a unit vector normal to the grating profile.

Assume also that the u_m satisfy an impedance condition defined by

$$\left.\frac{\partial u_m(x,y)}{\partial y}\right|_{y=0} = \beta_m\, u_m(x,0), \qquad a \leqslant x \leqslant b \qquad \ldots(A3.2)$$

where β_m is an eigenvalue.

The application of Green's Theorem to the region A yields

$$\oint_\Gamma \left(\frac{\partial u_\ell}{\partial n}\,\bar{u}_m - \frac{\partial \bar{u}_m}{\partial n}\,u_\ell\right) ds \;=\; \iint_A \left(\bar{u}_m \nabla^2 u_\ell - u_\ell \nabla^2 \bar{u}_m\right) da \qquad \ldots(A3.3)$$

where ds is an element of arc length and da of area. Simplification of this expression with the aid of the wave-equation and either of the boundary conditions (A3.1) gives

$$\int_a^b \left(\frac{\partial u_\ell}{\partial y}\,\bar{u}_m - \frac{\partial \bar{u}_m}{\partial y}\,u_\ell\right)_{y=0} dx \;=\; 0.$$

Using equation (A3.2), this reduces to

$$(\beta_\ell - \bar{\beta}_m) \int_a^b (u_\ell\, \bar{u}_m)_{y=0}\, dx \;=\; 0 \qquad \ldots(A3.4)$$

With $\ell = m$, equation (A3.4) implies that β_m must be real. With $\ell \neq m$ the same equation implies that functions $u_m(x,0)$ corresponding to different eigenvalues, are orthogonal on the interval $a \leqslant x \leqslant b$:

$$\int_a^b u\,(x,0)\;\bar{u}_m(x,0) \;=\; 0 \qquad (\ell \neq m)\,. \qquad \ldots(A3.5)$$

Appendix 4

EFFICIENCY SPECTRA FOR THE SEMI-CIRCULAR GROOVE GRATING

S and P polarization efficiency curves are presented for the perfectly-conducting semi-circular groove grating in both normal incidence and first-order Littrow mountings. Calculations were performed with the modal formalism of Chapter 6 and typically 17 plane-wave terms and 8 modal terms were used in the field expansions. Efficiency in the zeroth order for the normal incidence mounting, and in the -1 order for the Littrow mounting, is given as a function of normalised wavelength for the following groove radii:

Normal Incidence: a = 0.1, 0.2, 0.25, 0.3, 0.4, 0.5.

-1 Littrow Mount: a = 0.1, 0.15, 0.2, 0.25, 0.3, 0.35, 0.4, 0.45, 0.5.

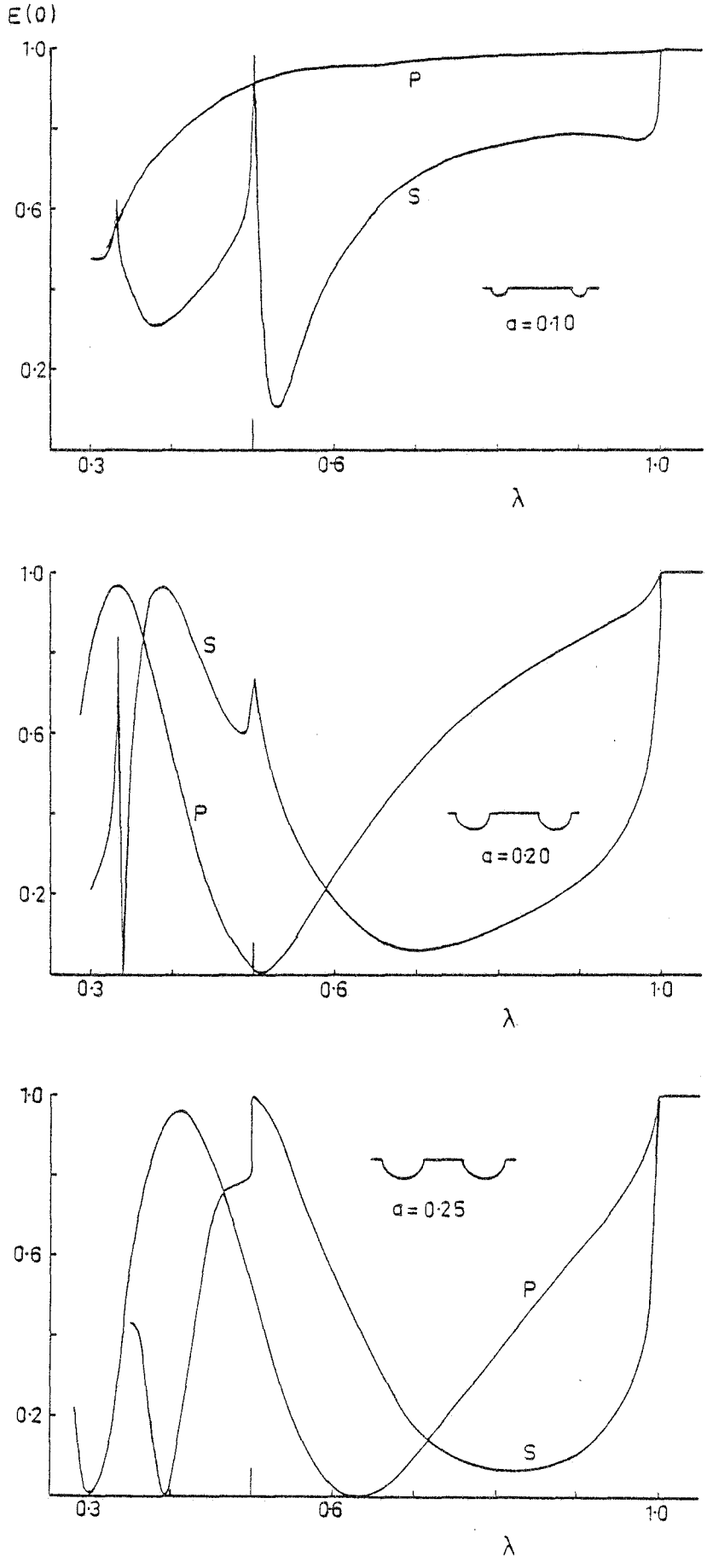

Normal Incidence Mounting

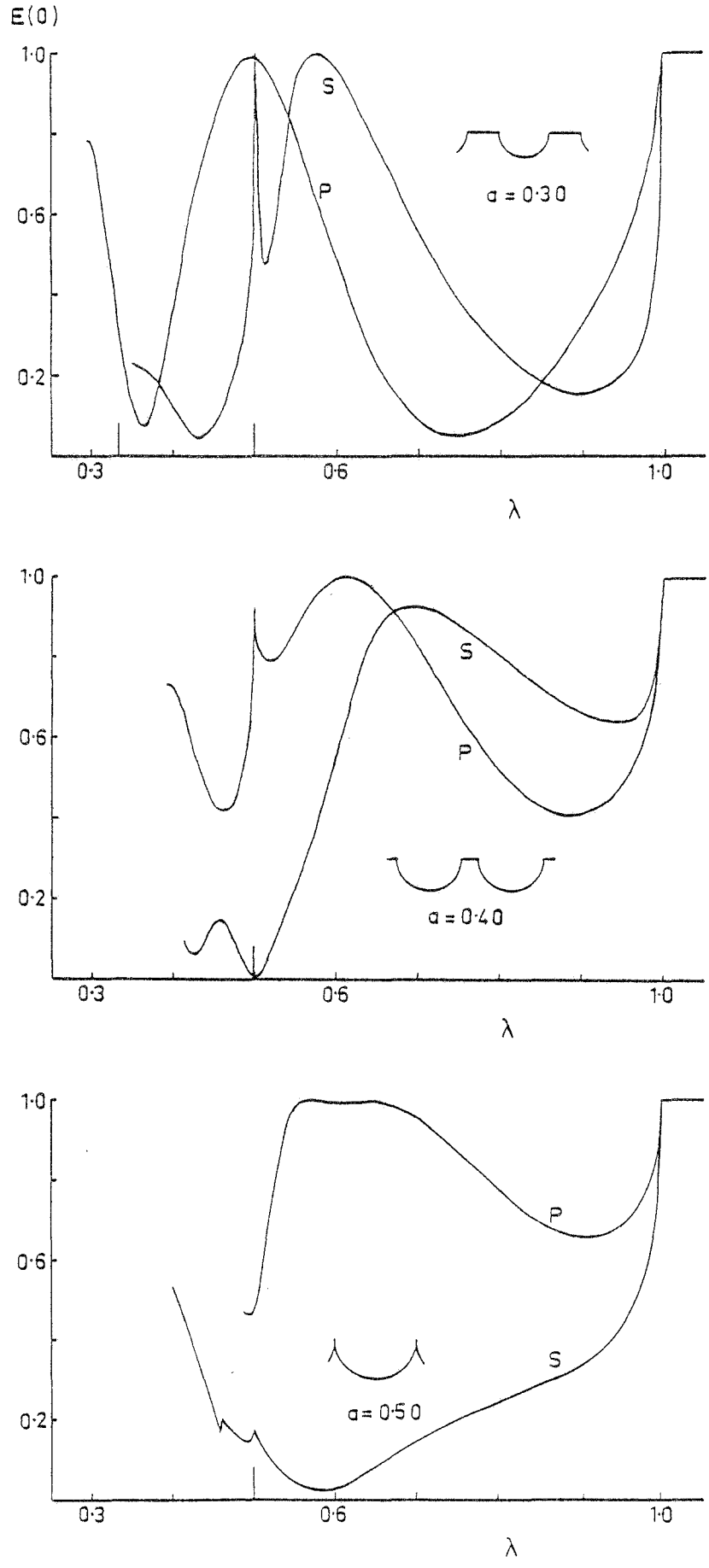

Normal Incidence Mounting

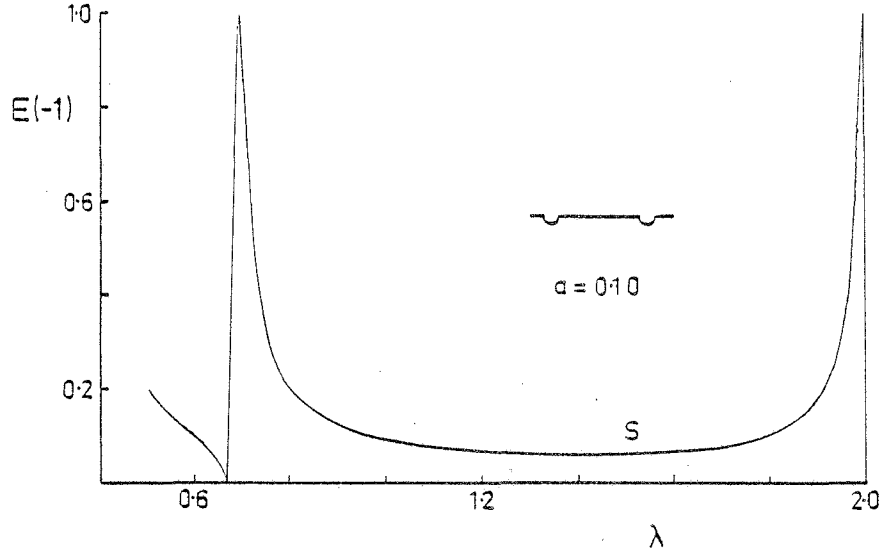

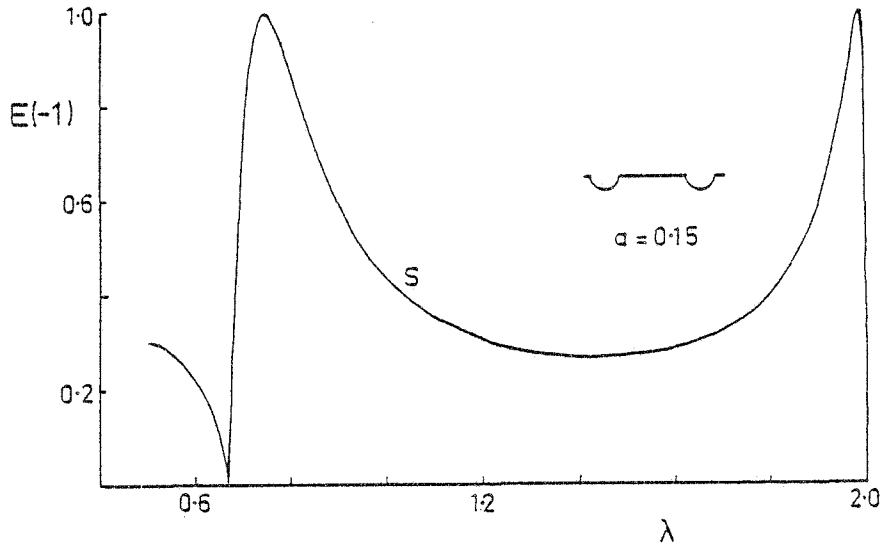

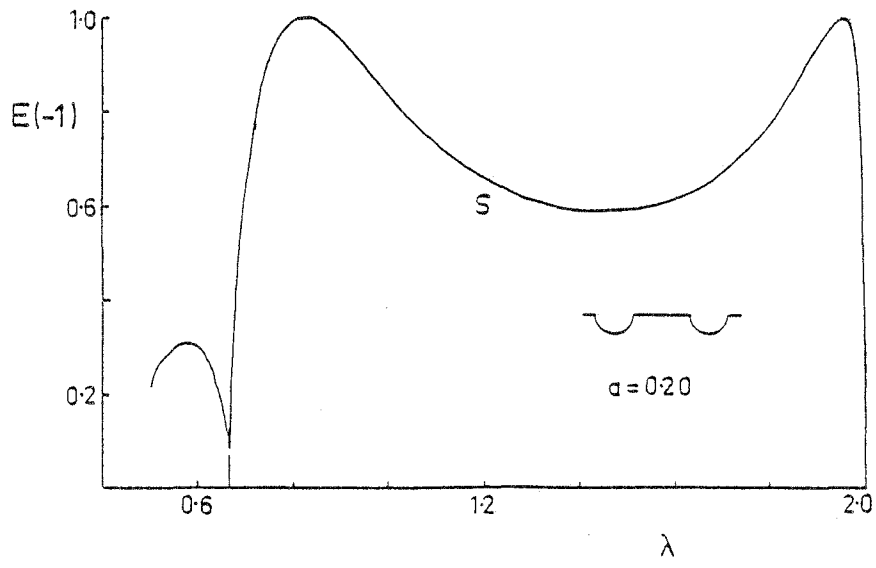

-1 Littrow Mounting

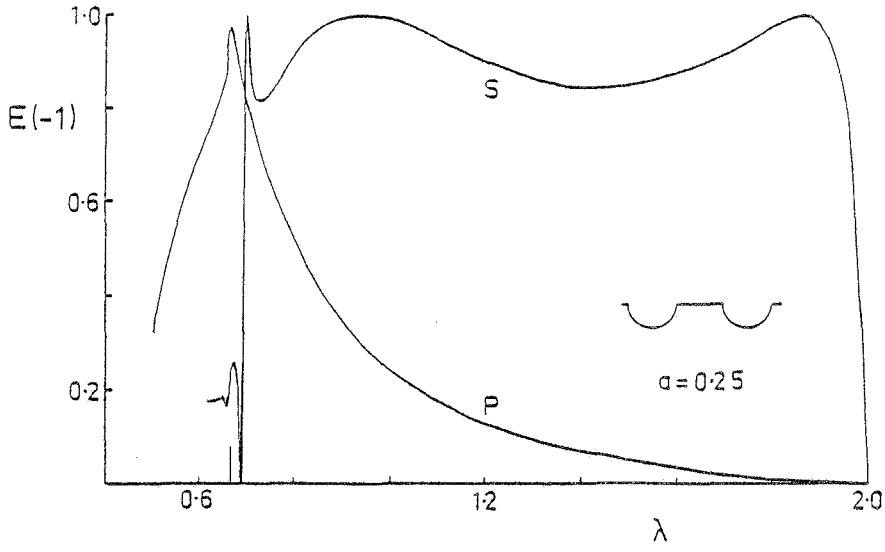

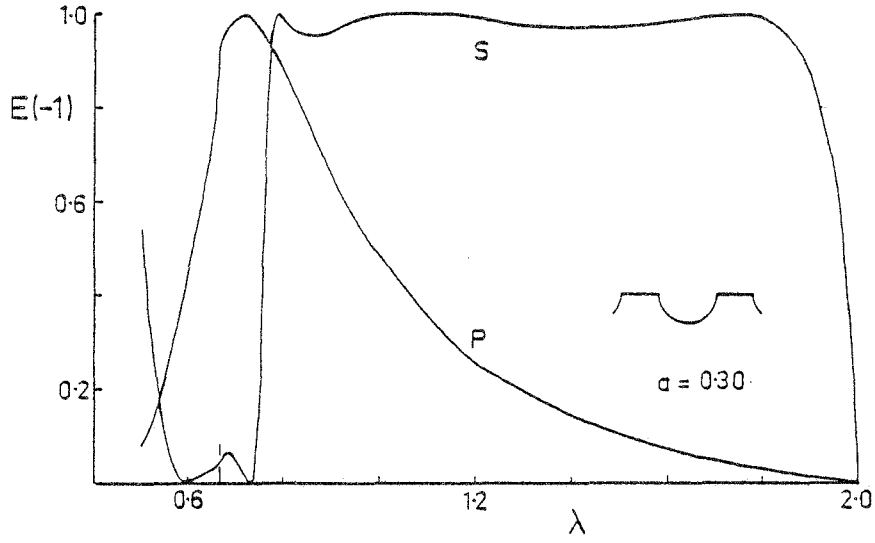

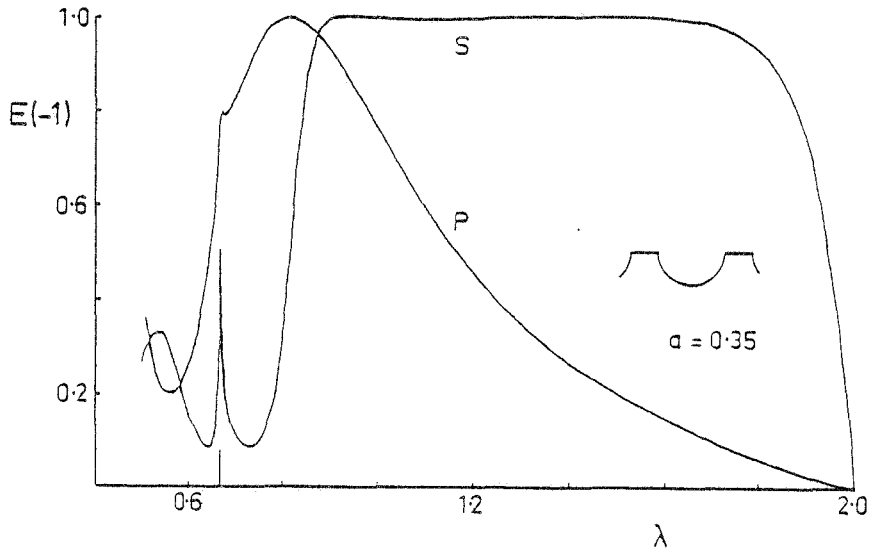

-1 Littrow Mounting

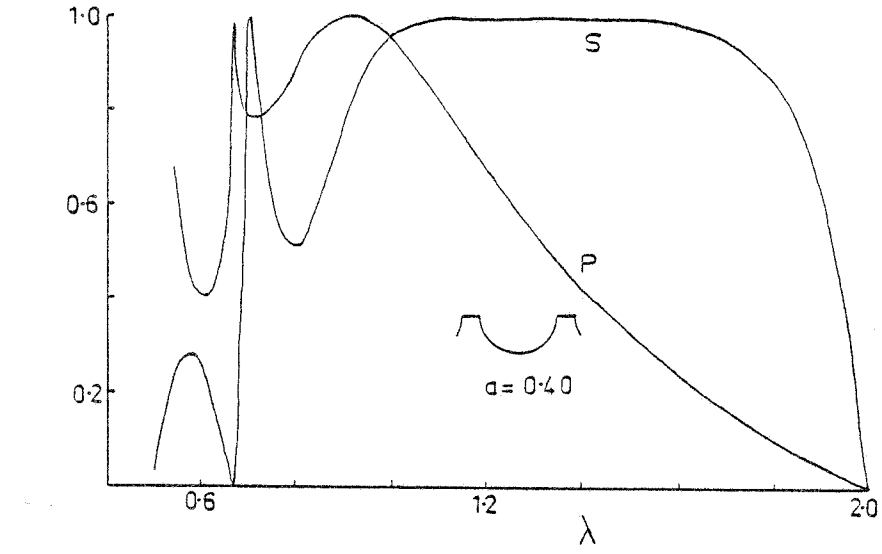

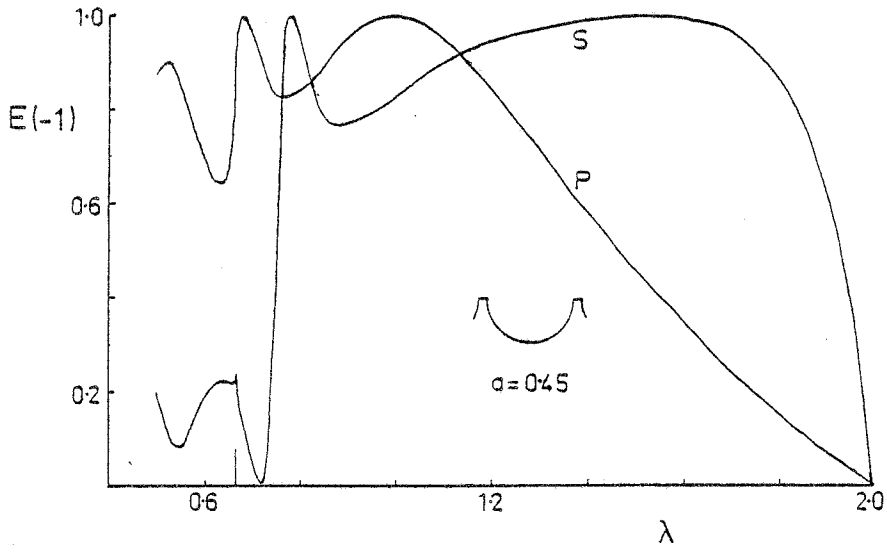

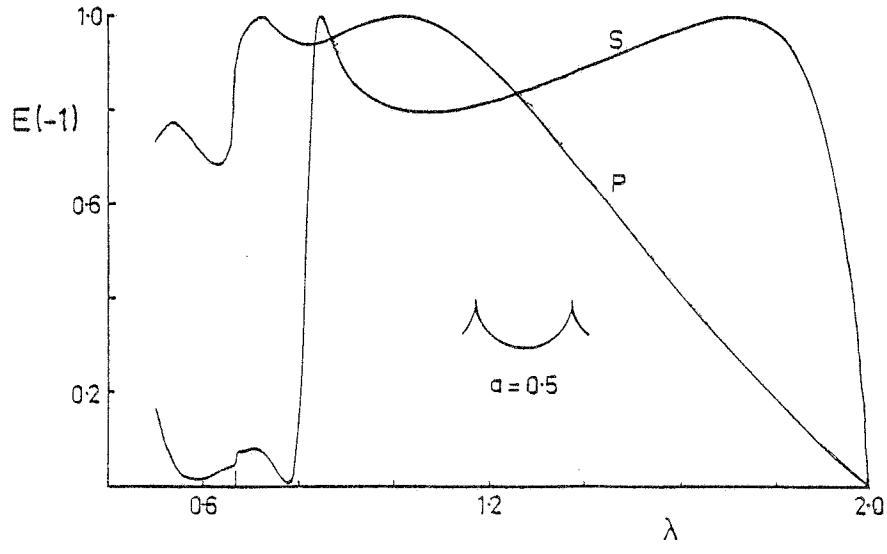

-1 Littrow Mounting